UNIVERSITÉ DE GENÈVE
Département d'astronomie

FACULTÉ DES SCIENCES
Professeur T. J.-L. Courvoisier

Dust in normal and active galaxies as observed by the Infrared Space Observatory and the Hubble Space Telescope

THÈSE

présentée à la Faculté des sciences de l'Université de Genève
pour obtenir le grade de Docteur ès sciences,
mention astronomie et astrophysique

par

Maria del Carmen POLLETTA

de

Italie

Thèse N° 3246

GENÈVE
Atelier de reproduction de la Section de physique
2001

Contents

Acknowledgments

I have somehow managed to finish my Ph.D. It has been among the most challenging experiences I have ever faced in my life (and I hope it will remain on the top of the list), but also one that taught me the most. I hesitated a lot in the course of these years and I thought to give up many times. Since I am still here, writing the last lines of this thesis, it is thanks to the precious support of those that assisted me during this journey. I am very indebted to all of them and glad to have this white page to thank them.

I will be always obliged to Prof. Thierry Courvoisier for his guidance and support and for being so efficient in pushing me when I needed it. I appreciated very much his advice, it will follow me wherever I go. He was an inexhaustible source of motivation and enthusiasm throughout this Ph.D., even at the tenth reduction of the ISOPHOT data. He gave me the freedom to explore each problem and to pose new questions myself, so that I could develop the creative problem-solving skills needed to do original research. He made me grow, not only as a scientist, but also as a person. For this, I am forever grateful.

It is a great pleasure for me to thank Prof. Nick Scoville. I admire his approach to unsolved problems and to statements that are generally accepted within the astronomical community. I enjoyed his stimulating professionality, his engaging enthusiasm and his ability to incorporate a personable exchange within a working environment. I owe him many thanks for his teachings about astrophysics, relationships and life. I also thank him for giving me the opportunity to work in CalTech, to collaborate with him and to analyse wonderful data. I consider me very fortunate to have met him.

I would like to thank Prof. Gilbert Bürki, Prof. Daniel Pfenniger and Prof. Martin Ward for accepting to be members of my committee. Their objective opinion about my thesis research means a lot for me and will be important for my next steps in the professional world.

This adventure would have never started without the help of Prof. Giorgio Palumbo. I thank him for helping me at the beginning when I was anxious to start a Ph.D. abroad and for taking care of me with his advice and encouragements.

I was helped in my work by several collaborators, Dr. Belinda Wilkes, Dr. Eric Hooper, Dr. Susan Stolovy and Shawn Ewald. I acknowledge them for answering many questions and teaching me many interesting things. A special thanks to Eric for his patience in helping me to improve my written English and to Shawn for welcoming me at my arrival at CalTech and introducing me to L.A.'s many restaurants, parks, ballrooms and pubs.

I would like to thank Prof. Louis Martinet for his stimulating lectures and the interesting conversations we had.

I could not deal with administration without the invaluable help of Martine Logossou. I thank her also for taking care of my mail during my long stay in the United States and for not letting me feel like the only alien from the female's planet in this male's world.

So unfriendly and mysterious, yet necessary were my daily co-workers, the computers. I owe many thanks to those who helped me in dealing with them, Alain and Jurek at the ISDC, Dennis and Gilles at the Observatory of Geneva and Patrick at CalTech.

The last months were not the hardest of this whole Ph.D., but they were difficult and sometimes I was not very patient. I thank all my friends, colleagues and roommates for supporting me. A special thanks to Marc Türler for helping me with LaTeX and Gimp. I am

very thankful to Greg for the wonderful routines he wrote for me and also for his immense patience, moral support and caring.

The working ambiance at the ISDC was pleasant and friendly thanks to several friends and colleagues. In particular, I wish to thank Nicolas M. for being a friend, Laurent for lodging me on several occasions and for his delicious dinners, Sandrine for helping me with the *Résumé* and Pierre for his advice and kindness. Many thanks also to past friends and colleagues; Davide for sharing good and bad moments, Marielle for her friendship and Stéphane for making me understand the difference between a good and a bad scientist.

I would like to mention a special thanks to Alexandre, he has been on my side for most of these years. His support and encouragement were a large part of what kept me going. His presence in my life provided balance and happiness.

I wish to have seen my family more often during these last years. I thank my mother for her love and caring at all times, for never making feel me guilty of my long absences and short presences and for always letting me know her thoughts. Thanks to my sister for taking care of my mother, for picking me up at the train station every time I was back, for lending me her car whenever I needed, for the other thousands of favours she made for me and, especially, for her love. I apologize to my brother for having missed all his performances, and for not being more present in his life.

I have made many friends along the way. They have helped me, one way or another, in my endeavour to complete my Ph.D. by sharing common experiences, frustrations, ideals and dreams. A special thanks to my friends Claudio, Marc, Francesco, Laurent J., Jérôme, Sandra, Maria Rita and Stan.

I extend a special thanks to my best friends, Tersilla, Paolo and Valeria, who helped me get through these years with their daily e-mails and friendship.

I would like to acknowledge the Observatory of Geneva, the INTEGRAL Science Data Centre and CalTech for supporting me logistically and financially during my Ph.D. research. This work has been mainly founded by the University of Geneva and by the FNS (*Fonds national suisse*). Several travels and participation to international meetings were financially supported by the Swiss Society for Astrophysics and Astronomy, the *Fonds T. et F. Turrettini* and by CalTech.

As I close this chapter of my life and I look back to these last years, I realize how much I changed. This Ph.D. was not only what is written in this thesis, but above all, a very rich personal experience.

Remerciements

J'ai réussi, d'une manière ou d'une autre, à finir mon doctorat. Il a été une des épreuves les plus difficiles de ma vie, mais aussi une qui m'a beaucoup enseigné. J'ai beaucoup hésité au cours de ces années et j'ai pensé d'arrêter plusieurs fois. Si je suis encore ici, en train d'écrire les dernières lignes de cette thèse, c'est grâce au soutien précieux de ceux qui m'ont aidé pendant ce voyage. Je suis très reconnaissante à eux tous et heureuse d'avoir cette page blanche pour les remercier.

Je serai toujours très reconnaissante envers Monsieur le Professeur Thierry Courvoisier pour sa direction, son soutien et pour avoir su me motiver dans les moments difficiles. J'ai beaucoup apprécié ses conseils, je les garderai toujours avec moi partout où je serai. Il a été une source inépuisable d'encouragement et d'enthousiasme au cours de ces années de doctorat, même à la dixième réduction des données ISOPHOT. Il m'a permis d'aborder différentes questions en pleine liberté, en me permettant ainsi de développer des outils originaux pour résoudre plusieurs problèmes, nécessaires à réaliser une recherche originale. Il m'a fait grandir, non seulement comme scientifique, mais aussi comme personne. Pour ceci, je lui serai reconnaissante à jamais.

C'est un grand plaisir pour moi de remercier Monsieur le Professeur Nick Scoville. J'admire son attitude devant les problèmes irrésolus et les pensées généralement acceptées dans la communauté astronomique. J'ai apprécié sa façon de travailler très stimulante, son enthousiasme contagieux et sa capacité à incorporer des échanges personnels dans un environnement de travail. Je le remercie pour ses enseignements sur l'astrophysique, les relations humaines et la vie en général. Je le remercie aussi pour m'avoir donné la possibilité de travailler à CalTech, de collaborer avec lui et d'analyser des données magnifiques. Je me considère très chanceuse de l'avoir rencontré.

J'aimerais remercier Messieurs les Professeurs Gilbert Bürki, Daniel Pfenniger et Martin Ward pour avoir accepter d'être membres de mon comité de thèse. Leur avis objectif sur mon travail de recherche signifie beaucoup pour moi et sera important pour mes prochaines étapes dans le monde professionnel.

Cette aventure n'aurait jamais pu commencer sans l'aide de Monsieur le Professeur Giorgio Palumbo. Je le remercie pour m'avoir aidé quand j'étais anxieuse de faire un doctorat à l'étranger et pour ses conseils et encouragements.

J'ai été aidé dans mon travail par plusieurs collaborateurs, Dr. Belinda Wilkes, Dr. Eric Hooper, Dr. Susan Stolovy et Shawn Ewald. Je leur suis très reconnaissante pour avoir répondu à beaucoup de mes questions et pour leur enseignements intéressants. Un spécial merci à Eric pour sa patience en m'aidant à améliorer mon anglais écrit et à Shawn pour m'avoir accueilli à mon arrivée à CalTech et pour m'avoir fait explorer les innombrables restaurants, parcs, salles de bal et pubs de Los Angeles.

J'aimerais remercier Monsieur le Professeur Louis Martinet pour ses cours très stimulants et pour les conversations intéressantes que nous avons partagé.

Je n'aurais pas pu m'occuper des taches administratives sans l'aide inestimable de Madame Martine Logossou. Je la remercie aussi pour s'être occupée de mon courrier pendant mon séjour aux États Unis et pour ne m'avoir pas fait sentir comme le seul être venant de la planète des femmes dans ce monde d'hommes.

Si hostiles et mystérieux, pourtant nécessaires étaient mes collaborateurs quotidiens, les ordinateurs. Je remercie grandement tous ceux qui m'ont aidé à les gérer, Alain et Jurek à l'ISDC, Dennis et Gilles à l'observatoire de Genève et Patrick à CalTech.

Les derniers mois n'ont pas été le plus durs de ce doctorat, mais ils ont été difficiles et parfois je n'ai pas été très patiente. Je remercie tout mes amis, collègues et colocataires pour m'avoir supporté. Un spécial merci à Marc Türler pour m'avoir aidé avec LaTeX et Gimp. Je suis très reconnaissante à Greg pour les programmes magnifiques qu'il a écrit pour moi et aussi pour son immense patience, soutien et amour.

L'ambiance de travail à l'ISDC était agréable et amicale grâce à plusieurs amis et collègues. En particulier, je souhaite remercier Nicolas M. pour être un ami, Laurent pour m'avoir loger en plusieurs occasions et pour ses délicieux dîners, Sandrine pour m'avoir aidé avec le résumé et Pierre pour ses conseils et sa gentillesse. Un grand merci aussi aux amis et aux collègues du passé, à Davide pour avoir partager les bons et les mauvais moments, à Marielle pour son amitié et à Stéphane pour m'avoir fait comprendre la différence entre un bon et un mauvais scientifique.

Je tiens a remercier très chaleureusement Alexandre, il a été à mes côtés pendant la plupart de ces années. Son soutien et encouragement ont grandement contribué à me faire continuer dans cette aventure. Sa présence a apporté équilibre et bonheur dans ma vie.

J'aurais aimé avoir visité ma famille plus souvent durant ces dernières années. Je remercie ma mère pour son amour et attention à tout instant, pour ne m'avoir jamais fait sentir coupable de mes longues absences et courtes présences et pour m'avoir toujours fait connaître ses pensées. Un grand merci à ma soeur pour s'être occupée de ma mère, pour être venue me chercher à la gare à chaque fois que je rentrais, pour m'avoir prêté sa voiture quand j'en avais besoin, pour les autres milliers de faveurs qu'elle a fait pour moi et, surtout, pour son amour. Je m'excuse auprès de mon frère pour avoir manqué tous ses spectacles et pour ne pas avoir été plus présente dans sa vie.

J'ai rencontré beaucoup d'amis en cours de route. Ils m'ont aidé, d'une façon ou d'une autre, du début à la fin de ce doctorat en partageant expériences, frustrations, idéaux et rêves. Un spécial merci à mes amis Claudio, Marc, Francesco, Laurent J., Jérôme, Sandra, Maria Rita et Stan.

J'aimerais remercier mes meilleurs amis, Tersilla, Paolo et Valeria, qui m'ont aidé au cours de ces années avec leurs quotidiens courriers électroniques et leur amitié.

Je suis très reconnaissante à l'observatoire de Genève, l'*INTEGRAL Science Data Centre* et CalTech pour m'avoir soutenu logistiquement et financièrement pendant mon doctorat. Ce travail a été principalement financé par l'Université de Genève et par le Fonds National Suisse. Plusieurs voyages et participation à des réunions internationales ont été financièrement soutenus par la Société Suisse d'Astrophysique et d'Astronomie, par les Fonds T. et F. Turrettini et par CalTech.

Ainsi je conclues ce chapitre de ma vie, je regarde en arrière et je réalise combien j'ai changé. Ce doctorat n'a pas été seulement ce qui est écrit dans cette thèse, mais surtout, une expérience personnelle très enrichissante.

Abstract

The effects of dust in galaxies and its interplay with other galactic components (stars, ionized and neutral gas) form the main subject of this thesis. The properties of the dust in normal and active galaxies, as absorber of optical and ultraviolet light and as emitter of infrared radiation are analyzed.

Two observational programs have been developed aimed at collecting large sets of optical and infrared data for a sample of active galaxies and for the grand design spiral galaxy M51 using the Infrared Space Observatory (ISO) and the Hubble Space Telescope (HST).

A sample of 22 active galactic nuclei, Seyfert and quasars, was observed at several wavelengths between 3 and 200 μm with the Imaging Photo-Polarimeter (ISOPHOT) on board ISO. The measured spectral energy distributions are presented and analyzed.

The infrared emission and the dust properties of the Narrow Line Seyfert 1 (NLSy1) galaxies are discussed. NLSy1 galaxies have similar infrared luminosities and spectra as "classical" Seyfert 1 galaxies. A comparison between the infrared spectral indexes and the optical emission line intensities suggests an anisotropic dust distribution and different degrees of absorption according to the inclination of the line of sight.

The properties of the infrared emission in radio loud and radio quiet quasars are analyzed and compared. The observed infrared emission in all quasars is thermal radiation from dust heated by the optical and ultraviolet radiation field associated to the AGN. A starburst can contribute to the observed infrared emission, but always less than the AGN ($\leq$27%).

The high spatial resolution and good sensitivity provided by the optical (WFPC2) and near-infrared (NICMOS) cameras on board HST show several new structures in M51 with an unprecedented detail.

From the measurements of the spatial displacements between molecular clouds, young star associations and HII regions, a maximum timescale of 4 Myrs between the beginning of the molecular gas compression and the formation of massive stars is estimated. The distribution of starforming sites along the spiral arms suggests a link between the star formation process and the spiral structure itself.

A sample of 1882 HII regions has been catalogued in the central (R<5 kpc) region of M51. Their size, luminosity, density, spatial distribution and extinction are measured and analyzed. The amount of extinction that affects the ionized gas in HII regions is measured using the ratio between the recombination lines H_α and Pa_α. The average extinction is ~ 3.2 mag. A model has been developed which predicts the amount of ionizing photons emitted by a distribution of OB star clusters. By comparing the observed luminosity function of the HII regions with the output of the model, the range and the spectrum of cluster masses are constrained. The maximum mass of a OB star cluster is interpreted as a saturation limit in the process of star formation in a molecular cloud.

In this work, original methods for the reduction of ISOPHOT and WFPC2 data are also presented. These new methods were developed because the standard reduction procedures could not be applied to the presented data.

Résumé

1. Introduction

Les galaxies sont des systèmes riches de gaz et poussières, éléments à partir desquels de nouvelles générations d'étoiles se forment. Comme ces étoiles vieillissent et meurent, elles éjectent une partie de leur masse dans l'espace, qui, en se mélangeant avec le gaz ambiant, forme la matière interstellaire. La matière interstellaire représente seulement quelques pourcent de la masse d'une galaxie (10% dans notre Galaxie). La plupart de ce milieu est composé de gaz ($\sim$ 99%) et une petite fraction ($\sim$ 1%) de poussières. Même si les poussières ne sont pas très abondantes, elles peuvent avoir des effets importants sur l'apparence d'une galaxie à cause de sa grande opacité à différentes fréquences, de 10^{14} Hz ($\sim$ 3 μm) dans l'infrarouge proche, à 2-3$\times10^{18}$ Hz ($\sim$ 10 keV) dans le domaine des rayons X. L'extinction due aux poussières peut modifier les paramètres photométriques de galaxies, tels que les profils de brillance, les luminosités et les couleurs, selon la quantité de poussières et sa distribution spatiale. Le rayonnement absorbé est ensuite réémis à des longueurs d'ondes plus grandes (infrarouge), cela modifie la distribution spectrale d'énergie ou SED (de l'anglais *spectral energy distribution*) des galaxies. Les poussières sont souvent associées aux bras spiraux des galaxies disques, aux noyaux de galaxies, aux bars et aux régions de formation stellaire. Leurs effets ont une influence importante sur notre interprétation de questions diverses:

1. les interactions entre les différentes composantes de la matière interstellaire et de celles-ci avec les étoiles;

2. le nombre d'objets absents dans les échantillons sélectionnés dans les rayons X, optiques et ultraviolets, parce qu'obscurci par les poussières;

3. les sources d'émission dans les noyaux de galaxies cachées par les poussières;

4. les différences spectrales entre les galaxies actives de type 1 et de type 2 et leur dépendance envers la masse et la distribution des poussières.

L'étude des effets des poussières dans les galaxies, l'investigation de leur rôle et leur interaction avec les autres composantes galactiques sont de première importance dans la compréhension des processus physiques qui ont lieu dans les galaxies.

Les signes les plus remarquables d'absorption de poussières dans les galaxies sont observés aux longueurs d'ondes optiques et, en particulier, sur les images de galaxies relativement proches avec une résolution spatiale capable de résoudre des objets avec une taille de quelques parsecs[1]. La meilleure résolution actuellement à disposition dans le domaine optique et proche infrarouge est fournie par le Télescope Spatial Hubble (HST). Dans l'infrarouge, les effets d'absorption peuvent être réduits de plusieurs ordres de magnitude par rapport aux observations optiques. Donc, la comparaison d'observations dans l'infrarouge proche et dans l'optique est un outil puissant pour l'estimation de la quantité d'extinction subie par la lumière stellaire.

[1] 1 parsec $\simeq 3.085\times10^{18}$ cm

Puisque les poussières rayonnent à des longueurs d'ondes plus longues (infrarouge moyen et lointain) que celles qu'elles absorbent, les mesures de quantité de poussières, de température et d'opacité peuvent être obtenues par des observations dans l'infrarouge moyen et lointain. Ces longueurs d'ondes sont inaccessibles du sol à cause de l'absorption de l'atmosphère et nécessitent une instrumentation spatiale. Le lancement de l' Observatoire Spatial Infrarouge (ISO) en 1996, sensible aux longueurs d'ondes infrarouge, a permis de pénétrer les régions poussiéreuses de galaxies.

Dans cette thèse, les propriétés (la distribution spatiale, la température, la source de chauffage, l'opacité, la masse) des poussières dans les galaxies, comme absorbant de lumière optique et ultraviolette et comme émetteur de rayonnement infrarouge sont examinées et discutées.

Deux programmes d'observations ont été développés sur la base d'une large base des SED dans l'infrarouge pour un échantillon de galaxies actives, Seyfert et quasars, et d'images à haute résolution dans l'optique et l'infrarouge pour la galaxie spirale M51. Les observations ont été principalement exécutées avec ISO et HST.

L'émission infrarouge des galaxies actives a été étudiée afin de comprendre son origine (thermique et/ou non-thermique), estimer les propriétés et le rôle des poussières dans les différents types (1 et 2) de galaxies actives et vérifier les prédictions du modèle unifié. L'échantillon de galaxies actives a été observé dans toute la bande spectrale infrarouge avec le *Imaging Photo-Polarimeter* ISOPHOT à bord d'ISO. Dans la suite, nous ferons référence à cette étude comme le **Projet ISOPHOT**.

La galaxie spirale M51 montre une variété intéressante de composantes et d'activités (de spectaculaires bras spiraux, un noyau actif, un jet radio, une barre, de grands ensembles de nuages massifs, des associations très brillantes d'étoiles massives en formation, de larges structures de poussières). Cette richesse de structures, ajoutée à sa proximité et sa petite inclinaison, font de M51, un des meilleurs laboratoires pour les études sur la structure galactique, sur la matière interstellaire et sur la formation stellaire. Ces questions sont traitées dans la deuxième partie de cette thèse, qui est basée sur une série d'observations optiques et infrarouges obtenues avec WFPC2 et NICMOS à bord de HST. Dans la suite, nous ferons référence à cette étude comme le **Projet HST**.

2. Le Projet ISOPHOT

Noyaux actifs de galaxies

Une galaxie active se distingue d'une galaxie classique par les composantes et les phénomènes très énergétiques régnants au sein du noyau. Pour cette raison on peut aussi utiliser la notion de noyau actif de galaxie ou AGN (de l'anglais *Active Galactic Nucleus*) à la place de galaxie active. Les régions centrales des AGN (un disque d'accrétion qui entoure un trou noir supermassif, selon le modèle standard d'unification (Antonucci 1993)) sont très brillantes à haute énergie (c.-à-d., dans l'ultraviolet et les rayons X). Au dessus de la source de haute énergie on distingue deux régions constituées de nuages de gaz ionisé, une qui s'étend de 0.01 à 0.1 parsec (1 parsec dans les quasars) caractérisée par une densité et des vitesses importantes (densité $\sim 10^{8-12}$ cm^{-3}, vitesse $\sim 10^{3-4}$ km s^{-1}), appelée région à raies larges ou BLR (de

l'anglais *Broad Line Region*). Une deuxième région s'étend à de plus grandes distances (100 parsec → 1kpc), avec de plus petites densités (10^{3-6} cm^{-3}) et vitesses (10^{2-3} km s^{-1}). Elle est appelée région à raies étroites ou NLR (de l'anglais *Narrow Line Region*). La BLR est une source de raies d'émission avec une largeur typique de 5000-20 000 km s^{-1} produites par le gaz qui est photo-ionisé par le rayonnement provenant de la source centrale. La NLR est aussi rayonnée par le flux d'énergie de la source centrale, mais sa plus grande distance et donc ses plus faibles vitesses font que les raies émises sont plus étroites (typiquement 100-2000 km s^{-1}). Ses faibles densités donnent lieu à des transitions interdites qui produisent des raies comme la raie de l'oxygène [OIII]λ5007Å.

A partir des régions plus extérieures du disque d'accrétion s'étend une distribution de gaz moléculaire et de poussières jusqu'à 1 kpc environ. Cette structure a une forme de tore, ce qui permet au rayonnement émis par la source centrale de s'échapper directement dans les zones d'ouvertures du tore (deux cônes symétriquement opposés), et bloque le rayonnement émis dans la direction parallèle au plan du tore à cause de l'interaction avec le tore même. Le rayonnement émis, après avoir interagit avec les poussières distribuées dans le tore, sera modifié sur tout le spectre électromagnétique selon la quantité de poussières, leur distribution, leur facteur de couverture et leur composition. Le tore moléculaire peut être une source importante de rayonnement infrarouge, puisqu'il est exposé à une importante source de chauffage provenant de l'AGN. Le rayonnement infrarouge peut être produit aussi par d'autres sources, comme les régions de formation stellaires dans la galaxie, puisque les étoiles jeunes sont des sources importantes de rayonnement ultraviolet et sont d'habitude entourées par des poussières. Une autre source d'émission infrarouge, observée dans les AGN radio bruyants est le jet radio: une structure très étendue en longueur et collimatée qui émet par du rayonnement synchrotron des fréquences radio aux rayons X. Le rayonnement émis par le jet peut, parfois, être dominant sur les autres composantes à cause du fait qu'il est collimaté et que son rayonnement peut être amplifié par l'effet Doppler.

Selon la présence du jet et la direction de la ligne de visée par rapport au plan du tore le spectre observé sera différent et l'AGN sera classifié comme galaxie de Seyfert, quasar ou radio galaxie de type 1 ou 2. Un schéma du modèle unifié est montré en Figure 2.4 dans le chapitre 3. Les différentes composantes et la classification des objets sont aussi indiqués.

Pour comprendre l' énergétique et la physique des AGN, il est nécessaire de déterminer les sources d'énergie qui contribuent à chaque fréquence et de séparer l'émission incidente de celle qui a été absorbée et réémise.

Objectifs scientifiques du projet ISOPHOT

Les questions principales sur lesquelles le projet ISOPHOT a été développé concernent les propriétés de l'émission infrarouge et des poussières dans les AGN, à savoir:

- Le mécanisme de rayonnement qui produit l'émission dans l'infrarouge lointain observée dans les AGN (non-thermique ou thermique).
- La distribution des poussières (dans les régions de formation stellaire et/ou dans le tore moléculaire).
- La source du rayonnement de chauffage des poussières (les étoiles en formation et/ou le disque d'accrétion).
- Les propriétés (température, opacité) des poussières.

- Le lien entre les sources d'émission infrarouge et radio.
- La compatibilité des propriétés du spectre infrarouge et des poussières dans les AGN avec le modèle unifié.

Ces questions peuvent être étudiées si on connaît la distribution spectrale dans les domaines radio et infrarouge d'un échantillon complet d'AGN et si on peut en contraindre la variabilité.

La décomposition spectrale est nécessaire pour distinguer les mécanismes d'émission produisant la SED observée, pour contraindre les propriétés des sources d'émission et leurs interactions. Le degré de variabilité peut confirmer la nature non-thermique de l'émission. Les variations sur des temps relativement courts peuvent être expliquées seulement si l'origine de l'émission est non-thermique, tandis que l'émission thermique ne devrait pas varier sur l'échelle de temps d'un an.

Ce type d'étude a pu être réalisée grâce aux observations d'ISOPHOT. ISOPHOT a fourni, pour la première fois, la possibilité de mesurer la SED des AGN dans l'infrarouge en mettant à disposition un grand nombre de filtres (25) sur un vaste domaine spectral (3–200 μm large).

Résultats

Les résultats du projet ISOPHOT sont contenus dans les publications suivantes:

ISOPHOT observations of narrow line Seyfert 1 galaxies.
M. Polletta, T.J.-L. Courvoisier, publié dans A&A 350, 765-776 (1999).

The Far-Infrared emission of Radio Loud and Radio Quiet Quasars.
M. Polletta, T.J.-L. Courvoisier, E.J. Hooper, B.J. Wilkes, publié dans A&A 362, 75-96 (2000).

Ces deux travaux sont résumés dans les deux sections suivantes.

2.1 Observations de galaxies de Seyfert de type 1 à raies étroites obtenues avec ISOPHOT

Les galaxies de Seyfert de type 1 à raies étroites se différencient des galaxies de Seyfert 1 classiques par les propriétés de leur spectre optique et X. Les raies permises, provenant de la BLR, sont plus larges que les raies interdites mais plus étroites que les raies de la BLR des galaxies de Seyfert 1 (500–2000 km s^{-1} dans les NLSy1 contre 5000–20 000 km s^{-1} dans les galaxies de Seyfert de type 1). Les raies interdites sont faibles par rapport à celles permises ([OIII]/H$\beta < 3$). Les spectres X sont plus raides et variables que ceux des Seyfert 1.

Les propriétés des poussières dans les galaxies de Seyfert de type 1 à raies étroites ou NLSy1 (de l'anglais *Narrow Line Seyfert 1 galaxies*) peuvent jouer un rôle fondamental dans l'explication de leurs propriétés particulières. En effet, la faible émission des raies interdites (comme l'[OIII]) et l'absence de raies larges d'hydrogène peuvent être expliquées si la majorité du flux ionisant est absorbé dans la partie intérieure de la NLR, réduisant ainsi la quantité de flux ionisant qui atteint les régions plus extérieures, et absorbant l'émission provenant de la région plus interne où les raies larges sont émises. La présence de poussières est indiquée par plusieurs observations. Des observations de spectropolarimétrie suggèrent que les poussières

sont responsables de la dispersion des photons optique (Goodrich 1989), et les observations de rayons X mou indiquent la présence d'absorption due en partie aux poussières dans quelques NLSy1 (Komossa et al. 1998). Cependant, dans l'infrarouge lointain ou FIR (de l'anglais *far infrared*), les NLSy1 montrent un haut degré de similarité avec les galaxies de Seyfert 1 classiques (Rodríguez-Pascual et al. 1997; Ulvestad 1995), ce qui suggère que les propriétés des poussières ne sont pas uniques parmi les galaxies de Seyfert.

Dans le travail présenté ici, les propriétés des poussières dans les NLSy1 sont examinées à travers l'analyse de leur émission infrarouge qui est un traceur direct des poussières (Barvainis 1990; Clavel 1989).

Un échantillon de quatre NLSy1 a été observé avec ISOPHOT entre 7 et 200 μm. Pour la réduction des données ISOPHOT une méthode originale a été développée. Les spectres infrarouge ont été analysés et ajustés par plusieurs composantes de corps gris (Gear 1988), modèle qui décrit l'émission thermique des poussières à une température bien définie (voir Figure 1). La distribution des températures, des opacités et des tailles des différentes composantes ont été mesurées. La comparaison avec les modèles courants de distribution des poussières dans les galaxies de Seyfert indique que les poussières à plus basses températures (T$\leq$60 K) sont peu opaques (N_H $\sim 1\times10^{21}\mathrm{cm}^{-2}$), alors que les poussières plus chaudes et plus proches de la source de chauffage sont caractérisées par de plus hautes opacités. Les luminosités et les spectres observés, sont similaires à ceux des galaxies de Seyfert 1 classiques. Dans trois cas les spectres observés sont compatibles avec les modèles de tore chauffé par le rayonnement émis par le noyau actif et ne nécessitent pas de source de photons supplémentaire comme par exemple une région de formation stellaire très active. Dans le cas de IRAS 13224-3809, par contre, un excès d'émission aux basses températures est observé, ce qui suggère une activité de formation stellaire importante.

Une corrélation entre les indexes spectraux entre 3 et 60 μm et les rapports des intensités des raies émises par la BLR et la NLR (H_α/H_β et [OIII]/Hβ) a été découverte. Cela est valable aussi bien pour les quatre NLSy1 observés par ISOPHOT, que pour toutes les NLSy1 (16 objets) avec des spectres infrarouge de bonne qualité et des rapports de raies mesurés. Ce résultat a suggéré une dépendance de l'absorption subie par le rayonnement émis de l'inclinaison de la ligne de visée par rapport à la distribution des poussières. Le scénario supposé est montré en Figure 2. Les régions centrales de ces objets sont probablement entourées par une distribution de poussières qui devient graduellement moins opaque le long de certaines directions. La région qui émet les raies doit s'étendre au delà des couches plus internes des poussières, puisque son émission est moins absorbée que celle des raies. Les poussières sont caracterisées par différents opacités et par une distribution anisotrope. Dans le cas où la ligne de visée traverse des régions moins opaques, la région émettrice de raies et les couches plus internes de la distribution de poussières seront moins absorbées, alors que dans le cas où la ligne de visé traverse des régions plus opaques, aussi bien les raies d'émission larges que le rayonnement produit par les poussières les plus chaudes seront partiellement absorbés. Puisque l'émission de la raie [OIII] est produite dans la NLR qui est plus étendue que la distribution de poussières, son intensité sera indépendante de la direction de la ligne de visée, mais le rapport [OIII]/H$_\beta$ augmentera à cause de la diminution du flux de la raie H$_\beta$ provenant de régions plus internes.

2.2 Les propriétés infrarouges de Quasars Radio Bruyant et Radio Silencieux

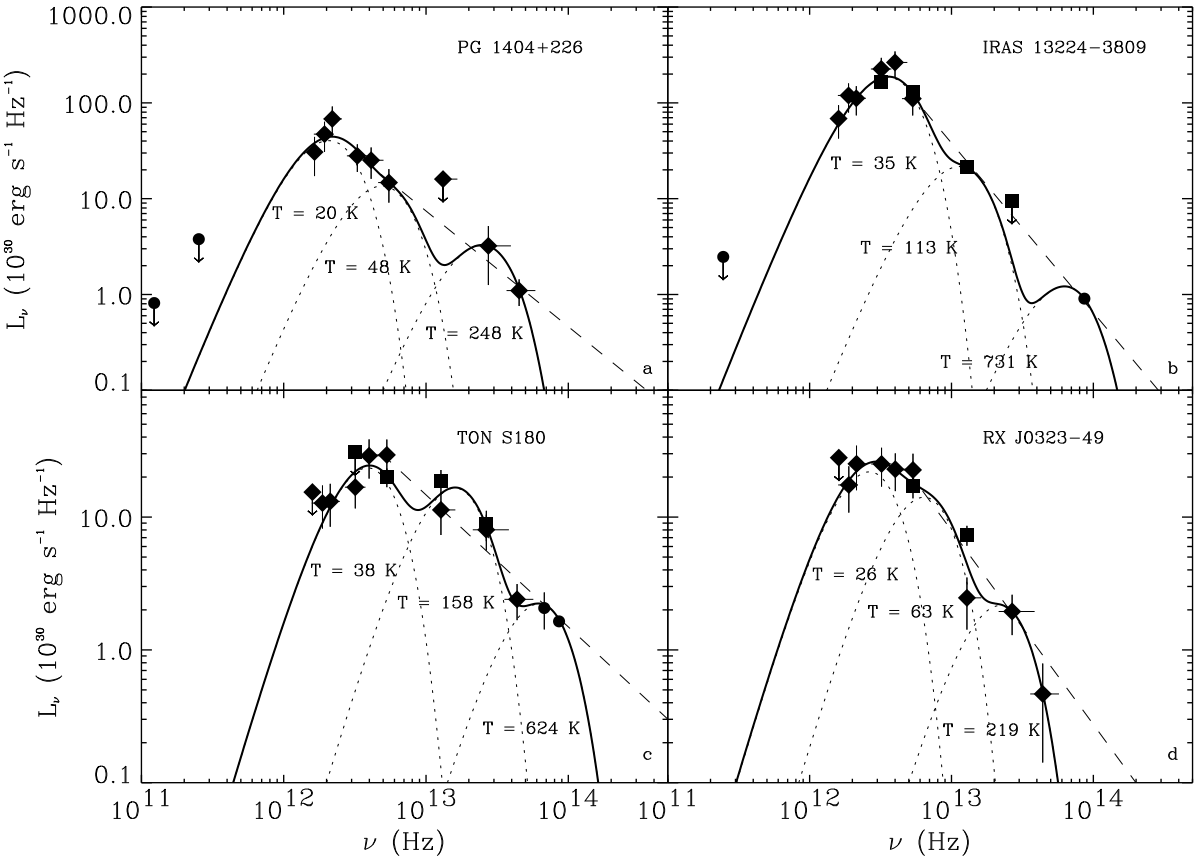

Figure 1: SED des NLSy1 PG1404+226 (a), IRAS13224−3809 (b), TONS180 (c) et RXJ0323−49 (d). Chaque courbe pointillée représente une composante de corps gris à la température indiquée. La courbe continue représente le spectre total obtenu en additionnant l'émission de chaque composante. La courbe en tiret représente une loi de puissance obtenue avec un ajustement linéaire des données entre 3 et 60 μm. Les flèches indiquent des limites supérieures à 5σ (3σ pour les données millimétriques). Les losanges représentent les données ISOPHOT, les carrés celles de IRAS et les cercles celles de IRAC1, SEST et IRAM.

Les quasars radio silencieux et radio bruyants (RQQ et RLQ, respectivement, de l'anglais *Radio Quiet Quasar* et *Radio Loud Quasar*) ont des propriétés spectrales similaires dans l'ultraviolet, l'optique et l'infrarouge, mais leurs puissances radio diffèrent de plusieurs ordres de magnitude (Elvis et al. 1994). Cette divergence a lieu aux longueurs d'ondes millimétriques où deux sources d'émission différentes coexistent, à savoir le rayonnement synchrotron émis par le jet et l'émission thermique des poussières froides (30-50 K) (Barvainis & Antonucci 1989).

L'émission radio dans les RLQ est principalement produite par un jet relativiste dont l'orientation peut produire un spectre radio plat ou raide (Urry & Padovani 1995). Sur la base du spectre radio observé, on peut classifier les RLQ comme des quasars radio bruyants à spectre plat ou FSRQ (de l'anglais *Flat Spectrum Radio Loud Quasar*), ou comme des quasars radio bruyant à spectre raide ou SSRQ (de l'anglais *Steep Spectrum Radio Loud Quasar*). La faible émission radio des RQQ vient principalement de sources compactes associées au noyau

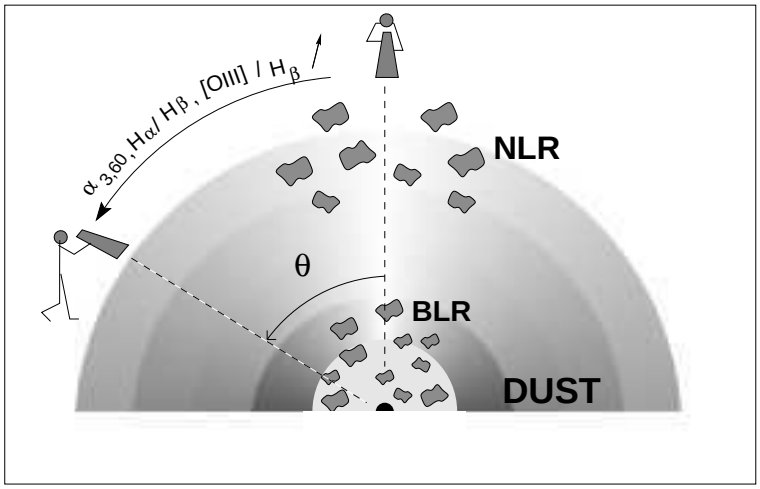

Figure 2: Représentation du scénario proposé pour expliquer les corrélations observées entre l'index spectral entre 3 et 60 μm ($\alpha_{3,60\mu m}$) et les rapports de raies H_α/H_β et [OIII]/Hβ. Les anneaux gris représentent la distribution des poussières. La température de poussières diminue à plus grands rayons, et l'opacité augmente avec l'angle θ. Les raies de la série de Balmer sont émises dans le BLR et dans le NLR. Les raies interdites, comme l'[OIII], sont émises dans la NLR après photo-ionisation du gaz de la part du flux émis de la région centrale. L'émission des poussières chaudes, près du centre, et des raies émises dans la BLR seront partiellement absorbées par la poussière à de plus grandes distances. En conséquence, pour des valeurs croissantes de l'angle θ, $\alpha_{3,60\mu m}$, le décrément de Balmer et le rapport [OIII]/H_β augmenteront. (Le flux dans la raie de l'oxygène reste inchangé parce qu'émis dans la NLR qui s'étend au delà de la distribution des poussières.)

(Kukula et al. 1998), probablement un jet radio avec une puissance cinétique $\sim 10^3$ fois inférieure à celle des RLQ (Miller et al. 1993). Les régions de formation stellaire associées à la galaxie hôte peuvent être aussi une source de rayonnement radio.

Plusieurs RLQ montrent des spectres infrarouge variables et polarisés. Ces observations suggèrent une origine non-thermique de l'émission infrarouge. Ceci est en général vrai pour les FSRQ, par contre plusieurs observations indiquent le contraire pour les SSRQ. Dans les SSRQ, l'émission infrarouge produite par les poussières est plus brillante que celle non-thermique produite par le jet (Antonucci, Barvainis & Alloin 1990). Parmi les RQQ, plusieurs objets montrent des spectres infrarouges qui sont trop raides pour être émis par une source non-thermique. Certaines RQQ sont riches en gaz moléculaire, ce qui indique la présence de poussières (Barvainis 1997). Ces observations sont une bonne indication en faveur d'une origine thermique de leur émission infrarouge.

Dans ce travail, les propriétés de l'émission infrarouge des RLQ et des RQQ (le mécanisme dominant qui émet, les propriétés des poussières, la source de chauffage) sont analysées. Cette étude a été effectuée sur un échantillon de 22 AGN (7 RQQ, 8 SSRQ, 3 FSRQ, 2 galaxies de radio (RG) et 2 radio quasars intermédiaires (RIQ)) en utilisant une large base de données fournis par ISOPHOT, par l'interféromètre du Plateau de Bure de l'IRAM, par SCUBA sur JCMT, et par les instruments de l'ESO, IRAC1 et SEST.

Les distributions spectrales d'énergie de tous les quasars dans l'intervalle de fréquences du radio à l'infrarouge ont été analysées et modélisées avec des composantes non-thermiques (émission synchrotron) et thermiques (émission de poussières).

Dans l'échantillon de quasars sélectionnés, le mécanisme dominant émettant dans l'infra-

rouge moyen et lointain est l'émission thermique des poussières qui sont chauffées par le rayonnement optique et ultraviolet produit dans les régions plus extérieures de l'AGN. Des sites de formations stellaires très actifs contribuent à des niveaux différents, mais toujours dans une moindre mesure que l'AGN ($\leq$27%).

Les températures d'équilibre, les tailles, les masses et les luminosités des différentes composantes des poussières ont été évaluées pour tous les quasars. Les tailles estimées varient entre 0.06 pc et 9.0 kpc, et les températures entre 43 K et 1900 K. La luminosité infrarouge totale varie de 2 à 760×10^{11} $L_\odot$. La masse des poussières recouvre un large intervalle, de 6×10^4 à 4×10^7 $M_\odot$. Les distributions de ces paramètres sont très similaires pour tous les types de quasars.

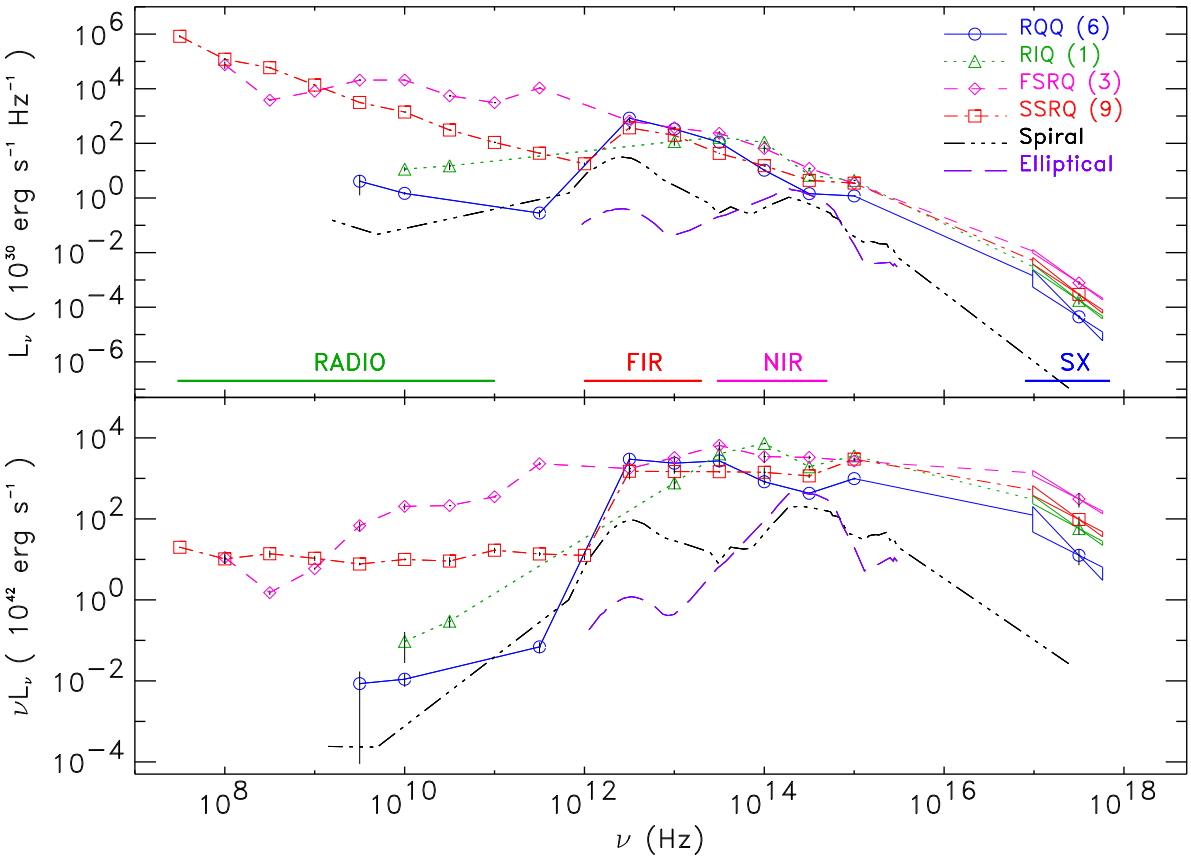

Figure 3: SED moyenne pour des échantillons de RQQ (courbe continue), RIQ (courbe pointillée), FSRQ (courbe en tiret), et SSRQ (courbe tiret-pointillée). Le nombre d'objets utilisé pour chaque classe est indiqué sur la figure avec le nom de la classe d'appartenance. Chaque symbole correspond à un intervalle de fréquence. Les SED de deux galaxies hôte sont aussi montrées: une galaxie spirale (courbe tiret-point-point-point), et une galaxie elliptique géante (courbe avec de longs tirets). Aucune normalisation n'a été appliquée.

Les différences et les similarités principales entre les différent types de quasars peuvent être déduits en comparant leurs SED moyennes montrées en Figure 3. Comme attendu (Sanders et al. 1989; Elvis et al. 1994), la plus grande différence entre les luminosités apparaît aux longueurs d'ondes radio. Une légère différence est observée à haute énergie (1 keV) et dans l'infrarouge proche ($\nu > 10^{14}$ Hz qui correspond à $\lambda < 3$ μm), alors que la luminosité et

le spectre dans l'infrarouge moyen et lointain est remarquablement similaire (voir Figure 3). Les SED de deux galaxies hôtes typiques (une elliptique géante et une galaxie spirale) dans leurs référentiels de repos sont aussi tracées en Figure 3. La grande différence du spectre infrarouge entre les quasars et les galaxies hôtes indique que la contribution de ces dernières est négligeable à toutes les fréquences. La similarité des spectres infrarouge des différents types de quasars suggère qu'afin d'obtenir des échantillons sans biais, la sélection doit être faite dans l'infrarouge moyen et lointain.

3. Le Projet HST

Le projet HST, développé au *California Institute of Technology (CalTech)* sous la direction de Monsieur le Professeur N.Z. Scoville, est basé sur une large base de données de la galaxie spirale M51 dans les domaines optique et infrarouge obtenues avec le Télescope Spatial Hubble (HST), et radio obtenues avec l'observatoire radio situé en *Owens Valley* ou OVRO (de l'anglais *Owens Valley Radio Observatory*).

M51 (NGC 5194), aussi connue comme *"Whirlpool galaxy"*, est la plus proche (9.6 Mpc de distance (Sandage et Tammann 1975)) des galaxies spirales qui présentent une structure à grande échelle, est aussi la première galaxie dans laquelle une structure spirale a été observé (Parsons 1850) et une des plus célèbres et bien étudiés systèmes en interaction. M51 est un excellent laboratoire pour étudier la structure spirale à grand échelle et la formation d'étoiles. Une image de M51 et de son compagnon est montrée en Figure 8.1.

Objectifs scientifiques du projet HST

Les questions principales qui ont constituées le sujet de cette étude sont les suivantes:

- la structure spirale, les processus physiques associés au flux de matière à travers les bras, l'emplacement de différents composants (le gaz moléculaire et ionisé, les étoiles jeunes, les poussières) le long des bras;
- la morphologie (taille typique des structures observées, leur concentration et emplacement);
- les couleurs de la galaxie à différents rayons et dans le noyau, dans les bras et dans la partie externe aux bras;
- la distribution de poussières ainsi que ses effets d'extinction et de rougissement sur la lumière stellaire de la galaxie;
- les structures nucléaires (la barre, l'AGN, les poussières);
- la formation d'étoiles massives.

Base de données

La récolte des données a commencé en 1995 et s'est terminée en 1999. Le choix de HST était fondamental puisqu'il est le seul instrument disponible avec les capacités nécessaires pour résoudre les structures galactiques, sujet de l'étude proposée.

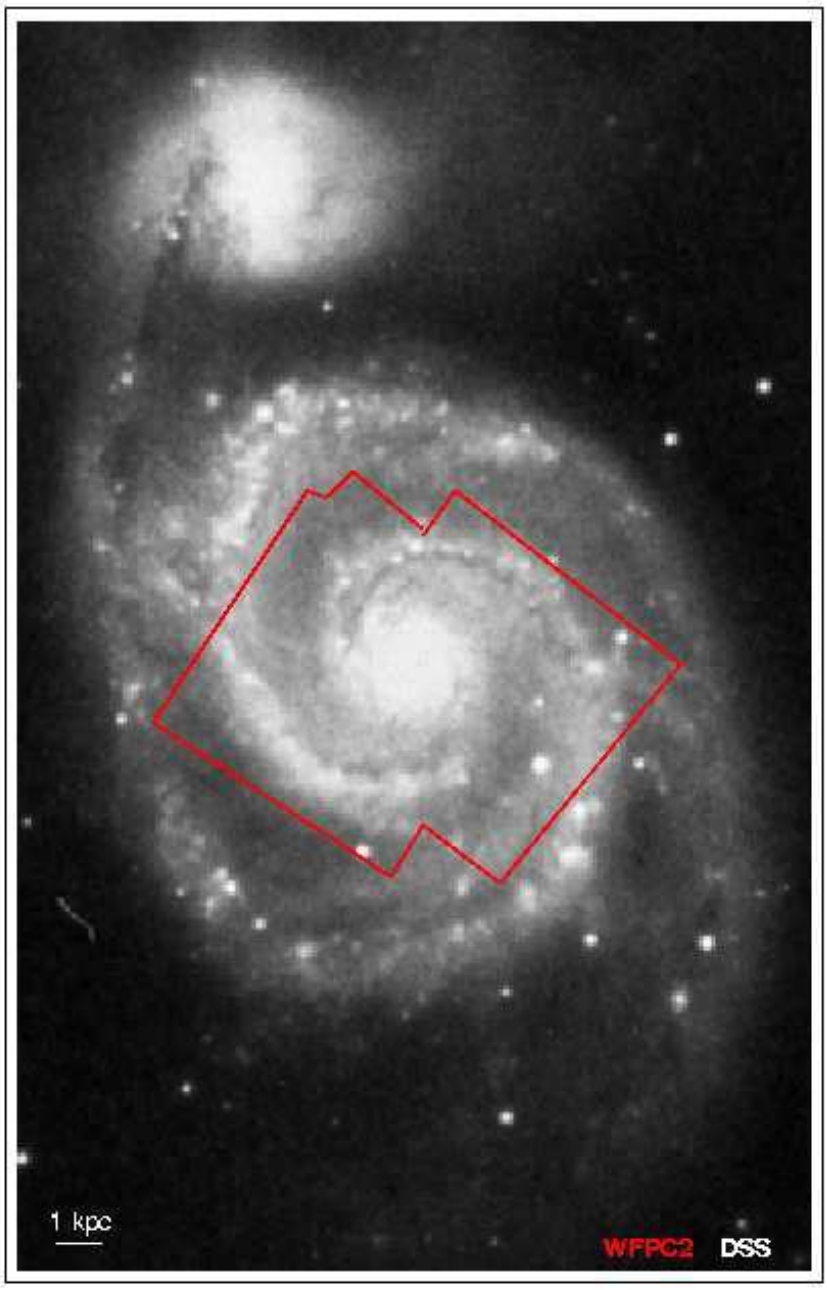

Figure 4: Image optique de la galaxie spirale M51 et de son compagnon NGC 5195. Les lignes rouges correspondent à la région observée par WFPC2. (Adapté d'une image de la *Digital Sky Survey*.)

Deux instruments à bord de HST ont été utilisés: la caméra infrarouge NICMOS, et optique WFPC2. Les observations effectuées sont les suivantes:

- Quatre mosaïques, composées de neuf images chacune, ont été obtenues avec la Caméra

3 de NICMOS, chacune avec un filtre différent. Trois filtres à bande large ont été utilisés pour mesurer le flux dans le continuum aux longueurs d'ondes 1.1 μm, 1.6μm et 2.2 μm et deux à bande étroite pour mesurer le flux dans la raie Pa_α à 1.87 μm et à 1.90μm. Le champ de vue total correspond à un carré de dimensions 2.′6×2.′6 ($\sim$ 7 kpc ×7 kpc) et la résolution spatiale est de 0.″2 par pixel.

- Trois séries d'observations effectuées avec la caméra optique WFPC2 couvrant différentes régions de M51 ont été assemblées jusqu'à couvrir un carré de dimensions 4.′7 × 3.′7 ($\sim$ 13 ×10 kpc) de la région centrale de M51. Les mosaïques ont été obtenues aux longueurs d'ondes correspondant aux filtres I (λ 8386Å), R (λ 6796Å), V (λ 5151Å) et B (λ 6796Å) pour le continuum et à la raie H_α (λ 6561Å). La résolution spatiale est de 0.″1 $\sim$ 4.6 pc per pixel et 0.″046 $\sim$ 2 pc per pixel dans une région centrale de dimension 37″×37″($\sim$ 1.7 kpc × 1.7 kpc).

  En Figure 8.1, les contours de la région observée par WFPC2, marqués en rouge, sont superposés à une image de M51 et de son compagnon prise de la *Digital Sky Survey.*

- Une région circulaire de 2.′5 de diamètre et d'une résolution spatiale de 2.″5 ($\sim$115 pc) a été observée dans la bande millimétrique correspondant à la raie de CO (2.6 mm). Ces données ont déjà été analysées, et les résultats publiés dans Aalto et al. (1999).

Résultats

L'analyse des données est encore en cours. Actuellement, un études a été sousmis et un autre est en phase de préparation:

HST Optical and Near Infrared Imaging of M51.
M. Polletta, N. Scoville, S.P. Stolovy, S. Ewald et al., en preparation

High Mass, OB Star Formation in M51: HST H_α and Pa_α Imaging.
N.Z. Scoville, M. Polletta, S. Ewald, S. Stolovy, R. Thompson et M. Rieke, 2001 sousmis à AJ

Ces travaux forment le sujet de la deuxième partie de la thèse et sont résumés dans les deux paragraphes suivants.

3.1 Étude des images obtenues avec l'HST aux longueurs d'ondes optiques et infrarouges de la galaxie M51

La haute résolution spatiale et la bonne sensibilité fournies par les instruments de l'HST ont permis d'observer avec une résolution sans précédents plusieurs nouvelles structures dans la galaxie M51. Les tailles de ces structures peuvent fournir des contraintes aux modèles théoriques utilisés pour expliquer la formation des structures galactiques. Les filaments de poussières qui tracent les deux bras spiraux ont une largeur caractéristique de 3″– 8″($\sim$ 140 – 370 pc). Dans la région entre les bras, on observe d'autres filaments de poussières de taille inférieure ($\sim$ 1″ ou $\sim$ 50 pc). Leur orientation est presque radiale, s'étendant des bras vers les régions extérieures aux bras avec une inclinaison de $\sim$ 40° par rapport aux bras. En correspondance de ces filaments on observe souvent des associations d'étoiles jeunes et

des régions HII (régions de gaz ionisées H^+). Une structure très régulière de filaments de poussières est observée dans la région centrale de la galaxie jusqu'à un rayon de ~ 1 kpc. Ces filaments sont organisés selon une structure spirale et régulièrement espacés ($\sim$72$\pm$24 pc). Ces structures sont probablement issues d'instabilités hydrodynamiques dans un disque non auto-gravitant (c.-à-d., par de la turbulence dans le gaz due à l'apport du matériel à plus grandes distances). La structure filamentaire disparaît en correspondance avec les bords de la barre stellaire située au centre. Cette dernière s'étend jusqu'à environ 600 pc de rayon le long de l'axe principal ($\sim$36° occidental du nord) et jusqu'à environ 300 pc le long de l'axe secondaire.

Le long des bras spiraux et dans une région à une distance de $\sim$1.5 kpc du centre, on observe plusieurs associations d'étoiles massives de type OB, souvent associées à des régions HII (tracées par l'émission de H_α). Ces régions sont caractérisées par une activité importante de formation stellaire. Une source de H_α très lumineuse est observée dans la région nucléaire s'étendant jusqu'à environ 200 pc du centre. Cette émission est fortement corrélée avec l'émission du jet radio. La correspondance observée suggère une interaction entre le jet et la matière environnante, c'est probablement un choc qui est à l'origine de l'ionisation du gaz.

Les profils radiaux de la luminosité des étoiles (tracée par l'émission dans les bandes larges K, H, J, I, R, V, B) et du gaz (tracé par l'émission dans les bandes étroites associées aux raies de H_α, Pa_α et CO) fournissent une estimation des effets d'extinction en fonction du rayon, dans les bras et dans les régions extérieures. Les profils deviennent de plus en plus plats en allant des longueurs d'onde longues à celles plus courtes. Ce résultat est attendu si la population d'étoiles vieilles du bulbe est plus concentrée au centre et les poussières sont distribuées dans le disque.

Puisque les bras sont des zones de formation stellaire et que l'extinction y est importante, les profils radiaux de toute la galaxie ne représentent pas bien la population du disque. C'est pourquoi les profils des bras et des régions extérieures aux bras ont été calculés séparément. Le profil exponentiel n'est pas un bon ajustement pour les profils des bras qui montrent plusieurs irrégularités. Les profils des régions entre les bras diminuent comme une fonction exponentielle, de façon similaire aux profils associés à toute la galaxie. L'aplatissement de ces profils à des longueurs d'onde plus courtes est moins prononcé que pour toute la galaxie.

La rotation des bras de M51 est telle que les étoiles et le gaz entrent dans les bras sur leurs bords intérieurs concaves et les laissent sur leurs bords externes convexes. Pendant que le gaz interstellaire traverse le potentiel gravitationnel du disque, il est périodiquement comprimé par les bras. Les nuages de gaz moléculaires interagissent avec les ondes de densité en se déplaçant vers les bras. Cette interaction, probablement sous forme de choc, provoque une augmentation de la concentration de nuages dans la zone interne des bras. Ces fronts de chocs pourraient expliquer l'excès de densité de gaz observé dans les bras (compression du gaz), et de la concentration des étoiles jeunes (formation d'étoiles) qui se sont vraisemblablement formées à partir du gaz moléculaire. Selon ce scénario, on s'attend à ce que les régions HII soient en aval des poussières et des nuages de CO.

Les étoiles massives peuvent être tracées par des observations du continu dans la bande B, le gaz moléculaire par le CO, les poussières par des couleurs infrarouge$-$optiques (par exemple V$-$H), les photons ionisants émis par les étoiles en formation par des raies de recombinaison d'hydrogène (par exemple les raies de recombinaison $H_\alpha\lambda$6563 et $Pa_\alpha\lambda$ 1.87μm).

Si on connaît la vitesse de la matière se déplaçant à travers les bras, la distance entre les différents traceurs fournie une estimation du temps qui s'est écoulé entre le début de la compression des nuages moléculaires et la formation des étoiles et des régions de HII. La vitesse

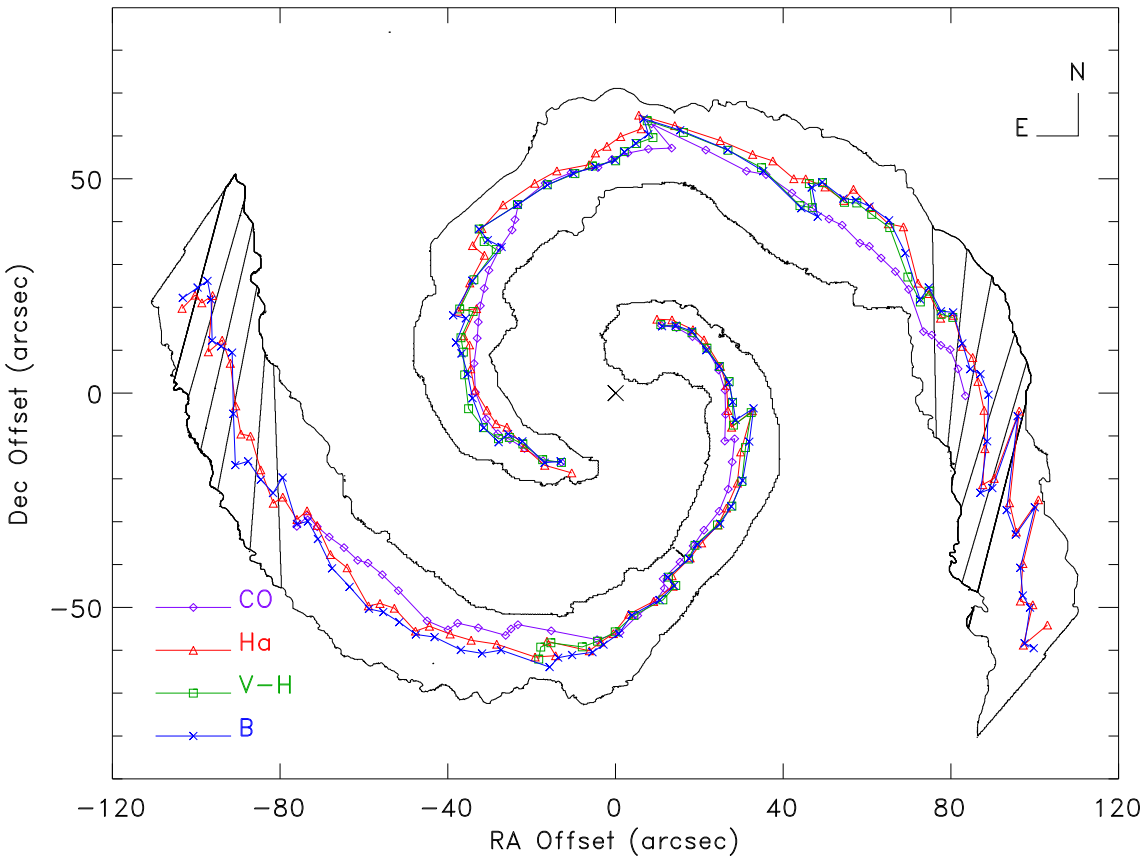

Figure 5: Positions des centroïdes le long des bras pour différents traceurs (CO en pourpre, H_α en rouge, la couleur V−H en vert et B en bleu). Les contours des bras sont tracées par la courbe pleine noire. Dans une partie des deux bras, quelques exemples des régions sélectionnées pour calculer les positions des centroïdes sont tracés.

du gaz le long la direction perpendiculaire au bras est de $\sim$ 30 km s^{-1} (Roberts et Stewart 1987). Les distances mesurées le long de la direction orthogonale aux bras sont, en moyenne, 84 et 139 pc entre l'H_α et le CO (voir Figure 5) pour les bras à NE et à SW, respectivement. Ces distances correspondent à une durée de $\sim$ 2.8 et 4.5 $\times 10^6$ ans. La distance mesurée entre le continu B et le CO est de $\sim$ 110 pc dans les deux bras, correspondant à $\sim$ 3.6 $\times 10^6$ ans. Une distance plus petite est mesurée entre la couleur V−H et le CO, $\sim$ 68 et le 97 pc, correspondant à $\sim$ 2.2 et 3.2 $\times 10^6$ ans. Le processus entier, du choc du gaz moléculaire avec le bras à l'ionisation de gaz par les nouvelles étoiles formées, prend alors environ 3-5 $\times 10^6$ ans.

3.2 Formation d'étoiles OB massives dans M51: étude des images en H_α et Pa_α

Les étoiles massives OB jouent un rôle critique dans l'énergétique et la dynamique du milieu interstellaire, dans les phases d'évolution galactique, et dans l'activité de formation stellaire dans les bras spiraux. Néanmoins, les mécanismes de formation d'associations d'étoiles OB

restent mal compris, en effet, nous n'avons aucune certitude quant aux similairités et aux différences des processus de formation des étoiles de grande et petite masse. Les régions HII tracent les propriétés des régions de formation d'étoiles massives et celles d'associations d'étoiles de type OB.

Les flux des raies de recombinaison d'hydrogène (e.g., H_α) sont proportionnels au taux d'émission du continu de Lyman émis par les étoiles massives sous l'hypothèse que tous les photons ionisant sont localement absorbés. Ainsi la luminosité en H_α est indicative de l'émission du continu de Lyman et par conséquent de la masse d'étoiles massives (après avoir corrigé par l'extinction et avoir défini une fonction de masse initiale). La fonction de luminosité des régions HII peut être utilisée alors pour étudier la distribution de masse des associations d'étoiles OB.

La population d'étoiles massives dans M51 a été étudié en utilisant les images des raies d'émission H_α et Pa_α obtenues avec WFPC2 et NICMOS sur HST. Les résolutions de 0.1 et $0.2''$par pixel des deux cameras, respectivement, correspondent à une resolution de 4.6 et 9 parsecs en M51. Le rapport des flux des deux raies, H_α/Pa_α est un indicateur d'extinction.

Une image en couleur réelle, correspondante aux $281''\times223''$ centrales de M51 observés par WFPC2, est représentée en Figure 10.1. L'image montre les régions HII en rouge superposées au continu dans les bandes I, V et B. Un échantillon de 1882 régions HII en H_α a été catalogué en utilisant un algorithme automatique. Les tailles sont distribuées dans un intervalle qui va de 10 à 100 pc. La fonction de luminosité pour les régions d'émission de H_α s'étend sur une intervalle de luminosité 10^{36} —10^{39} ergs s^{-1}. Aucune région n'a été trouvée avec une luminosité au-dessus de $L(H_\alpha) = 10^{39}$ erg s^{-1}, ce qui correspond à un facteur 6 inférieur au maximum obtenu après des études au sol. Ceci est probablement dû à la superposition de plusieurs régions de haute luminosité. Notre fonction de luminosité est aussi plus raide ($dN/dlnL \propto L^{-1.2}$) vers les plus hautes énergies de celles mesurées au sol ($L^{-0.5\rightarrow-0.8}$) — probablement dû aussi à la superposition de plusieurs régions.

Pour analyser les variations des propriétés de région de HII vis-à-vis de la structure galactique, la fonction de luminosité et les tailles des régions situées dans les bras ont été comparées avec celles situées dans la région entre les bras et la zone près du centre. Bien que les bras recouvrent seulement 30% de la surface du disque, elles contiennent 80% des régions HII. La fonction de luminosité est, en quelque sorte, plus plate dans les régions nucléaires et dans les bras que dans les zones entre les bras. Cependant, ceci pourrait être le résultat d'une superposition plus importante dans les régions à plus haute densité de surface. Aucune différence significative n'est vue dans les tailles et les densités des régions HII dans les bras ou à l'extérieur des bras.

Pour 326 régions qui ont été détectées à plus de 5 σ soit en H_α soit en Pa_α, les rapports d'intensités des raies indiquent des extinctions dans le visible, A_v, entre 0 et 5 mag. L'extinction moyenne est $A_v = 3.2$ mag. La moyenne pondérée est 2.4 mag, si le poids est associé à la luminosité observée et 3.0 si le poids est associé à la luminosité corrigée par l'extinction. En moyenne, les luminosités observées de H_α devraient être multipliées par un facteur 9.0 pour corriger les effets de l'extinction. La luminosité totale des associations OB et le taux de formation stellaires doivent aussi être corrigés par l'extinction.

Les luminosités corrigées par l'extinction varient dans un intervalle allant de 2×10^{36} à 2×10^{39} erg s^{-1}. Les régions les plus lumineuses ont des tailles de $\sim$ 100 pc. Celles-ci sont probablement dues au mélange de régions multiples. La limite supérieure pour les associations d'étoiles sera inférieure de quelque facteur. L'intervalle déduit des masses des associations est 100 — 2000 $M_\odot$. Ces limites de masses correspondent à $\sim 1/3$ de la masse de la région HII

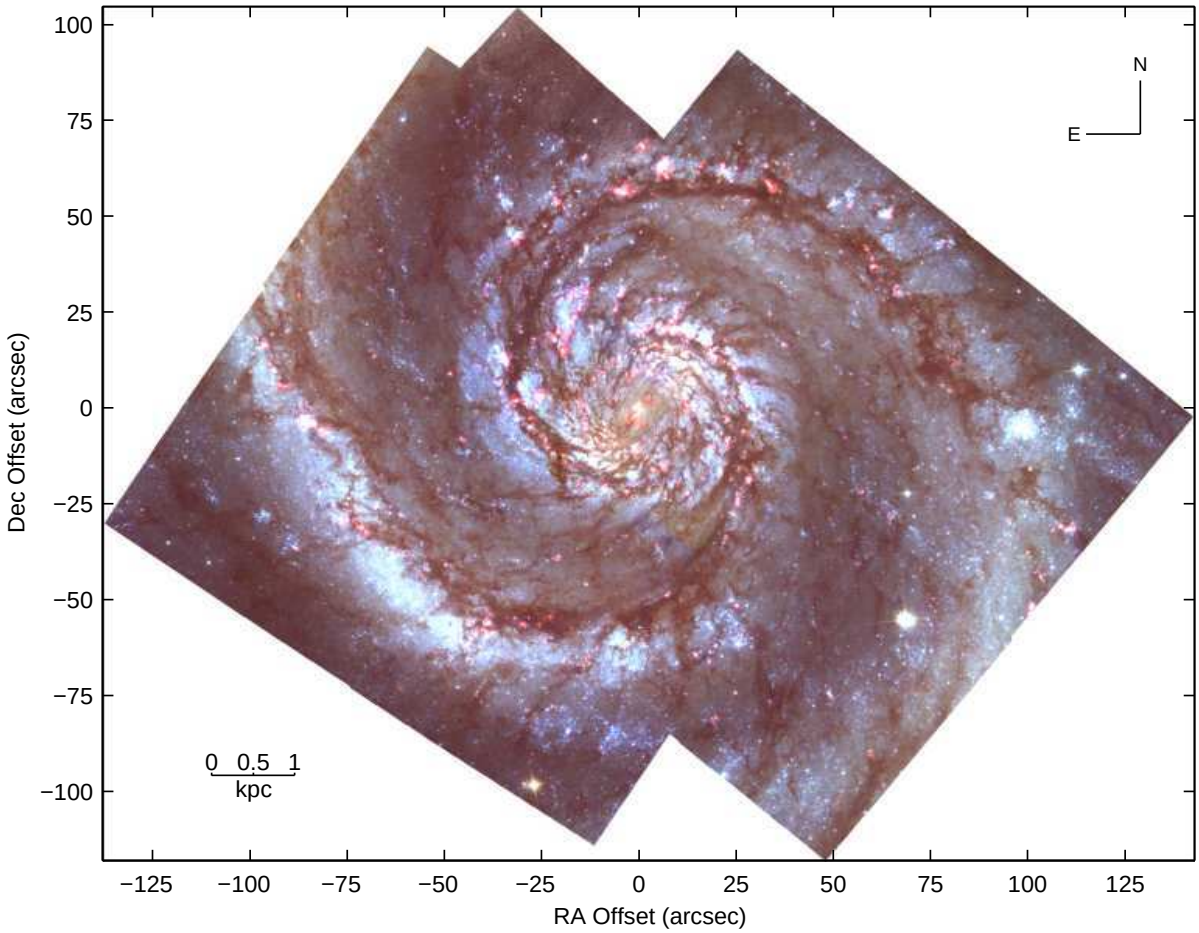

Figure 6: Combinaison en couleurs des images I et H_α en rouge, V en vert and B en blue obtenues avec WFPC2 d'une région correspondante au 281 × 223″centrale de M51.

M42 (Orion Nebulæ) et à la masse de W49 (la région HII la plus lumineuse aux longueurs d'ondes radio dans notre Galaxie). La limite supérieure à la fonction de luminosité correspond à un taux de production de photons ionisants $Q_{Lyc\,up} = 1.4{\times}10^{51}$ s^{-1} (sans corrections pour l'absorption des poussières du continu de Lyman ou UV qui s'échappe à travers le gaz diffus).

Le taux de formation stellaire dans M51, estimé à partir des luminosités H_α corrigées par l'extinction, est ~ 5 $M_\odot$ an^{-1} (avec une fonction de masse initiale de Salpeter entre 1 et 120 $M_\odot$) et la durée du cycle nécessaire pour la formation de ces étoiles à partir de la composante neutre de la matière interstellaire est de 10^9 années.

L'émission ultraviolette produite par une association d'étoiles OB a été modélisé en fonction de la masse de l'amas et de l'âge. Les paramètres du modèle (masse limite de l'amas et spectre de masse) peuvent être contraints par la fonction de luminosité des régions HII observées. La largeur du pic de la fonction de luminosité et son index spectral (-1.2) suggèrent un spectre de masse de type $dN(M_{cl})/dlnM_{cl} \propto M_{cl}^{1.5}$ et une masse limite ~ 2000 $M_\odot$. Cette limite correspond à la masse telle que la fonction de masse initiale est d'abord

peuplée jusqu'à $\sim$ 120 $M_\odot$, mais cette masse est seulement 1% de celle qui est disponible dans un nuage moléculaire géant typique. L'absence de masses plus grandes peut être due à une limite sur la formation des étoiles OB. Cette limite pourrait correspondre au moment où la pression de radiation sur les poussières environnantes dépasse l'auto-gravité du cœur de l'amas. Ceci peut se vérifier quand le rapport entre luminosité et masse stellaire est $\sim$ 1000 $L_\odot/M_\odot$, cette valeur correspond à un amas de masse $\geq$ 750 $M_\odot$. L'effondrement du cœur a été simulé avec un modèle hydrodynamique. Selon le modèle, une deuxième vague de formation stellaire pourrait se propager vers l'extérieur dans une coquille comprimée par la radiation qui entoure le coeur de l'amas.

Références

Aalto S., Huetemeister S., Scoville N.Z., Thaddeus P. 1999, ApJ, 522, 165
Antonucci R. 1993 ARA&A, 31, 473
Antonucci R., Barvainis R., Alloin D. 1990, ApJ, 353, 416
Barvainis R. 1990, ApJ, 353, 419
Barvainis R. 1997, dans Proc. of ESA/IAC Conference *Quasar Host* , eds. D. Clements & I. Perez-Fournon (Berlin: Springer-Verlag)
Barvainis R., Antonucci R. 1989, ApJS, 70, 257
Clavel J., Wamsteker W., Glass I. 1989, ApJ, 337, 236
Elvis M., Wilkes B.J., McDowell et al. 1994, ApJS, 95, 1
Gear W.K. 1988, *Millimetre and Submillimetre Astronomy*, eds. R.D. Wolstencroft & W.B. Burton
Goodrich R.W. 1989, ApJ, 342, 224
Komossa S., Greiner J. 1998, dans Proc. *High Energy Processes in Accreting Black Holes*, eds. J. Poutanen & R. Svensson
Kukula M.J., Dunlop J.S., Hughes D.H., Rawlings S. 1998, MNRAS, 297, 366
Miller P., Rawlings S., Saunders R. 1993, MNRAS, 263, 425
Roberts W.W., Stewart G.R. 1987, ApJ, 314, 10
Rodríguez-Pascual P.M., Mas-Hesse J. M., Santos-Lleó M. 1997, A&A, 327, 72
Sandage A., Tammann G.A. 1975, ApJ, 196, 313
Sanders D.B., Phinney E.S., Neugebauer G. et al. 1989, ApJ, 347, 29
Ulvestad J.S., Antonucci R.R.J., Goodrich R.W. 1995, AJ, 109, 81
Urry C.M., Padovani P. 1995, PASP, 107, 803

Introduction

Galaxies contain interstellar gas and dust, the raw materials out of which new generations of stars are born. As these stars age and eventually die, they eject some of their mass back into space, where it mixes with ambient gas and forms the interstellar matter. The interstellar matter accounts for only a few percent of the mass[2] of a galaxy (e.g., 10% in our Galaxy). Most of the interstellar matter is in the form of gas ($\sim$ 99%) and a small fraction ($\sim$ 1%) in form of dust. Even if the dust is not very abundant, it can have profound effects on a galaxy's appearance:

1. the optical appearance of galactic structures, like spiral arms, can be greatly modified by large quantities of dust;

2. spectacular dust lanes are observed in images of external galaxies, particularly in spiral and irregular systems;

3. the spectral energy distribution of galaxies can be modified by dust absorption and scattering: the optical-ultraviolet light is absorbed and re-radiated at longer wavelengths (i.e., infrared) before it can escape the galaxy;

4. photometric parameters of galaxies, such as surface brightness profiles, total luminosities and colors, depend on the amount of dust as well on its spatial distribution;

5. star formation as determined from ultraviolet fluxes can be severely underestimated, thus altering our perception of the star formation in galaxies;

6. large infrared luminosities are observed in galaxies with powerful ultraviolet sources (e.g., starforming regions, active nuclei) in presence of large amount of dust.

These effects have an important influence on our interpretation of different questions. How do the different components of interstellar matter interact with each other and with stars? How many objects are missing from our counts in optical, ultraviolet and soft X-ray surveys, because they are obscured by dust? What are the emission sources in the nuclei of galaxies that are hidden by dust? How much energy is reprocessed and re-emitted at lower frequencies? Is the amount and/or the distribution of dust responsible for the large differences observed among active galaxies? In summary, assessing the effects of dust in galaxies, investigating its role and interaction with the other galactic components is of primary importance in understanding the physical processes undergoing in galaxies themselves.

The most extraordinary signs of dust absorption in galaxies are observed at optical and ultraviolet wavelengths and, in particular, on images of relatively nearby galaxies with a spatial resolution capable to resolve objects of a few parsecs[3] in size. The best resolution at optical and near-infrared wavelengths is currently provided by the Hubble Space Telescope (HST). By moving into the infrared, the effects of absorption can be reduced by several order of magnitudes relative to optical observations. Therefore, the comparison of near-infrared

[2] In this work, we will refer to the mass as the luminous mass, that excludes the dark matter.

[3] 1 parsec $\simeq 3.085\times10^{18}$ cm

and optical observations of galaxies is a powerful tool to estimate the amount of extinction on the stellar light.

Since dust re-radiates at longer wavelengths (mid- and far-infrared) than it absorbs, direct measurements of dust amount, temperature and opacity can be obtained by mid- and far-infrared observations. These wavelengths are inaccessible from the ground because they can not propagate through the atmosphere. Observations above the terrestrial atmosphere are necessary to capture infrared photons. The launch of the Infrared Space Observatory (ISO) in 1996 had opened up a new venue for exploring dusty regions of galaxies providing, finally, a window to observe them in the mid- and far-infrared.

In this thesis, the properties (spatial distribution and location, temperature, heating source, opacity, amount) of the dust in galaxies, as absorber of optical and ultraviolet light and as emitter of infrared radiation are investigated and discussed. Optical and infrared observations are among the most powerful tools available to perform this kind of study. Two observational programs have been developed aimed at collecting large sets of optical and infrared data for a sample of active galaxies, Seyfert and quasars, and for the grand design spiral galaxy M51. The observations were mainly performed with ISO and HST.

The work on active galaxies consists on a study of their infrared emission aimed to understanding its origin (thermal and/or non-thermal), estimating the properties and the role of the dust in different types of active galaxies and probing the unified model. The sample of active galaxies was observed in the whole infrared spectral band with ISOPHOT on board the Infrared Space Observatory (ISO). We will refer to this study as the **ISOPHOT Project**.

The spiral galaxy M51 shows an interesting variety of components and activities (a spectacular spiral pattern, an active nucleus, a radio jet, a bar, large massive cloud complexes, very bright stellar associations with many high mass stars with enhanced associated star formation, a striking pattern of dust lanes). This richness of structures and phenomena, in addition to its proximity and low inclination makes one of the best laboratories for studies of galactic structure, interstellar matter and star formation. Some of these topics form the subject of the second part of this thesis. This study is based on a set of optical and near-infrared observations obtained with HST. We will refer to this part as the **HST project**.

The **ISOPHOT** and **HST projects** form the two major parts of this work. The ISOPHOT project is presented in chapters 3, 4, 5 and 6, and the HST project in chapters 7, 8, 9 and 10. An introduction to the interstellar medium components and their properties, and a general overview of galaxies are presented in chapters 1 and 2, respectively. The first chapters of each part, chapters 3 and 7, contain a description of the instruments on-board ISO and HST used to collect the set of analyzed data. These chapters also include the main steps of the data reduction, scientific objectives and results in extragalactic studies obtained with these instruments. In chapters 4 and 8, the basic ideas of the two projects and the aimed objectives are presented. The results obtained from the ISOPHOT project are reported in chapters 5 and 6 as published. The HST project re-groups many sub-projects dedicated to different, but related, studies of the physics of galaxies. At the moment of the drawing up of this thesis, we had completed two works. In the first, we present the observations, the reduction method, the resultant images and a preliminary analysis (chapter 9). In the second work, we discuss the star formation process and the properties of the HII regions (chapter 10). Final conclusions are summarized at the end.

Chapter 1

The Interstellar Matter of Galaxies

The interstellar medium and interstellar matter, or ISM represents a composite dynamical entity containing several elements as rarefied gas (atoms and molecules), dust particles (solid grains), a magnetic field, and relativistically moving electrons, proton and other atomic nuclei that fill the space between stars. The average mass distributions in percentages and densities of several components present in the ISM and of the stellar component in disc galaxies are reported in Figure 1.1.

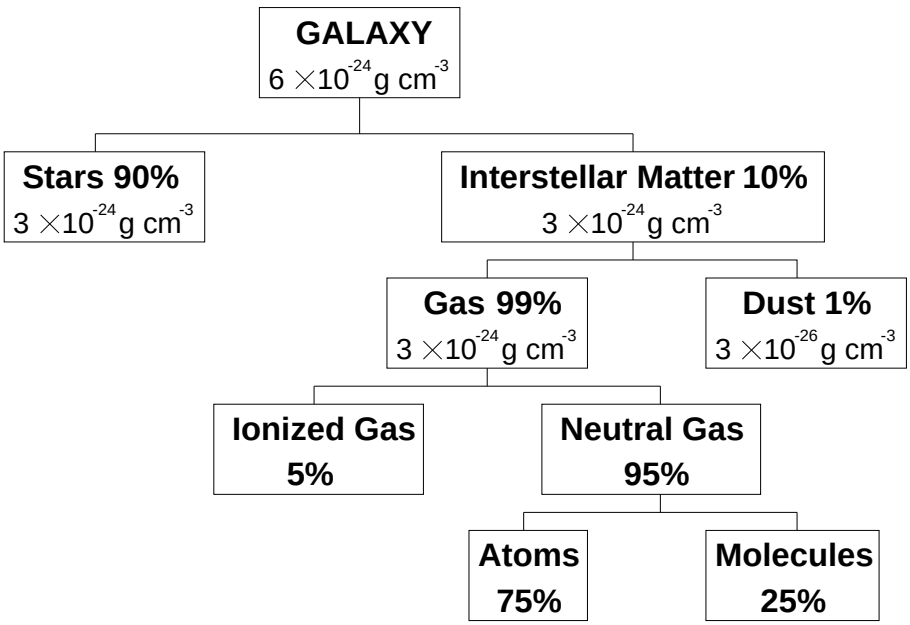

Figure 1.1: Mass and density distribution of the main components in the Galaxy.

The properties of the ISM constituents that are discussed in this work, such as the gas (i.e., ionized (HII) and molecular) and the interstellar dust, are described in the following sections (1.1 and 1.2, respectively). The radiation processes through which they emit are presented in section 1.3. For more details on the physics of the ISM the reader is referred to the book by Spitzer (1978).

1.1 Gas in the Interstellar Medium

The amount of gas, neutral and ionized, varies in galaxies considerably with their morphological type, increasing in order from elliptical to spheroidal, spiral and irregular galaxies (see galaxy classifications in chapter 2). In disk galaxies, the molecular gas is much more concentrated towards the centre of the galaxy than atomic gas (HI) whose distribution is slightly depressed at the centre and more extended than the distribution of starlight at larger distances from the centre. The gas is not uniformly distributed, but partially clumped into clouds of varying density.

In the following sections, the properties of the ionized and molecular gas will be described. The reader interested in the properties of atomic hydrogen is referred to the papers by Kulkarni and Heiles (1988) and Dickey and Lockman (1990).

1.1.1 Ionized Gas (HII Regions)

The gas can be excited by ionizing radiation from hot stars, planetary nebulæ, active galactic nuclei and/or by the passage of a powerful shock wave. As stars are born and die, they can produce large transient pressure increases in the surrounding interstellar gas, giving rise to a rapid outward expansion or explosion of this medium. These explosions may be driven by ultraviolet photons which ionize and heat the gas, or by high-velocity expulsion of mass, as from a supernova or bright early-type star.

The interstellar gas in mostly composed by hydrogen. Hydrogen is ionized by photons of wavelength shortward of 912Å (corresponding to energies exceeding 13.60 eV, the ionization energy of H). Stars of high surface temperature are sources of strong ultraviolet radiation. Their emission, therefore, ionizes the surrounding gas within some limiting distance from the stars, while material beyond this distance remains largely neutral. Since the heated gas will be at a much higher pressure than the surrounding cool gas, it will tend to expand. The region of ionized hydrogen is called **HII region** and occupies a volume called Strömgren sphere.

Such regions tend to be very conspicuous around early O stars, since these are the most luminous in the far-ultraviolet. The development of an HII region is conditioned by the transitory nature of the energy source. During the lifetime of an O star (i.e., less than 10^7 years), interstellar gas moving at 10 km s^{-1} will travel less than 100 pc, which is comparable with the diameter of the larger HII regions (see typical size values in Table 1.1). Thus, before an HII region has extensively expanded, its central energy source will be extinguished.

Typical densities in HII regions range from 10 to 10^4 cm^{-3}, and can reach 3×10^5 cm^{-3} in ultracompact HII regions (HII regions excited by a single type O or early B star). Numerical values of the radius of a Strömgren sphere at a density $N(H^+)$ of 1 cm^{-3} around different types of OB stars are reported in Table 1.1. The tabulated values have been calculated theoretically by models of stellar atmospheres and assuming a gas temperature equal to 7500 K.

Since O stars have been formed recently in clusters or associations, presumably born within clouds of relatively dense cold gas, the gas and dust left over from the star formation process are often still in the vicinity, showing signs of obscuration by dense, dark, and presumably neutral clouds. The presence of dust within HII regions is indicated both by the presence of scattered starlight, giving an observable optical continuum, and by the presence of observable infrared radiation emitted by the heated dust.

In regions far from associations of young stars, a diffuse but weak galactic ionized hydrogen emission can be present. This ionized gas may be attributed to HII regions around B stars

Table 1.1: Typical values of Strömgren spheres

Spectral type	M_V	T_{star} (K)	$log\, Q$ (phot s^{-1})	R_S (pc)
O5	−5.6	48 000	49.67	108
O6	−5.5	40 000	49.23	74
O7	−5.4	35 000	48.84	56
O8	−5.2	33 500	48.60	51
O9	−4.8	32 000	48.24	34
O9.5	−4.6	31 000	47.95	29
B0	−4.4	30 000	47.67	23
B0.5	−4.2	26 200	46.83	12

Q is the Lyman continuum ionizing photon production rate; R_S is the radius at which the density of electrons and protons is 1 cm^{-3}.

and possibly other ultraviolet sources such as the nuclei of planetary nebulæ and other dying stars.

1.1.2 Molecular Gas

Clouds of cold molecular and atomic hydrogen represent the raw material from which stars can be formed in the disk of galaxies if they become gravitationally unstable and collapse. The dense, molecular ISM is the birth site of OB star clusters.

Most of the molecular gas in galaxies is contained in cool ($T \simeq 10$ K) giant molecular clouds (GMC) (10^5 - 10^7 $M_\odot$) of volume averaged hydrogen density ~ 200 cm^{-3} (Scoville and Sanders 1987). Molecular hydrogen (H_2) dominates in these massive clouds, which may contain up to 10^5 $M_\odot$, but other molecules such as CO, CS and HCN can be also very prominent.

Heteronuclear molecules (e.g., CO, CS, HCN) have a net dipole moment, and consequently radiate when they spin. The transition energies of these molecules are much smaller than those of H_2, and the lines fall in the mm wave-bands rather than in the ultraviolet. Molecular clouds can thus be detected by their millimetre-radio frequency emission. CO lines at 1.3 and 2.6 mm are among the most important lines used to trace molecular clouds.

1.2 Interstellar Dust

The interstellar dust (Whittet 1992) is concentrated in the plane of disk galaxies and is far from being uniformly spread, but rather associated with cool, dense, molecular gas clouds and with spiral arms.

Vast quantities of hot gas stream out of red giants, and smoke particles precipitate out of this gas, in particularly cool regions of galaxies. Some of these smoke particles eventually gather together to form comets, asteroids and planets, but the vast majority remains in the interstellar space forming the interstellar dust. Much smaller sources of dust are supernovæ, novæand hot stars. It is currently not certain whether the stars are the only source of dust grains or whether grains also form directly in interstellar clouds.

The composition of interstellar dust is not well-known. Observations of interstellar extinction (see section 1.2.1) are well explained by a mixture of graphite and silicate grains (Mathis, Rumpl and Nordsieck 1977; Draine and Lee 1984); however, alternative constituents are possible.

The size distribution of dust grains can be described by a power law (Draine and Lee 1984)

$$\frac{dN(a)}{da} \propto a^{-3.5} \tag{1.1}$$

where a is the grain size and $dN(a)$ gives the number of dust particles with sizes between a and $a+da$. The size of dust particles ranges from 0.005 μm 1.0 μm (Mathis, Rumpl and Nordsieck 1977).

1.2.1 Effects of dust on stellar light: extinction and reddening

Dust grains are effective absorbers of photons whose wavelength is comparable to, or smaller than the characteristic size of the dust grains, but are poor absorbers of longer wavelength photons. They re-emit radiation at wavelengths much greater than those of the absorbed light. Since most dust grains are smaller than ca. 0.1 μm, ultraviolet radiation is effectively absorbed by interstellar dust, whereas far-infrared radiation can pass even through dense interstellar clouds.

Dust has two major effects on light passing through it:

1. The light is dimmed by the dust. This is called **interstellar extinction**.

Most of the energy radiated by stars emerges at wavelengths that can be absorbed by dust grains. Furthermore, young, luminous stars generally live in regions rich in dust - they are born in dense clouds, and in their brief lifetimes cannot get far away from the cloud of their birth. Hence, a significant fraction of the energy radiated by the stars is absorbed by dust grains.

2. The light that does pass through the dust is depleted in blue wavelengths (reddened), through scattering and absorption (conversion of the absorbed photon energy into heat), because dust grains favor scattering of blue light. This is called **interstellar reddening**. The resultant transmitted light is redder than it would have been otherwise. This implies that transmitted light appears redder and reflected light bluer.

The amount of **extinction** A_ν, expressed in magnitudes, at the frequency ν is defined as the difference between the observed ν-band magnitude $m(\nu)$ and the magnitude $m_0(\nu)$ that would be observed in the absence of dust:

$$A_\nu \equiv m(\nu) - m_0(\nu) = -2.5\, log \frac{F_\nu}{F_{\nu,0}} \tag{1.2}$$

where $F_{\nu,0}$ is the stellar flux measured by the observer in the absence of extinction.

The **reddening** or **colour excess**, E($\nu_1 - \nu_2$), in some colour $\nu_1 - \nu_2$ is defined as the difference between the observed colour, $m(\nu_1)-m(\nu_2)$, and the intrinsic colour, $m_0(\nu_1)-m_0(\nu_2)$:

$$E(\nu_1 - \nu_2) \equiv [m(\nu_1) - m(\nu_2)] - [m_0(\nu_1) - m_0(\nu_2)] = A_{\nu_1} - A_{\nu_2}. \tag{1.3}$$

The curve in Figure 1.2 shows the ratio A_λ/A_V between the extinction at wavelength λ and the extinction in the visual V-band (5550Å). This curve is called the **extinction**

curve or **extinction law**. A set of theoretical curves is also reported in Figure 1.2. Each theoretical curve corresponds to a specific dust component whose extinction effects depend on the wavelength λ. The effects of extinction due to small graphite grains (average size $\bar{a}$=0.025 μm) have been included to fit the observed peak at the wavelength corresponding to their size. Those due to grains of SiC ($\bar{a}$=0.075 μm) have been added to fit the optical and infrared regions. The effects of extinction due to small magnesium and aluminium silicate grains ($\bar{a}$=0.045 μm) increase in the ultraviolet, although not so much as observed. While the

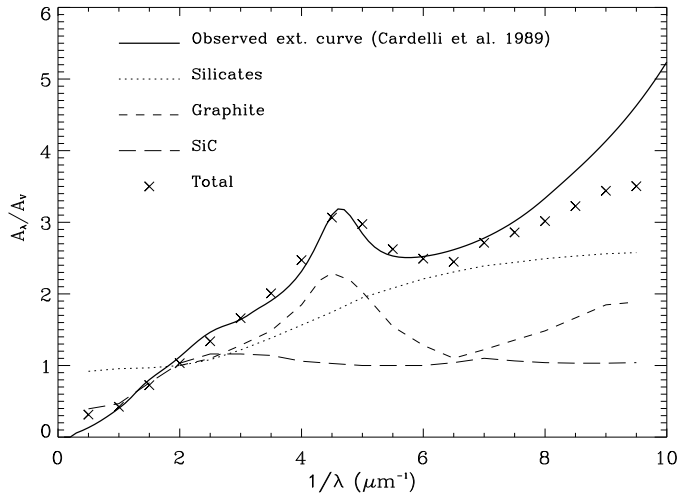

Figure 1.2: The ratio of A_λ to A_V is plotted against the reciprocal wavelength in microns (solid curve). The other curves are computed theoretically for grains of three different types (see text), with the sum of the three shown by the crosses.

theoretical fit to the mean observational curve shown in Figure 1.2 is one of the best of the many that have been proposed (Aannestad and Purcell 1973), it is not completely satisfactory and unique.

The slope of the extinction curve towards the ultraviolet can be expressed through the following parameter:

$$R_V \equiv \frac{A_V}{A_B - A_V} = \frac{A_V}{E(B-V)} \tag{1.4}$$

where B denotes the blue B-band (4440Å). Low R_V values ($\simeq$3) are measured for steeply-rising extinction curves, and high R_V values ($\simeq$5) for flatter extinction curves. The most adopted value is $R_V = 3.1$ that is derived for lines of sight that do not pass through dense molecular clouds (Schultz and Wiemer 1975; Snedden et al. 1978).

Empirically, along any line of sight, the colour excess, $E(B-V)$, is approximately proportional to the column density N_H[1] of interstellar hydrogen atoms, irrespective of whether the hydrogen atoms are in form of HI or H_2 molecules. The line of best fit gives a value of

[1]The column density N_H corresponds to the number of hydrogen atoms in a column along the line of sight 1 cm^2 cross section. It can be derived from measurements of absorption of X-ray radiation or of 21-cm, L(H_α) or H_2 emission.

5.4×10^{21} mag^{-1} cm^{-2} for $N_H/E(B-V)$. While this ratio includes hydrogen in H_2 as well as in neutral hydrogen, an additional correction of roughly 10 percent must be made for ionized H in the HII zones. Specifically, one has (Bohlin et al. 1978; Kent, Dame and Fazio 1991)

$$E(B-V) = \frac{N_H(\mathrm{cm}^{-2})}{5.8 \cdot 10^{21} \ \ \mathrm{mag}^{-1}\mathrm{cm}^{-2}}. \tag{1.5}$$

The relatively close correlation between $E(B-V)$ and N_H indicates a constant dust to gas ratio.

Measuring extinction and reddening

OB stars are ideal for determining extinction and reddening because they are highly luminous and can be observed from large distances, over which the column density of dust can become significant. They are intrinsically blue (hence, strongly susceptible to reddening) and they have distinctive spectra that can be classified with high precision. From the difference between the intrinsic and apparent colours of a star, it is possible to determine the reddening produced by the dust distributed in between the star and the observer.

Reddening also affects the line emission. Since reddening depends on the radiation wavelength, the ratios between the intensities of emission lines at different wavelengths change as a function of reddening. Dust preferentially absorbs the shorter wavelength (i.e., $H_\beta\lambda4861$Å is more absorbed than $H_\alpha\lambda6563$Å). The difference between the observed and the predicted values of line ratios, therefore, provides an estimate of reddening. However, observed differences might also indicate that assumptions made for the predicted values (i.e., the case B condition, see section 1.3.3) are not valid and/or that optical depth effects are important. Of particular consequence are the very large optical depths possible for extended partially ionized regions past the Strömgren distance, where strong Ly_α trapping and subsequent collisional Balmer line enhancement from the n=2 level can decrease both the Ly_α/H_β and Pa_α/H_α ratios.

1.2.2 Dust scattering and absorption

Interstellar dust particles may be treated as bodies of regular shape as spheres, cylinders, as well as core-mantle concentric spheres. Spherical particles are considered to provide a satisfactory representation of randomly oriented irregular-shaped interstellar grains. Light scattering by a spherical particle has been studied by Mie (1908) and Debye (1909). The basic problem is the following: a plane-polarized electromagnetic wave is incident on a sphere of radius a and complex refractive index m, after interacting with the particle, the forward beam has lost a certain amount of energy. Part of the electromagnetic wave's energy is **scattered** out of the forward beam and part is **absorbed** by the sphere. For particles of radius a, these amounts of energy equal equal the incident energy multiplied by the dust grain cross section for **scattering**, $Q_\nu^{sca}\pi a^2$, and for **absorption**, $Q_\nu^{abs}\pi a^2$. The coefficients Q_ν^{sca} and Q_ν^{abs} are called scattering and absorption efficiency factors, respectively. These factors are dimensionless functions of a, m and of the wavelength λ of the incident radiation. The extinction cross section corresponds to the sum of the scattering and absorption cross sections:

$$Q_\nu^{ext}\pi a^2 = (Q_\nu^{abs} + Q_\nu^{sca})\pi a^2. \tag{1.6}$$

Extensive calculations of the optical efficiency factors Q_ν^{ext}, Q_ν^{sca}, and Q_ν^{abs} can be found in Spitzer (1978). The fraction Q_ν^{sca}/Q_ν^{ext} of light that is scattered, is called *albedo*. In

Figure 1.3, the absorption and extinction efficiency factors of graphite and silicates grains of radius a equal to 0.01 μm against the reciprocal wavelength are shown (data from Draine 1985).

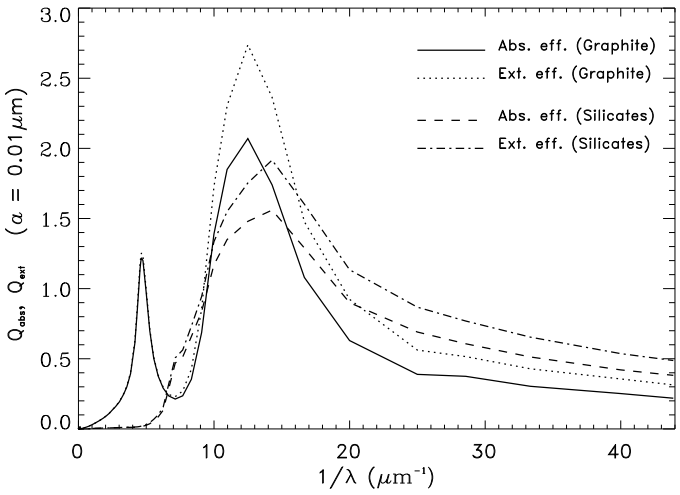

Figure 1.3: Absorption and extinction efficiency factors for spherical dust grains of radius $a = 0.01$ μm against the reciprocal wavelength in microns.

For an ensemble of particles of any specified type, the bulk absorption efficiency factor or mass absorption coefficient is defined as

$$k_{m,\nu}^{abs} = \frac{\pi a^2 Q_\nu^{abs}}{\frac{4}{3}\pi a^3 \rho} = \frac{3Q_\nu^{abs}}{4a\rho} \qquad \text{cm}^2 \ \ \text{g}^{-1} \tag{1.7}$$

where ρ is the material density. Similar definitions can be made for the bulk scattering and extinction efficiency factors, $k_{m,\nu}^{sca}$ and $k_{m,\nu}^{ext}$. Equation (1.7) is based on the hypothesis that all the grains are identical. In reality, it should be integrated over all the parameters characterizing the grains, including chemical composition, size, shape, and orientation.

1.2.3 Radiation transfer through dust grains

Spherical isotropic grains in the line of sight of a star will have an important effect on the intensity of radiation received from it. The intensity of radiation I_ν in a specified direction at a point is defined as the amount of radiant energy crossing a unit area per unit time, through unit solid angle and per unit frequency interval. If $d\sigma$ is an element of area normal to the specified direction, $d\omega$ is an elementary solid angle centred about the same direction, the amount of energy in the frequency range ν, $\nu+d\nu$ crossing this surface through the solid angle $d\omega$ per unit time will be

$$I_\nu d\sigma d\nu d\omega. \tag{1.8}$$

In the case of a right circular cylinder of cross sectional area dA, length dl and axis aligned with the line of sight of a star (see Figure 1.4), the energy in the solid angle $d\omega$ flowing into

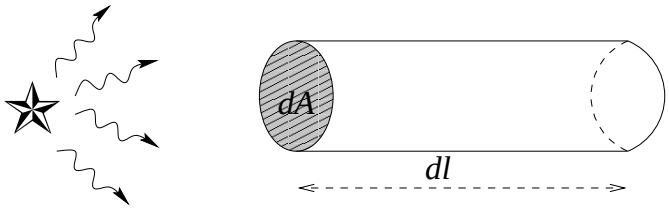

Figure 1.4: Elementary cylindrical column in line of sight to a star.

the cylinder per unit time is

$$I_\nu dA d\nu d\omega. \tag{1.9}$$

The change of I_ν resulting from interaction with matter is governed by the equation of transfer. This equation is derived by considering the flow of energy in and out the ends of the cylinder, and using the absorption and emission coefficients k_ν^{abs} and j_ν^{em}. The emission coefficient, or emissivity, j_ν^{em} is defined so that $j_\nu^{em}\, dV\, d\nu\, d\omega\, dt$ is the energy emitted by the volume element dV (equal to $dl\, dA$) in the intervals $d\nu$, $d\omega$, and dt, whereas $k_\nu^{abs}\, I_\nu\, dV\, d\nu\, d\omega\, dt$ is the corresponding energy absorbed from a beam of specific intensity I_ν. k_ν^{abs} is called linear absorption coefficient and is expressed in cm^{-1}. It can be derived from the mass absorption coefficient using $k_\nu^{abs} = \rho k_{m,\nu}^{abs}$ and from the absorption efficiency factor using $k_\nu^{abs} = nQ_\nu^{abs}\pi a^2$, where n is the number of particles per unit of volume.

If we assume that the photons travel in straight lines, the change of I_ν along a distance dl, taken along a light ray, equals

$$\frac{dI_\nu}{dl} = -k_\nu^{abs}\, I_\nu + j_\nu^{em}. \tag{1.10}$$

We define the "optical depth" τ_ν backward along the ray path by the expression

$$d\tau_\nu = -k_\nu^{abs}\, dl; \tag{1.11}$$

at the observer $\tau_\nu = 0$, and if k_ν^{abs} is positive, τ_ν increases toward the source. If we consider the radiation received from a region or cloud of total optical thickness $\tau_{\nu r}$, equation (1.10) may be integrated to yield

$$I_\nu = I_\nu(0)e^{-\tau_{\nu r}} + \int_0^{\tau_{\nu r}} \frac{j_\nu^{em}}{k_\nu^{abs}} e^{-\tau_\nu} d\tau_\nu. \tag{1.12}$$

In this equation, $I_\nu(0)$ denotes the value of I_ν on the far side of the emitting region from the observer, where $\tau_\nu = \tau_{\nu r}$. The ratio j_ν^{em}/k_ν^{abs} may vary with τ_ν.

In thermodynamic equilibrium, I_ν equals $B_\nu(T)$, the Planck function where T is the kinetic temperature of the dust. Under the hypothesis of thermodynamic equilibrium ($dI_\nu/dl = 0$), equation (1.10) gives

$$j_\nu^{em} = k_\nu^{abs} B_\nu(T) \tag{1.13}$$

a relationship known as Kirchhoff's law.

If the hypothesis of thermodynamic equilibrium is valid over the pathlength, equation (1.12) becomes

$$I_\nu = I_\nu(0)e^{-\tau_{\nu r}} + B_\nu(T)(1 - e^{-\tau_{\nu r}}), \tag{1.14}$$

where the first term represents the intensity of the radiation coming from the stellar source after travelling through the cylinder and the second term represents the light scattered and/or emitted by the dust in the cylinder.

The optical depth $\tau_{\nu r}$ depends on the absorption efficiency factor Q_ν^{abs} and on the column density, N, of the absorbing material (i.e., number of grains in a column of 1 cm^2 cross section stretching from the star to the observer) as expressed by

$$\tau_{\nu r} = N\pi a^2 Q_\nu^{abs}. \tag{1.15}$$

1.3 Radiative processes

1.3.1 Thermal radiation by dust

For a solid particle, the energy gain usually results from absorption of photons and from collisions with the gas, whereas the loss results in infrared radiation. Within the solid material composing the interstellar grains, the exchange of vibrational energy between atomic nuclei is generally much more rapid than the exchange of energy with the external radiation field. This condition assures the existence of an equilibrium velocity distribution at the kinetic temperature T.

Under these conditions a solid particle of temperature T absorbs a fraction Q_ν^{abs} of the radiation of frequency ν that hits it, then the outgoing flux at its surface is $Q_\nu^{abs} B_\nu(T)$ where $B_\nu(T)$ is the Planck or blackbody function. This radiation is called greybody emission. Greybody emission refers to the thermal continuum emission from a non-perfect blackbody. Before introducing the greybody function, a brief description of the blackbody function is presented.

Blackbody emission

A blackbody is a body in thermal equilibrium with its surroundings and is both a perfect absorber and perfect emitter of radiation. Blackbody radiation is isotropic, unpolarized and has a smooth continuous emission spectrum. A blackbody has a unique defining temperature T. No radiation falling onto a blackbody is reflected and therefore the radiation we see from a blackbody is a property of its emission alone. This follows a uniquely defined form given by Planck's radiation equation

$$B_\nu(T) = \frac{2h\nu^3}{c^2(e^{h\nu/kT} - 1)} \quad \mathrm{erg\,cm^{-2}\,sr^{-1}\,Hz^{-1}\,s^{-1}} \tag{1.16}$$

where h is the Planck's constant, c is the velocity of light in vacuum, k is Boltzmann's constant and T is the absolute temperature. In Figure 1.5 a blackbody function at a temperature T=50 K is shown by a solid line.

Equation (1.16) can be simplified mathematically at frequencies less than the peak (Rayleigh-Jeans region). The Rayleigh-Jeans region is defined by the frequency range where $h\nu/kT <<$

1. The exponential term can be expanded to give $e^{h\nu/kT} = 1 + h\nu/kT +$ higher powers in $h\nu/kT$, which can be neglected. Equation (1.16) then reduces to

$$B_\nu(T) = \frac{2h\nu^2 kT}{c^2}. \tag{1.17}$$

When this is plotted on a logarithmic scale of $log\, B_\nu\ versus\ log\, \nu$, it is a straight line of slope 2 (see dashed line in Figure 1.5).

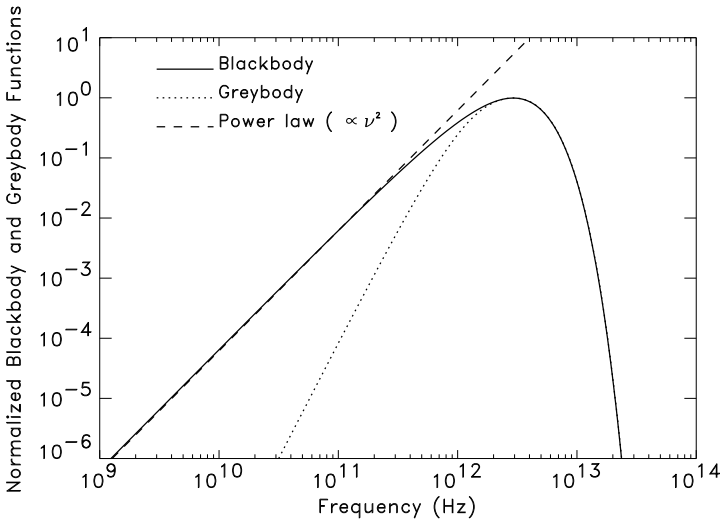

Figure 1.5: The solid curve represents the emission from a blackbody (Planck function) at a temperature $T = 50$ K. The dotted curve represents the emission from a greybody at the same temperature T. The dashed line represents a power law of slope 2 ($\propto \nu^2$).

The flux density, $S_\nu(T)$, of a blackbody of radius r, observed at a distance is D, is

$$S_\nu(T) = \Omega B_\nu(T) \approx \frac{\pi r^2}{D^2} B_\nu(T) \quad \mathrm{erg\,cm^{-2}\,Hz^{-1}\,s^{-1}} \tag{1.18}$$

where Ω is the solid angle subtended by the source.

Greybody emission

A greybody is a semi-opaque source, it absorbs, scatters and re-emits a photon after modifying its energy. The absorption capability depends on the energy of the photon. Dust grains in thermal equilibrium emit as greybodies.

The greybody radiation can be described as a blackbody emission modified by the absorption efficiency Q_ν^{abs}. The absorption efficiency can be described as a function of the form

$$Q_\nu^{abs} = Q_{\nu_0}^{abs} \left(\frac{\nu}{\nu_0}\right)^\beta \tag{1.19}$$

where $Q_{\nu_0}^{abs}$ is the value of the absorption efficiency at the reference frequency ν_0, and β is the frequency dependence index. The spectral index β is generally unknown, along with the

dust temperature and the optical depth, but can be deduced from observations and used to place constraints on grain composition. A value $\beta = 1$ seems to be plausible for $\lambda < 100$ μm (Hildebrand 1983; Rowan-Robinson 1992), while there is observational evidence for a steeper ($\beta \simeq 2$) absorption efficiency at longer wavelengths. The difference in the absorption efficiency is not unexpected, since the composition, size and heating process of grains emitting in the mid-IR (25–60 μm) (i.e., grains are bigger and transiently heated) are different from those in the far-IR ($\lambda > 100$ μm) (i.e., grains are smaller and emit at thermal equilibrium) (Whittet 1992).

The observed emergent flux density, S_ν, emitted by centrally heated dust derived after integration of $Q_\nu^{abs} B_\nu(T)$ along the ray path from the source to the observer, is given by

$$S_\nu = \Omega B_\nu(T)[1 - e^{-\tau(\nu/\nu_0)}] \text{ erg cm}^{-2} \text{ Hz}^{-1} \text{ s}^{-1} \tag{1.20}$$

where ν is the observing frequency, Ω is the solid angle subtended by the source, T is the temperature and $\tau(\nu/\nu_0)$ is the optical depth.

In the Rayleigh-Jeans region (i.e., $h\nu/KT << 1$) the greybody emission takes the simple form of a power law of slope $2+\beta$ ($S_\nu \propto \nu^{2+\beta}$). In this region, the emitted spectrum can, therefore, be very similar to the non-thermal self-absorbed synchrotron emission (see section 1.3.2). In many astrophysical cases, both radiation mechanisms (thermal and non-thermal) can emit in the Rayleigh-Jeans spectral region and produce similar spectra making hard to distinguish the origin of the observed spectrum.

Dust emission *vs* heating source

The spectral luminosity of an individual grain at a temperature T in the infrared is:

$$L_{\nu,ir}^{gr} = 4\pi \cdot \pi a^2 Q_{ir}^{abs} \cdot B_\nu(T) \text{ erg Hz}^{-1} \text{ s}^{-1} \tag{1.21}$$

where the factor 4π comes from the integration of the solid angle Ω over the spherical grain and πa^2 is the geometrical cross-section of the grain.

When exposed to an ultraviolet radiation field of energy density u_{UV}, a grain will come into equilibrium when the rate at which energy is absorbed equals the rate at which it is radiated:

$$\pi a^2 \int u_{UV} c Q_{UV}^{abs} d\nu = \int L_{\nu,ir}^{gr} d\nu \tag{1.22}$$

where Q_{UV}^{abs} is the grain absorption efficiency. The first member in equation (1.22) can be written as

$$\pi a^2 \int u_{UV}\, c\, Q_{UV}^{abs} d\nu = \pi a^2 \frac{L_{UV} Q_{UV,0}^{abs} e^{-\tau_{UV}}}{4\pi D^2} \tag{1.23}$$

where L_{UV} is the total ultraviolet luminosity, D the distance of the grain from a central heating source and τ_{UV} the dust optical depth to the ultraviolet continuum. After replacing equation (1.23) in equation (1.22) and Q_{IR}^{abs} with $Q_{IR,0}^{abs}(\nu/\nu_0)^\beta$ (see equation (1.19)) and integrating the second member in equation (1.22) it follows

$$\frac{L_{UV} Q_{UV,0}^{abs} e^{-\tau_{UV}}}{4\pi D^2} = 8\pi Q_{IR,0}^{abs} \frac{h}{c^2} \left(\frac{k}{h}\right)^{4+\beta} T^{4+\beta} \Gamma(4+\beta)\zeta(4+\beta) \tag{1.24}$$

where Γ is the gamma function and ζ is the Riemann zeta function. Using this equation, it is possible to derive the distance from the central source. For a spherical geometry the distance D is:

$$D = \left(\frac{L_{UV}}{T_{gr}^{4+\beta}}\right)^{1/2} \left[\frac{Q_{UV,0}^{abs} e^{-\tau_{UV}}}{Q_{IR,0}^{abs}} \frac{c^2 h^{3+\beta}}{32\pi^2 k^{4+\beta}} \cdot \frac{1}{\Gamma(4+\beta)\zeta(4+\beta)}\right]^{1/2}. \quad (1.25)$$

If, instead of a central heating source, there is a distributed heating situation, as in case of a region of star formation where stars and dust are mixed, the heating flux $(L_{UV}/(4\pi D^2))$ in equation (1.24) will be expressed by $L_*/(4\pi\bar{r}^2)$ where L_* is the stellar luminosity per heating star and $\bar{r}$ represents the average spacing of the stars (Stein 1996).

1.3.2 Synchrotron radiation

A charged particle that moves in a magnetic field spirals around the field lines and radiates because the Lorentz force is accelerating it towards the field line along which it is spiraling. A population of relativistic particles with Lorentz factors[2] γ which are distributed as a power law $N(\gamma) \propto \gamma^{-s}$ generates synchrotron radiation with an emissivity $j_\nu \propto \nu^{-(s-1)/2}$ that is also a power law with respect to frequency (see e.g., Rybicki and Lightman 1979).

At high frequencies the spectra of many synchrotron sources (e.g., the lobes of radio galaxies (see chapter 2)), are observed to fall off as $f_\nu \propto \nu^{-0.75}$. If these sources are optically thin to synchrotron radiation, it follows that the underlying electron spectrum has $s \simeq 2.5$. At low frequencies, the spectra of synchrotron sources tend to $f_\nu \propto \nu^{5/2}$ as a result of self-absorption: a synchrotron photon from one electron is likely to be absorbed by another.

1.3.3 Line emission

Emission lines can be produced by several processes:

1. recombinations free-bound (in Figure 1.6, the transitions corresponding to some hydrogen emission lines are shown);

2. forbidden transitions (e.g., [OIII] λ 5007 Å; [SII] $\lambda\lambda$ 6716/6731 Å). Those transitions can occur in low density gas conditions (e.g., in the Narrow Line Region of Active Galaxies where the density ranges from 10^3 to 10^6 cm^{-3});

3. molecular rotations (e.g., CO λ 2.6 mm);

4. hyperfine transitions (H 21-cm emission line).

Here, we discuss only optical recombination lines that will be subject of the following studies (chapter 10).

[2]The Lorentz factor γ of an electron corresponds to $(1 - \frac{v^2}{c^2})^{1/2}$ where v is the electron speed and c is the speed of light.

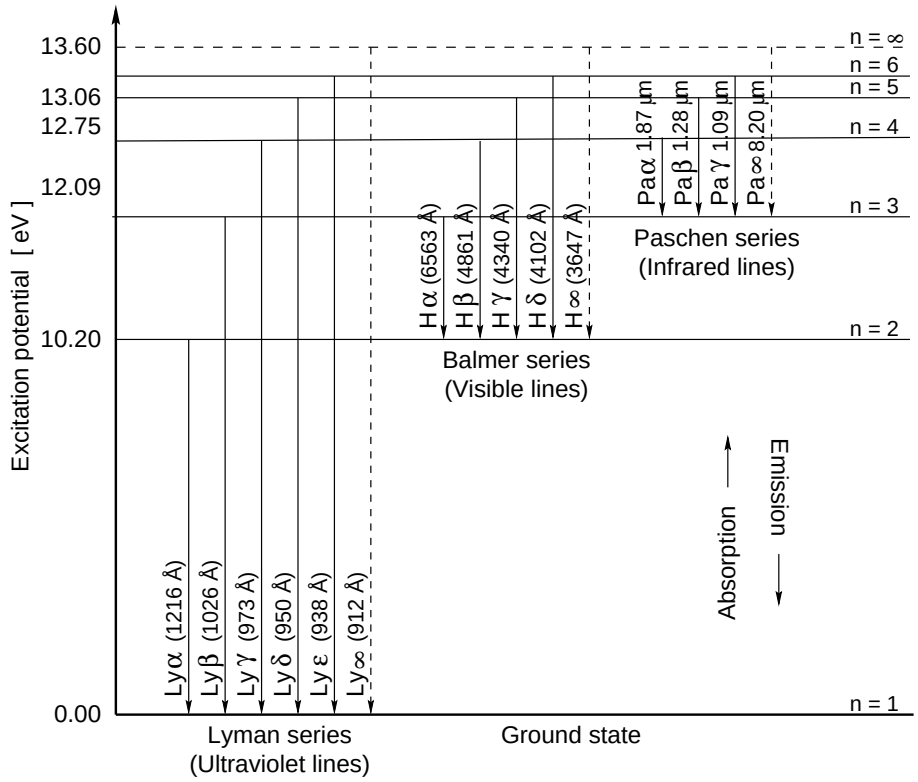

Figure 1.6: Grotrian diagram for hydrogen with transitions of the Lyman, Balmer and Paschen series indicated and the corresponding energy levels (n) and excitation potential (adapted from Türler 2000).

Optical recombination lines

The emission in the Balmer series, such as H_α (6561Å), is, generally, observed from extended regions around O stars (HII regions) and from galactic disks. These lines are produced by excited H atoms cascading to their ground state following the capture of an electron by a proton.

The energy emitted in a hydrogen line (i.e., H_α, transition $3 \rightarrow 2$) per unit volume per second per steradian (the so-called volume emission coefficient), is determined by the expression

$$j(\mathrm{H}_\alpha) = \frac{h\nu_{32}}{4\pi} A_{32} n_3 = \frac{h\nu_{32}}{4\pi} \frac{A_{32} 16 h^3}{(2\pi m k T)^{3/2}} b_3 e^{\chi_3/kT} n_e n_p \propto \alpha_{32} n_e n_p \ \mathrm{erg\ cm^{-3}\ sr^{-1}\ s^{-1}} \quad (1.26)$$

where n_e and n_p are the numbers of electrons and of protons per cubic centimetre, A_{32} is the probability of a spontaneous transition from level 3 to level 2, ν_{32} is the frequency of the transition, m is the proton mass, k is the Boltzmann constant, T is the temperature, h is the Planck constant, b_3 is a correction factor, and χ_3 is the energy of level 3 relative to zero potential energy at infinity. The production coefficient α_{32} (also called effective recombination coefficient) is defined so that $\alpha_{32} n_e n_p$ equals the total number of photons emitted per second and per cubic centimetre in the transition from level 3 to 2 (Kaplan and Pikelner 1970).

The luminosity emitted in the H_α line is defined as

$$L(H_\alpha) = \int 4\pi j(H_\alpha) dr \quad \text{erg cm}^{-2}\ \text{s}^{-1}, \tag{1.27}$$

where the integral is taken along the line of sight. After replacing equation (1.26) in equation (1.27), the radiation intensity can be expressed as a function of a single parameter, the emission measure EM[3].

$$L(H_\alpha) \propto \int n_e n_p dr \propto \text{EM} \quad \text{erg cm}^{-2}\ \text{s}^{-1}. \tag{1.28}$$

The number of ionizing photons absorbed by an HII region per unit time can be deduced from the observed intensity of any Balmer lines. Each photo-ionization of a hydrogen atom is associated with a hydrogen atom reaching its ground state by emission of a Lyman-series photon. A Lyman-series photon emitted within a HII region is very unlikely to escape from the HII region because the ground-state hydrogen atoms, which are very abundant in the HII region, offer a large cross section for its absorption. The excited hydrogen atom produced by absorption of a Ly_α photon or by one of the higher members of the series, has a finite chance of emitting two or more photons before returning to its ground state. Thus each time a Lyman-series photon is absorbed, there is non-negligible probability for the emission of a less energetic Lyman-series photon plus one or more photons of the hydrogen series (e.g., Balmer, Paschen). It follows that the creation of a Ly_α photon is associated with the creation of a Balmer-series photon. Thus, the rate of creation of all Balmer-series photons should equal the rate of ionization of hydrogen atoms (Zanstra 1927).

In many astrophysical cases, the line emitting gas properties are simplified applying an approximation called case B condition. This approximation is valid in the case of large optical depth conditions for Lyman lines. Every Lyman-series photon is scattered many times in the gas, and ultimately, this results in the conversion of all the Lyman lines into a Ly_α photon, a Balmer line photon and other photons as well.

The case B condition can be applied to HII region around a star. That means that all the ionizing photons emitted by the star are absorbed by the HII region. Thus, the total number of ionizations in the HII region per unit time is equal to the number of ionizing photons emitted per unit time, and since the HII region is in equilibrium, these ionizations are just balanced by the total number of recaptures per unit time. This balance can be expressed by the following equation

$$\int_{\nu_0}^{\infty} \frac{L_\nu}{h\nu} d\nu = Q(H) = \int_0^{R_S} n_p n_e \alpha dV \tag{1.29}$$

where L_ν is the luminosity of the star per unit frequency interval, α is the recombination coefficient, $Q(H)$ is the total number of ionizations in the HII region per unit time and R_S is the radius of the HII region. The luminosity of the entire HII region in a particular emission line (e.g., H_α), also depends on recombinations throughout its volume:

$$L(H_\alpha) = \int_0^{R_S} n_p n_e \alpha_{eff}^{H_\alpha} dV. \tag{1.30}$$

[3]The emission measure EM is defined as the integral of the density squared along the line of sight.

From equations (1.29) and (1.30) it results that the number of photons emitted by the HII region in a specific recombination line such as H_α is directly proportional to the number of photons emitted by the star with $\nu \geq \nu_0$.

The values of $j(H_\alpha)/n_p n_e$ and the intensities of other Balmer lines relative to H_α in case B approximation and for different temperatures can be found in Osterbrock (1989).

Assuming the case B condition, the relative numbers of atoms in two different levels (and thus temperature) can be derived from the ratio of the intensities in two spectral lines. For temperatures between 5 000 K and 20 000 K, the ratio of the strengths of the Balmer lines, H_α/H_β (Balmer decrement), is predicted to lie between 2.75 and 3.0. The H_α/H_β line ratios observed in many HII regions lie in this range.

Bibliography

Aannestad P.A., Purcell E.M. 1973, ARA&A, 11, 309
Bohlin R.C., Savage B.D., Drake J.F. 1978, ApJ, 224, 132
Debye P. 1909, Ann. Physik, 30, 59
Dickey J.M., Lockman F.J. 1990, ARA&A, 28, 215
Draine B.T. 1985, ApJS, 57, 587
Draine B.T., Lee H.M. 1984, ApJ, 285, 89
Hildebrand R.H. 1983, QJRAS, 24, 267
Kaplan S.A., Pikelner S.B. 1970, "The Interstellar Medium" (Cambridge: Harvard University Press)
Kent S.M., Dame T.M., Fazio G. 1991, ApJ, 378, 131
Kulkarni S.R., Heiles C. 1988, in "Galactic and extragalactic radio astronomy" (New York: Springer-Verlag)
Mathis J.S., Rumpl W., Nordsieck K.H. 1977, ApJ, 217, 425
Mie G. 1908, Ann. Physik, 25, 377
Osterbrock D.E. 1989, "Astrophysics of Gaseous Nebulæ and Active Galactic Nuclei", (Mill Valley, CA: University Science Books)
Rybicki G.B., Lightman A.P. 1979, "Radiative Processes in Astrophysics", (New York: Wiley-Interscience Publication)
Rowan-Robinson M. 1992, MNRAS, 258, 787
Schultz G.V., Wiemer W. 1975, A&A, 43, 133
Scoville N.Z., Sanders D.B. 1987, in "Interstellar processes" (Dordrecht: D. Reidel Publishing Co.)
Snedden C., Gehrz R.D., Hackwell J.A., York D.G. Snow T.P. 1978, ApJ, 223, 168
Spitzer L. 1978, "Physical Processes in the Interstellar Medium" (New York: Wiley)
Stein W.A. 1996, AJ, 112, 909
Türler M. 2000, PhD Thesis
Whittet D.C.B. 1992, "Dust in the Galactic Environment" (Bristol: IOP Publishing)
Zanstra H. 1927, ApJ, 65, 50

Chapter 2

Normal and Active Galaxies

Galaxies are large, isolated assembly of stars bound together by gravitational interactions whose sizes, shapes and luminosities vary enormously. The galaxy masses range from some million times that of the Sun[1] (e.g., the smallest dwarfs) to several trillion (10^{12}) solar masses (e.g., giants). Diameters range from few thousands to several 100 000 light years[2]. According to their shape, galaxies are regrouped in four main groups: spiral, ellipticals, irregulars and spheroidals (Hubble 1936).

Spiral galaxies usually consist of two major components: a flat, large disk and an ellipsoidal bulge component. The disk often contains a lot of interstellar matter and young (open) star clusters and associations often arranged in conspicuous and striking spiral patterns and/or bar structures. The bulge consists of an old stellar population without interstellar matter, and often associated with globular clusters. The young stars in the disk are classified as stellar population I[3], the old bulge stars as population II[4].

Spiral galaxies can take many forms; 10% of them fall into the class of grand-design spiral galaxies whose disks in the optical bands are dominated by two great arms, but most of them have more or less ratty or flocculent spiral structure (Elmegreen and Elmegreen 1987). There are two distinct groups of spiral galaxies, known as normal and barred spirals. The normal spirals show a more or less spherical nucleus, while the central regions of the barred spirals are elongated into a bar shape (Kormendy 1982). 50–60% of all disk galaxies are barred; the fraction of barred galaxies increases to 60–80% in near-infrared studies (Knapen, Shlosman and Peletier 2000). Each group is further divided into several sub-classes on the basis of the size of the nuclear bulge, the degree of opening of the arms, the fragmented nature and presence of star formation within the arms, and the presence of inner or outer ring features.

Elliptical galaxies have the simplest appearance with no pronounced structures, although many have a bright central nucleus. The rotation of elliptical is too slow to be responsible for their shape. There is strong evidence from the light distribution within the galaxies that many ellipticals are, in fact, triaxial ellipsoids with three unequal axes. They have little or no global angular momentum (i.e., do not rotate as a whole; of course, the stars still orbit the centres of these galaxies, but the orbits are statistically oriented such that the orbital angular momentum is small). Normally, elliptical galaxies contain very little or no

[1] 1 $M_\odot = 1.99\times10^{33}$ gr

[2] 1 light year = 9.46×10^{17} cm = 0.31 pc

[3] Stars of population I have solar composition, the brightest stars are blue and they are associated with gas clouds.

[4] Stars of population II are metal-poor, by factors of 10-1000. The brightest stars are red.

interstellar matter, and consist only of old population II stars. They appear like the luminous bulges of spirals, without a disk component. However, for some ellipticals, small disk components have been discovered, so that they may be representatives of one end of a common scheme of galaxy forms which includes the disk galaxies. Elliptical galaxies are subdivided according to their ellipticity.

The **spheroidal** or **lenticular galaxies** appear to be an intermediate structure between ellipticals and spirals. They are flat, disk-like systems, with a central condensation or bar, and they have similar rotation properties to spirals.

Often due to distortion by the gravitation of their intergalactic neighbours, **irregular galaxies** do not fit well into the scheme of disks and ellipsoids, but exhibit peculiar shapes. They contain huge amounts of gas and dust and their appearance is dominated by brilliant gas clouds and luminous stars scattered irregularly across the face of the galaxy.

A more detailed description of spiral galaxies, which are the subject of subsequent studies (see chapter 9 and 10), is given in the following sections.

2.1 Properties of spiral galaxies

2.1.1 The spiral structure

The spiral structure consists of young, bright stars in differential rotation (i.e., the angular speed, Ω, is inversely proportional to the radius R). If the spiral structure was differentially rotating, too, as suggested by its association with stars, it would wind up very tightly in a relatively short time scale (**winding dilemma**). This dilemma can be solved if stars follow slightly elliptical orbits with correlated orientations (Lin and Shu 1964). As is apparent from Figure 2.1, this arrangement produces **spiral density waves**. Material travels around undisturbed elliptical orbits; sometimes many orbits come close together increasing the density. The spiral structure is primarily a standing wave pattern that preserves its shape over a differentially rotating disk. The correlation among these elliptical orbits is due to a feedback

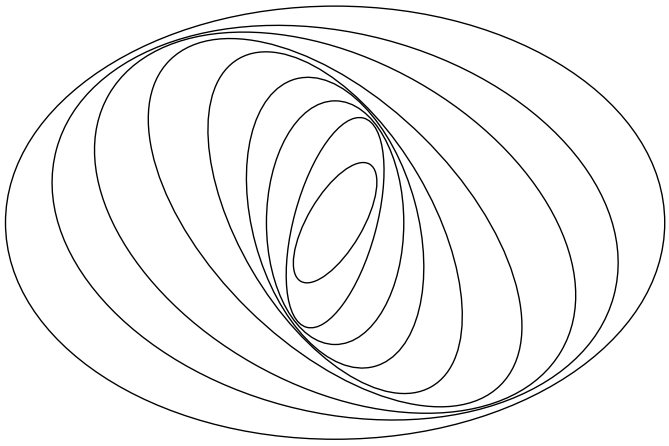

Figure 2.1: Orbits arrangement according to the density wave theory in a disk galaxy.

loop. As orbits start to correlate, the density increases, and the gravitational potential is mod-

ified, forcing the material to elliptical orbits. The correlation among the orbits is enhanced and the density increases further. Hence, the spiral structure arises through the interaction between the orbits and the gravitational forces of the stars of the disk.

The theory of spiral density waves does not predict the existence of persistent spiral arms, or quasi-stationary spiral structure. In order to drive and maintain the observed system, exciting mechanisms are required. Some can be transient, such as local instabilities in the stars or gas (e.g., bars) and tidal interactions with other galaxies, and some can be more steady, resulting from wave reflections and self-amplification in the disk (**modal theory**). The **modal theory** suggests that any galaxy with enough gas and a massive enough disk, and with a wave reflector in the central regions, can act like a resonant cavity. The cavity will amplify any tiny perturbation, internal or external, and create a global standing wave pattern or wave mode. According to this theory, the incoming waves would refract near the central regions because of either the bulge, or the lack of gas in the inner disk, or perhaps from a bar, and convert into longer-wavelength outward-moving waves. The outward moving waves would then reflect at corotation[5] in the middle of the galaxy and return inward, with some amplification, to reinforce the original spiral. In this way, the galaxy could generate a standing wave pattern. Such a wave would also continue to propagate outward outside the corotation. A review about spiral structure can be found in Athanassoula (1984).

The spiral arms have a pattern rotating like a rigid body with an angular "pattern speed" Ω_p. Throughout the regions where these waves exist, Ω_p is assumed less than Ω_c, where $r_c\Omega_c(r)$ is the "circular velocity" at the corotation radius r_c. Thus, the stars and the gas, moving around the galactic centre at about the circular velocity, will move through the pattern of density waves. The flow of the interstellar material through the spiral pattern is described in next section.

2.1.2 Spiral flow of stellar and interstellar material

In the majority of cases, the spiral arms are trailing[6] – stars and gas enter the arms on their concave, inner edges and leave them on their convex, outer edges. As the interstellar gas travels over the gravitational potential of the disk, it is periodically compressed. Large-scale shock fronts may then appear near the inner edges of the spiral arms where the gravitational potential is larger. Perhaps, these fronts account for some of the excess gas density observed in the arms and the concentration of bright, early-type stars, which have presumably formed from this gas.

High densities corresponding to the spiral arms compress the galactic magnetic fields and, consequently, produce a maximum in the radio continuum emission by synchrotron process. Bright stars appear "down-stream" from the peak in the radio continuum emission. Emission from molecular gas (traced by CO) peaks just "up-stream" of the arm's crest in the mass distribution. The HI peaks slightly towards the arms' convex side relative to the peak of CO emission, slightly down-stream of the peak in CO. Emission from ionized gas similarly peaks down-stream of the peak in CO. The near coincidence of the H_α and HI emission suggests that both arise through heating and dissociation of molecular gas by hot short-lived stars that form where the molecular density and CO emission are greatest.

[5]The corotation radius is defined as the distance from the centre at which the centrifugal force balances the mean gravitational force of the galaxy.

[6]A trailing arm is one whose outer tip points in the direction opposite to galactic rotation, while the outer tip of a leading arm points in the direction of the rotation.

These observational facts suggest that molecular gas clouds overtake the spiral arm from behind and concentrate into the density wave. The compression triggers the formation of stars. The massive stars are so short-lived that they die before they can leave the spiral arm. The less massive stars emerge from the front of the arm with the remains of the gas cloud. The new formed stars ionize the surrounding gas producing HII regions. The ionized gas then recombines forming neutral hydrogen.

2.1.3 Color gradients in disk galaxies

Disk galaxies are complex systems, which display a conspicuous disk and often an elliptical-like bulge and/or a bar, pronounced spiral arms, and significant quantities of dust. Dust absorbs and scatters blue light more strongly than the red light. Figure 2.2 shows how absorption and

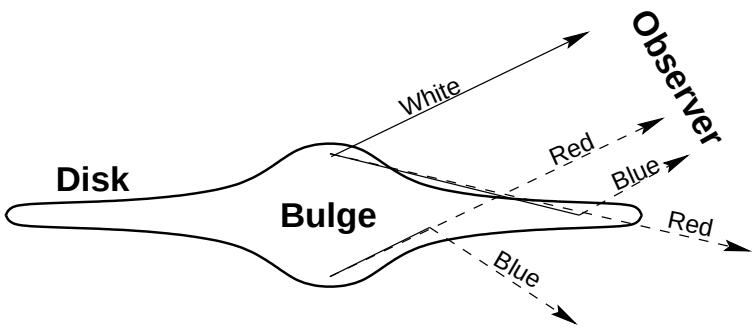

Figure 2.2: Effects of scattering and absorption of light by dust on the images of disk galaxies. Light from the top of the bulge reaches the observer without obstruction by dust in the disk. Light from the lower portion of the bulge is partially absorbed by the disk. Some light is forward scattered by the disk into the path to the observer. (Adapted from Binney and Merrifield (1998).)

scattering lead to colour and brightness asymmetries: the light received by the observer from the part of the bulge on the near side of the galaxy's major axis[7] is more strongly absorbed than the light from the far side, because much of the former has to pass right through the absorbing dust within the disk. Scattering by dust within the disk has precisely the opposite effect. Light emitted by the upper half of the bulge in Figure 2.2, is strongly forward scattered off by the dust in the disk and thus contributes extra blue light to the galaxy's image on the near side of the major axis. However, less light is scattered toward the observer by the far side of the disk. As a consequence, the near side of the image tends to be bluer and brighter than the far side. The relative importance of these two competing effects varies with the angle of inclination i of the galaxy's disk to the plane of the sky. At very large inclinations (e.g., edge-on galaxies), light is heavily absorbed, and forward scattering cannot make up for the light lost by absorption, which produces dark lanes across the image of the galaxy.

The effects of dust on photometric parameters depend on the amount of dust in the disk, as well as its distribution. For example, if the dust forms a smooth, vertically extended layer, it will profoundly affect inclination-dependencies; however, if it is confined to small clumps around luminous stars, it will have a negligible effect on inclination-dependencies. Extensive

[7]The major axis is given by the intersection of the galaxy disk and the plane of the sky.

discussions on this problem can be found in Giovanelli et al. (1995) and Davies and Burstein (1995).

Besides orientation effects, there are other potential causes of colour gradients in disks (i.e., the disk becomes steadily bluer in the outer region) related to the different stellar composition of the bulge (dominating inside a few kpc) and of the disk (dominating outside a few kpc): (i) gradients in the degree of internal extinction by dust, (ii) gradients in the mean ages of stars, and (iii) metallicity gradients. In practice, all three factors can be in competition in the galaxy, with the result that many major-axis colour profiles show no systematic trend.

2.1.4 Star formation in disk galaxies

In disk galaxies, star formation occurs in regions where the gas disk is unstable to **gravitational perturbation** growths (Kennicutt 1989; 1998). This can be empirically expressed as a condition of the gas surface density:

$$\Sigma_{gas} > \Sigma_{crit} = \frac{\alpha\kappa\sigma_{gas}}{3.36G} \equiv Q\Sigma_{gas} \tag{2.1}$$

where σ_{gas} is the velocity dispersion of the gas; α is a dimensionless constant near unity, that accounts for deviations of real disks from the idealized Toomre thin disk, single fluid model; Q is a dimensionless parameter (**Toomre parameter**) and κ is the epicyclic frequency

$$\kappa = \sqrt{2}\frac{v_{circ}}{R}\left(1 + \frac{R}{v_{circ}}\frac{dv_{circ}}{dR}\right)^{1/2} = \sqrt{2}\frac{v_{circ}}{R}(1+\beta)^{1/2} \tag{2.2}$$

with v_{circ} being the circular velocity at a particular galactocentric radius R, and $\beta \equiv d\,ln\,v_{circ}/dln\,R$, which is 0 for a flat rotation curve (Toomre 1964; 1977; Quirk 1972). From the outermost galactic star forming regions, Kennicutt (1989) finds $\alpha \simeq 0.67$, assuming $\sigma_{gas} =$ 6 km/s. Where $Q = (\alpha k\sigma_{gas} \;/\; \pi G\Sigma_{gas}) < 1$, the gas disk is gravitationally unstable, and fragments into bound clouds. Spiral density waves decrease the local value of Q, and often $Q < 1$ in the arm region and > 1 in the interarm region (e.g., Kuno et al. 1995). This may explain the larger fraction of star formation sites along the spiral arms.

When stars form, the energy they release raises σ_{gas}. Thus, star formation self-regulates such that the ISM is rapidly depleted until $\Sigma_{gas} \sim \Sigma_{crit}$ and $Q \sim 1$ (e.g., Silk 1997; Kennicutt 1989; Downes and Solomon 1998).

Where $Q \lesssim 1$, the averaged surface density of the star formation rate[8] ($\overline{\Sigma_{SFR}}$) in disk systems, is observed to be correlated with the combined surface density of atomic and molecular hydrogen ($\overline{\Sigma_{gas}}$) (Kennicutt 1998)

$$\overline{\Sigma_{SFR}} \propto \overline{\Sigma_{gas}}^{N}, \tag{2.3}$$

with $N \sim 1.4 \pm 0.15$ (see Figure 2.3). This relationship is known as **Schmidt law**, since it was predicted by Schmidt in 1959.

Gravitational interactions, however, may not be the real trigger for star formation; other processes have been proposed to explain the observed correlation between the star formation rates and gas density. Star formation can be induced in gas passing through **spiral** or **bar density waves**, or in correspondence of the shock front between **colliding clouds** (Scoville, Sanders and Clemens 1986; Tan 2000).

[8]The SFR gives the stellar mass that has been created in unit of time ($M_\odot$ yr^{-1}).

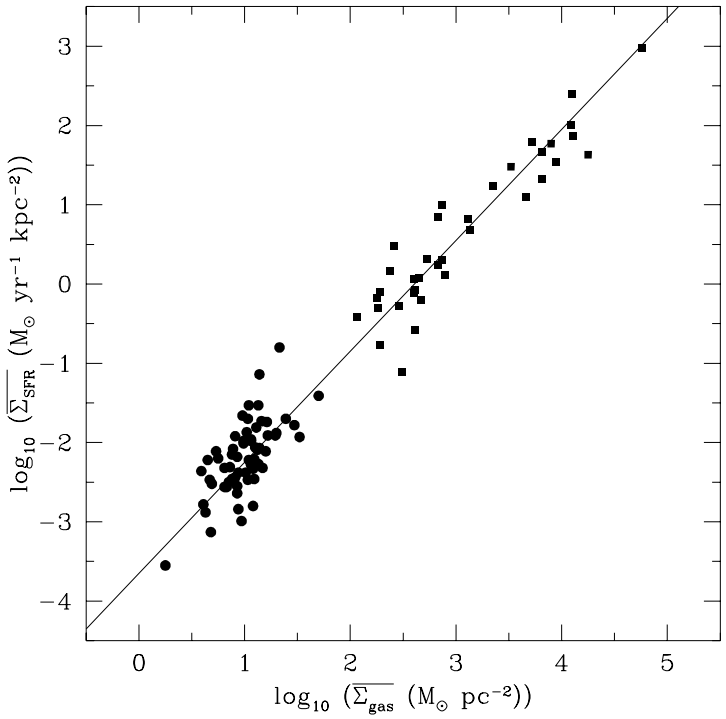

Figure 2.3: Schmidt law : $\overline{\Sigma_{SFR}} \propto (\overline{\Sigma_{gas}})^N$ (Kennicutt 1998). Data are disk averaged quantities for normal galactic disks (*solid circles*) and circumnuclear starburst disks (*solid squares*). The line is a least-squares fit with index $N = 1.40$. Systematic uncertainties between the normalization of the normal and starburst samples are of the order of a factor of two.

Star formation as traced by HII regions

Massive, young stars are the source of the vast majority of ionizing photons at distances in excess of tens of parsecs from the galactic nucleus. Their ionizing flux creates HII regions around them. Therefore, HII regions are a primary probe of high-mass star formation and of the properties of OB star clusters. A direct measure of the number of ionizing photons (Lyman continuum emission), and hence, of the mass of high-mass stars (correcting for extinction and assuming an initial mass function (IMF; see Appendix A)) is provided by the H_α luminosity emitted in HII regions. The luminosity function (LF) of HII regions, whose luminosity is given by the H_α luminosity, can then be used to study the distribution of masses and birth rates of OB associations.

The differential HII LF is usually parameterized as a power law:

$$N(L)dL = AL^{-\alpha}dL, \tag{2.4}$$

where $N(L)dL$ is the number of HII regions with luminosities in the range L to $L + dL$. Some interesting features are common in the HII LF of external galaxies. These features, listed below, have usually been interpreted as resulting from corresponding differences in star formation properties:

1. A large number of galaxies shows a break in slope of their LF, with the fainter HII regions showing a shallower slope compared with the high-luminosity objects.

   This break has been interpreted as a physical transition between normal and supergiant HII regions.

   The steepening of the luminosity function can be a result of either the evolutionary decay of the Lyman continuum emission from clusters as they age or of the mass distribution of the stellar associations and their high-mass stars.

2. The HII LFs of spiral galaxies sometimes show steeper slopes in the interarm regions than in the arm regions.

   The different slope can be due to a difference in gas dynamics and in the molecular cloud mass spectrum or to an aging effect in the interarm populations.

3. The slope of the HII LF varies with the morphological type of galaxy.

The study of HII LF is certainly an important and useful tool to understand the star formation process and the properties of massive star clusters.

The total mass of the new born stars can be determined from the rate at which they produce ionizing photons. Assuming that the rate of formation of massive stars has been approximately constant over the relatively short lifetimes of these objects (< 10 Myr) we can infer the rate at which massive stars are forming (SFR) from the number currently present. Thus, the H_α luminosity of a galactic disk, corrected for extinction, lead rather directly to the rate at which massive stars are forming within it, using the empirical correlation found by Kennicutt, Tamblyn and Congdon (1994)

$$\mathrm{SFR}(\mathrm{M}_\odot\ \mathrm{yr}^{-1}) = \frac{L(\mathrm{H}_\alpha)}{1.26 \times 10^{41}\ \mathrm{ergs\ s}^{-1}} \tag{2.5}$$

2.2 Peculiar galaxies: Starburst – AGN – ULIRG

There are galaxies which show a higher level of activity and larger luminosities than normal galaxies. Some of them are associated with bursts of star formation (**Starburst galaxies** and **Ultra Luminous Infrared Galaxies**), others with accretion on super massive black holes (**Active Galactic Nuclei**) and others with both (some **Ultra Luminous Infrared Galaxies** and **Active Galactic Nuclei**). A description of these systems is given below.

2.2.1 Starbursting system

A starburst is a burst of star formation that is too strong to be supported over the lifetime of a galaxy by all of the gas contained in the galaxy. Starbursting systems often involve jets, tails, or ring-like structures, but are extremely varied in form and do not conform to any set pattern. These systems tend to be blue, an indication of a significant number of stars born within the last Gyr. Many starbursting galaxies have suffered a catastrophic collision with other galaxies, which suggests that the burst of star formation is probably induced by interactions (Schweizer 1990; Barnes and Hernquist 1992).

Since starburst systems contain a large amount of dust which is heated by the young stars radiation field, they usually are very bright infrared (IR) sources and they suffer from substantial extinction at optical and ultraviolet (UV) wavelengths.

2.2.2 Active Galactic Nuclei

A galaxy with a central point-like source hundred of times brighter than the galaxy it-self is called active galactic nucleus (AGN). AGN show rapid variation in their brightness, which implies a small size of their emitting region (significantly less than a parsec). They are the most luminous (up to 10^{16} $L_{\odot}$) long-lived sources in the Universe. AGN emit strong radiation over the entire observable electromagnetic spectrum, from radio wavelengths to X- and γ-rays. The details of our understanding of these systems will not be described in this work. The reader is referred to the books by Robson (1996) and Krolik (1998).

The unified model and AGN classification

One presently popular model (i.e., the **standard unified model** (Antonucci 1993)) suggests that AGN are physically very similar objects and that the differences in their observational properties may be largely explained by three factors: (i) intrinsic luminosity; (ii) the presence of a jet; and (iii) orientation. The last two properties reflect their strongly anisotropic radiation patterns. Figure 2.4 illustrates the geometry inferred from observations of AGN as depicted by the standard unification model.

According to this model, a powerful energy source, probably a super-massive black hole (SMBH), lies at the centre of an accretion disk. The central regions of the AGN produce strong X-ray emission (and relativistic jets in radio-loud sources) along with thermal emission from the accretion disk. Much of this radiation is re-processed by dust and gas within the galaxy, modifying the optical-X-ray spectral energy distribution (SED). This results in strong IR emission from material further out in the galaxy, such as a dusty torus surrounding the accretion disk. The source's radiation is absorbed by the torus in all directions except along a cone around the torus's symmetry axis. Along the torus's axis and close to the central regions (0.01 $\rightarrow$ 0.1 pc) dense (10^{8-12} cm^{-3}) and fast-moving (10^{3-4} km s^{-1}) gas clouds are distributed. The gas in these clouds is photo-ionized by the energetic radiation field produced by the central regions (e.g., the accretion disk) and emits broad permitted emission lines. The region where these clouds are distributed is called broad line region (BLR). When the line of sight goes through the cone, the emission from this region is visible and the system is classified as a **type 1 Seyfert** or a **QSO** depending on the luminosity. At larger distances from the nucleus (100 pc $\rightarrow$ 1 kpc), another emission line region is present. This region contains clouds of gas at lower density (10^{3-6} cm^{-3}) and lower velocities (100-1000 km s^{-1}), which emit permitted and forbidden narrow lines. For these properties it is called narrow line region (NLR). When the line of sight goes outside the cone, only these narrow lines are visible. An object with only narrow lines in its optical spectrum is classified as a **type 2 Seyfert** or a **type 2 QSO**. A new class of Seyfert galaxies has been recently discovered with peculiar optical spectra. These are characterized by narrow permitted lines, as observed in type 2 objects, and ratios between the intensities of forbidden and permitted lines similar to those observed in type 1 objects. These systems are called **Narrow Line Seyfert 1 Galaxies**.

Unification in terms of orientation also accounts successfully for the phenomenology of radio-loud AGN. Radio jets emerge, at relativistic speeds, along the cone symmetry axis. When the jet is pointing toward the observer the system is classified as a **blazar**. In a **blazar**, the emission from the jet (synchrotron radiation) is Doppler shifted (see Appendix B) to higher frequencies and Doppler boosted to larger luminosities. The boosted synchrotron radiation dominates the emitted spectrum and produces a featureless continua at all frequencies. When

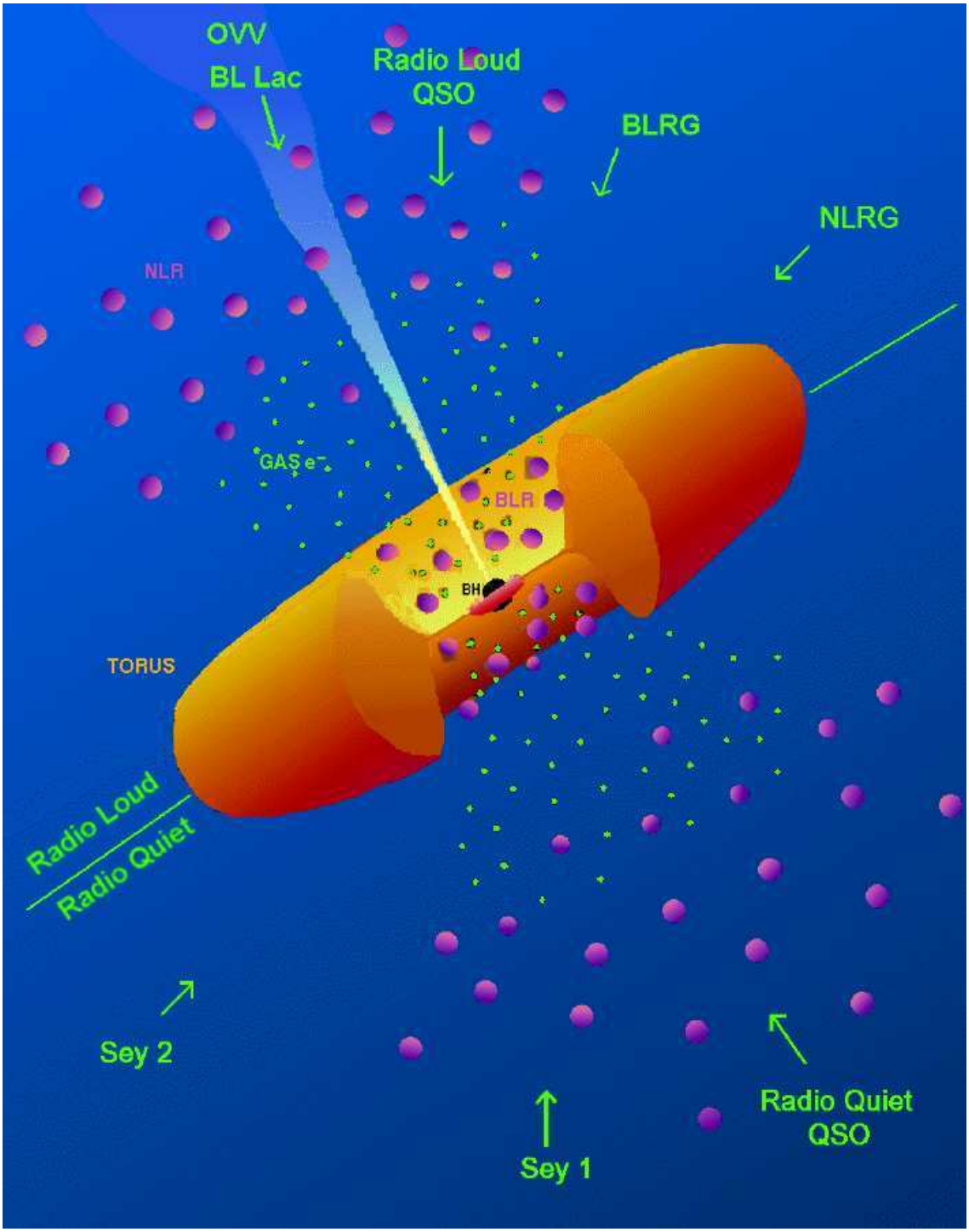

Figure 2.4: Schematic representation of the AGN unified model. Radio loud objects, containing a relativistic jet, are represented in the upper part of the figure; radio quiet, devoid of a large jet, are represented in the lower part. The main AGN components are reported in an unrealistic scale: the central BH (black hole) surrounded by the accretion disk, the clouds in the BLR and in the NLR, the molecular torus and the jet. The arrows represent the inclination of the observer's line of sight in respect of the AGN. At those inclinations the observer would classify the AGN as indicated by the names (see Table 2.1). (Adapted by Urry and Padovani (1995).)

Table 2.1: AGN Classification and Main properties

Observed properties	Name of Type		Present components[a]
	Radio Quiet	Radio Loud	
Broad[b] permitted lines			
Narrow[c] high excitation forbidden lines	• Seyfert 1	• Broad Line Radio Galaxy	Central engine + BLR
IR-opt-UV-X continuum	• QSO	• Quasars	+ NLR
Low polarization		(FSRQ & SSRQ)	
Variability			
Narrow[c] high excitation forbidden and permitted lines	• Seyfert 2	• Narrow Line	Hidden engine
Non-stellar continuum	• ULIRG	Radio Galaxy	+ NLR
Narrow[c] low excitation lines	• LINER	• LINER	Weak engine
Weak continuum			+ NLR
Strong continuum			
absent or weak lines		• BL Lac	Central engine
High polarization		• Blazar	or amplified jet
Dramatic and fast variability			

[a] See section 2.2.2 and Figure 2.4. [b] $v \simeq$5000-30 000 km s^{-1} [c] $v \simeq$200-1000 km s^{-1}

the jet axis forms 15-45% degrees with the line of sight, the boosted synchrotron radiation from the jet, the thermal radiation from the accretion disk and the optical line emission are visible and the object is classified as a **radio loud quasar**. When the jet is roughly in the plane of the sky, the galaxy is characterized by a "double-lobed" structure with a central source coinciding with the optical galaxy; such a system is classified as a **radio galaxy**. The radio lobes expand on either side of the central galaxy to many galaxy diameters. The separation of the two outer lobes may be from 100 kpc to a few Mpc. Among the radio galaxies there are systems of type 1, called **broad line radio galaxies (BLRGs)** and systems of type 2, called **narrow line radio galaxies (NLRGs)**.

The observed spectral energy distribution of AGN depends upon factors such as the amount and nature of obscuring material, the inclination of the line of sight and the amount of beamed emission related to the jets. The main properties of the different types of AGN are summarized in Table 2.1. The unified model predicts isotropy of far-IR and hard X-ray emissions in AGN, because, at these wavelengths, the radiation emitted by the jet should not dominate and the dusty torus should be transparent.

Other models have been proposed which can be alternative to the unification theory. The AGN power may be produced by accretion of matter in the form of stars and dissipation of the kinetic energy through stellar collisions rather than in a disk (Paltani and Courvoisier 1997;

Torricelli et al. 2000). Intrinsic differences, (e.g., starburst activity, amount of obscuring material) between objects of type 1 and 2, and not their orientation, might explain the differences in their observed properties (Dultzin-Hacyan 1995).

Radio Loud objects, jets and boosting effect

An AGN is classified as radio-loud if its emitted power per unit frequency at 5 GHz (6 cm) is larger than $5{\times}10^{31}$ ergs s^{-1} Hz^{-1}. These large radio luminosities are produced by several components:

1. a compact core with a flat radio spectrum ($S \propto \nu^{-\alpha}$; $\alpha \sim 0.0 \pm 0.2$), that is unresolved on the scale of an arcsec and opaque to its own radiation over a broad range of radio frequencies,

2. a relativistic jet extending from the compact core to large distances (up to 2 Mpc),

3. lobes at the end of the jet, with steep spectra indicating an older age of the emitting particles (i.e., electrons),

4. hot-spots with a spectrum slightly flatter than that of the surrounding regions (lobes) indicating local re-acceleration of the emitting electrons.

The powerful relativistic jet gives rise to the beaming properties observed in the blazar phenomenon. Since the jet components (i.e., blobs) are moving relativistically, their emission is changed by relativistic time dilatation. It turns out that for jets moving towards the observer, the observed emission, S^{obs}, is boosted in energy over that emitted in the rest frame, S^{em}, as shown by the following equation

$$S^{obs} = S^{em}[\gamma(1 - \beta cos\theta)]^{-(3+\alpha)} \tag{2.6}$$

where α is the spectral index of the radiation flux (which we define by $S_\nu \propto \nu^{-\alpha}$), θ is the angle between the direction of the jet and the line of sight, β is the ratio between the speed of the jet components, v, and the speed of light, c, and γ is the Lorentz factor given by $(1 - \beta^2)^{-1/2}$ (see chapter 1 section 1.4.2). The term $[\gamma(1 - \beta cos\theta)]^{-1}$ is called Doppler factor $\mathcal{D}$ (see Appendix B), and $\mathcal{D}^{-(3+\alpha)}$ is the boosting factor. For a jet heading toward the observer, assuming typical values observed in blazars, $\alpha = 0.75$, $\beta = 0.95$ and $\theta = 10^\circ$, the boosting factor is ~ 370.

The boosting effect and different orientations of the jet with respect to the observer's line of sight can produce different observed radio spectra even if the source is intrinsically the same. Sources with the jet slightly inclined from the line of sight (small θ), are dominated by strong radio emission from the compact core and, therefore, they usually show flat spectra ($\alpha \sim 0.0$) extending to the highest radio frequencies and in some cases into the submillimetre region. From the shape of their radio spectra, these sources are classified as Flat Spectrum Radio Loud Quasars (FSRQ). Sources with more inclined jets (larger θ) show radio spectra dominated by the emission from more extended radio components as the lobes and, therefore, show steep radio spectra ($\alpha \sim -0.7$). They are classified as Steep Spectrum Radio Loud Quasars (SSRQ).

Energetic

The energy source in AGN is ultimately derived from the gravitational energy of falling matter, in particular, gas that is falling into a supermassive black hole (10^{6-10}M$_\odot$). Inevitably the gas acquires a swirling motion as it falls, creating an accretion disk in orbit about the black hole. This gaseous disk suffers frictional (and possibly magnetic) heating to very high temperatures, perhaps creating a corona above the disk. As the resulting light is radiated away, the material sinks closer to the black hole, eventually falling inside the black hole's event horizon and increases the mass of the black hole. In the meantime, new material has fallen onto the accretion disk to replenish the fuel supply. The gravitational energy is released by viscous dissipation as the gas flows through a rotating disk around the central nucleus. The gravitational potential energy released by the accretion of a mass m onto the surface of a body of mass M and radius r is:

$$E_{acc} = \frac{GMm}{r} \tag{2.7}$$

and the rate at which the gravitational energy is released is given by:

$$L_{acc} = \frac{dE_{acc}}{dt} = \frac{GM}{r} \cdot \frac{dm}{dt} = \frac{GM\dot{m}}{r} \tag{2.8}$$

where $\dot{m}$ is the accretion rate. The accreted mass is transformed in radiation energy with an efficiency η

$$E = \eta mc^2 \tag{2.9}$$

and the rate at which the energy is emitted ($L = dE/dt$) is:

$$L = \eta \dot{m} c^2. \tag{2.10}$$

The value of η depends on the binding energy of the maximally bound orbit around a black hole (i.e., 5.7% for a Schwarzschild black hole and 42% for a Kerr or rotating black hole), which is an order of magnitude larger than the nuclear burning efficiency, typical of stars.

For a black hole of mass M$_{BH}$ an approximate upper limit on its power is given by the Eddington luminosity corresponding to equivalent radiation pressure and gravitational attraction[9]:

$$L_{Edd} = \frac{4\pi GMm_p c}{\sigma_T} \simeq 3 \cdot 10^4 \left(\frac{M_{BH}}{M_\odot}\right) \quad L_\odot \tag{2.11}$$

where G is the gravitational constant, m_p is the mass of a proton and σ_T is the Thompson interaction cross-section.

Host galaxy

In the case of nearby low-power AGN, such as LINERs and Seyfert nuclei, the host galaxies appear to be fairly normal spiral galaxies. Radio galaxies, almost without exception, are found to be elliptical galaxies, although in many cases their morphology are somewhat disturbed. All radio loud quasars seem to be hosted by giant elliptical galaxies, while the majority of radio quiet quasars are hosted by spiral galaxies and some of them in ellipticals (Taylor et al. 1996). It seems that there is no direct correspondence between the luminosity of an AGN and the luminosity of its host galaxy.

[9] 1 $L_\odot$ = 3.33×10^{33} erg s^{-1}

2.2.3 Ultra Luminous Infrared Galaxies

Numerical simulations show that torques and shocks during a merger efficiently remove angular momentum from the gas in merging galaxies, which flows to the galaxy centre(s) (e.g., Mihos and Hernquist 1996). The gas gets compressed and is expected to form stars. This is generally confirmed observationally. Observations of the well-known Antennae galaxies beautifully reveal wide-spread star and star cluster formation (Whitmore et al. 1999). Often the star formation is dust-enshrouded causing a majority of the energy to be emitted in the IR. In the most spectacular cases, this leads to Ultra Luminous Infrared Galaxies (ULIRGs). Such galaxies are defined by their large IR luminosities ($\geq 10^{12}$ $L_{\odot}$). Most of them are seen to be interacting systems or merger remnants.

The nature of the dominant power source in ULIRGs is still debated between an AGN and/or a starburst. In some cases the presence of an (obscured) AGN is unambiguous from the observation of strong X-ray emission, as in NGC 6240 (e.g., Vignati et al. 1999). Genzel et al. (1998) have used IR emission-line diagnostic ratios from ISO data to address the nature of the energy source of ULIRGs more quantitatively. They find that 70–80% of the ULIRGs in their sample are predominantly powered by recently formed massive stars, and 20–30% by a central AGN. In several ULIRGs, more than 50% of the bolometric luminosity is due to a heavily dust enshrouded AGN (Sanders 1999). Half of the known ULIRGs probably have both an active nucleus and starburst activity.

2.2.4 Relative contributions of starburst- and accretion-powered emission to AGN SEDs

The most luminous long-lived sources in the Universe are AGN and ULIRGs, with luminosities up to $10^{13}L_{\odot}$. While the overall SED of AGN is quite flat from far-IR to optical/UV wavelengths, that of ULIRGS strongly peaks in the far-IR and decreases toward shorter wavelengths suggesting a domination by dust emission in massive starbursts (see Figure 2.5). However, the detection of AGN components in ULIRGs (Iwasawa 1999) and of starburst activity in AGN (Genzel and Cesarsky 2000), indicate that accretion and starburst processes are linked. The connection between star formation and nuclear activity in galaxies has been the subject of a number of recent studies. On the theoretical side, models such as those of Perry and Dyson (1985) and Norman and Scoville (1988) propose that a nuclear young stellar cluster is the reservoir of fuel for the AGN. On the observational side, Terlevich, Diaz, and Terlevich (1990) have argued that for a number of Seyfert 2 galaxies, circumnuclear starbursts are necessary to explain the strength of the Ca II triplet (at 8500 Å) in absorption. Starbursts also have been proposed as the source of the blue unpolarized continuum observed in Seyfert 2 galaxies (Tran 1995a, 1995b, 1995c) by Cid Fernandes and Terlevich (1992, 1995). Heckman et al. (1995) have proposed the same on the basis of the International Ultraviolet Explorer (IUE) spectra of the brightest Seyfert 2 galaxies in the UV. Detailed studies of individual cases have been performed by Heckman et al. (1997), who have shown UV images and spectra of the circumnuclear starburst around Mrk 477. González Delgado et al. (1998) have analyzed similar data for the starbursts around the Seyfert 2 nuclei of NGC 7130, NGC 5135, and IC 3639. The latter studies have shown the most unambiguous signatures of massive starbursts around these nuclei, but have been performed for only four galaxies.

In order to understand the energetics of these systems (AGN and ULIRGs), it is necessary to quantify how much starburst emission is present in AGN SEDs (and *vice versa*).

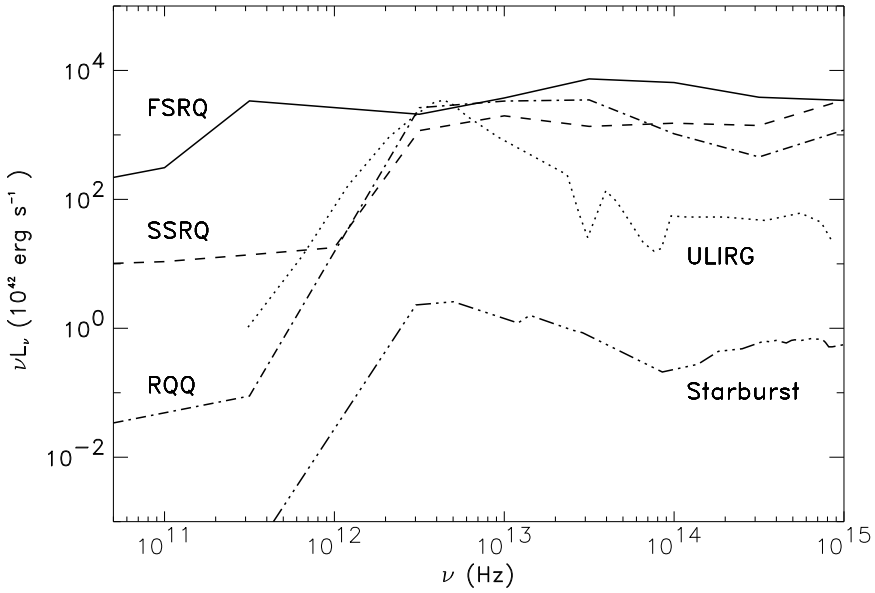

Figure 2.5: Average spectral energy distribution from radio (5×10^{10} Hz; 6 mm) to optical (1×10^{15}; 3000 Å) frequencies for Flat Spectrum Radio Loud Quasars (FSRQs), Steep Spectrum Radio Loud Quasars (SSRQ), Radio Quiet Quasars (RQQ), Ultra Luminous Infrared Galaxies (ULIRGs) and Starburst Galaxies.

Bibliography

Antonucci R. 1993, ARA&A, 31, 473

Athanassoula E. 1984, Phys. Reports, 114, 319

Barnes J.E., Hernquist L.E. 1992, ARA&A, 30, 705

Binney J., Merrifield M. 1998, "Galactic Astronomy" (Princeton: Princeton University Press)

Cid Fernandes R., Terlevich R. 1992, in ASP Conf. Proc. 31, ed. A.V. Filippenko (San Francisco: ASP)

Cid Fernandes R., Terlevich R. 1995, MNRAS, 272, 423

Davies J.I., Burstein D. 1995, NATO Advanced Science Institutes (ASI) Series C: Mathematical and Physical Sciences, eds. J.I. Davies and D. Burstein (Dordrecht: Kluwer Academic Publishers)

González Delgado R.M., Heckman T., Leitherer C., Meurer G. et al. 1998, ApJ, 505, 174

Downes D., Solomon P.M. 1998, 507, 615

Dultzin-Hacyan, D. 1995, Revista Mexicana de Astronomia y Astrofisica Serie de Conferencias, 3, 31

Elmegreen D.M., Elmegreen B.G. 1987, ApJ, 314, 3

Genzel R., Lutz D., Sturm E., Egami E. et al. 1998, ApJ, 498, 579

Genzel R., Cesarsky C.J. 2000, ARA&A, 38, 761

Giovanelli R., Haynes M.P., Salzer J.J., Wegner G. et al. 1995, AJ, 100, 1059

Heckman T.M., Krolik J.H., Meurer G., Calzetti D. et al. 1995, ApJ, 452, 549

Heckman T.M., González Delgado R., Leitherer C., Meurer G.R. et al. 1997, ApJ, 482, 114

Hubble E. 1936, "The Realm of the Nebulæ" (New Haven: Yale University Press)

Iwasawa K. 1999, MNRAS, 302, 961

Kennicutt R.C. 1989, ApJ, 344, 685

Kennicutt R.C. 1998, ApJ, 498, 541
Kennicutt R.C., Tamblyn P., Congdon C.E. 1994, ApJ, 435, 22
Knapen J.H., Shlosman I., Peletier R.F. 2000, ApJ, 529, 93
Kormendy J. 1982, in "Morphology and Dynamics of Galaxies" Twelfth Advanced Course of the Swiss Society of Astronomy and Astrophysics eds. L. Martinet and M. Mayor (Berlin: Springer-Verlag)
Krolik J.H. 1999, "Active Galactic Nuclei: from the central black hole to the galactic environment" (Princeton: Princeton University Press)
Kuno N., Nakai N., Handa T., Sofue Y. 1995, PASJ, 47, 745
Lin C.C., Shu F.H. 1964, ApJ, 140, 646
Mihos J.C., Hernquist L. 1996, ApJ, 464, 641
Norman C., Scoville N. 1988, ApJ, 332, 124
Paltani S., Courvoisier T.J.-L., 1997 A&A 323, 717
Perry J.J., Dyson J.E. 1985, MNRAS, 213, 665
Quirk, W.J. 1972, ApJ, 176, L9
Robson I. 1996, "Active Galactic Nuclei" eds. J. Wiley & Sons (Chichester: Praxis Publishing)
Sanders D.B. 1999, Astrophysics and Space Science, 266(1/2), 331
Schweizer 1990, in "Dynamics and Interactions of Galxies", ed. Wielen R. (Berlin: Springer-Verlag)
Scoville N.Z., Sanders D.B., Clemens D.P. 1986, ApJ, 310, L77
Silk J. 1997, ApJ, 481, 703
Tan J.C. 2000, ApJ, 536, 173
Taylor G.L., Dunlop J.S., Hughes D.H., Robson E.I. 1996, MNRAS, 283, 930
Terlevich E., Diaz A.I., Terlevich R. 1990, MNRAS, 242, 271
Toomre A. 1964, ApJ, 139, 1217
Toomre A. 1977, ARA&A, 15, 437
Torricelli-Campioni G., Foellmi C., Courvoisier T.J.-L., Paltani S., 2000, A&A, 358, 57
Tran H.D. 1995a, ApJ, 440, 565
Tran H.D. 1995b, ApJ, 440, 578
Tran H.D. 1995c, ApJ, 440, 597
Urry, Padovani P. 1995, PASP, 107, 803
Vignati P., Molendi S., Matt G., Guainazzi M. et al. 1999, A&A, 349, L57
Whitmore B.C., Zhang Q., Leitherer C., Michael F.S. et al. 1999, AJ, 118, 1551

Part I

The ISOPHOT project

Chapter 3

The Infrared Space Observatory

The European Space Agency's (ESA) Infrared Space Observatory (ISO; Kessler et al. 1996) is an astronomical satellite that was operational between November 1995 and May 1998. ISO's orbit was highly-elliptical with a perigee at around 1000 km, an apogee at 70500 km and a period of almost 24 hours. The lowest parts of the orbit lay inside the Earth's van Allen belts of trapped electrons and protons. Inside these regions ISO's detectors were scientifically unusable due to effects caused by radiation impacts. ISO spent almost 17 hours per day outside the radiation belts and during this time all detectors could be operated.

ISO covered the infrared range of the electromagnetic spectrum from 2.5 to 240 μm. Since the atmosphere prevents most infrared photons from reaching the ground, a space telescope is needed to detect this kind of radiation.

Observing the cool universe requires cool instruments, working at temperatures close to absolute zero ($-$ 273° C). In order to keep the temperature low, a large liquid-helium cryostat, filled with 2286 litres of superfluid helium, was installed on board ISO. ISO's lifetime was limited by its helium supply; hence nearly all observations had to stop when this coolant liquid got depleted after almost 30 months.

The satellite essentially consists of a large liquid-helium cryostat; a telescope with a 60 cm diameter primary mirror; four scientific instruments and the service module (see Figure 3.1).

3.1 ISO capabilities, goals, results, and discoveries

ISO was the first infrared astronomy satellite to have high spatial and spectral resolution, good sensitivity and wide wavelength range. Targets ranged from Solar System to the most distant proto-galaxies. The capability of the infrared radiation to escape dusty regions and, at the same time, to trace thermal emission from dust, and to see directly mid- and far- infrared emission lines, which suffer very little absorption and are sensitive to a very wide range of densities and ionization level, enabled ISO to explore several topics in the extragalactic domain:

1. intense star formation in galaxies;
2. emission from dust heated by AGN;
3. collisions of galaxies;
4. violent eruptions in galactic cores.

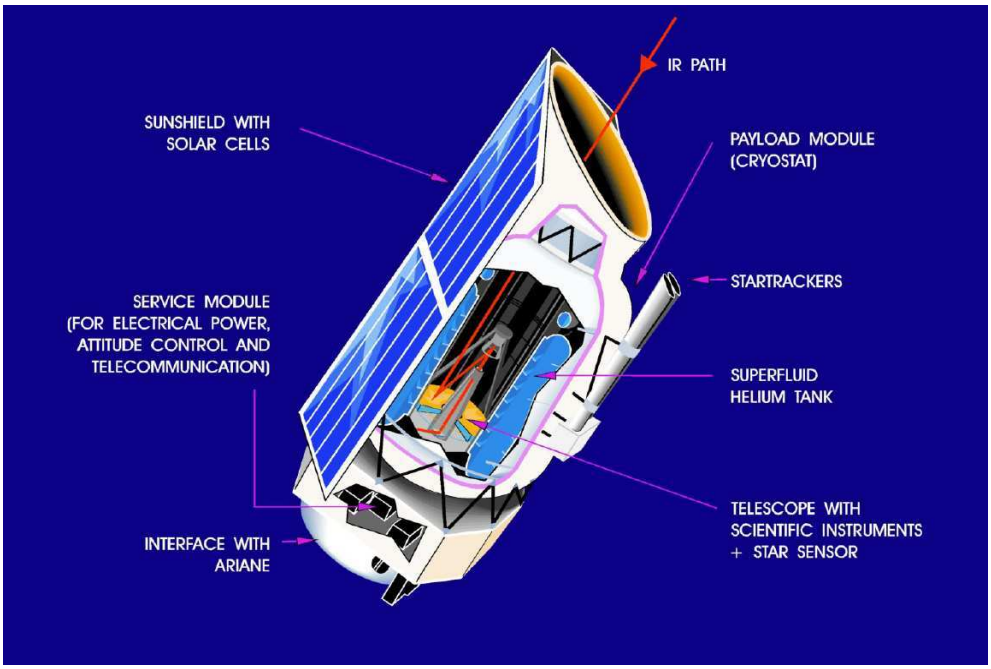

Figure 3.1: The ISO spacecraft

Some of the results obtained so far by ISO in the extragalactic concern:

1. Dust in the apparently empty space between the galaxies (Stickel et al. 1998).
2. Star formation in our Galaxy (Lutz et al. 1996).
3. The nature of ULIRGs. Infrared emission line studies of ULIRGs show a wide and continuous range of behaviour ranging from pure starburst to accretion on a SMBH dominated sources, the latter being primarily at high luminosities (Clemens 1999; Fisher et al. 1999; Lutz et al. 1999; Rigopoulou et al. 1999; Haas et al. 2000; Genzel et al. 2000).
4. The infrared emission sources in AGN (the stellar component of the galaxy, the nucleus and the radio jet) (Carilli and Barthel 1996; Pérez García et al. 1998, 2000; Alexander et al. 2000; Clavel et al. 2000; Tansley et al. 2000)

Many of ISO's discoveries haven't come out yet because they are still being processed by the researchers.

3.1.1 The Science instruments

The infrared radiation collected by the single 60 cm telescope in ISO was sent via a pyramidal mirror to four instruments. A selection of fields of view (FOV) and filters was available, to suit the nature of the object examined. The four instruments and their characteristics (wavelength coverage, FOV, and spatial resolution) are described in Table 3.1.

Table 3.1: Main Characteristics of the ISO Instruments

Instrument and Main Function	λ Range (μm)	Outline Description	Spatial Resolution
ISOCAM Camera and polarimeter	2.5 - 17	32×32	Choice of 1.5, 3, 6 or 12″per pixel
ISOPHOT Imaging Photo-polarimeter	2.5 - 240	(i) Multi-aperture, multi-band photo-polarimeter (3-120 μm) (ii) Far-infrared camera 50-100 μm: 3×3 pixels 100-240 μm : 2×2 pixels (iii) Spectrophotometer (2.5-12 μm)	(i) Choice of diffraction-limited to 3′apertures (ii) 43″per pixel 89″per pixel (iii) 24″×24″ aperture
ISO-SWS Short-Wavelength Spectrometer	2.5 - 45	(i) Two gratings 2.5-45 μm (ii) Two Fabry-Pérot interferometers 15-30 μm	(i) 14″×20″ 14″×27″ 20″×33″ (ii) 10″×39″
ISO-LWS Long-Wavelength Spectrometer	45 - 196.8	Grating and Two Fabry-Pérot interferometers	1′.65 diameter aperture

Since this work is based on a large dataset obtained with the Imaging Photo-Polarimeter (ISOPHOT), a detailed description of only this instrument, its detectors, capabilities and performances will be presented in the following sections.

3.2 The Imaging Photo-Polarimeter

ISOPHOT (PHT) was composed of 3 subsystems, or sub-instruments, optimized for specific photometric modes. Only one sub-instrument could be used at a time. The sub-instruments were:

- PHT-P, a multi-filter, multi-aperture photo-polarimeter with three single detectors covering the wavelength range 3 - 120 μm.
- PHT-C, two photometric far-infrared (FIR) cameras for the wavelength range 50 - 240 μm.
- PHT-S, two grating spectrophotometers, operated simultaneously, for the wavelength ranges of about 2.5 - 5 μm and 6 - 12 μm.

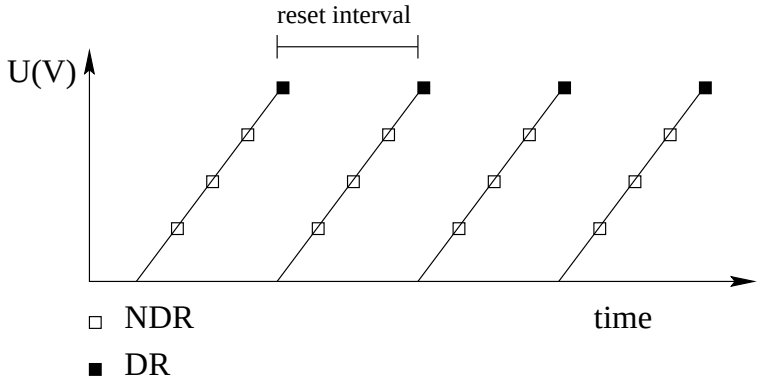

Figure 3.2: PHT read-out cycles. NDR is the non-destructive read-out, DR is the destructive read-out which resets the detector

In addition, PHT was equipped with two sets of three polarizers, one set for the PHT-P detector group and one for the PHT-C detectors, covering the whole wavelength region from 3 to 240 μm.

A focal plane chopping mirror (FPC) was included for beam switching and modulation within the FOV of the instrument. For absolute photometric measurements, two fine calibration sources (FCSs) were used as standard reference sources.

The ISOPHOT detectors were either Si doped or Ge doped photo-conductors. Each detector pixel was connected to one input channel of a cold readout electronics (CRE). In case the detector was receiving infrared photons from an astronomical or internal source, the voltage V at the output of the CRE increased as a function of time. The voltage increase per time interval was dependent on the amount of the current through the detector which was in turn dependent on the number of photons falling on the detector. In the following sections, this voltage increase or slope (in V/s) will be referred to as signal.

Once signals from calibration standards have been measured, it is possible to relate the signal to a power from the source in the filter band.

By applying a sample pulse the voltage was clamped and during the integration, the clamped signal was read out through a multiplexer. Since the output voltage should stay within a limited range, the voltage was reset by short circuiting the capacitors using both the ground as well as the reset switch. A reset pulse was applied in addition to a sample pulse after a number of desired voltages had been sampled. The readout associated with this reset is called the destructive readout (DR), the other sampled voltages are called non-destructive readouts (NDR). The time between two reset pulses (in seconds) is called the fundamental integration time or reset interval (RI). All readouts collected during one reset interval are part of one integration ramp or simply ramp. In Figure 3.2 the readout data stream is shown schematically. The voltage of the first readout after reset is not zero but starts at an arbitrary voltage level. This level is called the reset level, since it has more or less the same value during a measurement.

3.2.1 ISOPHOT Detector Subsystems

PHT-P: Subsystem PHT-P was designed for sensitive, high precision photometry and polarimetry, using three different detectors types (in parenthesis the detector material is given):

- P1 (Si:Ga) 10 filters: 3.3 - 16 μm
- P2 (Si:B) 2 filters: 20 and 25 μm
- P3 (Ge:Ga) 2 filters: 60 and 100 μm

All apertures (5.0, 7.6, 10, 13.8, 18, 20×32, 23, 52, 79, 99, 120, 127×127 and 180 arcsec) were circular except two that were rectangular and square.

PHT-C: PHT C100 was a 3×3 array of elements. The effective size of the pixels on the sky was $43\farcs5 \times 43\farcs5$, the distance between the pixel centres ('pitch') was $46\farcs0$.

PHT C200 consisted of 4 pixels arranged in a 2×2 matrix. The effective size of the pixels on the sky was $89\farcs4 \times 89\farcs4$, the distance between the pixel centres was $92\farcs0$.

There were 6 filters for C100 covering the wavelength range from 50 to 100 μm and 5 for C200 covering the wavelength range from 100 to 240 μm.

Table 3.2 gives a list of PHT-P and PHT-C filters including the central wavelength, the widths, and the transmission.

3.2.2 Instrument Modes

The three main PHT observing modes were photometry, spectrophotometry and polarimetry. In the photometric mode PHT, observers could choose three different observing modes, raster, staring and chopped, according to the selected targets, point-like or extended. In the following sections, only the photometric modes used during the observations presented in this work will be described: chopping and mapping.

Chopping Mode

In chopper mode the FOV of the detector was swapped using the FPC mirror between the source (on-source position) and adjacent fields on the sky (off-source position) several times.

There were three different chopper modes available for single pointing photometry. The chopper modes used in this work are illustrated in Figure 3.3 and described below:

- Rectangular - The satellite pointed to the position between the source and an off-source position, and the chopper moved alternately between these two positions.
- Triangular - Chopping occurred to two positions on either side of the source. The satellite pointed to the source position, and the chopper moved from one off-source position to the source and then to the other off-source position and finally back to the source, and so forth. In this way, the source was observed twice during each cycle and each of the off-source positions once.

Table 3.2: PHT-P and PHT-C filter characteristics.

Filter	λ_C (μm)	$\Delta\lambda$ (μm)	R_{mean}	Filter	λ_C (μm)	$\Delta\lambda$ (μm)	R_{mean}
P1				C100			
3.29	3.30	0.22	0.12	50	67.3	57.8	0.04
3.6	3.59	1.00	0.14	60	60.8	23.9	0.11
4.85	4.86	1.55	0.17	70	80.1	49.5	0.15
7.3	7.43	3.38	0.29	90	95.1	51.4	0.39
7.7	7.64	0.84	0.26	100	103.5	43.6	0.30
10	9.99	1.86	0.35	105	107.0	37.4	0.22
11.3	11.36	0.77	0.31				
11.5	11.89	6.51	0.51	C200			
12.8	12.83	2.33	0.55	120	119.0	47.3	0.13
16	15.14	2.86	0.38	135	161.0	82.5	0.22
				160	174.0	89.4	0.44
P2				180	185.5	71.7	0.37
20	21.08	9.43	0.33	200	204.6	67.3	0.26
25	23.81	9.18	0.39				
P3							
60	60.06	25.48	0.12				
100	101.63	40.15	0.32				

λ_C is the central wavelength, $\Delta\lambda$ is the width and R_{mean} the average relative system response derived from the bandpasses (filter transmission function convolved with the relative spectral detector response normalized to its maximum value).

Mapping Mode

The mapping or raster mode consisted in a sequence of observations on a two-dimensional regular grid created by a sequence of spacecraft pointings (M×N, where M is the number of raster points, and N the number of raster legs). The detector setting remained unchanged for all pointings. A special raster mode was the so-called telescope nodding consisting of multiple linear scans across the source ($\Delta N = 0$, where ΔN is the displacement of the detector along the rater legs).

The covered region of the sky and the relative position of the object in the two mapping modes are shown in Figure 3.4.

Choice of PHT observing mode

Depending on the structure of the background flux (e.g., flat background, infrared cirrus, or with strong gradients), a different chopper mode was preferred prior to the launch. Chopping

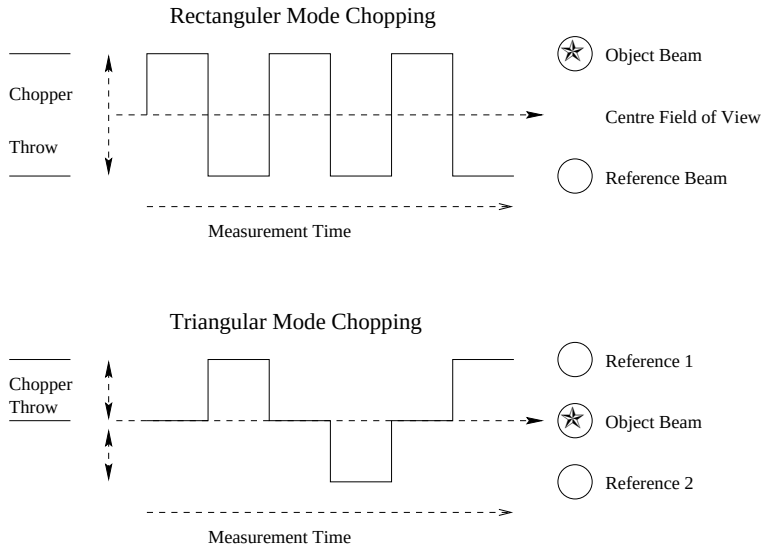

Figure 3.3: Chopper modes. The solid curves represent the chopping cycles. To the right the projection on the sky is illustrated.

was recommended, if the sky background was expected to be comparable to the source flux, or stronger. After the launch it was found that the fastest chopper frequencies meant significant signal losses of the differential signal with regard to the stabilized signal difference given by raster observations. Therefore, the raster mode was recommended as a better alternative for slow signal modulation of very bright and intermediate sources against the sky background. This last observing mode was also recommended in the studies of point sources on complex backgrounds or extended sources (sizes of more than 3 arcmin).

3.2.3 Fine Calibration Sources (FCSs) and their calibration

The internal fine calibration sources acted as stable reference sources and were used for photometric calibration of PHT-P or PHT-C observations. In terms of data collection, internal calibration measurements were similar to the celestial measurements except that they utilized one of the internal FCSs by imaging it via the chopper mirror. There were two identical FCSs which could be operated independently. Each FCS consisted of two Thermal Radiation Sources (TRSs).

One FCS measurement was obtained at the end of a sequence of measurements with a given detector subsystem for single pointing photometric observations. In case of multi-filter observations using more than one detector subsystem, several FCS measurements were collected. For long observations using raster mode, the actual measurement was bracketed by two internal calibration measurements.

By controlling the source temperature between 5 K and 300 K with an accuracy of ΔT$\sim$0.1 K, different flux levels in the range $5{\cdot}10^{-17}$ to $\geq 10^{-12}$ W on the detector could be applied to the PHT-P and PHT-C detectors. The temperature was accomplished by tuning the electrical heating power of the FCSs. The internal calibration was performed with the last filter used with the current detector. This meant that there was one FCS calibration per detector used and per more than one filter. It was assumed that the response of the detector is linear in the measured power range. By relating the in-band power of the calibration target to its

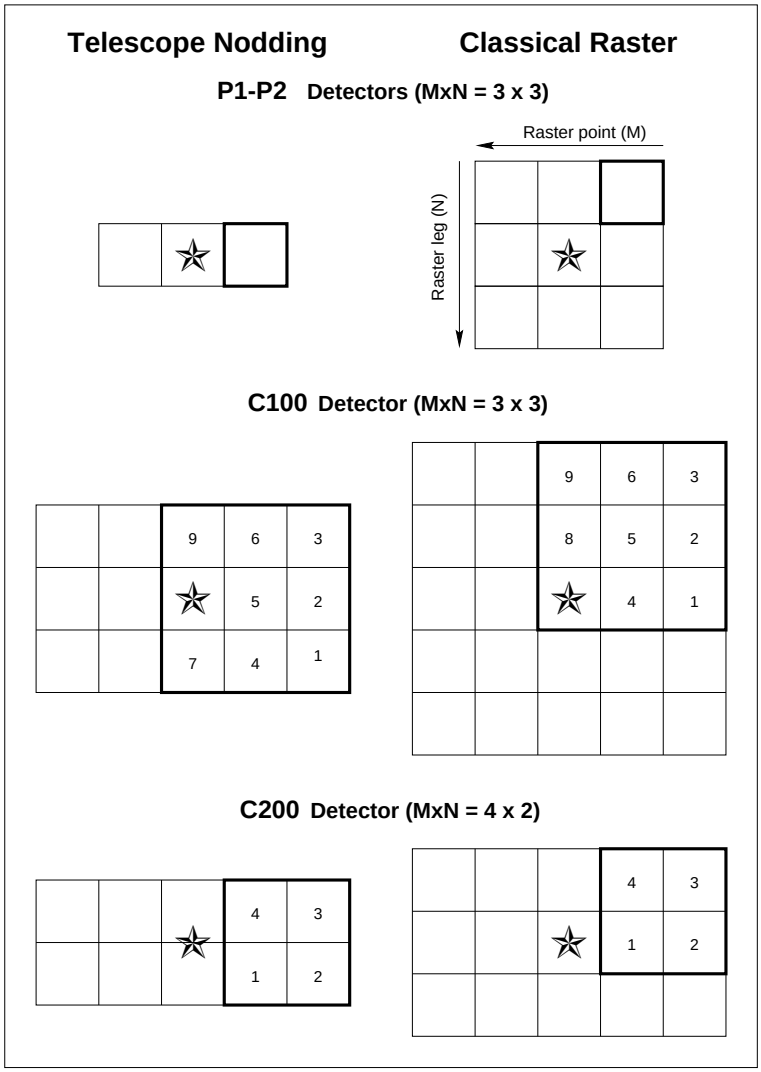

Figure 3.4: Schematic representation of the two observing modes used for mapping observations: telescope nodding (scan) on the left side and classical raster on the right side. The position of the source in the different cases is represented by a star. The bold square represents the initial FOV of the detector on the sky. The numbering corresponds to the pixels numbers. The numbers in parenthesis refer to the number of raster points (M) $\times$ the number of raster legs (N).The detectors move first from the left to the right, then in the opposite direction. In the case of classical raster, at each change of the horizontal direction, the detector shifts down one step. In the case of telescope nodding, the detector does not move along the raster leg direction (ΔN = 0), but scans N times the same sky region. All the steps are separated by the pixel size. The reported pixel sizes do not correspond to the real proportions.

corresponding signal, the FCS signals were converted to in-band powers. These together with the commanded FCS heating powers were used to derive the FCS power calibration tables.

3.2.4 The ISOPHOT Interactive Analysis (PIA)

The ISOPHOT Interactive Analysis (PIA) is a scientific and calibration data analysis tool for ISOPHOT data reduction. The data reduction consists basically of removal of instrumental effects and flux calibration.

In detail, the data reduction includes the following steps:

1. Correct for non-linearity.

2. Correct for cosmic particle hits (glitches) on read-out level. A cosmic radiation event ("glitch") generally results in a jump of two consecutive read-out values, i.e., in a step within the "ramp".

3. Determine signal (in V/s) per integration ramp.

   The output of each of the integrating PHT detectors consists of the read-out value as a function of time. A number of non-destructive integrating read-outs (NDRs) are followed by a destructive read-out at which the integration plateau is reset, in principle, to zero. Each sequence of NDRs defines a ramp (voltage as a function of time); the steeper the ramp, the higher the signal (and the power on the detector) is. Thus the signal values are derived by fitting a 1st order polynomial to each ramp. After this processing step the data consist of the signal as a function of time.

   The next step is to combine all the signal values (SRD: signal per ramp data) into a representative signal for each chopper plateau (SCP).

4. Analyze/edit data to minimize the effect of drifts in detector response.

   The detectors show transient drift/memory effects on time scales of the order of a few seconds up to a few minutes (in the worst cases). Thus the true signal values corresponding to the incoming flux are not obtained immediately, rather they are approached asymptotically after some time. Fortunately, in many cases this behaviour is a monotonic rise; however, a considerable number of pathological cases show an overshoot followed by a slow decay. PIA provides different ways of handling the detector drift problem.

5. Determine signal per chopper plateau.

   For every chopper plateau in a measurement averages and medians of the corresponding signals are calculated (SCP).

6. Correct for reset interval effect.

   The signals obtained from the CRE output are partly dependent on the used reset interval (ramp integration time) for sampling.

7. Perform dark current subtraction.

   The signal per ramp contains a more or less constant component coming from the dark current in the detectors.

8. Calculate actual response (for FCS measurements).

   The response of the detector(s) is derived from the FCS calibration measurement. For the response computation, the mean signals of the FCS measurements are compared to

the known optical power on the detector corresponding to the electrical power applied to the FCS.

9. Perform vignetting correction.

   When the chopper throw is large, all PHT detectors can be telescope vignetted.

10. Subtract background within a measurement (for chopped measurements).

    "Internal" background subtraction refers to the calculation of the source signal from an on-source/off-source chopped measurement.

11. Correct for signal losses caused by chopping between different fluxes (chopper frequency dependence) (for chopped measurements).

    The subtracted value from an on-source/off-source chopped measurement depends in the first approximation on the chopping frequency used (and in a second order on the signal difference between both levels).

12. Convert signal (V/s) into in-band power (W).

    To convert signal per chopper plateau in V/s to in-band power in W it is necessary to know the response of the detector, which varies during a revolution. The actual responses, as calculated from the associated FCS measurement are used.

13. Subtract a measurement containing the background (externally) (for raster measurements).

In Figure 3.5 an example of data taken in chopper mode at different level of the reduction are shown: the edited raw data (ERD), the signal per ramp data (SRD), the signal per chopper plateau data (SCP), and the Astrophysical Application Data (AAP). Steps 1, 2, and 3 are applied on ERD; 4, and 5 on SRD; 6, 7, 9, and 10 on SCP; and 12 on AAP. In the Figure, the background subtraction (step 10) was not performed.

3.3 Infrared background radiation

The infrared sky has a complex structure due to the numerous emission sources in the interstellar gas (Herbstmeier et al. 1998). **Stray radiation** and **background radiation** from sources other than the target increase the noise and thus affect the detectability of a source.

Stray radiation comes into the focal plane in the form of thermal self-emission of the optical subsystem or as spurious light from bright infrared emitters (Sun, Earth, Moon, Jupiter).

The two components which contribute most to the celestial **background** in the infrared are the **zodiacal light** and the **diffuse galactic** emission (galactic cirrus clouds, dust in the smoothly distributed intercloud medium). Zodiacal light dominates at the shorter ISO wavelengths (λ <50 μm). The diffuse galactic emission is more important at the longer wavelengths (λ <100 μm). The amount of zodiacal emission depends on wavelength, the ecliptic coordinates of the object, and the satellite orientation. The diffuse galactic emission has a dependence on galactic coordinates. While the galactic emission has a significant

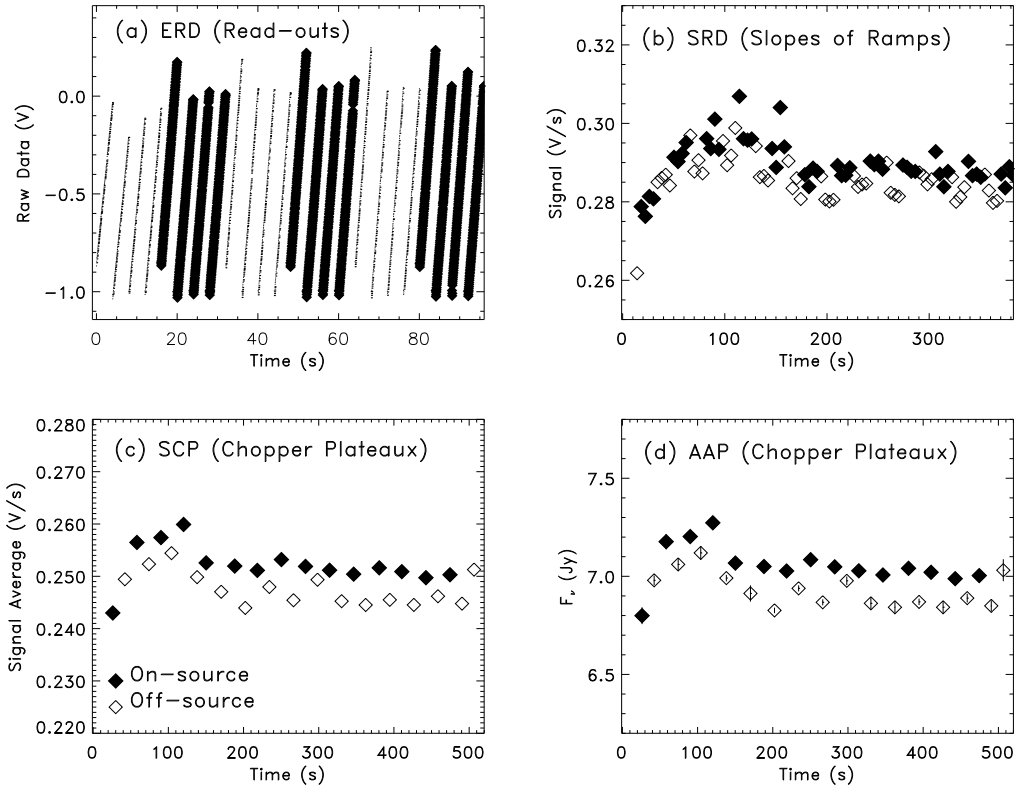

Figure 3.5: (a) First 100 seconds of integration time. Dots represent read-outs measured off-source; full diamonds represent read-outs measured on-source. (b) First 400 seconds of integration time. Empty diamonds represent slope values of ramps measured off-source; full diamonds represent slope values of ramps measured on-source. (c) Complete observation: 512 seconds of integration time. Empty diamonds represent averages per chopper plateau of the slopes measured off-source; full diamonds represent averages per chopper plateau of the slopes measured on-source. (d) Same as in panel (c), but after calibration. Uncertainties are reported only in panel (d). The data correspond to the P2 observation at 25 μm of the quasar PG 1543+489.

fraction of intensity in lines and broad spectral features, the zodiacal light is expected to be dominantly continuum radiation.

A third type of background emission can occur in the vicinity of strong infrared objects. If the target object is close to, but not confused with a stronger infrared source, then the background radiation may be dominated by emission in the tail of the point spread function of the stronger object.

The infrared detectors of the ISO instruments are very sensitive to impacts by high energy particles and gamma rays. Each impact produces a spike in the pixel or detector output, which can severely degrade the quality of a photometric measurement or – in the worst case – ruin parts of a source spectrum.

These effects are minimized prior the observation through a specific observing plan depending on the characteristics of the pointed source and the surrounding background, and afterwards during the reduction procedure.

3.4 ISO's predecessors and successors.

After Sir F. William Herschel's discovery of infrared (1800), which showed that the Sun emits infrared radiation, astronomers tried to see if other objects in the universe gave out infrared waves. In 1856, astronomers used thermocouples to detect infrared radiation from the Moon. In the early 1900's, infrared radiation was successfully detected from the planets Jupiter and Saturn and from some bright stars such as Vega and Arcturus. However, the insensitivity of the early infrared instruments prevented the detection of other near-infrared sources. Works in infrared astronomy remained at a low level until breakthroughs in the development of new, sensitive infrared detectors were achieved in the 1960's.

During the past few decades, infrared astronomy has become a major field of science due to the rapid advances in infrared detector technology.

In addition to absorbing most of the infrared radiation from cosmic sources, the Earth's atmosphere itself radiates in the infrared which interferes with infrared observations. This is why it is best to get above as much of the atmosphere as possible to observe in the infrared. To do this, infrared detectors have been placed on balloons, rockets and airplanes, allowing astronomers to study longer infrared wavelengths.

In the 1970s, astronomers around the world began to consider the possibility of placing an infrared telescope on a satellite in orbit around the Earth. This telescope would be above the Earth's atmosphere and could view the sky at the far-infrared wavelengths which were difficult to detect on Earth. It could view a large area of the sky and observe regions for a longer period of time.

By 1977, an international collaboration was formed by the Netherlands, United States and Great Britain to develop IRAS - the Infrared Astronomical Satellite. After many years of hard work and after overcoming several complications, IRAS was successfully launched on January 25, 1983. The entire telescope was cooled to a temperature of just a few degrees above absolute zero because otherwise the telescope itself would emit infrared radiation (heat) which would interfere with the observations.

The IRAS mission would last as long as the liquid helium did. For the next ten months, IRAS scanned more than 96 percent of the sky four times, providing the first high sensitivity all sky map at wavelengths of 12, 25, 60 and 100 μm. IRAS increased the number of cataloged astronomical sources by about 70%, mapping about 250 000 cosmic infrared sources and large areas of extended emission. IRAS discoveries included very strong infrared emission from interacting galaxies as well as wisps of warm dust called infrared cirrus which could be found in almost every direction of space. IRAS also revealed for the first time the core of our galaxy, the Milky Way. In the study of AGNs, IRAS carried out several results: the infrared continuum of AGN is independent of its type or radio-loudness (Sanders et al. 1989; Elvis et al. 1994) and is dominated by thermal emission from cool and warm dust (Chini et al. 1989; Barvainis 1990; Hughes et al. 1993; Antonucci et al. 1990) at least some of which is heated by the central AGN. Sources which are beamed towards us are thought to have an additional, non-thermal component in the infrared linked to the radio emission (Hoekstra, Barthel and Hes 1997).

In November 1989, the COBE satellite was launched to study both infrared and microwave characteristics of the cosmic background radiation (the remains of the extreme heat that was created by the Big Bang). Over a ten month period, COBE mapped the brightness of the entire sky at several infrared wavelengths and discovered that the cosmic background radiation is not entirely smooth, showing extremely small variations in temperature. These variations

may have led to the formation of galaxies.

The Infrared Telescope in Space (IRTS), launched in March 1995, was Japan's first infrared satellite mission. During its 28 day mission, IRTS surveyed about 7% of the sky with four instruments: A Near and Mid Infrared Spectrometer which covered wavelengths of 1.4 to 4 μm and 4.5 to 11 μm respectively, a Far Infrared Line Mapper which studied Oxygen and Carbon spectral lines at 63 and 158 μm, and a Far infrared Photometer which studied the sky at four bands centred at 150, 250, 400, and 700 μm. This data should add to our knowledge of cosmology, interstellar matter, late type stars and interplanetary dust.

The European Space Agency launched the Infrared Space Observatory (ISO) in November 1995. ISO, which observed at wavelengths between 2.5 and 240 μm, not only covered a much wider wavelength range than IRAS but was also more sensitive than IRAS and viewed infrared sources with much better resolution (100 better in angular resolution at 12μm). ISO was operating for about 2.5 years (3 times times longer than IRAS). While IRAS was an infrared survey mission, ISO was created to study specific astronomical objects in detail. ISO results have confirmed and extended the picture provided by IRAS of AGN. A decrease in strength of the non-thermal component and resulting increased dominance of the warm dust emission is observed as the AGN decreases in radio-loudness (Haas et al. 1998; 2000; Polletta et al. 2000). Decomposition of the FIR SEDs in Seyfert galaxies and quasars has demonstrated the presence of the cool and warm dust components and quantified their absolute and relative strengths (Wilkes et al. 2000, Pérez García et al. 1998; Polletta et al. 2000).

In the last 18 years), only four (IRAS, COBE, IRTS and ISO) infrared satellites were launched. At present, the interest of the astronomical community in infrared astronomy has largely increased. In the next eight years four infrared satellites will be operating (SIRTF, Astro-F, Herschel and NGST).

NASA's infrared space telescope called Space Infrared Telescope Facility (SIRTF) is already scheduled for launch in July 2002 and it should be operational for 2.5-5 years. SIRTF will consist of a 0.85 meter telescope, a camera, a spectrograph, and a photometer. SIRTF will be much more sensitive than prior infrared missions and will study the universe at a wide range of infrared wavelengths (3.5-180 μm).

The Japanese space agency ISAS has planned the infrared space mission IRIS (Infrared Imaging Surveyor) that will be launched in 2003 and should last for 1.5 years. It will have a near and mid infrared camera and a far infrared scanner (2-25 μm and 50-200 μm).

Further ahead in time ESA is preparing a space telescope (Herschel) for far infrared and submillimetre astronomy due to be launched in 2005, and should be operational for 3 years. Herschel will perform spectroscopy and photometry over a wide range of infrared wavelengths (80-670 μm).

A mission that is still in a definition phase is NGST (The Next Generation Space Telescope). NGST is a NASA's infrared space mission planned for 2008 that will have extremely good sensitivity and resolution in the near-mid infrared (0.5-20 μm).

These missions will be used to study the formation and evolution of galaxies, star formation, interstellar matter, ultra luminous infrared galaxies, active galactic nuclei and the early universe.

Bibliography

Alexander T., Lutz D., Sturm E., Genzel R. et al. 2000, ApJ, 536, 710

Antonucci R., Barvainis R., Alloin D. 1990, ApJ, 353, 416
Barvainis R. 1990, ApJ, 353, 419
Carilli C.L., Barthel P.D. 1996, A&ARv, 7, 1
Chini R., Biermann P.L., Kreysa E., Gemünd H.-P. 1989, A&A, 221, L3
Clavel J., Schulz B., Altieri B., Barr P. et al. 2000, A&A, 357, 839
Clements D.L. 1999, Ap&SS, 266, 233
Elvis M., Wilkes B.J., McDowell et al. 1994, ApJS, 95, 1
Fischer J., Luhman M.L., Satyapal S., Greenhouse M.A. et al. 1999, Ap&SS, 266, 91
Genzel R., Cesarsky C.J. 2000, ARA&A, 38, 761
Haas M., Chini R., Meisenheimer K. et al., 1998, ApJ, 503, L109
Haas M., Klaas U., Coulson I., Thommes E., Xu C. 2000, A&A, 356, L83
Herbstmeier U., Abraham P., Lemke D., Laureijs R.J. et al. 1998, A&A, 332, 739
Hoekstra H., Barthel P.D., Hes R. 1997, A&A, 319, 757
Hughes D.H., Robson E.I., Dunlop J.S., Gear, W.K. 1993, MNRAS, 263, 607
Kessler M.F., Steinz J.A., Anderegg M.E., Clavel J. et al. 1996, A&A, 315, L27
Lutz D., Feuchtgruber H., Genzel R., Kunze D. et al. 1996, A&A, 315, L269
Lutz D., Veilleux S., Genzel R. 1999, ApJ, 517, L13
Pérez García A.M., Rodríguez Espinosa J.M., Santolaya Rey A.E. 1998, ApJ, 500, 685
Pérez García A.M., Rodríguez Espinosa J.M., Fuensalida J.J. 2000, ApJ, 529, 875
Polletta M., Courvoisier T.J.-L. 1999, A&A, 350, 765
Polletta M., Courvoisier T.J.-L., Hooper E.J., Wilkes B.J. 2000, A&A, 362, 75
Rigopoulou D., Spoon H.W.W., Genzel R., Lutz D. et al. 1999, AJ, 118, 2625
Sanders D.B., Phinney E.S., Neugebauer G., Soifer B.T., Matthews K. 1989, ApJ, 347, 29
Stickel M., Lemke D., Mattila K., Haikala L.,K., Haas M. 1998, A&A, 329, 55
Tansley D., Birkinshaw, M., Hardcastle M.J., Worrall D.M. 2000, MNRAS, 317, 623
Wilkes B. J., Hooper E. J., McLeod K. K., Elvis M. S. et al. 2000, Lecture Notes in Physics, vol. 548, p. 177, eds. D. Lemke, M. Stickel, K. Wilke (Berlin: Springer-Verlag)

Chapter 4

The ISOPHOT project

The standard model for AGN includes a super-massive black hole (SMBH) surrounded by an accretion disk in the center of a galaxy. The central regions of the AGN produce strong high energy emission (i.e., ultraviolet and X-ray). Much of this radiation is re-processed by dust and gas within the nuclear region and the host galaxy, resulting in a modification of the spectral energy distribution (SED). Since the optical, ultraviolet and soft X-ray radiations are absorbed and re-emitted in the infrared, the observed SED will depend upon factors such as the amount, distribution and nature of obscuring material.

In order to understand the AGN energetics and physics, it is necessary to know the amount of energy emitted at each frequency and separate the direct (ultraviolet and X) and reprocessed (infrared) emission.

Infrared (IR) radiation contains a large and unique amount of information, regarding both the missing high energy radiation and the reprocessing material. Infrared radiation is as much rich of information as it is hard to decrypt. IR photons can be produced through several processes, thermal and non-thermal, by components in the nuclear region, as well as in the host galaxy. The dusty torus dictated by AGN unification schemes can be an important source of IR radiation, since it is exposed to the high energy radiation field emitted by the nucleus. Starforming regions in the galaxy can also contribute to the IR emission, since they emit ultraviolet radiation and are usually embedded in dusty regions. A relativistic jet can also produce large, sometimes even dominating, amounts of IR photons through synchrotron process.

The investigating power of IR astronomy, the large amount of unsolved questions in this spectral domain and the progresses made in IR instrumentation led us to the development of an observational project with ISOPHOT on board ISO.

4.1 Scientific objectives

The main questions that we intended to address with our project were:

- Which radiation mechanism produces the observed far-IR emission in AGN (non-thermal or thermal radiation)?
- Where is the dust located and how is it distributed (in starforming regions, in a circumnuclear starburst, in the molecular torus)?
- What produces the radiation that heats the dust (forming stars, an accretion disk)?

- What are the properties (temperature, opacity) of the dust?
- Is there a link between the IR and the radio emission source?
- Are the properties of the IR SED and of the dust in AGN compatible with the predictions of the unified model ?

These questions can be investigated by analyzing the spectral energy distribution (SED) from radio to IR energies of a complete sample of AGN, by comparing multi epoch observations and by measuring the degree of polarization of the IR radiation.

The spectral decomposition is necessary to distinguish the emission mechanisms producing the observed SED, to constrain the properties of the emitting components and to understand their interplay.

Multi epoch observations provide flux variability measurements. The degree of variability can state the non-thermal nature of the emission. Relative short-time variations can indeed be explained only if the origin of the emission is non-thermal, whereas thermal emission is not expected to vary on time-scales of a year.

Since relatively high levels of polarization (>10%) are expected only in case of non-thermal emission, polarization measurements can probe the non-thermal origin of the emitted radiation.

4.2 The ISOPHOT project

ISOPHOT had provided for the first time an opportunity to gather essential information about the IR SED of AGNs, using a large set of filters (25) on a broad spectral domain (2.5–240 μm) for spectrophotometry, and giving the possibility to measure variability and polarization.

The ISOPHOT project was sub-dived into three sub-programs: 1. definition of the IR SED of some AGNs (quasars and narrow line Seyfert 1 galaxies); 2. study of IR variability and 3. polarization in quasars. A description of the three programs is reported in Table 4.1. Our project was, at the same time, part of a larger project involving two Guarantee Time (GT) programs: the European Core Program focused on low-redshift quasars (Haas et al. 2000), and the US Key Project on quasars spanning a wide range of redshifts and SEDs (Hooper et al. 1999, 2000; Wilkes et al. 2000). The objective of these projects was to define the IR SED of a complete sample of quasars with ISOPHOT. Our program was complementary to these large-scale efforts in selecting those objects, missing in the target list of the GT programs, that completed the quasar sample. In our project we also included some narrow line Seyfert 1 galaxies (NLSy1) because of their peculiar properties.

The third project was never performed, even if scheduled. The ISOPHOT Team postponed polarization observations towards the end of the mission. Unfortunately, when the observation had to be performed (May 2, 1998) the temperature of the helium cryostat increased making the observation unfeasible.

The ISOPHOT dataset was complemented with a set of submillimetre and near-IR observations in order to better cover the wavelength range where thermal emission is expected to contribute. Four sub-programs were performed using different ground-based facilities. The list of the programs, instruments, number of sources and wavelengths of the performed observations are listed in Table 4.2.

Table 4.1: ISOPHOT programs

Program	Prop. obj.	Obs. obj.	Detectors	AOT[a]	Observing Mode
1. ISO spectra of a sample of AGN.	37	11	P1, P2 C100, C200	PHT03 PHT22	chopper
2. Far-infrared variability of a large sample of quasars.	30	9	P1, P2 C100, C200	PHT03 PHT22	raster
3. Polarimetry of 2 radio loud quasars.	2	0	P2 C100, C200	PHT50 PHT51	chopper

[a] AOT: Astronomical Observation Template.

Table 4.2: Millimeter and near-IR programs

Program	Instr.	N. obj.
a) Near Infrared photometry of a quasar sample.	SEST	12
Testing dust emission models.	IRAC1	12
b) Millimetre continuum of quasars with far-infrared excess.	IRAM	4
c) Sub-Millimetre continuum of radio-loud and radio-quiet quasars.	SCUBA	4

4.3 ISOPHOT Data Statistics

In Figure 4.1 a summary of the obtained results (number of detections and upper limits per observation mode) is presented. An upper limit is given if the ratio between signal and noise is less than 3. In total, we performed 157 chopper observations of which 53% were detections, and 37 raster observations of which only 38% were detections.

The relatively large amount of non-detections is due to the loss of sensitivity of ISOPHOT after the launch. The observing times, being defined on the basis of the on-ground calibrations, were, once the instrument was in flight too short to obtain a good signal to noise. The in flight detector sensitivities were roughly a factor of two less than the predicted preflight values. After the launch, serious problems due to the ionising radiation effects and flux memory effects in the detectors, were discovered. This meant that chopped observing modes were less stable than staring or raster modes. For this reason we preferred the raster observing mode for our second sub-program (defined after ISO launch).

The effects on the data due to the unexpected in flight problems required some changes to the data reduction, as first envisioned. A standard reduction procedure is still under development and the calibration under study to minimize these effects. Up to now, only specific methods have been applied to the data reduction, based, partially, on the standard procedure (PIA), provided by the ISOPHOT Team, and, partially, on techniques developed by the data owners. These methods are quite successful, but the systematic uncertainties on the

data are still too large ($\sim$ 30 %) to make a detailed spectral analysis and constrain physical parameters. We first developed a reduction method to apply to the set of chopped data obtained for the sample of Seyfert galaxies (see chapter 5), then this method was improved to be applied to fainter objects as quasars (see chapter 6). An original reduction procedure for raster data was also developed for the analysis of quasars data (see chapter 6).

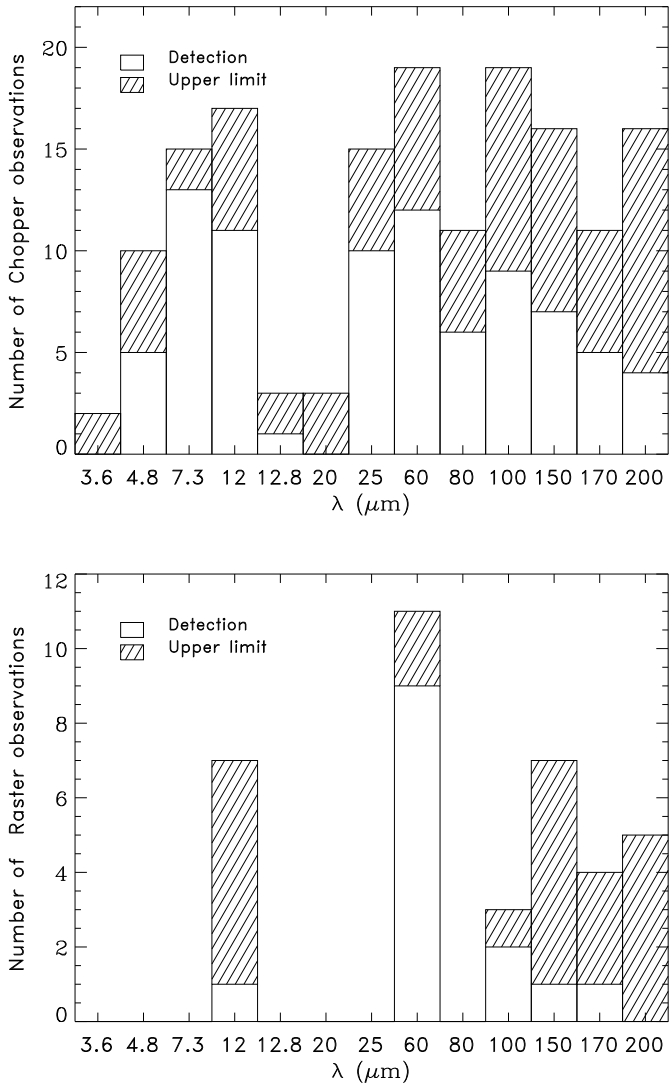

Figure 4.1: Statistical results of our ISOPHOT projects for chopper (top) and raster (bottom) observations. Each box corresponds to the number of observations performed with a filter. The central wavelength of each filter is reported on the x axis.

4.4 Results

The results obtained from our ISOPHOT project are reported in chapters 5 and 6 as published:

ISOPHOT observations of narrow line Seyfert 1 galaxies.
M. Polletta, T.J.-L. Courvoisier, published in A&A 350, 765-776 (1999).

The Far-Infrared emission of Radio Loud and Radio Quiet Quasars.
M. Polletta, T.J.-L. Courvoisier, E.J. Hooper, B.J. Wilkes, published in A&A 362, 75-96 (2000).

Bibliography

Haas M., Klaas U., Coulson I., Thommes E., Xu C. 2000, A&A, 356, L83
Hooper E.J., Wilkes B.J., McLeod K.K., Elvis M.S. et al. 1999, Bull. A.A.S. 195, 9803
Hooper E.J., Wilkes B.J., McLeod K.K., Elvis M.S. et al. 2000, Bull. A.A.S. 197, 2007
Wilkes B.J., Hooper E.J., McLeod K.K., Elvis M.S. et al. 2000, Lecture Notes in Physics, vol. 548, p. 177, eds. D. Lemke, M. Stickel, K. Wilke (Heidelberg: Springer-Verlag)

Chapter 5

ISOPHOT observations of narrow line Seyfert 1 galaxies

Astron. Astrophys. 350, 765-776 (1999)

ASTRONOMY
AND
ASTROPHYSICS

ISOPHOT Observations of Narrow Line Seyfert 1 Galaxies

M. Polletta[1,2] **and T.J.-L. Courvoisier**[1,2]

[1] Geneva Observatory, Ch. des Maillettes 11, CH-1290 Sauverny, Switzerland
[2] Integral Science Data Centre, Ch. d'Ecogia 16, CH-1290 Versoix, Switzerland

Received 31 March 1999 / Accepted 6 September 1999

Abstract. Broad infrared spectra (7-200 μm) of four NLSy1 galaxies, obtained with the imaging photopolarimeter (ISOPHOT) on-board ISO, are presented. ISOPHOT data have been analyzed applying a (non standard) method that is described in details.

The infrared spectra of the four selected NLSy1 galaxies have been analyzed in order to derive the distribution of luminosities, temperatures, opacities and sizes of the emitting dust. A comparison between infrared ($\alpha_{3,60}$) and optical emission line (H_α/H_β and [OIII]/H_β) properties suggests that NLSy1 galaxies suffer different degrees of dust absorption according to the inclination of the line of sight.

Key words: Galaxies: individual: (TONS180, RXJ0323-49, IRAS13224-3809, PG1404+226) – Galaxies: photometry – Galaxies: Seyfert – Infrared: galaxies.

1. Introduction

Narrow-line Seyfert 1 galaxies (NLSy1) are defined by their optical emission line properties : permitted lines are only slightly broader than the forbidden lines, and narrower than in typical Seyfert 1 galaxies (FWHM (H_β) $\simeq$ 500 - 2000 km s^{-1}); strong emission features from FeII (optical multiplets centered at 4750, 5190 and 5300 Å), and high-ionization optical lines are often present (Osterbrock and Pogge 1985; Goodrich 1989), and forbidden lines emission is relatively weak ([OIII]/$H_\beta < 3$). Although the emission lines widths and ratios have given a designation to this class long ago, it is only recently that the singular nature of these objects has been discovered thanks to X-ray observations. Indeed, many NLSy1 have soft X-ray spectra much steeper than in normal broad emission lines Seyfert 1 galaxies (photon index $\Gamma \simeq$ 3-5), and the soft X-ray emission shows rapid and/or large amplitude variations (Boller, Brandt and Fink 1996). In spite of the different spectral shape, the soft X-ray luminosities are similar to those observed in Seyfert 1 galaxies. At higher energies (> 2 keV) the NLSy1 galaxies show a relatively weak hard power law, slightly steeper than observed in Seyfert 1 galaxies (Brandt, Mathur and Elvis 1997; Otani, Kii and Miya 1996; Comastri et al. 1998; Pounds, Done and Osborne 1995). Several NLSy1s have exceptionally strong EUV/soft X-ray excesses, when normalized by the optical/UV continuum (Rodríguez-Pascual, Mas-Hesse, and Santos-Lleó 1997). A red optical continuum spectrum and relatively strong infrared (IR) emission are observed in several NLSy1s (Halpern and Oke 1987). In the far-IR (FIR) and radio domains the NLSy1s show a high degree of similarity with normal Seyfert 1 galaxies (Rodríguez-Pascual, Mas-Hesse, and Santos-Lleó 1997; Ulvestad, Antonucci and Goodrich 1995).

The relative weakness of low density forbidden line emission and the absence of broad hydrogen wings in NLSy1 galaxies may be understood if most of the ionizing flux is absorbed in the inner forbidden line region, thus reducing the amount of ionizing radiation reaching the low density clouds, and absorbing the internal broad-line region. Absorbing dust in the circumnuclear environment is then a likely cause for the peculiar emission line properties in NLSy1 galaxies. This hypothesis has also been suggested by spectropolarimetry and soft X-ray observations. Spectropolarimetry observations indicate that dust scatters the optical photons in several NLSy1 galaxies (Goodrich 1989), and soft X-ray observations indicate the presence of a dusty warm absorber along the line of sight of some NLSy1 galaxies (Komossa and Greiner 1998).

Our purpose is to investigate the role of the dust in NLSy1 galaxies through the analysis of their infrared (IR) emission. The IR radiation in Seyfert galaxies can be considered as the direct tracer of dust (Barvainis 1990; Clavel, Wamsteker and Glass 1989). The infrared emission carries information on dust at different scales, and temperatures: on cool dust (T = 15-35 K) in the interstellar medium heated by the stellar radiation field of the host galaxy at 1.5 kpc, on warm starburst-related dust (T = 20-50 K) at few hundred, and/or kiloparsec scales, and on AGN-related dust extending from 1 pc to 1 kpc (T = 35-2000 K). A well sampled infrared spectral energy distribution is necessary to trace the dust distribution from the circumnuclear region to the kiloparsec scales of the host galaxy.

Send offprint requests to: Maria.Polletta@obs.unige.ch

The Infrared Space Observatory (ISO; Kessler et al. 1996) has devoted several programs to study NLSy1 galaxies observing in total 16 NLSy1s at several wavelengths between 7 and 200 μm. Results obtained with the Imaging Photo-Polarimeter (ISOPHOT; Lemke et al. 1996) on board ISO for four NLSy1 galaxies (TONS180, RXJ0323-49, IRAS13224-3809, and PG1404+226) are presented here. We also present observations at millimeter and near-infrared wavelengths of the selected NLSy1 galaxies that have been performed to complete, and better sample their infrared spectral energy distribution (SED).

2. Observational dataset

We selected four NLSy1 galaxies on the basis of their singular behaviour in the ultraviolet and/or soft X-ray energy bands (see classification and optical spectra in Grupe 1996, Boller, Brandt and Fink 1993, Véron-Cetty and Véron 1998). Source names, coordinates and redshifts, taken from the Nasa Extragalactic Database (NED)[1], are listed in table 1. In order to study their infrared emission we performed a program of observations that has involved several observatories : the Infrared Space Observatory, the IRAM interferometer on Plateau de Bure in France (Guilloteau et al. 1992), the IRAC1 and the Swedish ESO Submm Telescope (SEST) telescopes of the European Southern Observatory (ESO) at La Silla.

ISOPHOT observations have been performed for all the selected sources, while just few objects have been observed with the other observatories listed above. ISOPHOT observations and data reduction are described in the next section.

TON S180, and IRAS 13224-3809 have been observed in the near-IR with the IRAC1 telescope on June 21^{st}, 1996. We measured a flux density of 23±2 mJy in the L(3.7 μm) photometric band, and of 29±9 mJy in the M(4.7 μm) photometric band from TON S180, and of 11±1 mJy in the L photometric band from IRAS 13224-3809. IRAS 13224-3809 has also been observed at millimeter wavelengths with the SEST telescope on November 3^{th}, 1995. The measured flux density is 21±10 mJy at 1.3 mm after reduction to outside the atmosphere, correction for the gain elevation characteristic of the telescope, and calibration with Uranus. The NLSy1 PG 1404+226 has also been observed at millimeter wavelengths, using the IRAM interferometer on Plateau de Bure on May 19^{th}, 1998. Three of the five antennas in compact configuration have been used, and 3C 273 was the calibrator. PG1404+226 was observed during 2.6 hours. We measured a flux density of 1.97±1.55 mJy at 112.0 GHz, and 10.03±7.2 mJy at 230.5 GHz. All the millimeter data show a very low signal to noise ratio, therefore we allot 3σ upper limits to the fluxes.

[1] The NASA/IPAC Extragalactic Database (NED) is operated by the Jet Propulsion Laboratory, California Institute of Technology, under contract with the National Aeronautics and Space Administration.

Table 1. Basic properties

Source Name	RA (2000) (h m s)	Dec (2000) ($^\circ$ $'$ $''$)	z
TON S180	00 57 19.9	−22 22 59	0.062
RX J0323.2-4931	03 23 17.2	−49 30 50	0.071
IRAS13224-3809	13 25 19.6	−38 24 55	0.067
PG 1404+226	14 06 21.9	+22 23 47	0.098

3. ISOPHOT observations and data reduction

Photometric data at 9 wavelengths between 7.3 and 200 μm have been obtained for each object using the P1, P2, C100, and C200 detectors. The P1, and P2 detectors have been used for the short wavelength observations. They are single detectors collecting a fraction of the source signal depending on the chosen aperture. The observations have been performed through a circular aperture of 13.8″ in diameter at 7.3 μm, of 23″ at 12 μm, and of 52″ at 25 μm in order to have the same intensity fraction (90%) of the source flux at each wavelength. For long wavelength observations the C100 and C200 array cameras have been used. They have respectively nine, and four detector pixels each covering respectively an area of 43.5″ × 43.5″, and 89.4″ × 89.4″ on the sky. All the observations have been performed deflecting the radiation beam from the source (on-source position) to adjacent fields on the sky (off-source position) several times in order to measure the background emission (chopper observing mode). Triangular and rectangular chopping modes have been used. In the triangular chopper mode the background emission is measured in two different regions, while in the rectangular chopper mode it is measured in only one position. Observing dates, filters, exposure times, chopping mode, and measured fluxes are reported in table 2.

3.1. First steps of the data reduction : from ERD to AAP level

The first part of the data reduction has been performed using version 7.3 of the ISOPHOT Interactive Analysis (PIA) tool (Gabriel et al. 1997). We used the raw data that have been processed with version 7.0 of the Off-Line Processing (Laureijs et al. 1998). The raw data form a sequence of detector read-outs distributed in 2^n (n is an integer between 2 and 6) sets of four response curves or ramps, according to the integration time (Edited Raw Data: ERD in Volts). Each set of four ramps represents a chopper position (on- and off-source). Each ramp is corrected for the non-linearity of the detector response, and for contamination of cosmic particle events (glitches). Two criteria are applied to recognize and remove read-outs affected

by glitches. Those read-outs at more than 4.5σ from the average are removed. Among the remaining values, the read-outs at more than 3.0σ from the new average and the subsequent data points are removed until the value has decreased to 1σ from the average (see the PIA User manual for more details; Gabriel et al. 1998). After applying the non-linearity correction, and the deglitching to the ERD, a straight line is fitted to each ramp, in order to determine its slope or Signal per Ramp Data (SRD in Volt/s).

The SRD are corrected for highly discrepant points (value at more than 3σ from the average signal) still contaminated by glitches, for the orbital dependent dark current, and for the signal dependence on the ramp integration time (reset time interval) to obtain an average Signal per Chopper Plateau (SCP in Volt/s).

After applying flat-fielding correction, the SCP data are calibrated to obtain the Standard Processed Data (SPD in unit of Watts). Since the detector response varies with time, it is determined at the time of the observation by measuring the flux emitted by two thermal Fine Calibration Sources (FCS1 and FCS2) on board. Data from FCS1 are used because they are the best calibrated. The FCS1 signal is checked in order to remove data with large uncertainties. The removal of data with large uncertainties is equivalent to using the weighted mean of all FCS1 data. After the flux calibration the AAP (Auto Analysis Product) data are obtained. They are a sequence of 2^n off- and on-source flux measurements (in Jansky) each corresponding to a chopper position. The reduction from the AAP level to the final results is performed using our own IDL routines, and not following the standard pipeline.

3.2. From the AAP level to final results

The last steps of the data reduction before determining the source flux, are the background subtraction, the deletion of remaining highly discrepant points, and the correction for transient effects, vignetting and point spread function.

In the case of the C100 detector only the central pixel pointed on the source is considered to derive the flux density since the eight border pixels contain only a small fraction of the central point source and summing these values would therefore only increase the noise (but see section 4). In the case of the C200 detector the source signal is equally distributed on the four pixels of the array, therefore the final source flux is computed by adding the values measured by each pixel.

3.2.1. Background subtraction

The background is measured at each off-source position. Since in some cases the instruments show long term drift effects (the measured signal varies with observation time), the background signal is re-estimated in order to remove this effect. New background estimations are obtained by computing the weighted mean of each couple of consecutive off-source measurements. These computed background fluxes are then subtracted from the on-source values measured in between each couple of off-source measurements. In fig. 1 the data obtained from RXJ0323-49 with the central pixel of the C100 detector at 80 μm are reported to illustrate the method. In this example the data are two series of eight on-source ($\diamond$), and eight off-source ($\times$) measurements. The computed background values (B) are represented by squares ($\Box$) (the meaning of empty and filled symbols is described in the following section). Since the sequence of chopper plateau ends with an on-source position, we used the weighted mean of the two last on-source measurements, and the flux observed in the last off-source position to have the last couple of on- and off-source values. After subtraction of the background estimates (B) from the associated on-source measurements (S), 2^{n-1} source flux measurements are obtained. These values are further checked before computing the final source flux.

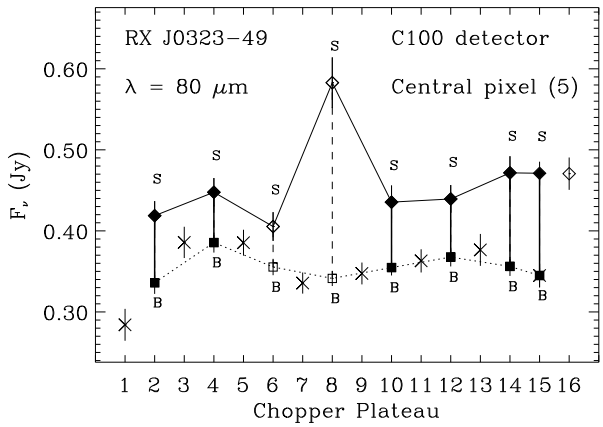

Fig. 1. AAP data of the central pixel (5) of the C100 detector obtained for the observation of RXJ0323-49 at 80 μm. $\diamond$ represent on-source measurements, $\times$ off-source measurements, $\Box$ interpolated off-source measurements. The last on-source value is obtained by interpolating two on-source measurements. Selected couples of off- and on-source measurements after deletion of discrepant points are indicated by filled symbols (see section 3.2.2).

3.2.2. Deletion of remaining highly discrepant points

At this reduction level a further check of the data is required, since instability effects of the detectors may still affect the data. Such effects are not yet well known, it is therefore difficult to recognize and remove them. We resort to a simple method based on statistics, and not on the *a priori* knowledge of most recurrent observed effects. With the assumption that the differences between each couple of on- (S) and off-source (B) values are nor-

mally distributed around the weighted mean value with a width given by the measured standard deviation of the distribution, all the measurements with values that are less probable than a limit defined on the basis of the number of available points can be rejected (Chauvenet's criterion in Taylor 1982). An example of the application of this criterion is shown in fig. 1. Among the eight differences obtained from all the couples of on- (S) and off- (B) values, the Chauvenet's criterion selects six couples S-B (thick solid lines) indicated by filled symbols, and rejects two couples S-B (dashed lines). The final source flux is derived from the weighted mean of all the selected differences S-B. The associated uncertainty is the standard deviation of the weighted mean σ_S. If the measured fluxes are smaller than σ_S, an upper limit to the flux is given equal to 5σ, where σ is the standard deviation of the whole distribution of differences.

In the C100 observation at 80 μm of TON S180 the Chauvenet's criterion rejects the only two flux values available because they are at more than $1.15\sigma_S$ from the weighted mean. However, since our criterion takes into account only statistical uncertainties and not systematic errors, that are of the order of 30% (see section 3.3), and since the two measurements are consistent at 2.5σ with the weighted mean, we consider the final flux value as reliable.

3.2.3. Vignetting correction

C100 and C200 data are further corrected for the signal loss outside the beam of the telescope (vignetting). The PIA default vignetting correction factors have been computed considering the dependency only on the distance of the chopper positions and on the filter, but recent investigations have shown that they depend also on the time per chopper plateau (M. Haas, private communication). The PIA vignetting correction factors may overestimate the flux value. In order to estimate the effects of this correction, we compared the results obtained without correcting for vignetting with the corrected fluxes. The median value of the computed differences expressed in percentage is 2% for the C100 data, and 67% for the C200. The vignetting correction for the C100 data is negligible, therefore we adopted the fluxes corrected for vignetting using the PIA default values. On the contrary, in the case of the C200, the vignetting correction is very large. Since the right correction factors are not yet available, new estimations for the C200 data are obtained averaging the vignetting corrected, and the not corrected values. Since the values corrected for vignetting and those not corrected have different statistical uncertainties, the uncertainty σ_{tot} we use is the quadratic sum of the uncertainties σ_i obtained in the two cases. If both the measured fluxes are smaller than their own uncertainties σ_i, an upper limit to the flux is given equal to $5\sigma_{tot}$. If at least one measurement is larger than its uncertainty σ_i, but the average flux is smaller than σ_{tot}, an upper limit to the flux is given equal to the maximum flux value (the maximum flux value is the corrected for vignetting flux) plus the correspondent σ_i.

3.2.4. Correction for transient effects and point spread function

A correction for the signal loss due to transient effects depending on the time per chopper plateau is applied to the computed fluxes. Since short integration times do not permit to the C100, and C200 detectors to reach the full signal, the observed flux can be reduced by large factors, typically up to 68 % for the C100 detector, and up to 12% for the C200 detector for the shortest observations. The correction factors we use are the PIA default values.

The computed fluxes are finally corrected for the point spread function (psf) of each detector by using the default PIA values derived empirically. In the case of the C200 detector the theoretical point spread function values are slightly different from the empirical values (Laureijs et al. 1998), and the difference becomes important ($\sim$30%) at 200μm. We used different point spread function correction factors for vignetting corrected fluxes, and not corrected ones, in order to have the largest difference between the two values. For P1, P2, and C100 data we use the PIA default psf values.

3.3. Calculation of systematic uncertainties

During the data reduction only statistical errors have been taken into account, however the accuracy of the absolute photometric calibration depends mainly on systematic errors (detector transient effects, calibration response, dark current, point spread function), and it is currently known to be better than 30 % (Klaas et al. 1998). Therefore we associate to the measured flux an uncertainty that is the quadratic sum of their σ_S and the 30% (for the C200 measurements we use 67% to take into account the uncertainty in the vignetting correction) of the measured value. The associated statistical and systematic uncertainties are reported in the last two columns of table 2. These values will be used in the following fitting procedure of the spectral energy distributions (SEDs).

4. Comparison with IRAS

All four NLSy1s have been previously observed by IRAS. The fluxes in the four IRAS bands have been taken from the NED database. All the objects have been detected previously by IRAS in at least two filters, with the exception of PG1404+226 for which IRAS has given only upper limits. ISOPHOT gives in most cases results consistent with IRAS data (within 1σ, and within 2.2σ at 25μm for RXJ0323-49), and supplies new measurements to IRAS upper limits. However, large differences are obtained for IRAS 13224-3809. At long wavelengths both

Table 2. Details of ISOPHOT Observations

Det.	λ (μm)	Exp. (s)	Chopper Mode	F_ν (mJy)	Uncertainty† Stat.	Syst.
TON S180 (Obs. date: June 06, 1997)						
P1	7.3	128	T	33.7	1.5	10.
P1	12	64	T	113.	3.	34.
P2	25	128	T	159.	30.	48.
C100	60	128	R	412.	25.	124.
C100	80	16	R	406.	54.	122.
C100	100	128	R	235.	16.	71.
C200	150	128	R	184.	22.	123.
C200	170	128	R	179.	22.	120.
C200	200	128	R	<216.		
RX J0323.2-4931 (Obs. date: June 16, 1997)						
P1	7.3	512	T	5.0	1.8	1.5
P1	12	256	T	20.9	3.2	6.3
P2	25	512	T	26.5	7.9	8.0
C100	60	128	R	243.	31.	73.
C100	80	128	R	246.	24.	74.
C100	100	128	R	270.	33.	81.
C200	150	128	R	270.	41.	181.
C200	170	128	R	187.	34.	125.
C200	200	128	R	<300.		
IRAS 13224-3809 (Obs. date: August 23, 1996)						
C100‡	60	64	R	1346.	194.	404.
C100‡	80	64	R	3208.	170.	962.
C100‡	100	64	R	2744.	171.	823.
C200	150	64	R	1357.	52.	909.
C200	170	64	R	1451.	50.	972.
C200	200	64	R	833.	150.	558.
PG 1404+226 (Obs. date: December 22, 1996)						
P1	7.3	2048	T	6.3	0.5	1.9
P1	12	1024	T	18.4	4.9	5.5
P2	25	2048	T	<91.41		
C100	60	128	R	84.	20.	25.
C100	80	128	R	144.	29.	43.
C100	100	128	R	160.	18.	48.
C200	150	128	R	389.	36.	261.
C200	170	128	R	269.	25.	180.
C200	200	128	R	175.	50.	117.

† In units of mJy. ‡ Obtained considering all the pixel of the detector array.

IRAS and ISO detected IRAS 13224-3809, but consistent values (within 1σ) are obtained only if all the pixels of the C100 detector are taken into account. The fluxes measured by the central pixel are indeed 44% and 39% of the fluxes obtained by using all pixels, respectively at 60 and 100 μm. Looking at the signal obtained by each pixel of the C100 camera an excess in between pixel 2 is observed at all three filters, as shown in fig. 2 for λ=100 μm. Moreover, an excess in pixel 3 is measured by each filter of the C200

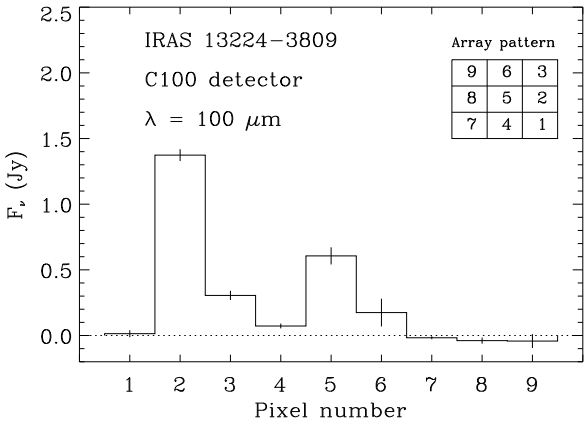

Fig. 2. Measured source flux by each pixel of the C100 detector of IRAS 13224-3809 at 100 μm. Dotted line represents the zero level flux.

detector, as shown in fig. 3, where the vignetting corrected C200 data at 150μm are shown.

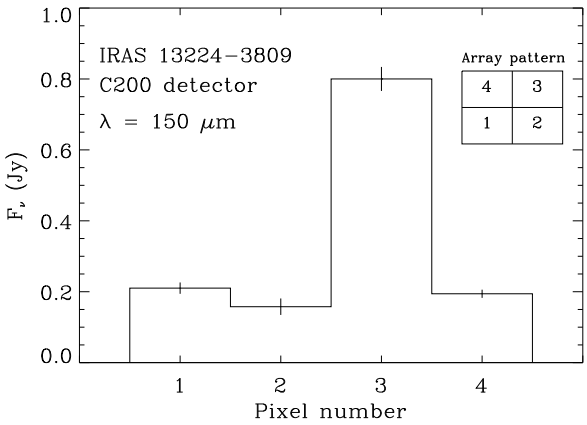

Fig. 3. Measured source flux by each pixel of the C200 detector of IRAS 13224-3809 at 150 μm.

A check of the pointing of the instruments has revealed an incorrect reference position for the source, that is located outside the beam of the P1, and P2 detectors, between pixel 2, and 5 of the C100 detector, and in pixel 3 of the C200. The position of each pixel projected on the sky, and the source position are shown in fig. 4. The cause of the bad pointing was the use of wrong source coordinates. Unfortunately we cannot use P1, and P2 data, since the source was outside the instruments beams, but the long wavelength measurements can be used provided that we take data from all the pixels. With this choice also the data of IRAS 13224-3809 are consistent with IRAS results at 60, and 100 μm.

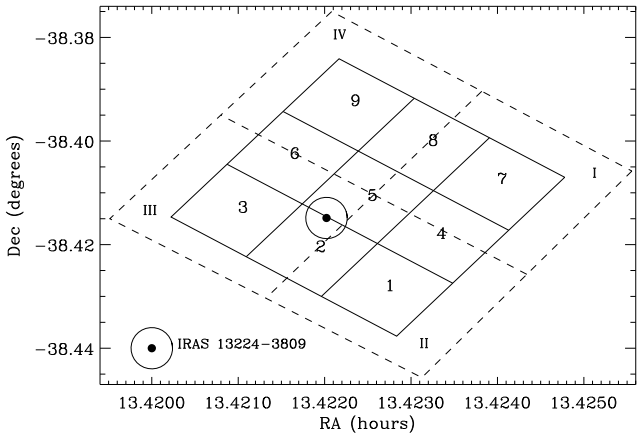

Fig. 4. Projection of the C100 (solid line), and C200 (dashed line) detectors on the sky region covered during the observation fo IRAS 13224-3809. The circle indicates the position of the source on the sky (NED). The number 1-9 indicate the pixels of the C100 detector, and I-IV the pixels of the C200. The coordinates are at epoch 2000.

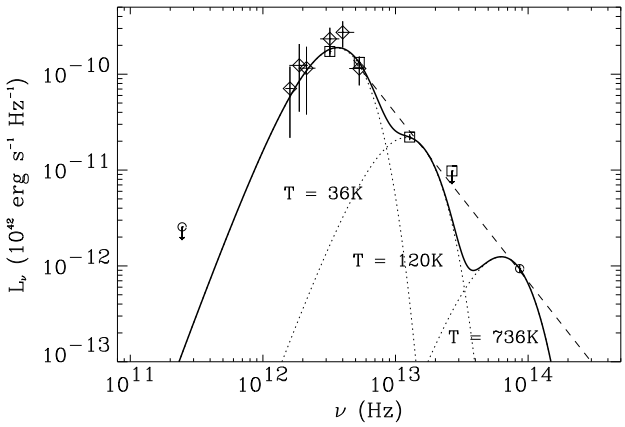

Fig. 5. Spectral energy distribution of IRAS 13224-3809 considering data from all the pixels of the C100 and of the C200 detectors. Dotted lines represent single grey body components at the indicated temperature, and the solid line the composite spectrum obtained summing each single component. The dashed line represents the power law obtained fitting data between 3 and 60 μm. Arrows indicate 5σ upper limits (3σ for millimeter data). Diamonds are ISOPHOT data, squares are IRAS data, circles are IRAC1, and SEST data.

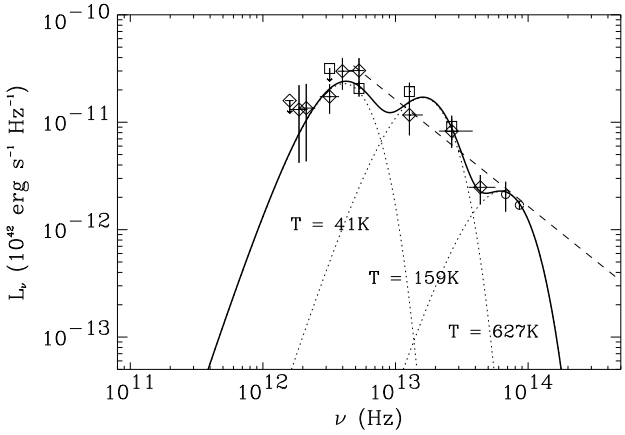

Fig. 6. Spectral energy distributions of TONS180. The symbols and the curves have the same meaning as in fig. 5.

5. Spectral fits

All the data for the four objects considered in this study have been converted to monochromatic luminosities in the rest frame of the object (H_0 = 75 km s^{-1} kpc^{-1}) using the following equation :

$$L_{\nu em} = 4\pi d_L^2 F_{\nu obs}/(1+z)\,, \qquad (1)$$

where $F_{\nu obs}$ is the monochromatic flux in the observer's frame, and d_L is the luminosity distance to the object :

$$d_L = \frac{cz(1+z/2)}{H_0(1+z)}\,, \qquad (2)$$

The SEDs of each object are shown in 5, 6, 7, and 8.

Assuming that the infrared emission in NLSy1 galaxies is thermal as observed in normal Seyfert 1 galaxies, the grey body radiation model can be used to fit the observed SEDs. An isothermal grey body at the temperature T emits at the frequency ν a flux density given by the following equation (Gear 1988):

$$F_\nu = \Omega \cdot B(\nu, T) \cdot (1 - e^{-\tau}) \qquad (3)$$

where Ω is the solid angle subtended by the source, $B(\nu, T)$ is the Planck function for a blackbody of temperature T, and τ is the optical depth of the dust. We derived the optical depth from the extinction curve computed by Draine and Lee (1984) for a mixture of graphite and silicate grains with radii varying between 0.005 and 0.25 μm (Mathis, Rumpl, and Nordsieck 1977). The derived optical depth curve is reported in fig. 9 for an hydrogen column density of 10^{24}cm^{-2}. The optical depth dependence on the frequency can be approximated by a power law of type $\tau = (\nu/\nu_0)^\beta$, where β expresses the dependence of the dust emissivity on the frequency ($\propto \nu^\beta$). The power law approximation is valid only in some wavelength ranges : 1-7 μm, and 20-500 μm, because of the silicate feature at 10 μm. A power law with β equal to 1.87 is a good fit to the optical depth curve, as shown by the dashed curve superimposed to the optical depth curve in fig. 9. The normalization of the curve is given by ν_0 that is strictly related to the hydrogen column density. We derived the following relationship between the hydrogen column density N_H and the value of ν_0 :

$$N_H = C \cdot \nu_0^{-\beta} \qquad \text{atoms cm}^{-2} \qquad (4)$$

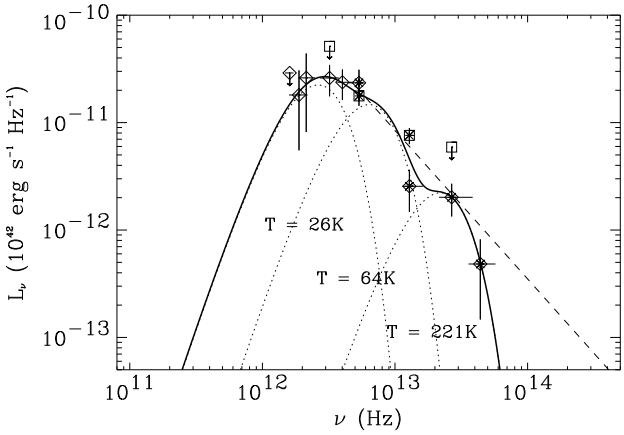

Fig. 7. Spectral energy distribution of RXJ0323-49. The symbols and the curves have the same meaning as in fig. 5.

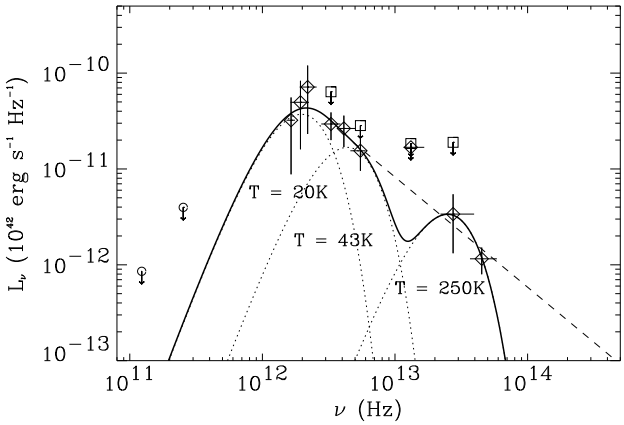

Fig. 8. Spectral energy distribution of PG 1404+226. The symbols and the curves have the same meaning as in fig. 5. IRAM data are reported with circles.

where ν_0 is expressed in Hz, and C = $3.85{\cdot}10^{47}$, in the requested unit, in the wavelength range 20-500 μm, and C = $6.33{\cdot}10^{48}$ in the wavelength range 1-7 μm. Note that this relationship gives the same extinction cross section (τ/N_H) as that measured at 250 μm by FIRAS and DIRBE for dust at high galactic latitude (Boulanger et al. 1996). The observed infrared SEDs are smooth and indicate a wide and probably continuous range of temperatures, not describable by a single grey body component, but rather by several grey body components at different temperatures. A non-linear least squares fit was used in the fitting procedure leaving free the solid angle Ω, and the temperature T, while the frequency ν_0 (hence the hydrogen column density) and the emissivity exponent β have been fixed. We assumed β equal to 1.87. The choice of the value of ν_0 is critical, because it is strictly related to the opacity of the source, and then to its size. Indeed, the value of Ω changes dramatically when ν_0 varies. The

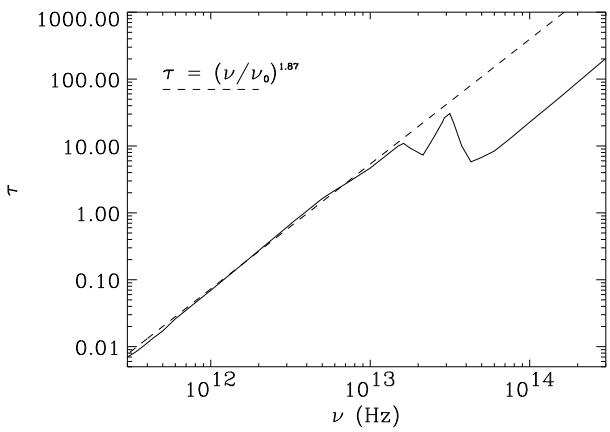

Fig. 9. Optical depth curve derived for a mixture of graphite and silicate grains (Draine and Lee 1984) scaled to a hydrogen column density of $1.{\cdot}10^{24}$ cm^{-2}. The dashed line represents the power law approximation of the optical depth in the wavelength range 20-500 μm adopted in this paper.

relationship between Ω and the size of the source (R) is $\Omega = \pi R^2/d_L^2$. In order to illustrate the effect of the choice of ν_0, we considered two extreme opacity regimes to model the observed SED of IRAS 13224-3809 from 60 to 200 μm. First, we fixed ν_0 to $3.0{\cdot}10^{12}$ Hz, corresponding to a hydrogen column density of $1.8{\cdot}10^{24}$ atoms cm^{-2}, and secondly we chose the ν_0 value corresponding to a hydrogen column density of $5.3{\cdot}10^{21}$ atoms cm^{-2}. The first value corresponds to one of the highest hydrogen column density values measured in Seyfert galaxies. The second one corresponds to the optical extinction estimated from the Balmer decrement observed in IRAS 13224-3809 (Boller et al. 1993). It has been derived using the relationship between the Balmer decrement and the optical extinction, valid for photo-ionized zones (case B) (Ward et al. 1987):

$$A_V = 6.67 \cdot log\left(\frac{H_\alpha/H_\beta}{2.85}\right) \quad (5)$$

and assuming the canonical relations : $N_H = 5.8{\cdot}10^{21}$ E(B-V) cm^{-2} mag^{-1}, and A(V)/E(B-V) = 3.1 (Whittet 1992). The temperature, and the size of the source obtained fitting the SED of IRAS13224-3809 in the two different regimes of opacity are illustrated in fig. 10 and in fig. 11, where the line contours in the size and temperature plane are shown. In the case of lower opacity (ν_0 higher, and N_H lower) the source region is more extended and the equilibrium temperature of dust grains is lower than in the case of higher opacity ($\sim$4500 pc in size and 36 K in temperature in the low opacity case as opposed to $\sim$200 pc and 45 K in the high opacity case).

We applied both models also to the observed SEDs of the other three NLSy1 galaxies. In the high opacity model the same hydrogen column density of $1.8{\cdot}10^{24}$ cm^{-2} used for IRAS 13224-3809 has been assumed. In

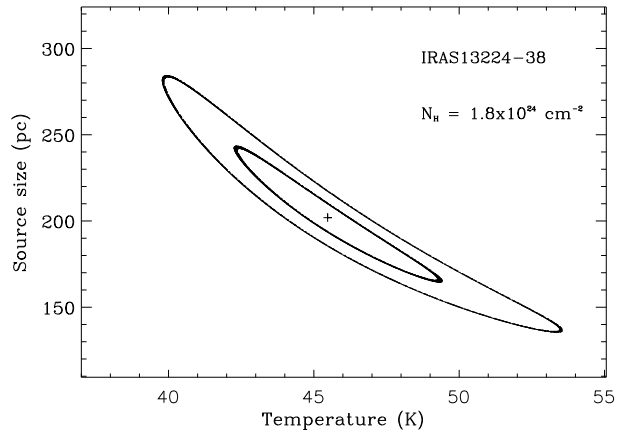

Fig. 10. Contour plot in the source size and temperature plane for the cold component of IRAS 13224-3809 in the high opacity model. Line contours are at 90%, and 99% confidence limits.

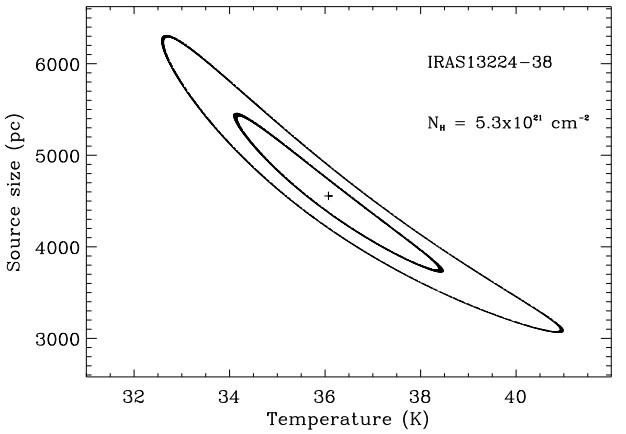

Fig. 11. As in fig. 10, but for the low opacity model.

the low opacity case we assumed a hydrogen column density corresponding to that derived from the measured Balmer decrement value for PG1404+226, and RXJ0323-49 (respectively N_H=1.07·10^{21}cm^{-2}, and 1.97·10^{21}cm^{-2}) (Miller et al. 1992, and Grupe 1996). While for TON S180 we chose the column density associated to our Galaxy in the direction of the source (N_H=1.55·10^{20} cm^{-2}, Dickey and Lockman 1990). This assumption is justified by a measured Balmer decrement value (Comastri et al. 1998) that is lower than expected in the case of no reddening.

The best fitting curves in the low opacity case of the observed infrared SEDs are shown in figs. 5, 6, 7, and 8. The thick solid line represents the sum of the grey bodies, each one of which is shown with a dotted line. Spectra fitted with the high opacity model are not shown because their spectral shape is very similar to those given.

6. Discussion

6.1. Dust opacity

Any model which seeks to explain the entire infrared emission in terms of thermal dust emission must involve a dust distribution with a range of temperatures, opacities, and distances from the heating source. It is not realistic to expect that dust at different temperatures will have the same optical depth because density and size are likely to differ. The real opacities of the NLSy1 galaxies are probably intermediate between the two extreme solutions considered above. The data do not constrain them, neither favor one of the two extreme solutions ($\Delta\chi^2_\nu \sim$ 0.001-0.015). However, indications on dust opacity can be derived by considerations on dust distribution.

Since the two extreme regimes imply dusty region sizes that are very different, a comparison with those expected by current models for Seyfert galaxies may give indications on the more likely model.

The temperatures and the sizes obtained in the two opacity cases for each grey body component are listed in in table 3. In the case of large opacities the estimated sizes of the dust emission regions vary from 0.2 pc for the hottest component (1000 K), to $\sim$ 500 pc for the coldest one (20 K), and in the case of low opacities the minimal estimated size is 0.3 pc, and the maximal 20 kpc. In current models for Seyfert galaxies hot dust (T = 1000-2000 K) is located just outside of the broad line region ($\sim$ 0.1-1 pc from the central engine), warm dust (T = 35-250 K) in the narrow line region (10-2000 pc), and dust at several temperatures (T = 50-1000 K) in a dusty torus extending from 1 pc to 1 kpc. In some Seyfert galaxies star forming regions at few hundred parsecs, up to kiloparsec scales can also contribute to the observed IR emission by heating dust up to T = 35-50 K. The same distribution of sizes and temperatures as observed in Seyfert galaxies can be derived if the emitting dust heated by an ultravi-

Table 3. Best fit parameters of the infrared spectra.

Source Name	High opacity T (K)	High opacity R (pc)	Low opacity T (K)	Low opacity R (pc)
TON S180	50	56	41	6924
TON S180	229	4.2	159	215
TON S180	1002	0.2	627	2.8
RX J0323-49	29	173	26	5648
RX J0323-49	81	21	64	527
RX J0323-49	315	1.1	221	10
IRAS 13224-38	45	202	36	4555
IRAS 13224-38	164	8.4	120	84
IRAS 13224-38	598	0.5	736	0.3
PG 1404+226	20	487	20	19977
PG 1404+226	52	51	43	1932
PG 1404+226	320	1.4	250	12

olet source of Seyfert galaxies luminosity is characterized by low opacity. Indeed the temperature T of dust grains at a distance r from a central heating source of luminosity L_{UV} is given by (Barvainis 1987):

$$T = \left[\frac{L_{UV}e^{-\tau_{UV}}}{Q_\nu \nu^{-\beta}} \frac{c^2 h^{3+\beta}}{32\pi^2 r^2 k^{4+\beta}} \frac{1}{\Gamma(4+\beta)\zeta(4+\beta)}\right]^{\frac{1}{4+\beta}} \quad (6)$$

where Γ is the gamma function, ζ is the Riemann zeta function, τ_{UV} is the dust optical depth to the ultraviolet continuum, and Q_ν is the absorption efficiency of the dust grains equal to $Q_{ext}(V)\cdot\tau(\nu)/\tau(V)$ (Bianchi, Davies and Alton 1999), where $Q_{ext}(V)$ is respectively equal to 0.076, and 3.2976, for dust grain radii of 0.01, and 0.1 μm. (Draine 1985). Assuming β=1.87, equation 6 becomes :

$$T = F \cdot \left[\frac{L_{UV,44}\cdot e^{-\tau_{UV}}}{r_{pc}^2}\right]^{\frac{1}{5.87}} \qquad K \quad (7)$$

where F, expressed in the required unit, is equal to 560 for dust grain radii of 0.1 μm, and to 1064 for dust grain radii of 0.01 μm, $L_{UV,44}$ is the ultraviolet luminosity in units of 10^{44} erg s^{-1}, and r_{pc} is the distance from the central source in parsecs. If we assume that the total absorption of the primary UV radiation by the grains occurs at $\tau_{UV} = 3$ (Barvainis 1987), the distances and the corresponding temperatures will be the same as those observed in Seyfert galaxies. The resulting range of values for UV luminosities of 10^{43} erg s^{-1} to 10^{45} erg s^{-1}, and for grain radii of 0.01 to 0.1 μm is represented in fig. 12 by the region comprised between the two solid lines. The parameters obtained in the low, and high opacity regimes are also reported in the figure. As expected, the computed parameters assuming $\tau_{UV} = 3$ are in good agreement with those derived in the low opacity case. The high opacity case is also acceptable, but only for the high temperature components. The comparison between the estimates of temperatures and sizes obtained in the two extreme regimes, and the observed values in Seyfert galaxies thus suggest that cold dust is characterized by low opacities, while the warm/hot dust may also be more opaque. In consequence, the IR reradiation at long wavelengths (T $\leq$ 60 K) will be isotropic, and orientation-independent. On the contrary, at shorter wavelengths (T > 60 K) the dust may self-absorb its emitted radiation, and the observed emission may depend on orientation.

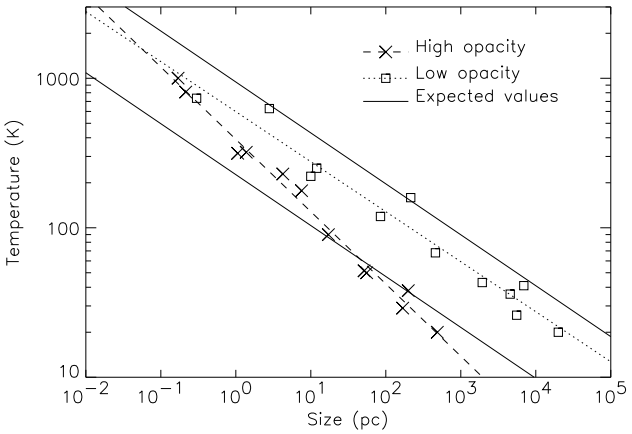

Fig. 12. Temperature and source size for each grey body component in the low opacity (□), and high opacity (×) regimes. The dotted line is the best fit linear interpolation of low opacity parameters, and the dashed line of high opacity parameters. The region within solid lines represent the parameter space for dust grain with radius = 0.01-0.1 μm, and UV optical depth τ_{UV} =3, heated by UV luminosities L_{UV} = 0.1-10·10^{44} erg s^{-1} (see section 6.1).

6.2. Infrared luminosities

Previous work on the infrared emission of NLSy1 galaxies (Halpern and Oke 1987) indicate high infrared luminosities as a property of this class of objects. Although the number of objects is small to produce meaningful statistics, we tried to see if this property characterizes also the NLSy1 galaxies studied here. The infrared luminosity of our NLSy1 galaxies has been computed by integrating all the fitted grey body components in the entire observed infrared range (see table 4), and compared with those typical of broad emission line Seyfert 1 galaxies. The most luminous objects of our sample, IRAS 13224-3809, and TON S180, belong to the category of luminous IR galaxies (L_{IR} >10^{11} L$_\odot$). The observed IR luminosities are in the same range as that of normal Seyfert galaxies.

Table 4. Infrared continuum properties, and optical extinction.

Source Name	L^a_{IR}	$\alpha^b_{25,60}$	$\alpha^c_{3,60}$	A^d_V
TON S180	13.8	0.3	0.99	....
RX J0323-49	6.4	1.2	1.38	1.05
IRAS 13224-38	34.5	2.0	1.77	1.84
PG 1404+226	6.5	...	1.22	0.57

[a]In unit of 10^{10} L$_\odot$. [b]Spectral index computed between 25 and 60 μm assuming $L_\nu \propto \nu^{-\alpha}$. [c]Spectral index computed between 3 and 60 μm assuming $L_\nu \propto \nu^{-\alpha}$. [d]Derived from the Balmer decrement using equation 5.

6.3. Starburst contribution

A recurrent question in the study of the infrared emission of Seyfert galaxies is the presence of a starburst, and its contribution to the observed emission. The presence of a starburst region has been found in a similar fraction of NLSy1, and of classical Seyfert 1 galaxies by Mas-Hesse et al. (1995) by identifying the dominant heating source. Starbursts tend to generate more emission from

cool dust than from hot dust when compared to AGN heated sources. The presence of this excess can therefore be recognized looking at the mid- and far-IR spectral shape. Indeed steep far/mid-IR spectra ($\alpha_{25,60}$ >1.25 where $L_\nu \propto \nu^{-\alpha}$) are typical of star forming regions, while flat far/mid-IR spectra ($\alpha_{25,60}$ = 0.50-1.25) are typical of AGNs (de Grijp, Lub and Miley 1987; Mas-Hesse et al. 1994).

The far/mid-IR spectral slope has been estimated for IRAS 13224-3809, TON S180, and RXJ0323-49 because flux measurements at 25, and 60 μm are available, and not for PG 1404+226 (table 4). TON S180, and RXJ0323-49 have $\alpha_{25,60} \leq$1.2 consistent with those observed in AGN dominated Seyfert galaxies, however the contribution from a weak star forming region cannot be excluded. The steep value found for IRAS 13224-3809, instead, suggests the presence of a component of cool dust that may be heated by a starburst.

6.4. The role of the dust in NLSy1 galaxies

The presence of dust in the nuclei of Seyfert galaxies can alter the way in which we perceive these objects. Dust can absorb the optical and ultraviolet continuum (reradiating this energy in the infrared), steepen the hydrogen line decrement, and block the soft X-rays. Several estimates of the extinction due to the presence of dust along the line of sight can be derived from observations at different energies, and a comparison among them can be an indicator of the dust distribution. The extinction due to the dust along the line of sight cannot be derived from the optical depth observed in the IR, because the observed IR SEDs do not allow us to constrain it. The observed SEDs give just a range of wavelengths (from $\sim$ 1 to less than 100 μm) at which the dust could become transparent. However, it is possible to derive an estimate of the dust extinction from the observed IR SEDs by measuring the steepness of the power law obtained by fitting all the IR data at wavelengths shorter than 60 μm, where the effects of opacity become important. If the distribution of dust with radius is characterized by a constant covering factor (fraction of the sky covered by dust, as seen by the central continuum source) the emitted spectrum will have a power law shape of type $L_\nu \propto \nu^{-\alpha_{int}}$. Apparently steeper spectra may indicate that self-absorbed emission prevents short wavelength radiation from escaping (case *1*), or that the properties in the dust distribution are not the same in different objects (case *2*), i.e. the contribution from cool/cold dust is very high compared to that from the hot one.

In the first case (case *1*) steeper spectra indicate higher extinction. The extinction can be estimated if we know the intrinsic infrared spectrum, and if we can measure the emerging one. The amount of visual extinction internal to the selected sources required to steepen the power law index from α_{int} to the observed α will be :

$$A_V = \frac{(\alpha_{int} - \alpha_{\lambda_1,\lambda_2}) \cdot ln(\lambda_1/\lambda_2)}{ln\left(10^{0.4(R_{\lambda_1} - R_{\lambda_2})}\right)} \quad (8)$$

where λ_1 and λ_2 are the (rest) wavelengths between which the spectral index is measured and the function $R(\lambda) = \frac{A_\lambda}{A_V}$ is the reddening law at the wavelength λ (Clavel 1998). The extinction in magnitude A_λ is proportional to the optical depth $\tau(\lambda)$, thus the function $R(\lambda)$ can be derived from the extinction curve. If we take as extinction curve that from which we have derived the optical depth curve reported in fig. 9 (Draine and Lee 1984), and, if we choose $\lambda_1 = 3$ μm, and $\lambda_2 = 60$ μm, equation 8 becomes :

$$A_V = 77.44 \cdot (\alpha_{3,60} - \alpha_{int}) \quad (9)$$

If all the emitting warm/hot dust is also responsible for the reddening of the Balmer lines, the optical extinction as derived in equation 9 will be the same as that obtained using equation 5. This assumption leads to the following relationship between the spectral slope $\alpha_{3,60}$ and the Balmer decrement :

$$\alpha_{3,60} = 0.086 \cdot log(H_\alpha/H_\beta) + \alpha_{int} - 0.039 \quad (10)$$

In order to test this prediction we compared the H_α/H_β values of the NLSy1 galaxies studied here with the slope of the power law obtained by fitting the observed data between 3 and 60 μm. This wavelength range has been chosen in order to have the best IR slope estimate. A broad wavelength range will contain more data. We did not extended further the wavelength range because at $\lambda > 60$ μm a power law is on many cases not a good description of the spectrum, and at $\lambda < 3$ μm the flux may arise from another source, and thus turn over showing a near-IR excess. The infrared data have been fitted with a weighted least-square method. The weights have been computed assuming symmetrical uncertainties given by the half of the difference between the logarithm of the measured value plus its uncertainty and the measured value minus its uncertainty. This last hypothesis allows us to apply the χ^2 test to test the fit. The χ^2 test shows that a power law fit is acceptable at more than 99.86% of confidence. The best fit IR power laws are shown by the dashed lines in figs. 5, 6, 7, and 8. The best-fit slope values are reported in table 4. The flattest slope is $\alpha_{3,60}$ = 0.99 for TONS 180, and the steepest one is $\alpha_{3,60}$ = 1.77 for IRAS 13224-3809. The measured power law slopes vary in a range of 0.78, that corresponds to a range in the visual extinction values of 61 mag, provided that all objects have the same α_{int}. The variations in the H_α/H_β values correspond, instead, to a range in the visual extinction values of only 2.84 mag. Such a difference indicates that all the emitting dust can not be responsible for the reddening observed in the Balmer lines. In other words, the $\alpha_{3,60}$ values vary

with the H_α/H_β ratios more rapidly than predicted in equation 10.

Interestingly, this comparison has permitted to discover a strong correlation between the two parameters: H_α/H_β, and $\alpha_{3,60}$ for the selected sources. The correspondent values and their linear interpolation are shown in fig. 13, respectively with filled diamonds, and a dashed line. The linear correlation coefficient is 0.99, and the probability to obtain such a value from not correlated values is 0.80% (significance of the correlation at a 2.66 sigma level). A stronger correlation is indicated by the non-parametric Spearman's test for which the coefficient rank is 1.0, with a null associated probability to obtain such a value from not correlated values.

Since our sample contains very few sources, a research in the literature has been performed in order to extend it and check whether this correlation is a general property of NLSy1 galaxies. We selected 12 additional NLSy1 galaxies (Mrk957, IZw1, Mrk359, IRAS02262-4110, MRK142, MRK734, NGC4051, PG1211+143, Mrk766, MRK684, MRK478, and Mrk493) among a sample of 148 objects, classified as NLSy1 in the literature[2]. The following selection criteria have been applied : 1) availability of, at least, one Balmer decrement measurement (45 objects remain); 2) availability of, at least, three flux measurements at 3 different wavelengths between 3 and 60 μm (18 objects remain); 3) the largest difference between two Balmer decrement measurements, for the same source, had to be smaller than 2 (16 objects remain); and finally 4) the infrared spectrum had to be well described by a power law in the 3 - 60 μm wavelength range (12 objects remain). The Balmer decrement values for these sources have been taken from the literature[3]. In case of more than one measurement the median value was chosen. The infrared data have been retrieved from NED, and then fitted with a weighted least-square method, as for the initial sample of 4 NLSy1 galaxies. The observed correlation is still present with the additional 12 NLSy1 galaxies, as shown in fig. 13 by the solid line that represents the best fit line obtained considering all the 16 NLSy1 galaxies. The additional 12 NLSy1 galaxies are reported with empty diamonds in fig. 13. For the whole sample (16 objects) the linear correlation coefficient is 0.71, and the probability to obtain such a value from not correlated values is 0.41%, (significance at a 2.87 sigma level). For the same sample a non-parametric Spearman's test gives a correlation coefficient of 0.61, with an associated probability to obtain such a value from not correlated values of 1.13% (significance at a 2.54 sigma level).

[2] Véron-Cetty M.-P., and Véron 1998; Grupe 1996; Osterbrock and Pogge 1985; Bischoff and Kollatschny 1999; Giannuzzo et al. 1998; and Wisotzki and Bade 1997.

[3] Giannuzzo et al. 1998; Osterbrock and Pogge 1985; Halpern and Oke 1987; De Zotti and Gaskell 1985; Grupe 1996; Berriman 1989; Dahari and De Robertis 1988; Halpern and Moran 1998; Mulchaey et al. 1994; Grupe et al. 1998; and Miller et al. 1992.

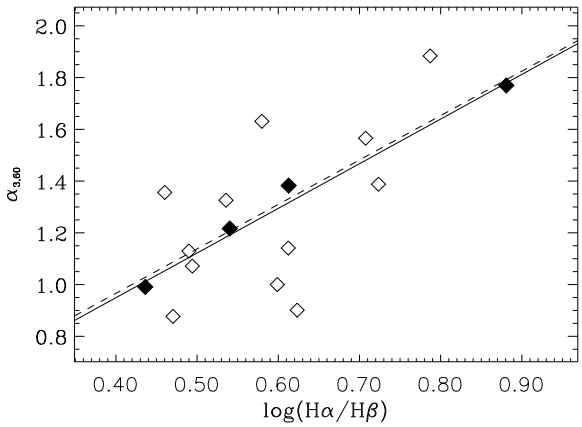

Fig. 13. Balmer decrement values vs the infrared spectral index α obtained fitting a power law in the 3-60μm range. Filled diamonds represent the four NLSy1 galaxies of our sample, and empty diamonds twelve additional NLSy1 galaxies. The solid line is the best linear fit obtained considering all the sixteen NLSy1 galaxies, and the dashed line is the best linear fit obtained considering only the four NLSy1.

The (weak) correlation between the infrared spectral slope and the Balmer decrement could be due to a selection effect, i.e. sources with flatter IR spectra and higher Balmer decrement may be absent because of a bias in the sample due to the selection criteria or to observational effects. Such a bias is not known to us. On the other side, a real physical link between the infrared and optical properties could be hidden by the difficulties in emission lines ratio measurements.

We performed another comparison between the optical and the IR properties of this kind of objects by using the ionization parameter, given by the line intensity ratio [OIII]/H_β available for the great majority of the sources. We searched in the literature[4] for the available measurements of this ratio for all the selected sources. In few cases more than one measurement has been found, thus the median value was computed, as done for the Balmer decrement data. The result of the comparison between the infrared spectral slope $\alpha_{3,60}$, and the ionization parameter [OIII]/H_β is shown in fig. 14: the [OIII]/H_β ratio increases when $\alpha_{3,60}$ increases. The two parameters are correlated significantly (Spearman's coefficient rank of 0.78, that is significant at 99.96%, that means at a 3.12 sigma level). If the correlations between the emission line ratios H_α/H_β and [OIII]/H_β, and the IR spectral slope $\alpha_{3,60}$ are real, a link between the processes that steepen the IR power law, and those that increase the lines ratios should be present. We have already examined the principal causes of a steep-

[4] Osterbrock and Pogge 1985; Halpern and Oke 1987; Grupe 1996; Dahari and De Robertis 1988; Grupe et al. 1998; Miller et al. 1992; Moran, Halpern and Helfand 1996; Goodrich 1989; and Comastri et al. 1998.

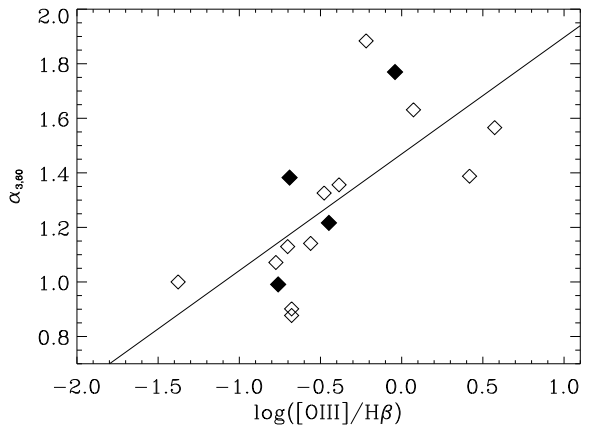

Fig. 14. Ionization indicator [OIII]/H_β versus the infrared spectral index $\alpha_{3,60}$. The solid line is the best linear fit obtained considering all the sixteen NLSy1 galaxies. Filled diamonds represent the four NLSy1 galaxies analyzed here, and empty diamonds twelve additional NLSy1 galaxies. The solid line is the best linear fit obtained considering all the sixteen NLSy1 galaxies.

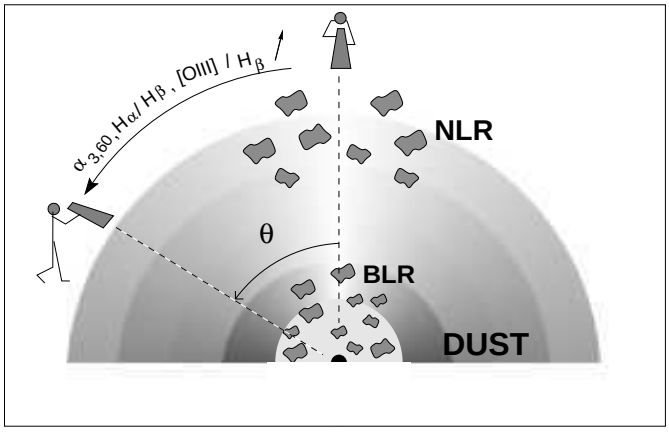

Fig. 15. Representation of the proposed scenario explaining the observed correlations. The gray rings represent the dust distribution. The dust temperature decreases at larger radii, and the opacity increases for larger values of the θ angle. Balmer lines are emitted in the BLR and in the NLR. The forbidden lines, as [OIII], are produced in the NLR by the ionizing continuum coming from the central region. The hot dust component in the inner region is partially absorbed by the dust at larger distances. At large values of the θ angle the BLR lines emission is absorbed by the dust producing higher Balmer decrements values, the hot dust emission is reduced by self-absorption, and because of lower H_β emission from the BLR, and unchanged [OIII]/H_β from the NLR, the observed [OIII]/H_β ratio increases (see text for more details).

ening of the IR spectrum (cases *1* and *2* above). Higher Balmer decrement values can be produced by dust reddening, and/or by radiative decay of the hydrogen atoms in which lower levels may be over-populated by collisional excitation in a dense plasma. The ionization parameter depends on the intensity of the ionizing source impinging on the NLR, and on the physical properties of the emitting gas (ionizing continuum, NLR density, and distance between the ionizing source and the emitting medium), while it does not depend strongly on the reddening from intervening material. An analysis of all the listed causes of steepening of the infrared power law, and of enhancement of the Balmer decrement, and of the ionization parameter, indicates that the observed correlations can be interpreted in terms of inclination dependent obscuration. Since the opacity of the dust responsible for the bulk of the observed IR emission is higher than that of dust attenuating the optical lines, these two dust components are distinct, but related (as indicated by the correlations of figs. 13, and 14). This may be the case if the central regions of these objects are surrounded by a distribution of dust which becomes gradually less opaque along some directions, i.e. near to the axial direction of a dusty torus, and if the BLR is more extended than the inner hot dust (see the proposed scenario in fig. 15). It is worth to note that the presence of line emitting gas extending further out than in normal Seyfert 1 galaxies is suggested by the observed width and variability properties of the emitted optical lines in NLSy1 galaxies (Giannuzzo et al. 1998). At low inclinations of the line of sight to the torus axis the BLR and the hottest dust component will be directly visible, while, at higher inclinations, the BLR, and the hottest dust component will be reddened since they will be observed through a dusty path. In this case the radiation coming from the extended BLR goes through dust less opaque than the hot dust radiation that is located along the torus plane. At higher inclinations of the line of sight the H_β emission coming from the BLR will decrease, while the [OIII]/H_β values associated to the NLR will be unchanged. Since we have not distinguished the H_β emission Balmer lines coming from the two regions, the observed [OIII]/H_β ratios will be enhanced at higher inclinations.

7. Conclusion

The broad band IR spectra provided by ISOPHOT for the four selected NLSy1 galaxies have allowed us to derive the distribution of temperatures of the emitting dust, and a possible range of opacities, and sizes. The comparison with current models of dust distribution in Seyfert galaxies favors lower opacities ($N_H \sim 1{\cdot}10^{21}\mathrm{cm}^{-2}$) for dust at low temperatures (T≤60 K), while warm/hot dust nearer to the heating central source may be characterized by higher opacities, and thus by an anisotropic emission.

The observed IR luminosities, and spectra are consistent with those of broad emission line Seyfert 1 galaxies. The presence of dust heated by a bright star forming region is suggested only for one of the four selected NLSy1

galaxies. It is, therefore, not a general property of NLSy1 galaxies.

A correlation between the Balmer decrement values, and the ionization parameters [OIII]/H_β with the slopes of the observed IR spectra measured for a small sample of NLSy1 galaxies (16 objects) is reported. The proposed scenario explains these correlations in terms of inclination dependent obscuration. In the case of high inclination angles, the radiation coming from an extended BLR is reddened by low opacity dust, while the hot dust radiation is absorbed by higher opacity dust located along the torus plane. For low inclinations of the line of sight the nuclear region is directly visible and no absorption effect is observed.

This interpretation is in contradiction with the model proposed by Ulvestad, Antonucci, and Goodrich (1995) in which the NLSy1 galaxies are the pole-on equivalent of Seyfert 2 galaxies.

Acknowledgements. We are grateful to R. Walter, S. Paltani, and D. Carrillo for preparing the observation program. We thank the Time Allocation Committee for awarding discretionary ISO observing time to this project. Martin Haas, Péter Ábrahám, B. Wilkes, and Eric J. Hooper are acknowledged for help in the ISOPHOT data reduction. R. Neri, and D. Nuernberger are acknowledged for assistance in the IRAM interferometer data reduction. We are also very grateful to the referee, J. Clavel, for carefullly reading this manuscript and for useful comments. The ISOPHOT data presented in this paper were reduced using PIA, which is a joint development by the ESA Astrophysics Division and the ISOPHOT consortium.

References

Barvainis R. 1987, ApJ, 320, 537
Barvainis R. 1990, ApJ, 353, 419
Berriman G. 1989, ApJ, 345, 713
Bianchi S., Davies J.I., and Alton P.B. 1999, A&AL, 344, 1
Bischoff K., and Kollatschny W. 1999, A&A, 345, 49
Boller T., Trümper J. Molendi S., Fink H. et al. 1993, A&A, 279, 53
Boller T., Brandt W. N., and Fink H. 1996, A&A, 305, 53
Boulanger F., Abergel A., Bernard J.-P., Burton W., Desert F.-X., Hartmann D., Lagache G., and Puget J.-L. 1996, A&A, 312, 256
Brandt W. N., Mathur S., and Elvis M. 1997, MNRAS, 285, L25
Clavel J., Wamsteker W., and Glass I. 1989, ApJ, 337, 236
Clavel J. 1998, A&A, 331, 853
Comastri A., Fiore F., Guainazzi M., Matt G. et al. 1998, A&A, 333, 31
Dahari O., and De Robertis M.M. 1988, ApJS, 67, 249
de Grijp M.H.K., Lub J., and Miley G.K. 1987, A&AS, 70, 95
De Zotti G., and Gaskell, C.M. 1985, A&A, 147, 1
Dickey J.M., and Lockman F.J. 1990, ARA&A, 28, 215
Draine B.T., and Lee H.M. 1984, ApJ, 285, 89
Draine B.T. 1985, ApJS, 57, 587
Gabriel C., Acosta-Pulido J., Heinrichsen I., Skaley D. et al. 1997, "The ISOPHOT Interactive Analysis PIA, a calibration and scientific analysis tool" in Proc. of the ADASS VI Conference, ASP Conf. Ser., Vol. 125, eds. G. Hunt & H.E. Payne
Gabriel C., Haas M., Heinrichsen I., and Tai-Dias W.-M. 1998, "The ISOPHOT Interactive Analysis User Manual"
Gear W.K. 1988, Millimetre and Submillimetre Astronomy, R.D. Wolstencroft and W.B. Burton (eds.)
Giannuzzo M.E., Mignoli M., Stirpe G.M., and Comastri A. 1998, A&A, 330, 894
Goodrich R.W. 1989, ApJ, 342, 224
Grupe D. 1996 Ph.D. Thesis, Göttingen Univesity
Grupe D., Wills B.J., Wills D., and Beuermann K. 1998, A&A, 333, 827
Guilloteau S., Delannoy J., Downes D., Greve A. et al. 1992, A&A, 262, 624
Halpern J.P., and Oke J.B. 1987, ApJ, 312, 91
Halpern J.P., and Moran E.C. 1998, ApJ, 494, 194
Laureijs R.J., Klass U., Richards P.J., and Schulz B. 1998, ISOPHOT Data Users Manual Version 4.0, SAI/95-220/Dc
Lemke D., Klaas U., Abolins J., Ábrahám P. et al. 1996, A&A, 315, L64
Kessler M.F., Steinz J.A., Anderegg M.E., Clavel J. et al. 1996, A&A, 315, L27
Klaas U., Laureijs R. J., Radovich M., and Schulz B. 1998, Report on the ISOPHOT Calibration Accuracies, ISO Science Op. Center Report (SAI/98-092/Dc)
Komossa S., and Greiner J. 1998, proc. of High Energy Processes in Accreting Black Holes (Sweden, June 29 - July 4, 1998), J. Poutanen and R. Svensson (es)
Mas-Hesse J.M., Rodríguez-Pascual P.M., De Cordoba L.S.F., and Mirabel F. 1994, ApJS, 92, 599
Mas-Hesse J. M. Rodríguez-Pascual P.M., De Cordoba L.S.F., Mirabel F. et al. 1995, A&A, 298, 22
Mathis J.S., Rumpl W., and Nordsieck K.H. 1977, ApJ, 217, 425
Miller P., Rawlings S., Saunders R., and Eales S. 1992, MNRAS, 254, 93
Moran E.C., Halpern J.P., and Helfand D.J. 1996, ApJS, 106, 341
Mulchaey J.S., Koratkar A., Ward M.J., Wilson A.S. et al. 1994, ApJ, 436, 586
Osterbrock D. E., and Pogge R. W. 1985, ApJ, 287, 166
Otani C., Kii T., and Miya K. 1996, Proc. Röntgenstrahlung from the Universe, eds. Zimmermann H. U., Trümper J., and Yorke H., MPE Report 263, 491
Pounds K. A., Done C., and Osborne J. 1995, MNRAS, 277, L5
Rodríguez-Pascual P.M., Mas-Hesse J. M., and Santos-Lleó M. 1997, A&A, 327, 72
Taylor J.R. 1982, An introduction to Error Analysis, The Study of Uncertainties in Physical Measurements, University Science Books
Ulvestad J.S., Antonucci R.R.J., and Goodrich R.W. 1995, AJ, 109, 81
Véron-Cetty M.-P., and Véron P. A catalogue of Quasars and Active Nuclei (8th Edition), European Southern Observatory Scientific Report, N. 18 - June 1998
Ward M. J., Geballe T., Smith M., Wade R., and Williams P. 1987, ApJ, 316, 138
Whittet D.C.B. 1992, Dust in the Galactic Environment, Institute of Physics Publishing, Bristol
Wisotzki L., and Bade N. 1997, A&A, 320, 395

Chapter 6

The Far-Infrared emission of Radio Loud and Radio Quiet Quasars

Astron. Astrophys. 350, 765-776 (1999)

ASTRONOMY AND ASTROPHYSICS

The Far-Infrared emission of Radio Loud and Radio Quiet Quasars

M. Polletta[1,2], T.J.-L. Courvoisier[1,2], E.J. Hooper[3], and B.J. Wilkes[3]

[1] Geneva Observatory, Ch. des Maillettes 11, CH-1290 Sauverny, Switzerland
[2] Integral Science Data Centre, Ch. d'Ecogia 16, CH-1290 Versoix, Switzerland
[3] Harvard-Smithsonian Center for Astrophysics, Cambridge, MA, USA

Received 15 March 2000 / Accepted 16 May 2000

Abstract. Continuum observations at radio, millimetre, infrared and soft X-ray energies are presented for a sample of 22 quasars, consisting of flat and steep spectrum radio loud, radio intermediate and radio quiet objects. The primary observational distinctions, among the different kinds of quasars in the radio and IR energy domains are studied using large observational datasets provided by ISOPHOT on board the Infrared Space Observatory, by the IRAM interferometer, by the sub-millimetre array SCUBA on JCMT, and by the European Southern Observatory (ESO) facilities IRAC1 on the 2.2 m telescope and SEST.

The spectral energy distributions of all quasars from radio to IR energies are analyzed and modeled with non-thermal and thermal spectral components.

The dominant mechanism emitting in the far/mid-IR is thermal dust emission in all quasars, with the exception of flat spectrum radio loud quasars for which the presence of thermal IR emission remains rather uncertain, since it is difficult to separate it from the bright non-thermal component. The dust is predominantly heated by the optical/ultraviolet radiation emitted from the external components of the AGN. A starburst contributes to the IR emission at different levels, but always less than the AGN ($\leq 27\%$). The distribution of temperatures, sizes, masses, and luminosities of the emitting dust are independent of the quasar type.

Key words: Galaxies: quasars – Radio continuum – Infrared.

1. Introduction

Radio quiet and radio loud (not blazar) quasars (RQQ and RLQ, respectively) have similar spectral properties in the ultraviolet (UV), optical, and infrared (IR), but their radio powers differ by several orders of magnitude (Elvis et al. 1994). This divergence takes place at millimetre (mm) wavelengths. At these wavelengths the contribution from two emission components merge, namely the synchrotron emission dominant in the radio domain and thermal emission from cool dust (30-50 K) in the far-IR (Barvainis & Antonucci 1989). It is still not entirely clear whether the distinction between RLQ and RQQ is a consequence of differences in their central engines or whether it merely reflects differences in their environments. The primary observational distinctions in the IR domain, and the proposed physical mechanisms to explain them are studied here, using the new insights provided by Infrared Space Observatory[1] (ISO; Kessler et al. 1996) measurements.

1.1. The Radio emission

Two main types of RLQ can be distinguished on the basis of their radio spectrum: the flat spectrum radio loud quasars (FSRQ), and the steep spectrum radio loud quasars (SSRQ). FSRQ show highly-collimated structures and very compact features, with flat or inverted radio spectra. SSRQ have radio spectra dominated by synchrotron emission from extended radio lobes. The lobes and a radio core in the centre of these objects are signs of a relativistic jet. According to the unified scheme (Barthel 1989; Urry & Padovani 1995) FSRQ are the counterparts of SSRQ in which the jet is aimed at the observer.

The origin of the much weaker radio emission in RQQ is far less certain. The majority of the total radio emission from the RQQ comes from the compact features in the nucleus (< 1 kpc for unresolved regions, and at least 2 kpc for the resolved ones) rather than the body of the host galaxy (Kukula et al. 1998). It has been proposed that the activity in RQQ is supplied by a starburst, i.e. thermal bremsstrahlung and synchrotron emission coming from strongly radiative supernovæ and su-

Send offprint requests to: Maria.Polletta@obs.unige.ch

[1] ISO is an ESA project with instruments funded by ESA Member States (especially the PI countries: France, Germany, the Netherlands and the United Kingdom) and with the participation of ISAS and NASA.

pernovæ remnants (SNRs) in a very dense environment where shocks accelerate electrons (Terlevich et al. 1992). Alternatively, if the energy supply arises from accretion onto a massive black hole, the radio emission from RQQ (as in RLQ) is caused by radio jets, but the bulk kinetic power of these jets is for some reason $\sim 10^3$ times lower than those of RLQ (Miller et al. 1993). This second hypothesis seems to be favored by recent studies, because of high brightness temperatures calculated (typical SN/SNRs have $T_B \leq 10^5$K), by the evidence of a pc-scale jet (Blundell & Beasley 1998) and by observations of flat/inverted and variable radio spectra (Barvainis et al. 1996).

Recently, quasars with intermediate radio luminosities have been discovered and labeled Radio Intermediate Quasars (RIQ) (Francis et al. 1993, Falcke et al. 1995). RIQ may represent the Doppler boosted counterparts of radio quiet quasars. This hypothesis is suggested by the variability observed at radio wavelengths (Falcke et al. 1996).

1.2. The Infrared emission

The presence of a dominant thermal (circumnuclear dust emission), or non-thermal (synchrotron radiation from the AGN) component in the IR continuum of quasars is still debated.

Many attempts to establish the origin of the IR emission in RLQ and RQQ have been performed through observations in the sub-millimetre (sub-mm) of quasars detected by IRAS (RLQ in Chini et al. 1989, and Antonucci et al. 1990; RQQ in **?**, Barvainis et al. 1992, Hughes et al. 1993, and Hughes et al. 1997; and both in Andreani et al. 1999, this last work is the only one based on an optically selected sample). The main test applied to recognize the presence of thermal emission in the IR spectra of the objects was based on the slope of the continuum emission ($F_\nu \propto \nu^\alpha$) connecting the far-IR and sub-mm data. A steep, $\alpha > 2.5$, continuum is strong evidence for thermal dust emission. Most of the sources studied have $\alpha < 2.5$ and are consistent with a dominant self-absorbed synchrotron emission component. However, some RQQ have spectral slopes as steep as $\alpha = 4.35$, which, along with observations of strong molecular gas (CO) emission (Barvainis 1997), give strong support to a thermal mechanism as the origin of the far-IR component in RQQ.

Among the RLQ, α is, at most, $\simeq 0.9$ for the FSRQ, and 1.1 for the SSRQ (Chini et al. 1989). Variability, shape of the continuum spectral energy distribution and, in some cases polarization, indicate that the radio, mm and far-IR emission of FSRQ is dominated by the synchrotron process (Lawrence et al. 1991). On the contrary, many SSRQ show evidence of thermal emission: their far-IR spectra are brighter than extensions of the radio emission (Antonucci et al. 1990), suggesting a different origin than the non-thermal radio component; and the flux is constant, consistent with it arising from a region much larger than a light year (Edelson & Malkan 1987). Moreover, the spectral energy distributions of some RLQ, both FSRQ and SSRQ, show evidence for a galaxy component: reddening, residual starlight, molecular gas (Scoville et al. 1993), and some thermal dust emission in the near-IR (Barvainis 1987). Both components, non-thermal synchrotron radiation and thermal dust emission, are probably present at IR wavelengths, as observed in the RLQ 3C273 (Robson et al. 1986; Barvainis 1987).

1.3. Relation between the Radio and Infrared emission

A tight, linear correlation is observed between the far-IR flux and the radio fluxes in AGN (Sopp & Alexander 1991), suggesting a common origin. RQQ and RLQ occupy well defined regions in Log(L(IR))–Log(L(Radio)) space, and show a relation with a similar slope, just shifted to higher radio power by a factor $\sim 10^4$ in RLQ. RQQ show a similar relation as spirals, starbursts, and ultra luminous IR galaxies (ULIRG), suggesting that their IR emission may arise from sufficiently energetic star formation in the host galaxy (Sopp & Alexander 1991). However, the majority of the bolometric luminosity in over half of known ULIRG seems to arise from a buried AGN (Sanders 1999). Additionally, the variable and flat spectra, and high brightness temperatures shown by many RQQ at radio frequencies (Barvainis et al. 1996) suggest that the radio emission is related to the AGN rather than to a starburst.

1.4. Proposed scenarios

The unified model (Barthel 1989; Urry & Padovani 1995) predicts that similar disk–like dust distributions exist in both RQQ and RLQ. Orientation of the active nucleus, environment, and jet luminosity all affect the relative contributions of thermal and non-thermal sources to the observed infrared luminosity (Chini et al. 1989).

Other scenarios have been proposed to explain the large differences in radio power between RQQ and RLQ: different spin of the central black hole (Wilson & Colbert 1995), or different morphological type of the host galaxy. Indeed, different radio powers are expected if one population of objects is fueled by mergers (ellipticals) and one is fueled by mostly internal processes within the galaxy (spirals) (Wilson & Colbert 1995). However, recent studies on the host galaxies of quasars indicate that the host galaxies of RQQ are in several cases elliptical and not always spiral galaxies (Taylor et al. 1996).

1.5. Open issues

A better knowledge of the radio and IR properties of quasars is required to test the unified model predictions, and answer the following questions:

1. What is the dominant mechanism emitting at IR wavelengths in RLQ and RQQ?
2. Do RLQ and RQQ have the same dust properties (temperature, source size, mass, and luminosity)?
3. Does an interplay between the radio and the IR components exist?

These questions can be addressed through the study of the spectral energy distributions (SED) of RLQ and RQQ. Here, we present the SEDs from radio to IR frequencies of a sample of 22 AGN (7 RQQ, 11 RLQ, 2 radio galaxies (RG) and 2 RIQ). The selected sample, even if incomplete and heterogeneous, is useful to address these questions thanks to several properties characterizing the sample (steep/flat radio spectra, radio loudness/quietness), and to the large amount of photometric data available in the radio, mm/sub-mm and IR domains. This work is based mainly on IR data provided by ISO. ISO data reduce the frequency gap between sub-mm and far-IR observations, better sample the IR spectral band with a larger number of filters than previous instruments, and increase the number of detected objects thanks to a higher sensitivity. The study of the IR emission of quasars will be extended in the future with the results of the European and of the U.S. ISO Key Quasar Programs providing a similar coverage of the IR SED for a larger sample of quasars (see first results in Haas et al. (1998), and Wilkes et al. (1999)).

2. Observational dataset

Source names, coordinates, and redshifts of the selected sample were taken from the NASA Extragalactic Database (NED)[2], and are listed in Table 1. Infrared observations were obtained for 18 of the sources with the Imaging Photopolarimeter on ISO (ISOPHOT; Lemke et al. 1996), and 3 were observed with IRAC1 on the 2.2 m ESO/MPE telescope. Millimetre and sub-mm data were obtained for 10 objects with the IRAM interferometer at Plateau de Bure in France (Guilloteau et al. 1992), the Sub-millimetre Common User Bolometer Array (SCUBA; Holland et al. 1999) on the James Clerk Maxwell Telescope[3] and the Swedish ESO Sub-mm Telescope (SEST) of the European Southern Observatory (ESO) at La Silla. The instruments used for each object are indicated in a footnote to Table 1.

The observational details (observing date, wavelength, and measured flux density) of IRAC1, SEST, IRAM, and SCUBA observations are reported in Table 2. The data obtained with the SEST telescope were reduced to outside the atmosphere, corrected for the gain elevation characteristic of the telescope, and calibrated with Uranus. All IRAM observations were performed in compact configuration. All five antenna were used during most of the observations, with the exceptions indicated in a footnote of Table 2. The calibrators were 3C 454.3 for 3C 47, and 22040+420 and 1928+738 during the two observations of HS 1946+7658. SCUBA observations yielded good results at 850 μm only due to marginal weather. The fluxes were calibrated using the canonical gain value of 220 Jy/V, since a calibration scan at 850μm was not done. The chosen value is relatively insensitive to the weather and should be good to within 20%. ISOPHOT observations and data reduction are described in the next section. These new observations were supplemented with literature data from radio to near-IR. We have also collected data at soft X-ray energies. For reasons of homogeneity we collected only ROSAT data, available for most of the sources. From published soft X-ray spectra we derived the flux at 1 keV corrected for absorption. The observed absorption is always

Table 1. Basic properties of the sample

Source Name	RA (J2000) $h\ m\ s$	Dec (J2000) $^\circ\ '\ ''$	Type†	z
3C 47[1,4]	01 36 24	+20 57 27	SSRQ	0.425
PKS 0135−247[1]	01 37 38	−24 30 53	FSRQ	0.831
PKS 0408−65[1,2]	04 08 20	−65 45 09	RG	...
PKS 0637−75[1,2]	06 35 47	−75 16 17	FSRQ	0.653
PG 1004+130[2]	10 07 26	+12 48 56	SSRQ	0.240
PG 1048−090[2]	10 51 30	−09 18 10	SSRQ	0.344
4C 61.20[1]	10 52 33	+61 35 20	SSRQ	0.422
PG 1100+772[1,5]	11 04 14	+76 58 58	SSRQ	0.312
PG 1103−006[2]	11 06 32	−00 52 52	SSRQ	0.423
PG 1216+069[1,2]	12 19 21	+06 38 38	RIQ[a]	0.331
PG 1352+183[1]	13 54 36	+18 05 18	RQQ	0.152
PG 1354+213[1]	13 56 33	+21 03 51	RQQ	0.300
PG 1435−067[1,3]	14 38 16	−06 58 21	RQQ	0.129
PG 1519+226[1]	15 21 14	+22 27 43	RQQ	0.137
PG 1543+489[1,5]	15 45 30	+48 46 09	RQQ	0.400
PG 1718+481[1]	17 19 38	+48 04 13	RIQ[a]	1.084
B2 1721+34[1]	17 23 20	+34 17 58	SSRQ	0.206
HS 1946+7658[1,4]	19 44 55	+77 05 52	RQQ	3.020
3C 405[1]	19 59 28	+40 44 01	NLRG	0.056
B2 2201+31A[1]	22 03 15	+31 45 38	FSRQ	0.295
PG 2214+139[3]	22 17 12	+14 14 21	RQQ	0.066
PG 2308+098[1,3]	23 11 18	+10 08 15	SSRQ	0.433

† SSRQ: Steep Spectrum Radio Loud Quasar; FSRQ: Flat Spectrum Radio Loud Quasar; RQQ: Radio Loud Quasar; RIQ: Radio Intermediate Quasar; NLRG: Narrow Line Radio Galaxy; RG: Radio Galaxy.
[1] Observed with ISOPHOT; [2] Observed with SEST; [3] Observed with IRAC1; [4] Observed with IRAM; [5] Observed with SCUBA.
[a] Classification in Falcke et al. (1996).

[2] The NASA/IPAC Extragalactic Database (NED) is operated by the Jet Propulsion Laboratory, California Institute of Technology, under contract with the National Aeronautics and Space Administration.

[3] The James Clerk Maxwell Telescope is operated by the Joint Astronomy Centre on behalf of the Particle Physics and Astronomy Research Council of the United Kingdom, the Netherlands Organization for Scientific Research, and the National Research Council of Canada.

Table 2. IRAC1, SEST, IRAM and SCUBA results

Source Name	Instrum.	Obs. Date (d m y)	λ (μm)	$F_\nu^\dagger$ (mJy)
3C 47	IRAM	14 07 98[1,2]	1300	17.0±2.3
		14 07 98[1,3]	3000	30.8±0.6
PKS 0408−65	SEST	30 11 95	1300	<30
PKS 0637−752	SEST	30 11 95	1300	724±37
			1300	905±31
PG 1004+130	SEST	30 11 95	1300	<39
PG 1048−090	SEST	30 11 95	1300	<18
PG 1100+772	SCUBA	17 01 99	850	6.8±2.4
PG 1103−006	SEST	30 11 95	1300	<27
PG 1216+069	SEST	30 11 95	1300	<45
PG 1435−067	IRAC1	21 06 96	3.7	12.1±0.4
			3.7	12.2±0.5
PG 1543+489	SCUBA	17 01 99	850	<5.4
HS 1946+7658	IRAM	20 05 98[4]	1300	<10.4
		20 05 98[4]	3000	<5.0
PG 2214+139	IRAC1	21 06 96	4.7	44.2±4.6
PG 2308+098	IRAC1	21 06 96	3.7	<17.56

† Upper limits to the flux are given at the 3σ level. [1] Also observed on July 17, and 22. [2] Only four antenna were used on July 17. [3] Only three antenna were used on July 14, and four on July 17, and 22. [4] Also observed on May 23.

compatible with the galactic absorption. The list of references from which data were retrieved, for each object, is reported in Table 3.

3. ISOPHOT observations and data reduction

Photometric data at several (up to 11) wavelengths between 3.6 and 200 μm were obtained for each object using the single-element P1 and P2 detectors plus the two array cameras, C100 (3 pixels × 3 pixels) and C200 (2 pixels × 2 pixels). Detector and observing parameters are listed in Table 4. Most of the observations (124 in total for 16 objects) were performed in chopper mode, and the remaining (37 for 10 objects) by mapping the region surrounding the target (scans or rasters).

In chopper mode the radiation beam is deflected from the source (on-source position) to adjacent fields on the sky (off-source position) several times in order to measure the background emission. Triangular (T) and rectangular (R) chopping modes were used. In the triangular chopper mode the background emission is measured in two different regions, while in the rectangular chopper mode it is measured in only one position. Observing dates, filters, apertures, exposure times, chopping mode, and measured fluxes are reported in Table 5 for each ISOPHOT chopper observations.

Table 3. List of references of selected published data

Source Name	References number†
3C 47	1, 2, 3, 4, 5
PKS 0135−247	1, 3, 5, 6, 7
PKS 0408−65	1
PKS 0637−75	1, 2, 3, 5, 6, 8, 9
PG 1004+130	1, 10, 11, 12, 13, 14, 15, 16
PG 1048−090	1, 3, 11, 14, 15, 17
4C 61.20	1, 3, 18
PG 1100+772	1, 2, 3, 12, 15, 17, 19, 20, 21
PG 1103−006	1, 12, 14, 15, 22, 23
PG 1216+069	2, 12, 14, 23, 24, 25, 26
PG 1352+183	2, 14, 15, 17, 25
PG 1354+213	2, 14, 15, 25
PG 1435−067	2, 14, 15, 25
PG 1519+226	2, 14, 15, 25
PG 1543+489	12, 14, 15, 25, 27, 28, 29
PG 1718+481	1, 2, 14, 23, 26, 30
B2 1721+34	1, 13, 17, 31
HS 1946+7658	25, 32
3C 405	1, 33, 34
B2 2201+31A	1, 2, 7, 13, 16, 20, 31, 35, 36, 37 38, 39, 40, 41
PG 2214+139	1, 12, 15, 29, 30, 42
PG 2308+098	1, 15, 30

† 1: NED; 2: Gezari et al. 1997; 3: Brinkmann et al. 1997; 4: van Bemmel et al. 1998; 5: Kühr et al. 1981; 6: Tornikoski et al. 1996; 7: Steppe et al. 1993; 8: Véron-Cetty & Véron 1998; 9: Tanner et al. 1996; 10: Wilkes et al. 1994; 11: Kapahi 1995; 12: Sanders et al. 1989; 13: Lister et al. 1994; 14: Neugebauer et al. 1987; 15: Miller et al. 1993; 16: Ennis et al. 1982; 17: Elvis et al. 1994; 18: Reid et al. 1995; 19: Antonucci et al. 1990; 20: Chini et al. 1989; 21: Lonsdale & Morison 1983; 22: Siebert et al. 1998; 23: Kellermann et al. 1989; 24: Blundell & Beasley 1998; 25: Yuan et al. 1998; 26: Falcke et al. 1996; 27: Andreani et al. 1999; 28: Barvainis et al. 1996; 29: **?**; 30: Wang et al. 1996; 31: Schartel et al. 1996; 32: Kuhn et al. 1995; 33: Robson et al. 1998; 34: Haas et al. 1998; 35: Bloom et al. 1999; 36: Hoekstra et al. 1997; 37: Mitchell et al. 1994; 38: Neugebauer et al. 1986; 39: Ghosh et al. 1994; 40: Neugebauer et al. 1979; 41: Teräsranta et al. 1992; 42: Hughes et al. 1993.

Table 4. ISOPHOT detector properties and covered sky region in mapping observations

Detector Name	λ (μm)	Pixel size ($''$)	Scan Coverage ($'' \times ''$)	Raster Coverage ($'' \times ''$)
P1	3.6, 4.8, 7.3, 12	-	52×156	-
P2	25	-	-	-
C100	60, 80, 100	43.5	138×230	230×230
C200	150, 170, 200	89.4	184×460	276×460

In mapping mode the telescope moves in a pattern around the source, providing more sky coverage than in the chopper mode (Table 4). P1 detector maps were performed with an aperture of 52″ during all observations, except one (B2 2201+31A) during which the chosen aperture was 23″. Observing dates, filters, exposure times, and measured fluxes are reported in Table 6. More details on mapping mode are reported in section 3.2.1.

3.1. First steps of the data reduction: from ERD to AAP level

The first part of the data reduction was performed using version 8.1 of the PHT Interactive Analysis (PIA)[4] tool (Gabriel 1997). We started the reduction with the raw data processed with version 8.7 of the Off-Line Processing (Laureijs et al. 1998). The raw data form a sequence of detector read-outs distributed in 2^n (n=2-6) sets of four response curves or ramps, as function of time (Edited Raw Data: ERD in Volts).

Each set of four ramps represents a sky position. Each ramp is corrected for the non-linearity of the detector response, and for contamination of cosmic particle events (glitches). The removal of read-outs affected by glitches is carried out by applying two median filtering techniques: the single-threshold technique that uses a threshold of 4.5 standard deviations (σ) for flagging bad read-outs and the two-threshold technique that uses a threshold of 3.0σ for flagging and 1.0σ for re-accepting read-outs. After applying the non-linearity correction and the deglitching to the ERD, a straight line is fitted to each ramp, in order to determine its slope or Signal per Ramp Data (SRD in Volt/s).

In most of the cases the first 25 or 50% (1 or 2 ramps of 4) of the signals per chopper plateau at the SRD level are discarded to enable the detector response to stabilize at the level corresponding to the source flux density. The remaining data are further corrected for highly discrepant points (value at more than 3σ from the average signal) still contaminated by glitches, for the orbital dependent dark current, and for the signal dependence on the ramp integration time (reset time interval) to obtain an average Signal per Chopper Plateau (SCP in Volt/s).

After applying flat-fielding correction using PIA values, the SCP data are calibrated to obtain the Standard Processed Data (SPD in unit of Watts). Since the detector response varies with time, it is determined at the time of the observation by measuring the flux emitted by two thermal Fine Calibration Sources (FCS1 and FCS2) on board. The FCS measurements are reduced in the same way as the scientific measurements up to this step. Data from FCS1 are used because they are the best calibrated. The FCS1 signal is checked in order to remove data with large uncertainties (this step is equivalent to computing the weighted mean of the FCS1 data).

In the case of mapping observations, the FCS1 is observed twice, before and after the observation of the source. The photometric calibration we use is the average value of the two FCS1 measurements.

After the flux calibration the AAP (Auto Analysis Product) data are obtained. They are a sequence of 2^n off- and on-source flux measurements (in Jy) each corresponding to a sky position. The reduction from the AAP level to the final results is performed using our own IDL routines, and not following the standard pipeline. This procedure was also applied in the reduction of ISOPHOT chopper data of a sample of Seyfert galaxies (Polletta & Courvoisier 1999).

[4] PIA is a joint development by the ESA Astrophysics Division and the ISOPHOT consortium.

Table 5. Details of ISOPHOT Observations performed in Chopper Mode

λ (μm)	Apt. (″)	Exp. (s)	Chop. Mode	F_ν (mJy)	Uncert.† Stat.	Syst.
3C 47 (January 30, 1997)						
4.8	23	128	R	<64.		
12.8	23	128	R	69.	10.	21.
20	23	128	R	<171.		
60	-	256	R	170.	52.	51.
100	-	256	R	246.	52.	74.
PKS 0408−65 (June, 05 1997)						
4.8	23	128	R	<26.		
12.8	23	128	R	<60.		
20	23	128	R	<84.		
60	-	128	R	<308.		
100	-	128	R	<162.		
PKS 0637−75 (June, 05 1997)						
4.8	23	128	R	<26.		
12.8	23	128	R	<43.		
20	23	128	R	<99.		
60	-	128	R	<117.		
100	-	128	R	<143.		
4C 61.20 (April, 27 1996)						
7.3	13.8	512	T	<35.		
12	23	256	T	<34.		
25	52	512	T	<110.		
60	-	128	R	<278.		
80	-	128	R	258.	48.	77.
100	-	128	R	<303.		
150	-	128	R	<267.		
170	-	128	R	<148.		
200	-	128	R	<335.		

† In units of mJy.

Table 5. (continued)

λ (μm)	Apt. ($''$)	Exp. (s)	Chop. Mode	F_ν (mJy)	Uncert.† Stat.	Syst.
PG 1100+772 (June, 17 1996)						
4.8	52	512	R	25.	7.	8.
7.3	52	512	R	32.	5.	10.
12	52	512	R	36.	8.	11.
25	120	512	R	54.	10.	16.
60	-	256	R	70.	14.	21.
100	-	128	R	<282.		
150	-	512	R	<417.		
200	-	512	R	<468.		
PG 1216+069 (July, 11 1996)						
4.8	52	512	R	50.	15.	15.
7.3	52	512	R	72.	6.	22.
12	52	512	R	90.	12.	27.
25	120	512	R	95.	26.	29.
60	-	128	R	65.	14.	20.
100	-	128	R	<140.		
150	-	512	R	<137.		
200	-	512	R	<149.		
PG 1352+183 (December, 14 1996)						
60	-	64	R	198.	23.	59.
80	-	64	R	<237.		
100	-	64	R	<213.		
150	-	64	R	<283.		
170	-	64	R	<240.		
200	-	64	R	<206.		
PG 1354+213 (June, 13 1996)						
7.3	13.8	2048	T	18.	5.	5.
12	23	1024	T	21.	5.	6.
25	52	2048	T	23.	7.	7.
60	-	128	R	<298.		
80	-	128	R	<194.		
100	-	128	R	<125.		
150	-	128	R	<170.		
170	-	128	R	<137.		
200	-	128	R	<280.		

† In units of mJy.

Table 5. (continued)

λ (μm)	Apt. ($''$)	Exp. (s)	Chop. Mode	F_ν (mJy)	Uncert.† Stat.	Syst.
PG 1435−067 (January, 07 1997)						
7.3	13.8	256	T	70.	9.	21.
12	23	64	T	<94.		
25	52	128	T	<718.		
60	-	64	R	<1111.		
80	-	64	R	<849.		
100	-	64	R	<333.		
150	-	64	R	<386.		
170	-	64	R	<369.		
200	-	64	R	<317.		
PG 1519+226 (February, 01 1997)						
7.3	13.8	256	T	32.	8.	10.
12	23	64	T	<48.		
25	52	64	T	76.	17.	23.
60	-	128	R	172.	44.	52.
80	-	128	R	<194.		
100	-	128	R	121.	22.	36.
150	-	128	R	<207.		
170	-	128	R	<151.		
200	-	128	R	<154.		
PG 1543+489 (May, 30 1996)						
4.8	52	512	R	20.	6.	6.
7.3	52	256	R	39.	4.	12.
12	52	256	R	45.	6.	14.
25	120	512	R	140.	13.	42.
60	-	128	R	470.	144.	141.
100	-	128	R	399.	55.	120.
150	-	128	R	455.	117.	182.
200	-	256	R	<377.		
PG 1718+481 (May, 30 1996)						
4.8	52	512	R	18.	3.	5.
7.3	52	256	R	24.	6.	7.
12	52	256	R	25.	6.	8.
25	120	512	R	44.	7.	13.
60	-	128	R	90.	1.	27.
100	-	128	R	56.	1.	17.
150	-	128	R	<251.		
200	-	256	R	<261.		

† In units of mJy.

3.2. From the AAP level to final results

The last steps of the data reduction before determining the source flux are the background subtraction, the deletion of remaining highly discrepant points, and the correction for effects depending on chopper plateau time, vignetting (only for chopper observations) and point spread function.

In the case of chopper observations with the C100 detector only the central pixel pointed on the source is considered to derive the flux density, since the eight border pixels contain only a small fraction of the central point source and summing these values would hence only increase the noise.

3.2.1. Background subtraction

In chopper observations the background is measured at each off-source position. Since in some cases the instruments show long term drift effects, the background signal is estimated near the time of each on-source measurement and subtracted. In the case of chopper observations the background estimates are obtained by computing the weighted mean of each pair of consecutive off-source measurements. The weights are computed from PIA statistical

Table 5. (continued)

λ (μm)	Apt. ($''$)	Exp. (s)	Chop. Mode	F_ν (mJy)	Uncert.† Stat.	Syst.
B2 1721+34 (April, 20 1996)						
7.3	13.8	512	T	19.‡	5.	6.
12	23	512	T	<26.‡		
25	52	512	T	<135.‡		
HS 1946+7658 (May, 27 1996)						
4.8	52	1024	R	<5.		
7.3	52	1024	R	4.5	1.2	1.4
12	52	1024	R	8.7	0.7	2.6
25	120	1024	R	47.	15.	14.
60	-	64	R	<230.		
100	-	64	R	<300.		
150	-	64	R	682.‡	17.	273.
200	-	64	R	378.‡	27.	151.
B2 2201+31A (November, 16 1996)						
3.6	5	2048	T	<17.		
4.8	7.6	1024	T	<52.		
7.3	13.8	256	T	45.	5.	14.
12	23	64	T	64.	8.	19.
12	23	64	T	<62.		
25	52	128	T	106.	25.	32.
60	-	128	R	193.	13.	58.
80	-	128	R	139.	11.	42.
100	-	128	R	212.	51.	64.
150	-	128	R	847.	97.	339.
170	-	128	R	699.	98.	280.
200	-	128	R	382.	97.	153.
PG 2308+098 (November, 26 1996)						
3.6	5	2048	T	<31.		
4.8	7.6	1024	T	13.	2.	4.
12	23	128	T	<39.		
PG 2308+098 (December, 12 1996)						
7.3	13.8	256	T	<21.		
12	23	128	T	16.	55.	5.
25	52	512	T	<108.		
60	-	128	R	<183.		
80	-	128	R	<174.		
100	-	128	R	<83.		
150	-	128	R	<201.		
170	-	128	R	<152.		
200	-	128	R	<214.		

† In units of mJy. ‡ Doubtful data. Discussed in Sec. 3.3 and 4.1.

uncertainties. Since the sequence of chopper plateaux ends with an on-source position, we used the weighted mean of the two last on-source measurements, and the flux observed in the last off-source position to determine the last pair of on- and off-source values, for a total of 2^{n-1} flux values.

Small maps of the regions immediately surrounding ten of the targets were constructed in one or both of the following ways (Fig. 1): multiple linear scans across the source and rastering the detector about the source. A scan with the P1 and C100 detectors consisted of three steps of the telescope, with this sequence repeated three times. Only the middle row of C100 pixels (8, 5, and 2, as depicted in Fig. 1) viewed the source. The C200 scans contained four steps, repeated twice, with the source centered between two pixels. Note that the source was observed in only the middle two steps of the C200 scan. The raster patterns were 3×3, 3×3, and 4×2 or 2×4, for the P1, C100, and C200 detectors, respectively. Each pixel viewed the source once in the raster maps. The step size between exposures for both scans and rasters was approximately equal to the pixel size, a little more to take into account the gap between pixels, for the C100 and C200 cameras, and equal to the aperture size for the P1 detectors, which resulted in a different total sky coverage for each detector (see Table 4). A background estimate for each on-source measurement was obtained from a weighted average of the flux measured in the raster or scan positions immediately preceding and following the source position by the same pixel. Using the same pixel to determine the background

Table 6. Details of ISOPHOT Observations performed in Raster Mode

Obs. date	λ (μm)	Exp. (s)	F_ν (mJy)	Uncert.† Stat.	Syst.
3C 47					
January, 31 1998	60	636	<129.		
PKS 0135−247					
December, 12 1997	12^d	1206	<199.		
PKS 0408−65					
June, 05 1997	170^a	195	<51.		
PKS 0637−75					
June, 05 1997	170^a	346	<180.		
March, 15 1998	150^a	387	<171.		
	200^a	387	<203.		
PG 1100+772					
August, 15 1997	60	348	<99.		
	100	348	<55.		
	$150^{b,c}$	579	<82.		
	$200^{b,c}$	579	<54.		
October, 28 1997	12^d	954	<161.		
	60^d	630	68.	22.	20.
November, 02 1997	150^a	579	<120.		
PG 1543+489					
November, 01 1997	12^d	864	<202.		
	60^d	630	269.	27.	81.
	$150^{a,d}$	574	279.	45.	84.

† In units of mJy. ^{a}4×2 map. ^{b}2×4 map. ^{c}Step amplitude of 90$''$. ^{d}Telescope nodding mode.

Table 6. (continued)

Obs. date	λ (μm)	Exp. (s)	F_ν (mJy)	Uncert.† Stat.	Syst.
PG 1718+481					
April, 20 1997	60	348	59.	16.	18.
	100	348	40.	13.	12.
	150[a]	323	<104.		
	200[a]	579	<56.		
November, 01 1997	12[d]	864	<164.		
	60[d]	630	69.	13.	21.
	150[a,d]	574	<145.		
HS 1946+7658					
April, 28 1997	60	348	49.	12.	15.
	100	348	79.	14.	24.
	150[a]	451	<114.		
	200[a]	579	<356.		
October, 26 1997	200[a]	579	<227.		
November, 17 1997	12[d]	954	<171.		
November, 18 1997	12[d]	954	<168.		
	60[d]	630	66.	15.	20.
December, 08 1997	60[d]	630	68.	20.	20.
3C 405					
October, 30 1997	60[d]	630	2360.	76.	708.
	170[a,d]	574	1582.	160.	475.
B2 2201+31A					
November, 20 1997	12[d]	852	55.	15.	17.
	60[d]	414	111.	20.	33.
	170[a]	387	<249.		

† In units of mJy. [a]4×2 map. [b]2×4 map. [c]Step amplitude of 90″. [d]Telescope nodding mode.

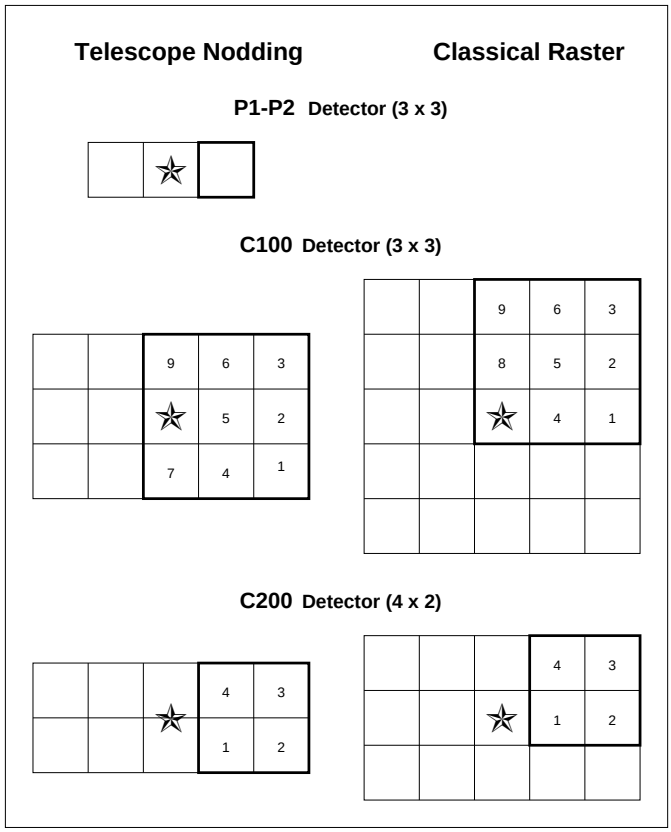

Fig. 1. Schematic representation of the two observing modes used for mapping observations: telescope nodding (scan) on the left side and classical raster on the right side. The position of the source in the different cases is represented by a star. The bold square represents the initial position of the detector. The numbering corresponds to the pixels numbers. The detectors move first from the left to the right, then in the opposite direction. In the case of classical raster, at each change of the horizontal direction, the detector shifts down one step. All the steps are separated by the pixel size. The reported pixel sizes do not correspond to the real proportions. The numbers in parenthesis refer to the number of horizontal steps × the number of repetitions for nodding and vertical steps of telescope motion in the raster maps.

reduced the impact of uncertainties in the flat field. The weighted average background was subtracted from each on-source measurement providing a sequence of source flux values.

Residual effects of detector instabilities, in both chopper observations and maps, produced occasional discrepant points, which were culled by one-pass sigma clipping. The threshold number of standard deviations to reject a flux value depended on the number of points in the sequence (Chauvenet's criterion in Taylor (1982)), ranging from 1.15σ to 2.66σ.

In the case of chopper observations with the C200 camera, the source flux was computed by adding together the fluxes measured by each of the four pixels. The source flux was divided between pairs of adjoining pixels in the C200 scans; these were averaged by weighting with their uncertainties. Table 6 lists the weighted mean of each flux sequence after clipping, or 3σ upper limits for non–detection, where σ is the quadratic sum of the statistical and systematic uncertainties (see section 3.3), also reported in the tables.

3.2.2. Vignetting correction

In the case of chopper observations with the C100 and C200 detectors, the data are further corrected for the signal loss outside the beam of the telescope (vignetting). The PIA default vignetting correction factors were computed considering the dependency only on the distance of the chopper positions and on the filter, but recent investigations have shown that they depend also on the time per chopper plateau (M. Haas, private communication).

The PIA default vignetting factors were applied directly to the data, resulting in little change to the flux values obtained with the C100 camera. However, the fluxes from the C200 detector are $\sim 80\%$, in median, larger after the vignetting correction. Given the uncertainty over the

accuracy of the vignetting factors, we averaged the fluxes derived with and without the correction and added the respective uncertainties in quadrature.

3.2.3. Correction for effects depending on the chopper plateau time and point spread function

In the case of chopper observations a correction for the signal loss due to effects depending on the time per chopper plateau is applied to the computed flux value. Since short integration times with the C100 and C200 detectors do not reach the full signal, the observed flux can be reduced by large factors, typically up to 68 % for the C100 detector, and up to 12% for the C200 detector for the shortest observations. The correction factors we use are the PIA default values.

All the computed fluxes are finally corrected for the point spread function (psf) of each detector using the default PIA values derived empirically in most of the cases. The available psf correction values correspond to a source position centered in a pixel or located in a corner of the pixel. In case of scans with the C200 detector we needed the psf correction corresponding to the target located in the middle of a side of the pixel. We derived it by assuming a bi-dimensional Gaussian function for the psf and constraining its parameters using the other two known values for each wavelength (30.6% at 150 μm, and 29.1% at 170 μm).

3.3. Calculation of systematic uncertainties

During the data reduction only statistical errors were taken into account, and not those in the absolute flux density calibration. The accuracy of the absolute photometric calibration depends mainly on systematic errors (detector transient effects, calibration response, dark current, point spread function), and it is currently known to be better than 30% (Klaas et al. 1998). The associated statistical and systematic uncertainties are reported in the last two columns of Table 5 and 6. We associate to the measured flux an uncertainty that is the quadratic sum of their statistical uncertainties and 30% (for the C200 measurements obtained in chopper mode we use 40% that corresponds to half of the uncertainty due to the vignetting correction) of the measured value. Among our ISOPHOT observations the datasets of B2 1721+34 were identified as failed after inspection of their quality by the ISO team because they were heavily affected by cosmic rays and thus scientifically useless. We report these data in Table 5, and indicate that they are doubtful in a footnote.

4. The spectral energy distributions

We report the first far-IR detection for 9 (4C 61.20, PG 1216+069, PG 1352+183, PG 1354+213, PG 1435−067, PG 1519+226, PG 1718+481, PG 2308+098, and HS 1946+7658) of the 18 sources observed with ISOPHOT. Among the remaining 9 sources, three (PKS 0135−247, PKS 0408−65, and PKS 0637−75) were not detected, and the remainings 6 were already detected by IRAS.

All the data were converted to monochromatic luminosities in the rest frame of the object (H_0 = 75 km s^{-1} Mpc^{-1}, q_0=0.5) using the following equation:

$$L_{\nu\,\mathrm{em}} = 4\pi d_{\mathrm{L}}^2 F_{\nu\,\mathrm{obs}}/(1+z), \quad (1)$$

where $F_{\nu\,\mathrm{obs}}$ is the monochromatic flux in the observer's frame, and d_{L} is the luminosity distance to the object. In the case of PKS 0408−65 we adopted a redshift value equal to 0.5, arbitrarily chosen, since no redshift measurement is available. This source will not be considered in the following analysis.

The spectral energy distributions (SEDs) as νL_ν versus ν in the rest frame of all sources are shown in Fig. 2. Upper limits are plotted only if there is no detection at that frequency at any epoch, and in cases of multiple upper limits at the same frequency from different epochs, only the most stringent is used. A broad band spectrum of a local galaxy in its rest frame, representing the AGN host galaxy, is superposed in each panel of Fig. 2. We chose the spiral galaxy M100, modeled by Silva et al. (1998), to which we added data in the radio (Becker et al. 1991; Gregory & Condon 1991; White & Becker 1992) and in the soft X-ray energy domains (Immler et al. 1998) in the case of RQQ, and the template of a giant elliptical galaxy (Silva et al. 1998) in the case of RLQ, RIQ and RG. The reported host galaxy template was not modified by any normalization. In many cases this is orders of magnitude below the observed luminosities, and even if it is shifted towards higher luminosities to reach the quasar SED, it will remain below at most frequencies.

4.1. The nature of the IR emission: thermal or non-thermal emission ?

The IR emission can have a thermal or non-thermal origin. Several investigation methods can be applied to identify the emission process:

1. The value of the slope of the sub-mm/far-IR spectral break can discriminate between optically-thick (self-absorbed) synchrotron and thermal emission from dust grains. The self-absorbed synchrotron model is characterized by a maximum value of the sub-mm/far-IR slope that is 2.5 ($F_\nu \propto \nu^\alpha$), if the radiation is emitted by an electron population with a simple power-law energy distribution, or somewhat larger ($\alpha \leq 3$) if a thermal electron pool or dual power-law energy distribution is invoked (de Kool & Begelman 1989; Schlickeiser et al. 1991). In either case the maximum synchrotron slope is attained only for a completely homogeneous source, otherwise it will be lower. The

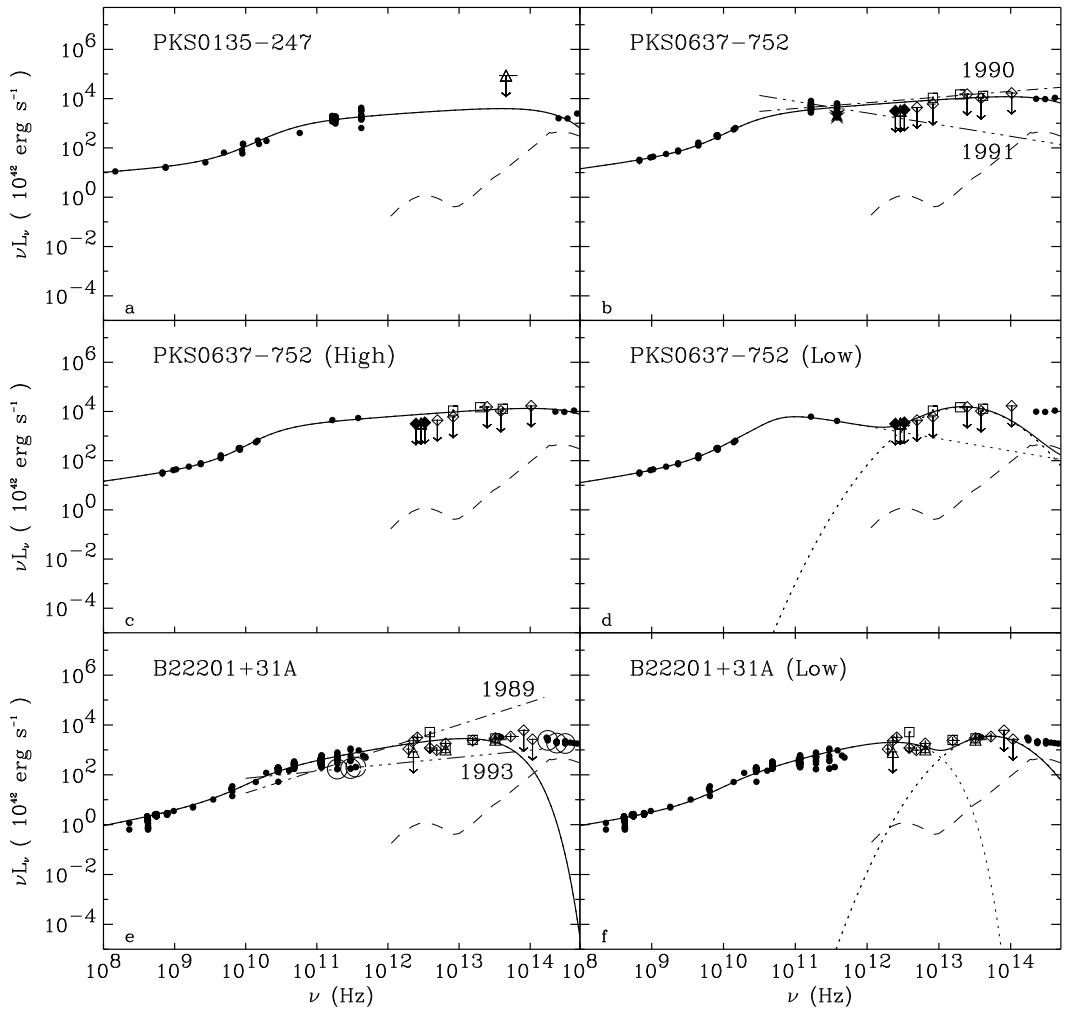

Fig. 2. SEDs as νL_ν versus ν in the rest frame of the objects. All sources shown on this page are FSRQ. Full circles represent literature data, stars SEST data, open diamonds ISOPHOT chopper data, triangles and filled diamonds ISOPHOT raster data at different epochs, and squares IRAS data. Arrows represent 3σ upper limits. The solid line represents the sum of all single fitted components represented by dotted lines. The dotted lines represent the best fit non-thermal models of the radio component (see section 4.2, and Table 7), and the parabolic fits of the IR component (see section 5.2). When more than one radio component is present a symbol is reported for each spectral component: C for core and L for lobe (L1 and L2 for two lobes). A typical host galaxy template (dashed line), a spiral galaxy in the case of RQQ, and a giant elliptical galaxy in the case of RLQ, RIQ and RG, is over-plotted. The radio spectrum of PKS 0637−752 was fit in two ways, using only the simultaneous mm data corresponding to the flattest power law fit (**c**) (dash-dot line in **b**) and the two corresponding to the steepest power law fit (**d**) (dash-dot-dot-dot line in **b**). The radio spectrum of B2 2201+31A was also fit in two ways, taking all data from radio to mid-IR (**e**) and only data from radio to far-IR (**f**). The flattest power law fit (dash-dot line in **e**) and the steepest one (dash-dot-dot-dot in **e**) measured during simultaneous mm observations of B2 2201+31A are reported. The big open circles in **e** correspond to simultaneous observations at mm and near-IR wavelengths.

asymptotic thermal sub-mm/far-IR slope is expected to be ≥ 3 since the optically thin thermal spectrum derives from Rayleigh-Jeans law with an additional parameter dependent on frequency, $F_\nu \propto B_\nu(T) \cdot \tau_{\rm d}$ where $\tau_{\rm d}$, the dust optical depth, is $\propto \nu^\beta$ with $\beta \simeq$1–2 (see section 4.3).

2. A non-thermal origin of the IR emission is indicated if relatively short time scale flux variability is observed, since a synchrotron component is expected to come from a very compact source. Most of the dust emission comes from an extended source with a long variability time scale.
3. A thermal origin can be attributed to the IR emission if a non-varying excess from any reasonable extrapolation from the radio domain in the plot νL_ν versus ν is observed (Hughes et al. 1997).

It is possible to distinguish the origin of the IR emission based on brightness temperature (Sanders et al. 1989) and polarization measurements, but the lack of these kind of data for the sample does not allow us to apply them.

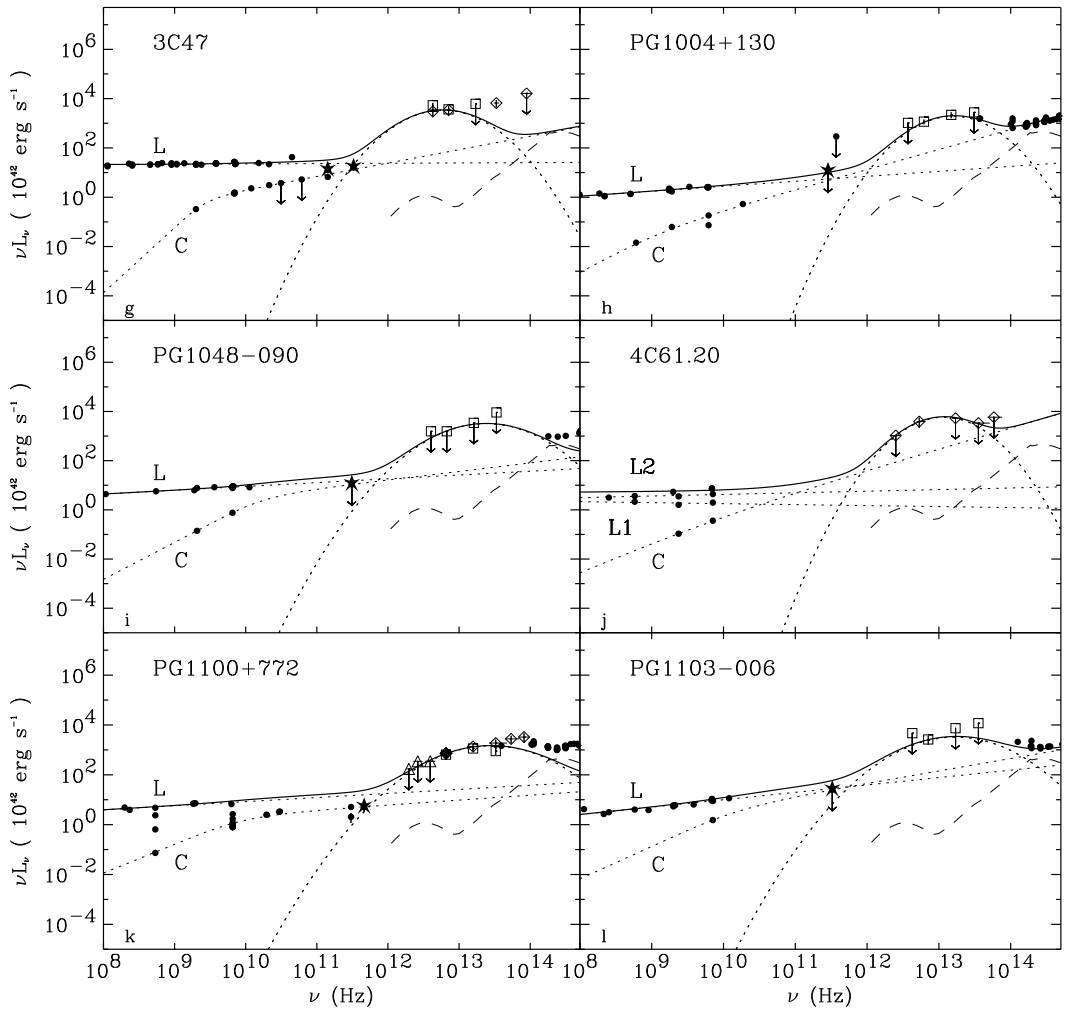

Fig. 2. Continued. SEDs for SSRQ are displayed on this page.

The first test will prove the thermal origin of the far-IR emission only if the coldest dust component is also the brightest one. Colder and less bright dust components will flatten the sub-mm/far-IR spectral slope. Two sources in the sample, PG 1543+489 and 3C 405, have a sub-mm/far-IR spectral index larger than 2.5. Their far-IR emission is therefore dominated by thermal radiation. The remaining sources have insufficient data at long wavelengths to constrain the sub-mm/far-IR spectral slope.

The observation of no variability is not conclusive, while if a flux variation is observed the non-thermal hypothesis will be strongly supported. This method can be applied only to those sources that were observed several times. In our sample, at least two IR observations (IRAS and ISOPHOT, or several ISOPHOT observations) at different epochs are available for ten sources (3C 47, PKS 0637−752, PG 1100+772, PG 1543+489, PG 1718+481, B2 1721+481, HS 1946+7658, 3C 405, B2 2201+31A, and PG 2214+139) (see Fig. 3). The data relative to the same observation epoch, instrument and observation mode are represented with the same symbol and connected by a line in Fig. 3. At least two measurements at the same wavelength are available for all the ten objects with the exception of PG 2214+139. Six sources (PG 1718+481, PG 1100+772, 3C 405, PG 1543+489, B2 1721+34, and PG 2214+139) show no sign of variability. Two of them also satisfy the first test. For two other sources (3C 47, and B2 2201+31A) the observed variation is only marginally $<1.6\sigma$, where σ includes the statistical and the systematic uncertainties. We consider their emission as constant in the span of our observations. In the case of PKS0637-752 we can only give a lower limit of the variation since the source was not detected by ISOPHOT. At wavelengths shorter than 60μm ISOPHOT and IRAS give consistent results, while at longer wavelengths they differ of more than 1.9σ.

The 150μm flux values for the high redshift source HS 1946+7658 differ by at least a factor of 6 between two epochs separated by less than a year (see Tables 5 and 6). Such extreme FIR variability is unlikely in a RQQ. The larger flux resulted from a chopped measurement, which is more susceptible at longer wavelengths to both back-

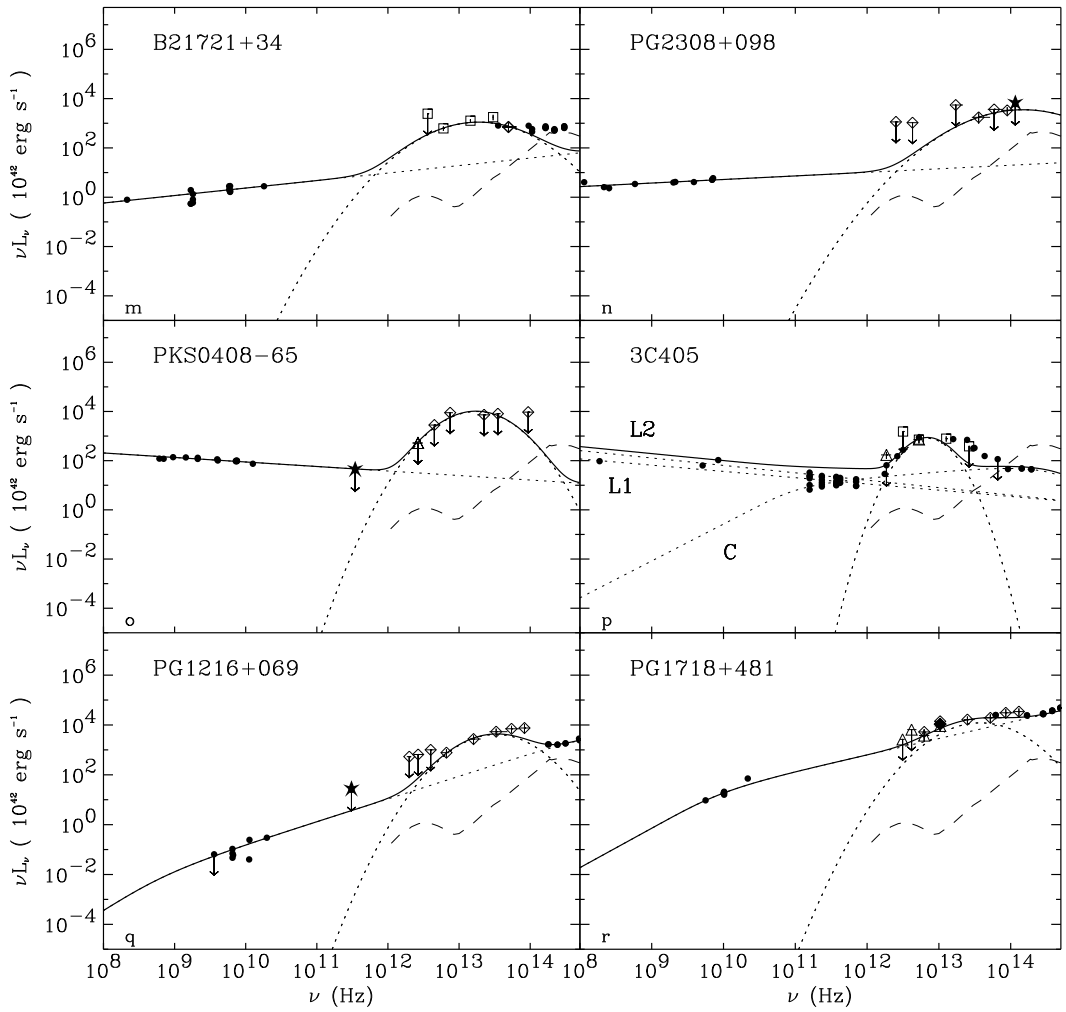

Fig. 2. Continued. The sources shown on this page include 2 SSRQ (m, n), 2 RG (o, p), and 2 RIQ (q, r). In the case of PG 2308+098 the star represents the IRAC1 measurement.

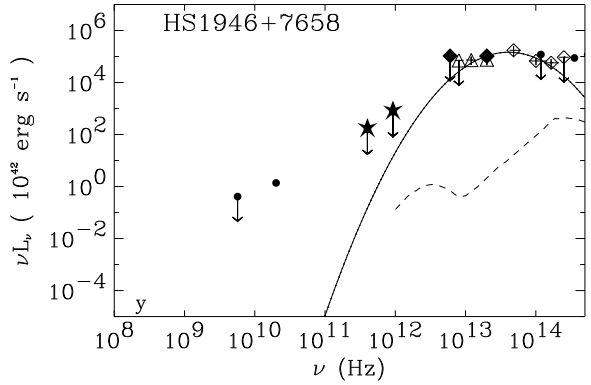

Fig. 2. Continued.

ground fluctuations and instrumental effects (e.g., a number of inadequately corrected cosmic ray strikes, unusually high detector drift, etc...) than the raster maps. Fig. 4 shows a 1.1×1.1 degree region around HS 1946+7658 at 100μm from IRAS, with the position of the source and the ISOPHOT chopper direction indicated. Bright cirrus structures are nearby, and the background ranges from 0.21 – 0.38 MJy/sr within 90″of the source (equivalent to 0.16 – 0.28 Jy on the C200 covered area) (IRSKY[5] version 2.5). A strong gradient in the direction SE–NW in the background emission is clearly shown, which coincides with the ISOPHOT chopper direction. These variations may be greater at longer wavelengths and with the better spatial resolution of ISOPHOT. As a consequence of the uncertainties for this source, chopped data at $\lambda > 100\mu$m for HS 1946+7658 will not be included in subsequent analysis.

The result of this method suggests that for all the selected objects, with the exception of PKS 0637−752, the IR emission is thermal in origin. The result is not very strong since a non-thermal process may also produce a constant flux. However, it is unlikely to measure the same flux from a non-thermal source during three different ob-

[5] IRSKY is An Observation Planning Tool for the Infrared Sky developed for NASA at IPAC, JPL/Caltech.

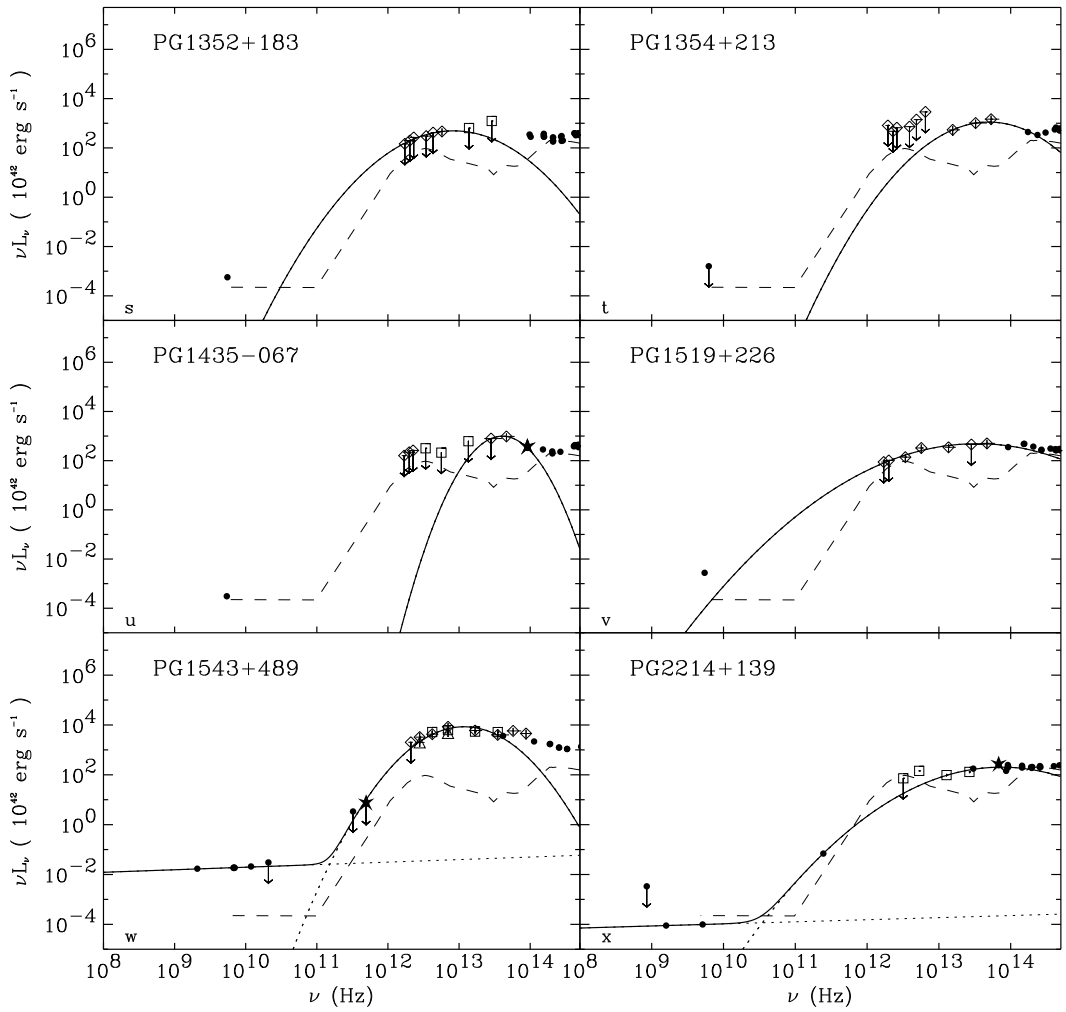

Fig. 2. Continued. All sources shown on this page are RQQ. In the case of PG 1435−067 the star represents the IRAC1 measurement.

servations performed in a range of 14 years (from 1983 to 1997) as observed in six objects (see Fig. 3).

The third test is the simplest, and it can be applied to the whole sample since a broad spectral coverage from radio to the IR is available for all the sources. Before applying this test we need to estimate the contribution from the non-thermal component in the IR and subtract it from the observed IR spectrum. The non-thermal contribution can be estimated by fitting the radio data with a reasonable model and then extrapolating it to higher frequencies (see next section).

4.2. Contribution of the radio non-thermal component in the infrared

In order to estimate the contribution of the radio non-thermal component in the IR domain, the radio continuum was fitted with some plausible models, and extrapolated to higher frequencies. In the following we will distinguish two components in the radio spectra of RLQ, the extended component (radio lobes), and the core component (unresolved core, jet, etc...).

The radiation emitted by compact sources, like the cores and the hot-spots of radio loud objects, can be modeled by a self-absorbed synchrotron emission spectrum. In the case of a homogeneous plasma with isotropic pitch angle distribution and power law energy distribution of the form $N(E) \propto E^{-s}$, this can be expressed as:

$$L_\nu \propto \left(\frac{\nu}{\nu_{\rm t}}\right)^{\alpha_1} \cdot \left[1 - \exp\left(-\left(\frac{\nu_{\rm t}}{\nu}\right)^{\alpha_1-\alpha_2}\right)\right] \cdot e^{-\frac{\nu}{\nu_{\rm cut\,off}}}, \quad (2)$$

where $\nu_{\rm t}$ is the frequency at which the optical depth of the plasma is equal to unity, and $\nu_{\rm cut\,off}$ is the frequency corresponding to the cut off energy of the plasma energy distribution, at which the energy gains and losses of the electrons are equal. The optically thick and optically thin spectral indices are denoted by α_1, and α_2. In the case of a homogeneous source, α_1 is expected to be 2.5, and α_2 is related to the exponent s of the plasma energy distribution by the relationship: $\alpha_2 = -(s-1)/2$. The superposition

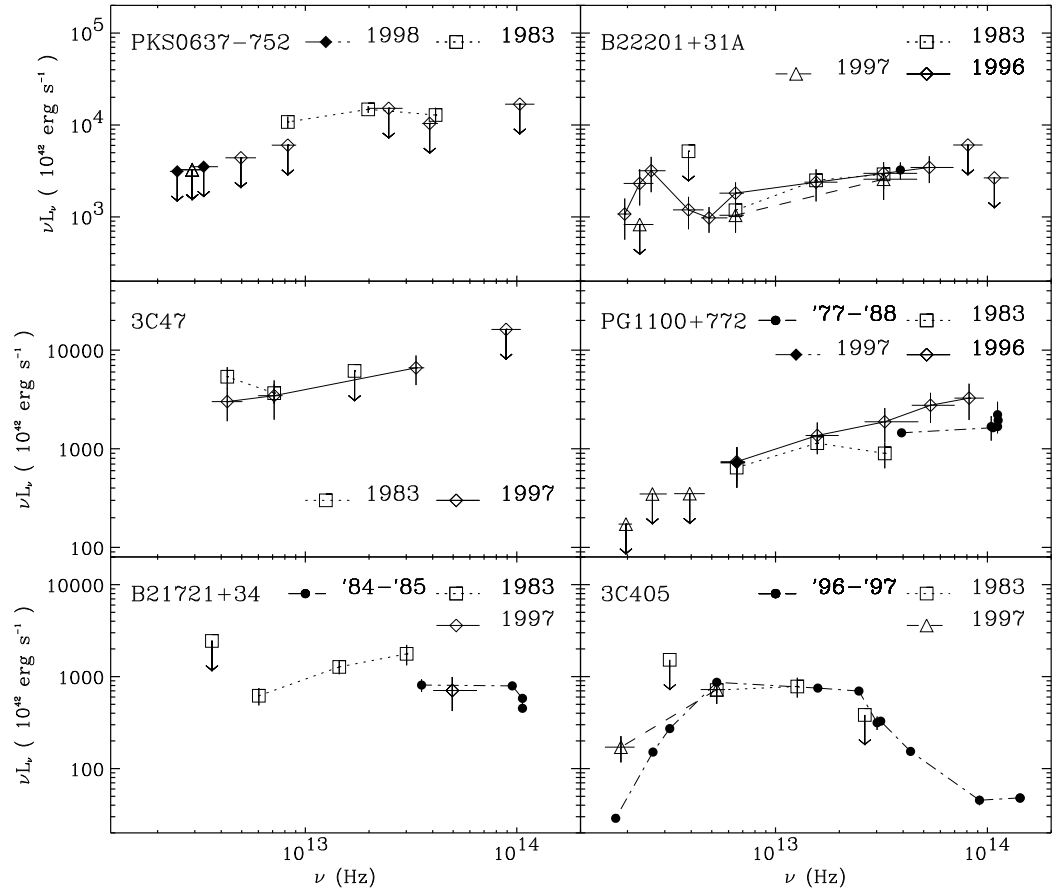

Fig. 3. IR data at different epochs. Symbols as in Fig. 2. Lines connect data relative to the same epoch. All objects are RLQ (2 FSRQ, 3 SSRQ, and 1 RG).

of several self-absorbed components can produce a flatter power law. In this case the spectral model of equation (2) will remain valid, but α_2 will not have the same meaning. If the source is optically thin, as in extended sources (radio lobes), the emitted spectrum can be expressed more simply as:

$$L_\nu \propto \left(\frac{\nu}{\nu_{\rm cut\,off}}\right)^{\alpha_2} \cdot \mathrm{e}^{-\frac{\nu}{\nu_{\rm cut\,off}}}. \quad (3)$$

In many cases the contribution of the synchrotron component at high frequencies is negligible compared to the observed emission, therefore a high energy cut off was not included in the model. The model is then represented by a broken power law of slopes α_1 and α_2, or by a simple power law of slope α_2, according to the presence/absence of self absorption.

The synchrotron model describes well the observed radio spectra of most of the sources in the sample. However, while in the case of SSRQ it is quite easy to separate the different components and hence apply a model for each of them, the spectral modeling is more difficult for FSRQ. For these sources we parameterize the emitted spectrum with an empirical equation that is valid if the resulting spectrum is produced by self-absorbed synchrotron emission or by optically thin synchrotron emission due to a hard electron spectrum produced through the acceleration processes in turbulent plasma (Wang et al. 1997). The observed flat radio spectra are described by the following equation:

$$L_\nu \propto \left(\frac{\nu}{\nu_{\rm b}}\right)^{\alpha_1} \cdot \frac{\left[1-\exp\left(-\left(\frac{\nu_{\rm t}}{\nu}\right)^{\alpha_1-\alpha_2}\right)\right]}{\left[1-\exp\left(-\left(\frac{\nu_{\rm b}}{\nu}\right)^{\alpha_0-\alpha_1}\right)\right]} \cdot \mathrm{e}^{-\frac{\nu}{\nu_{\rm cut\,off}}}, \quad (4)$$

where $\nu_{\rm b}$ is the frequency at which the spectrum flattens, α_0 is the spectral index observed at low frequencies ($\nu < \nu_{\rm b}$), and the other model parameters have the same meaning as in equation (2).

The observed SEDs from the radio to the mm energy domains were fitted with one or a combination of these models (see best fit parameters in Table 7). In some cases near-IR data have also been used in the fits, in particular when no data in between mm and near-IR frequencies constrained the spectrum to lie below the near-IR flux (PKS 0135−247, PKS 0637−752, 4C 61.20, PG 1004+130, PG 1216+069, PG 1718+481, 3C 405, and B2 2201+31A). In a few cases we fixed some model parameters, as indicated in a footnote of table 7, since the available data could not constrain them. The fixed values were chosen

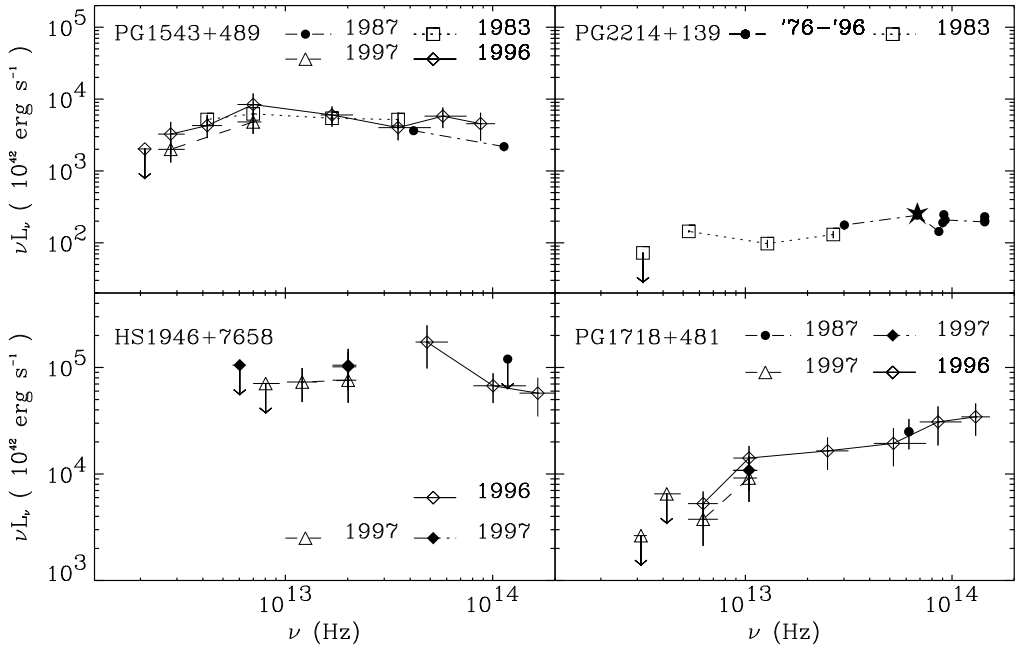

Fig. 3. Continued (3 RQQ, and 1 RIQ).

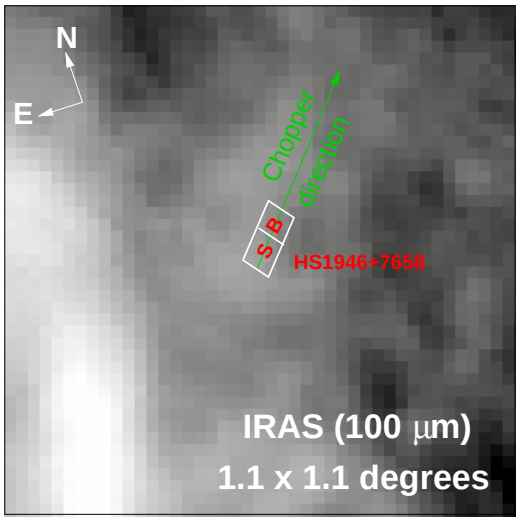

Fig. 4. IRAS observation at 100 μm of a sky region of 1.1×1.1 degrees around the source HS 1946+7658, whose position is indicated by S. The sky region where the background was measured is indicated by B. The white polygon represents approximatively the region observed by the C200 camera. The solid line indicates the chopper direction ∼41° to the West of North.

in the range of values that provided reasonable spectra with properties similar to those observed in other sources. Model *a* in Table 7 corresponds to equation (2). It was applied for modeling core spectra of PG 1216+069, and 3C 405. The same model without the cut off (*b*) was applied for modeling weak core spectra for which the high energy cut off was not constrained (3C 47, PG 1004+130, 4C 61.20, PG 1048−090, PG 1100+772, PG 1103−006, and PG 1718+481). A simple power law model (*c*) was used to fit the radio emission from the lobes of SSRQ and RG (3C 47, PKS 0408−65, PG 1004+130, 4C 61.20, PG 1048−090, PG 1100+772, PG 1103−006, B2 1721+34, 3C 405 and PG 2308+098) and the radio emission of RQQ (PG 1543+489, and PG 2214+139). Simultaneous observations available in the literature generally do not provide wide or well-sampled wavelength coverage, so all available data were used in the fits to the SEDs. The data and analysis are adequate for the central purpose of estimating the contribution of the non-thermal component to the IR emission. The model *d*, corresponding to equation (4), was applied to fit the radio emission of FSRQ (PKS 0135−247, PKS 0637−752, and B2 2201+31A). The value of the break frequency ν_b was arbitrarily fixed to 2.75 GHz, since it provides a good fit to the emitted spectrum of the three objects. In the case of PKS 0637−752 (Low) (see section 4.2.1) the cut off was not included in the model (*e*) since the high frequency part of the spectrum is very steep.

4.2.1. Uncertainties in the radio contribution estimate

The location of the high energy cut off is difficult to establish. Every power law relative to the optically thin emission was extended at higher frequencies until the spectrum turned down, and hence a cut off was required by the data. A spectral cut off was thus required only in five objects (PKS 0135−247, PKS 0637−75, PG 1216+069, 3C 405, and B2 2201+31A), but it could have been located at lower frequencies and present in other objects, too. In most of the cases this parameter does not affect the presence and the strength of the remaining IR flux, but its energy

Table 7. Best fit parameters of non-thermal models

Source Name Source	Model†	α_0	α_1	α_2	ν_t (10^9 Hz)	$\nu_{\rm cut\,off}$ (10^{14} Hz)
3C 47 (Core)	*b*		1.64	−0.45	2.98	
3C 47 (Lobe)	*c*			−0.99		
PKS 0135−247	*d*	−0.78	0.30	−0.80	69.52	2.00
PKS 0408−65	*c*			−1.19		
PKS 0637−752	*d*	−0.60	0.55	−0.78	37.20	4.49
PKS 0637−752 (Low)	*e*	−0.55	0.55	−1.50	75.12	
PKS 0637−752 (High)	*d*	−0.60	0.49	−0.78	41.28	4.22
PG 1004+130 (Core)	*b*		0.53	−0.19	2.00	
PG 1004+130 (Lobe)	*c*			−0.80		
4C 61.20 (Core)	*b*		0.20	−0.15	20.00 (F)	
4C 61.20 (Lobe 1)	*c*			−1.04		
4C 61.20 (Lobe 2)	*c*			−0.93		
PG 1048−090 (Core)	*b*		0.50	−0.65	20.00 (F)	
PG 1048−090 (Lobe)	*c*			−0.84		
PG 1100+772 (Core)	*b*		0.15	−0.80	11.00	
PG 1100+772 (Lobe)	*c*			−0.83		
PG 1103−006 (Core)	*b*		0.30	−0.50	20.00 (F)	
PG 1103−006 (Lobe)	*c*			−0.70		
PG 1216+069	*a*		0.76	−0.09	0.96	20.39
PG 1543+489	*c*			−0.90		
PG 1718+481	*b*		0.58	−0.34	11.45	
B2 1721+34	*c*			−0.69		
3C 405 (Core)	*a*		0.50 (F)	−0.74	126.00 (F)	3.58
3C 405 (Lobe 1)	*c*			−1.26		
3C 405 (Lobe 2)	*c*			−1.30		
B2 2201+31A (Low)	*d*	−0.52	0.60	−0.30	28.60	0.034
B2 2201+31A	*d*	−0.44	0.50	−0.50	34.89	0.24
PG 2214+139	*c*			−0.92		
PG 2308+098	*c*			−0.85		

† Model *a* corresponds to equation (2), and model *b* to the same equation without cut off; model *c* corresponds to a simple power law; model *d* to equation (4), and model *e* to the same equation without cut off.
(F) indicates a fixed value.

value may be important in FSRQ (PKS 0135−247, PKS 0637−75, and B2 2201+31A), since these objects have flat radio spectra for which extrapolation up to IR frequencies is comparable to the IR fluxes. For these sources a more accurate analysis of their radio spectra is needed. Since PKS 0135−247 was not detected in the IR, no further analysis can be performed. We concentrate only on PKS 0637−75 and B2 2201+31A. In order to better constrain the non-thermal radio spectrum, i.e. to find some evidence of a spectral cut off at sub-mm/far-IR frequencies, we searched in the literature for simultaneous observations at these wavelengths, and we selected those that showed the flattest and the steepest spectrum. For PKS 0637−75 the flattest mm power law, chosen among several simultaneous observations (Tornikoski et al. 1996), was measured on February 15th, 1990 (α(3.0-1.3 mm) = −0.77), and the steepest one was measured on April 4th, 1991 (α(3.0-1.3 mm) = −1.47). The two power laws are reported in Fig. 2b with a dashed, and a dashed-dotted line, respectively, plus displayed separately with flattest (Fig. 2c) and steepest (Fig 2d) spectral fits. The flattest spectrum overlaps the observed IR spectrum, leaving no additional IR component. On the contrary, the extrapolation of the steepest spectrum to IR frequencies is clearly below the observed IR spectrum, but the IR observations were not simultaneous to the mm observations. The source was observed by IRAS in 1983, and by ISO at different wavelengths in 1997. During the elapsed time the source became fainter in the far-IR, while shorter wavelength data from the two diferent epochs are consistent. In the following we will suppose that a thermal IR component is present, but dominating only at λ <60 μm, and we will analyze its properties and compare them with those observed in other sources.

For B2 2201+31A the flattest mm power law (α(1.0-0.87 mm) = −0.09) was measured on February 1989 (Chini et al. 1989), and the steepest one was measured on September 14th, 1993 (α(2.0-1.3-1.1 mm) = −0.72). The two power laws are reported in Fig. 2e with a dashed,

and a dashed-dotted line, respectively. The spectrum is in both cases quite flat, however the extrapolation of the 1993 spectrum lies below the IR spectrum. More than the sub-mm data, the analysis of the emission at shorter wavelengths gives important indications on the origin of the IR emission. B2 2201+31A was observed on September 15th, 1993 also in the near-IR (simultaneous sub-mm and near-IR data are indicated by large open circles in Fig. 2e). The near-IR data are above the extrapolation of the sub-mm data, suggesting the presence of two different spectral components in these two wavelength ranges (see the analogous case of 3C 273 in Robson et al. (1986)). This hypothesis is also suggested by the constant emission observed up to 60 μm. A non-thermal source is expected to vary more at higher frequencies, due to greater energy losses. All these considerations suggest the short wavelength continuum is dominated by a thermal component. As in the case of PKS 0637−75 we will suppose that an additional IR thermal component is present at $\lambda \leq 60$ μm.

These two sources (PKS 0637−752, and B2 2201+31A) are good examples of how variability can create an artificial IR spectral turnover, or hide a real one. An IR spectral turnover may be due to different luminosity states of the source at different epochs, instead of to the presence of a separate IR component. The weakness of the radio emission in RQQ precludes that its extrapolation could account for the IR emission for all reasonable assumptions on the radio variability. In SSRQ the extrapolation of the radio component in the IR is usually too faint to explain the IR emission, even if we take into account variability. The variability factors observed in two SSRQ in our sample, 3C 47 and PG 1004+130, are too small to explain the much higher IR fluxes, and this is probably true for the SSRQ in general. In the mm domain we measured a flux variation from the core of the SSRQ 3C 47 of a factor of ~ 2 in almost three years (the emitted flux density at ~ 100 GHz was equal to 16.3±0.9 mJy on September 1995 (van Bemmel et al. 1998), and equal to 30.8±0.6 mJy on July 1998 (this work)). The SSRQ PG 1004+130 was observed twice at 6 cm, in 1982 and in 1984, with a flux variation of a factor ∼2.5, from 12 mJy to 30 mJy (Lister et al. 1994).

In conclusion, the radio models shown in Fig. 2 indicate the presence of an additional IR component in almost the whole sample. According to the third test, this result indicates that the observed IR emission is of thermal origin. The properties of the IR emission in quasars will be derived and analyzed in section 4.3, after subtraction of the non-thermal contribution extrapolated from the radio domain.

4.3. Modeling of the IR component

The IR emission can be accounted for by reradiation of the central luminosity by gas and dust in warped discs in the host galaxies of the quasars (Sanders et al. 1989), in the outer edge of the accretion disc and in a torus of molecular gas within a few parsecs of the central energy source (Niemeyer & Biermann 1993; Granato & Danese 1994; Granato et al. 1997; Pier & Krolik 1992, 1993), and/or by starburst emission (Rowan-Robinson 1995). The host galaxy starlight contribution is probably negligible in the far/mid-IR since the host galaxy spectrum largely differs in shape and luminosity from the SED of the selected objects (see Fig. 2). We describe here the main observational properties of the different objects of each class and compare them using a very simple model of thermal emission: the grey body model. This model does not take into account the source geometry (toroidal, warped disc, etc). An isothermal grey body at the temperature T emits at frequency ν a luminosity density given by the following equation (Gear 1988, Weedman 1986):

$$L_{\nu\,\mathrm{em}} = 4\pi^2 r^2 \cdot \mathrm{B}(\nu_{\mathrm{em}}, \mathrm{T}) \cdot (1 - e^{-\tau_{\mathrm{d}}}), \quad (5)$$

where r is the radius of the projected source, B(ν,T) is the Planck function for a blackbody of temperature T, and τ_{d} is the optical depth of the dust. The optical depth can be approximated by a power law of type $\tau_{\mathrm{d}} = (\nu/\nu_0)^{\beta}$, where ν_0 is the frequency at which the dust becomes optically thin, and β is the dust emissivity index. A non-linear least squares fit was used in the fitting procedure, leaving the radius r, the temperature T, and the frequency ν_0 free to vary , while the emissivity exponent β was fixed equal to 1.87 (Polletta & Courvoisier 1999).

The observed IR SEDs are smooth and indicate a wide and probably continuous range of dust temperatures, describable by several grey body components. The best fit grey body models of the observed IR SEDs are shown in Fig. 5. The thick solid line represents the sum of non-thermal and grey body components. Each individual component is represented by a dotted line. The temperature (T) and the size (r) of each grey body component are listed in columns 5–10 of Table 8. It is worth noting that we could fit the observed IR spectra using a different optical depth function (different β, and ν_0 values). The optical depth value is important in a discussion of the source geometry in terms of an extended or compact heating source. In our models the optical depth values derived by the fits are low (<1) in the far/mid-IR, and $\simeq$1 in the near-IR ($\sim 3\mu$m). If the dust becomes optically thin at longer wavelengths, the real source sizes will be smaller than our estimates, and vice versa. Using our optical depth values, the estimated sizes of the observed dust components range between 0.06 pc and 9.0 kpc, and the temperatures between 43 K and 1900 K. The minimum temperature may be due to an absence of dust at large distances (few kpcs) or at low temperature, and/or to starlight heating to the orders of the inferred minima. The maximal temperature is generally explained as a drop in opacity caused by the sublimation of the most refractory grains at temperatures T $\sim$ 2000 K (Sanders et al. 1989). The total luminosi-

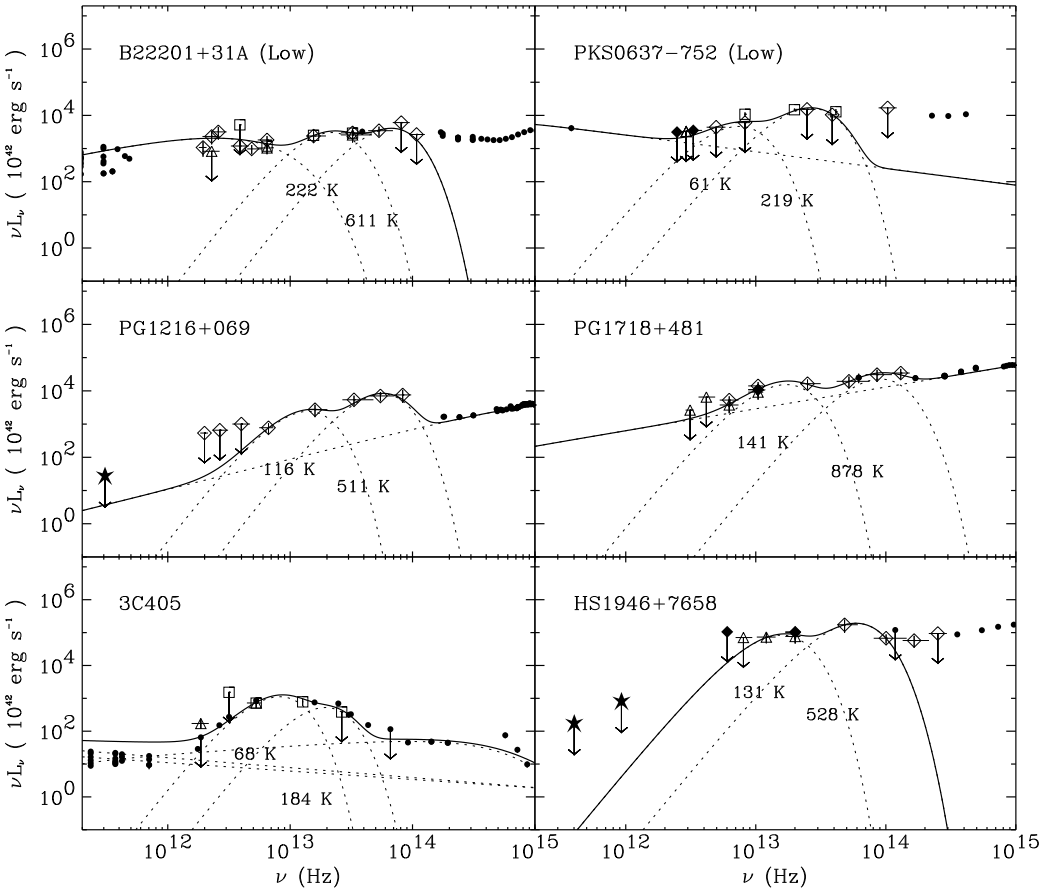

Fig. 5. SEDs as νL_ν versus ν in the rest frame of the objects (2 FSRQ, 2 RIQ, 1 RG, 1 RQQ). Symbols as in Fig. 2. Dotted lines represent the best fit non-thermal models of the radio component and the best fit grey body models of the IR component. The temperature of each grey body component is reported. The sum of all single fitted models is shown by a solid line.

Table 8. Best fit parameters of grey body models

Source Name	Total L(IR)	$\frac{L(60-200\mu m)}{L(3-60\mu m)}$	Log(M_d)	I Component		II Component		III Component	
	(10^{11} $L_\odot$)		($M_\odot$)	T (K)	r (pc)	T (K)	r (pc)	T (K)	r (pc)
3C 47	36.1	0.205	7.55	42.7	7621	208	109		
PKS 0637−752 (Low)	58.6	0.056	6.68	61.0	1923	219	276		
PG 1004+130	11.6	0.040	5.35	92.6	663	421	12		
4C 61.20	29.8	0.086	6.14	86.8	1401				
PG 1100+772	14.1	0.024	5.38	74.9	597	174	49	696	2.16
PG 1103−006	25.3	0.024	5.18	120.0	496			1322	0.33
PG 1216+069	28.8	0.007	4.76	115.8	310	511	8		
PG 1352+183	3.8	0.091	5.26	80.9	556			1584	0.11
PG 1354+213	9.3	0.001				211	23	898	0.98
PG 1435−067	2.8						4	465	
PG 1519+226	3.8	0.097	5.97	50.7	1264	168	41	591	1.34
PG 1543+489	49.9	0.202	7.54	46.0	8997	165	183	561	5.17
PG 1718+481	105.3	0.007	5.06	141.5	573			878	3.60
B2 1721+34	8.6	0.047	5.36	80.0	611	230	32	1800	0.11
HS 1946+7658	761.5	0.006	6.00	130.8	1294	528	37		
3C 405	4.6	0.137	5.79	67.7	1265	184	13		
B2 2201+31A (Low)	19.5	0.002				222	18	611	3.99
PG 2214+139	2.0	0.091	5.22	63.7	540	399	3	1900	0.06
PG 2308+098	11.1						6	569	

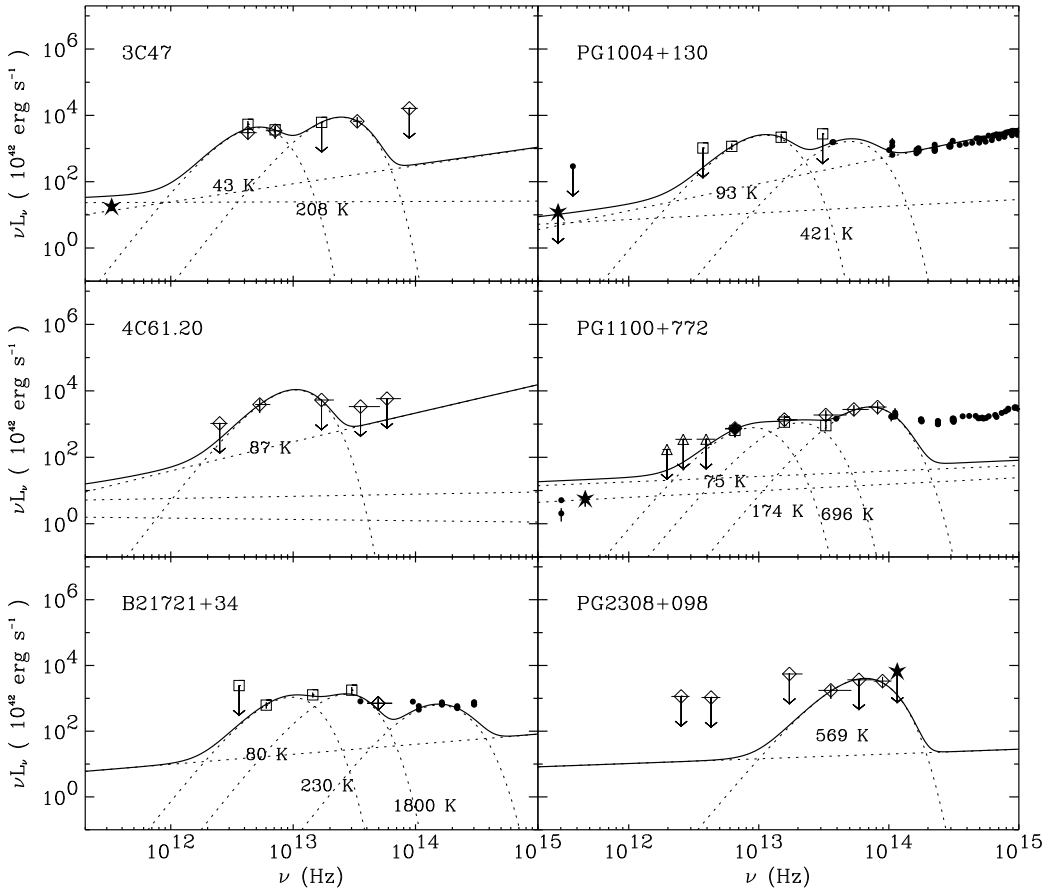

Fig. 5. Continued (6 SSRQ).

ties observed in the IR, obtained by integrating the grey body components (see column 1 in Table 8), vary over a wide range, from $2.0{\cdot}10^{11}$ $L_\odot$ to $7.6{\cdot}10^{13}$ $L_\odot$. No significant difference in the distribution of sizes, temperatures, and luminosities are observed among different types of quasars. We also derive the mass of each dust component at the measured temperature, using the following equation (Hughes et al. 1997):

$$\mathrm{M_d} = \frac{L_{\nu\,\mathrm{em}}}{K_\mathrm{d}(\nu_\mathrm{emis})}\frac{1}{\mathrm{B}(\nu_\mathrm{emis},\mathrm{T})}, \qquad (6)$$

where $K_\mathrm{d}(\nu_\mathrm{emis}) \propto \nu^\beta$, $\beta = 1.87$, is the rest-frequency dust absorption coefficient. The normalization is $K_\mathrm{d}(\nu_\mathrm{emis}) = 10\ \mathrm{cm^2 g^{-1}}$ at 250 μm (Hildebrand 1983), giving $K_\mathrm{d}(\nu) = 1.14\ \mathrm{cm^2\ g^{-1}}$ at 800 μm. The range of assumed values of $K_\mathrm{d}(\nu)$ at 800 μm in the literature is 0.4–3.0 $\mathrm{cm^2\ g^{-1}}$ (Draine & Lee 1984; Mathis & Whiffen 1989). Our dust mass estimates can thus differ by, at most, a factor 2.7. The derived values of dust masses are reported in column 4 of Table 8, and, separately for each class, in Fig. 6. Since the largest dust masses are located in the outer, less illuminated, lower temperature regions of the dust distribution, $\mathrm{M_d}$ is mainly constrained by far-IR data. Therefore, when sub-mm and far-IR data are not available, the real dust mass cannot be well measured. For this reason we did not report the dust and gas masses when the low temperature component was not constrained. The absence of data in the near-IR has a negligible effect on the dust mass estimate. As for the other parameters (T, L(IR), r), the dust mass distribution does not differ significantly among different types of quasars (see Fig. 6).

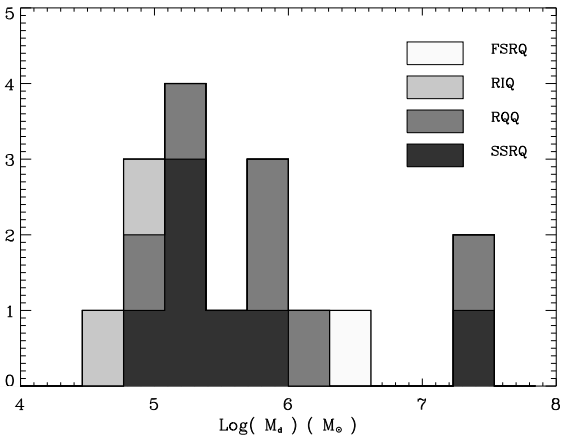

Fig. 6. Histogram of the dust masses for the different classes: RQQ, SSRQ, FSRQ, and RIQ.

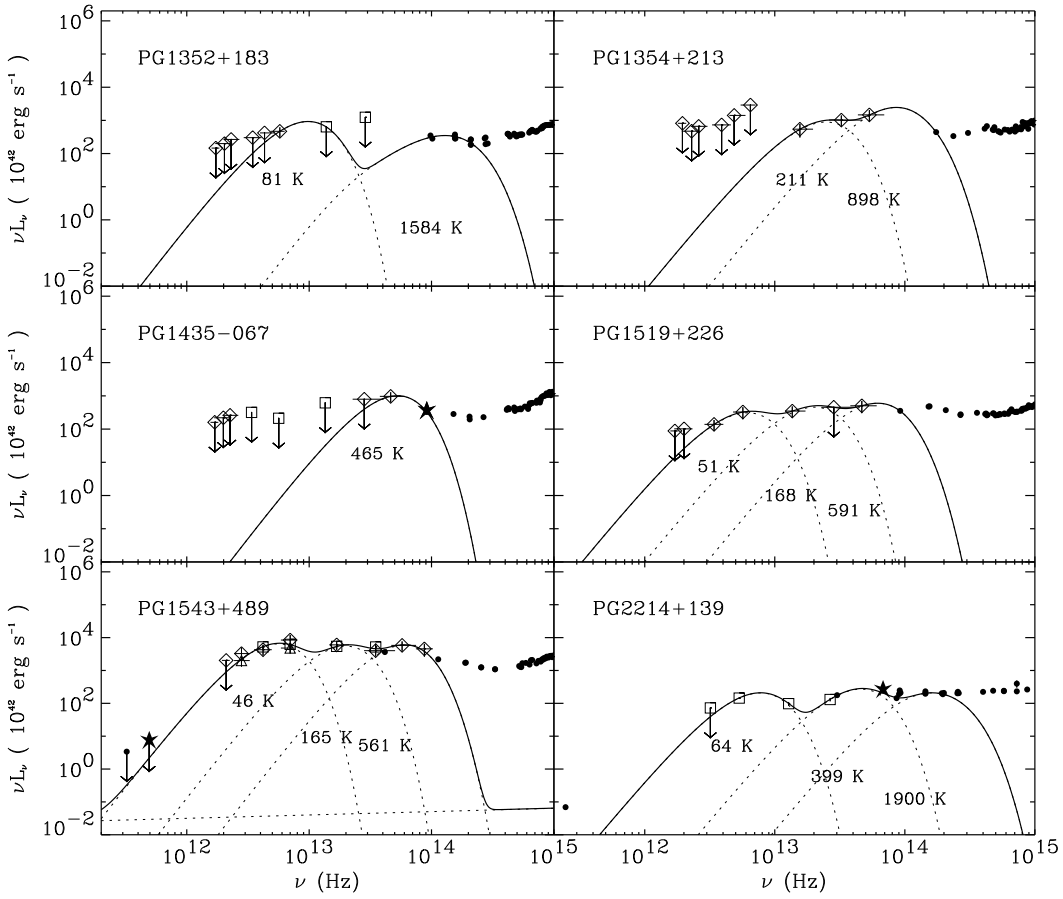

Fig. 5. Continued (6 RQQ).

5. Similarities and differences in the SED of RLQ and RQQ

The present sample contains a range of radio source classifications, with which we can elucidate the dependence of broad-band spectral features on radio properties, thereby testing some unification scenario predictions. The limitations of these tests lie in the sample's relatively small size and heterogeneous nature.

5.1. Average SED

A quick look at the main spectral differences between the different kinds of quasars is provided by the comparison of the average SED of RQQ, RIQ, FSRQ, and SSRQ (including the RG 3C 405). The SEDs are shown in L_ν–ν and νL_ν–ν spaces separately for each class over the radio/soft X-ray frequency range in Fig. 7. The broad spectra of two typical host galaxies (a giant elliptical and a spiral galaxy), in their rest frames and without any normalization, are also plotted in Fig. 7, as in Fig. 2. The average SEDs have been computed using the conventional mean, excluding upper limits. The width of each frequency bin is equal to 0.5 in Log(ν). The reported uncertainties correspond to the standard deviation of the mean of the data per frequency bin. All the data have been connected by straight lines. At soft X-ray energies we indicate the average power law $\pm$ 1σ computed from the distribution of best fit soft X-ray power law models of all objects of the same class (photon index Γ = 2.73$\pm$0.61 (RQQ), 2.39$\pm$0.19 (RIQ), 2.39$\pm$0.23 (SSRQ), and 2.25$\pm$0.12 (FSRQ)).

As expected, the largest difference in luminosity among the different classes appears at radio wavelengths. A smaller difference is observed at soft X-ray energies, and in the near-IR ($\nu > 10^{14}$ Hz corresponding to $\lambda < 3$ μm), while the luminosity and the spectral shape in the mid- and far-IR are remarkably similar (see Fig.7). The large difference in the IR spectral shape between quasars and the host galaxy templates indicates that the contribution from the host galaxy is negligible also at radio and soft X-ray energies, and not only in the far/mid-IR. This result is in agreement with previous studies on the broad SED of quasars (Sanders et al. 1989; Elvis et al. 1994). A quantitative comparison of the luminosity emitted at different frequencies by each quasar class is presented in the next section.

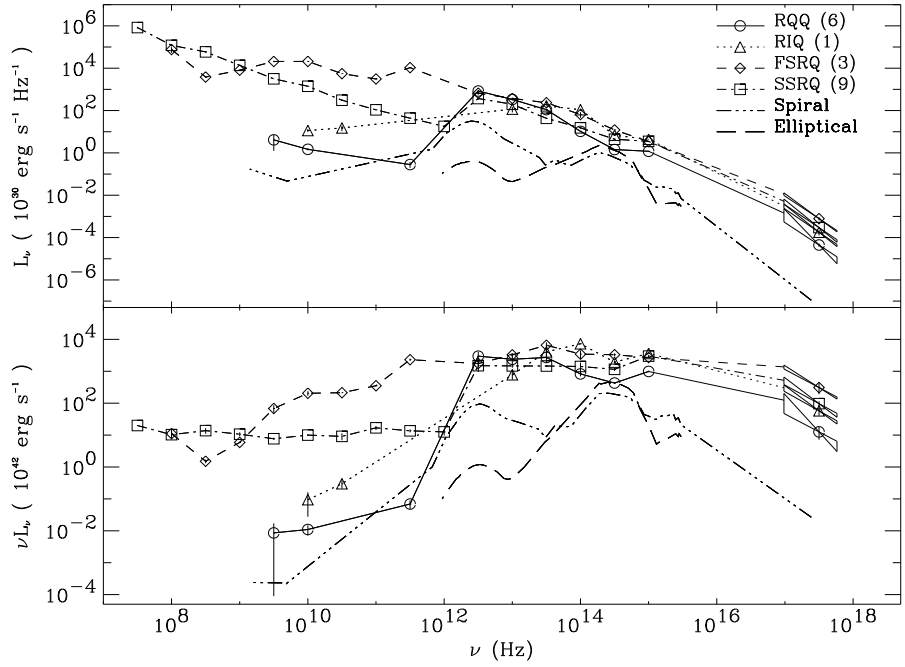

Fig. 7. The average quasar energy distribution for RQQ (solid line), RIQ (dotted line), FSRQ (dashed line), and SSRQ (dash-dot line). The number of objects that were used in each class is reported on the figure with the class name. A symbol is reported for each frequency bin, if at least one data point is available. The two high redshift objects of the sample: HS 1946+7658, and PG 1718+481, were excluded since they are characterized by very high luminosities that modify the average SEDs at a few frequencies producing an irregular spectral shape. Two host galaxy templates are also reported: a typical spiral galaxy (dash-dot-dot-dot line), and a giant elliptical galaxy (long dashed line). No normalization was applied to the reported curves.

5.2. Multi band luminosities

The IR component was also modeled by fitting a parabola in Log L$_\nu$–Log ν space (see Fig. 2). The parabola model gives a rough estimate of the strength and shape of the IR component, even if the spectral coverage is not complete. For several objects upper limits were also used in the fit. This model has by itself no physical meaning, however, it describes the IR component relatively well, it can easily be traced even with poor spectral coverage, and can take into account the whole IR emission of most of the objects in a larger wavelength range than the detailed grey body models. The parabola is too narrow to satisfy the observed IR SED in a few cases, e.g., in 3C 405 and PG 1543+489. In these cases we fitted only the far/mid-IR data where the IR emission usually peaks. The parabola parameters are its width, the frequency of maximum luminosity density ($\nu_{\rm peak}$) and the maximum luminosity density ($L_{\nu_{\rm peak}}$). The parabola fit to the IR component was applied to all objects of the sample, except PKS 0135−247, for which no IR data are available (see Fig. 2a). The distribution of the peak frequencies values ($\nu_{\rm peak}$) observed in the four different classes of objects is reported in Fig. 8. The distribution is quite similar for SSRQ and RQQ, ranging from $2.6{\cdot}10^{12}$ Hz (114 μm) to $3.6{\cdot}10^{13}$ Hz (8 μm), while it is shifted to higher frequencies for FSRQ and RIQ, ranging from $9.0{\cdot}10^{12}$ Hz (33 μm) to $2.8{\cdot}10^{13}$ Hz (11 μm). This difference may be due to the flat radio non-thermal component extending to high frequencies in FSRQ and RIQ, and dominating the dust emission.

We define the IR luminosity L(IR) as the product of the luminosity value at which each parabola peaks and the corresponding frequency ($L(\mathrm{IR}) = \nu_{\rm peak} \cdot L_{\nu_{\rm peak}}$). Note that this parameter does not depend on the width of the parabola. Only upper limits for L(IR) could be derived for PKS 0408−65 and PG 1040−090. The distribution of L(IR) is reported in Fig. 9. In this, and in the following histograms upper limits are shown with arrows, one per object. The similarity in the IR luminosities and spectra (see also Fig. 7) in all quasars suggest a similar origin.

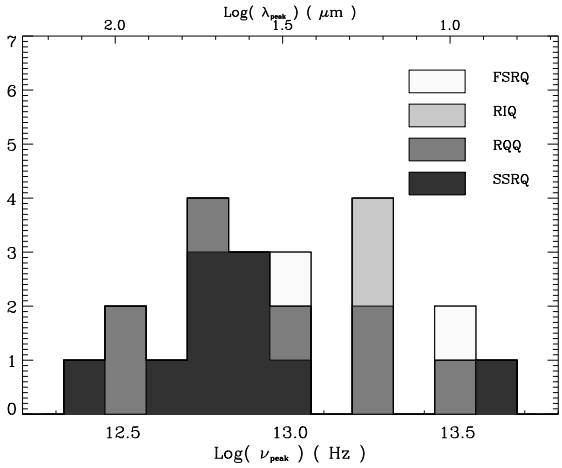

Fig. 8. Histogram of the IR peak frequency of the parabola model for the different classes: RQQ, SSRQ (including the RG 3C 405), FSRQ, and RIQ.

The radio emission in the RLQ arises from two very different spatial scales, the core and extended components. We calculated the average of νL$_\nu$ over the rest-frame interval 5–9 GHz for each spatial component in all of the RLQ, except PG 1354+213 and HS 1946+7658, which were undetected at these frequencies. Fig. 10 displays histograms for the two components separately, and Fig. 11 shows the distribution of the median of all measured νL$_\nu$

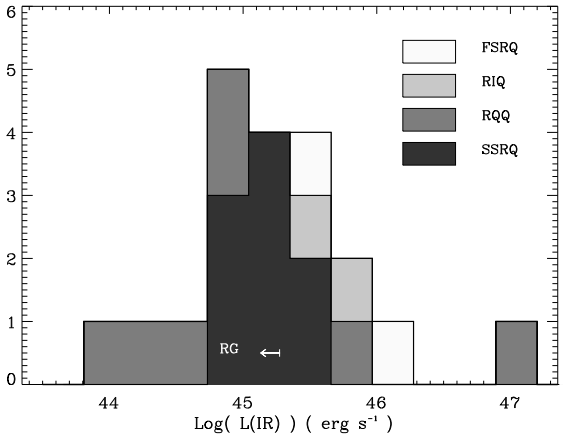

Fig. 9. Histogram of the peak luminosity of the IR parabola model for the different classes: RQQ , SSRQ (including the RG 3C 405 whose position is indicated), FSRQ, and RIQ.

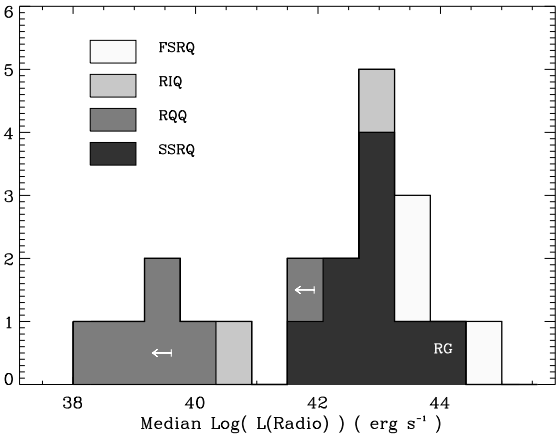

Fig. 11. Histogram of the median radio luminosity for the different classes: RQQ, SSRQ (including the RG 3C 405 whose position is indicated), FSRQ, and RIQ.

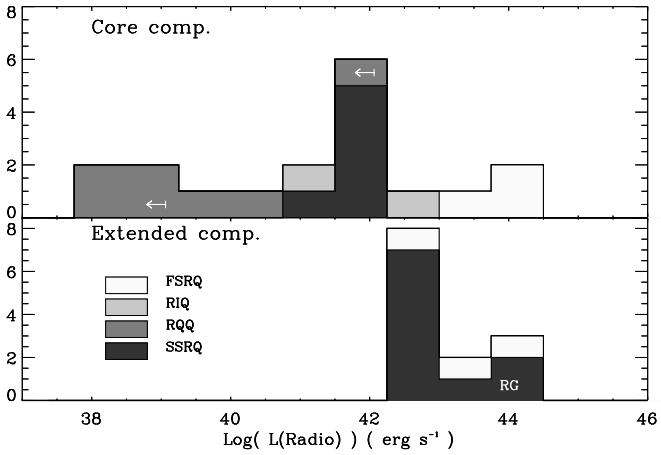

Fig. 10. Histogram of the core and extended components radio luminosity for the different classes: RQQ, SSRQ (including the RG 3C 405 whose position is indicated), FSRQ, and RIQ.

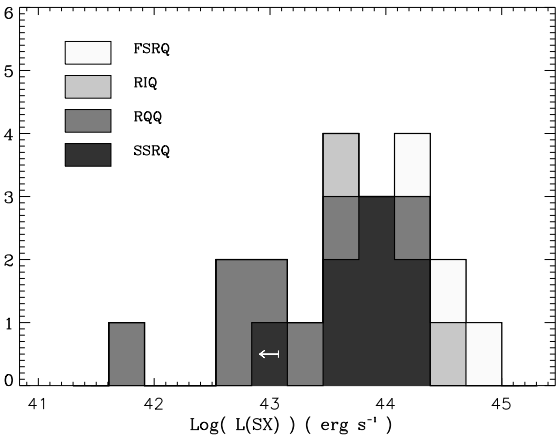

Fig. 12. Histogram of the soft X-ray luminosity at 1 keV for the different classes: RQQ, SSRQ, FSRQ, and RIQ.

over the same frequency range, without component distinction. The distribution of the median radio luminosity is bi-modal (Fig. 11). However, if we consider only core radio luminosities (top panel of Fig. 10), the SSRQ radio luminosity distribution shifts towards lower values, making a continuous distribution, rather than a bi-modal one, but without overlapping. The contribution from the extended components are very similar in FSRQ and SSRQ (bottom panel of Fig. 10). In the following analysis we will consider only the core luminosity L(Radio). When the core luminosity is not available (PKS 0408−65, B2 1721+34, 3C 405, and PG 2308+098), we report an upper limit corresponding to the average radio luminosity relative to the extended component.

In the soft X-ray, we define L(SX) as νL_ν with ν corresponding to 1 keV in the observer's rest-frame. The distribution of L(SX) for each class is reported in Fig. 12. In the soft X-ray, no data are available for 3C 405, and PKS 0408−65, and only an upper limit is available for PG 1004+130.

5.3. Origin of the observed luminosities

The main factors determining the observed luminosities are: the energy emitted by the central engine (AGN); the amplification due to Doppler boosting in a relativistic jet; and the contribution from a starburst. We will estimate the role of each of these parameters in producing the SEDs through the comparison of the observed radio, IR, and soft X-ray luminosities, represented by L(Radio), L(IR) and L(SX), respectively (see section 5.2 for their definition).

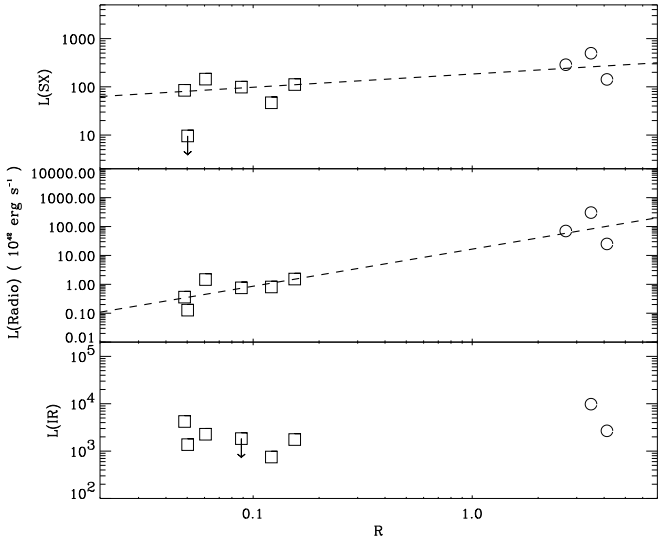

Fig. 13. Luminosity emitted in the soft X-ray, radio and IR domains compared to the parameter R given by the ratio between the radio luminosity of the core and of the extended components. The different symbols correspond to different classes of objects: squares for SSRQ, and circles for FSRQ. The dashed lines are the best fit lines.

5.3.1. Orientation effects in RLQ

The orientation of the beamed emission can be estimated from the radio core fraction R. This quantity, defined as the ratio between the core radio luminosity and the luminosity of the extended radio emission at 5–9 GHz in the rest frame, serves as an orientation indicator of the radio source with respect to the observer, measuring the relative strength of the core component (Hes et al. 1995). The core flux was not available for three SSRQ and one RG, thus the parameter R was not computed. In the case of FSRQ we computed the luminosity of the extended component in the frequency range 5–9 GHz by extrapolating the power law observed at low frequencies (power law index α_0 in Table 7).

The FSRQ are well separated from SSRQ in the distribution of the ratio R (see Fig. 13). This difference permits us to estimate the enhancement factor of the beamed emission after a few considerations. First, the observed radio emission in RLQ is mainly produced by the jet and its core rather than a starburst, since star-emitting ULIRG have much lower radio luminosity than RLQ (Colina & Pérez-Olea 1995). Second, we assume that the radio source is intrinsically identical in FSRQ and SSRQ, and that the difference in their radio emission is due only to the orientation of the beamed emission. After these approximations we can write

$$L(\text{Radio Core})_{\text{FSRQ}} = A \cdot L(\text{Radio Core})_{\text{SSRQ}} \quad (7)$$

where A is the amplification factor of the beamed emission. Since the luminosity of the extended components are the same for the flat and steep radio quasars (see above), using equation (7) we can derive a relation between the parameters R_{FSRQ} and R_{SSRQ}: $R_{\text{FSRQ}} = A \cdot R_{\text{SSRQ}}$. Replacing the observed values of R_{SSRQ} ($\simeq$ 0.05–0.15), and R_{FSRQ} ($\simeq$ 3–4) (see Fig. 13) in the above relation yields $A \simeq 20$–80.

Table 9. Correlation test results for FSRQ and SSRQ

X	Y	N	r_l	P_l (%)
Log(L(IR))	Log(R)	7	0.53	25.
Log(L(Radio))	Log(R)	9	0.94	0.03
Log(L(SX))	Log(R)	8	0.73	6.0

Fig. 13 displays L(Radio), L(SX), and L(IR) versus the core fraction R. Linear correlation results for these relations are reported in Table 9, where the parameter pairs are reported in the first two columns, the number of data pairs in the third, in column 4 the linear correlation rank (r_l), and in column 5 the associated probability to have such a correlation rank from uncorrelated values (P_l).

Higher radio and soft X-ray luminosities are observed in objects with higher values of the radio core fraction R (when the jet points towards us). The orientation effect is more important in the radio domain, as shown by the stronger correlation, than in the soft X-ray, and negligible in the IR. This implies that the radio core and a fraction of the total emitted soft X-ray luminosities are emitted anisotropically. We furthermore verified that R is not correlated with the redshift and thus that the above result is not an artifact of distance related biases in the measurement of R.

Assuming that the soft X-ray source is intrinsically identical in FSRQ and SSRQ, the observed difference in L(SX) arises from the orientation of the fraction, f, that is beamed. If the fraction of emitted radiation that is beamed is enhanced by a factor A, identical to that of the radio emission, the following relation between the soft X-ray luminosity in FSRQ and that in SSRQ will be valid:

$$L(\text{SX})_{\text{FSRQ}} = A \cdot f \cdot L(\text{SX})_{\text{SSRQ}} + (1-f) \cdot L(\text{SX})_{\text{SSRQ}}. \quad (8)$$

Using the average value of the ratio $L(\text{SX})_{\text{FSRQ}}/L(\text{SX})_{\text{SSRQ}}$ that is $\approx$ 3.2 $\pm$ 2.2, and the range of values obtained for the factor A, we derive a fraction $f \approx$ 3–12% for the beamed fraction of the soft X-ray component.

5.3.2. SSRQ *versus* RQQ

The radio and the soft X-ray luminosities are mainly produced by the AGN component (see sections 5.1 and 5.3.1). The comparison between the luminosities emitted in the radio and soft X-ray domains is then equivalent to a comparison of the AGN power in the two types of quasars. The radio core emission of SSRQ is on average 200 times higher

than that of RQQ (see Fig. 10) and the soft X-ray luminosity is on average 8 times higher in SSRQ than in RQQ (see Fig. 12). Since the SSRQ show luminosities higher than RQQ not only at radio and soft X-ray energies, but also in the hard X-ray domain (Lawson & Turner 1997), we argue that the bolometric AGN luminosity is much higher in SSRQ than in RQQ. The difference in the AGN power should be observable at all frequencies where the AGN emission dominates. We have already pointed out the similarity in IR luminosities and spectra of SSRQ and RQQ (see Figs. 7 and 9). This similarity suggests that the origin of the dominant IR component is not AGN-related. The candidate is then a starburst.

Some indication of the dominant IR emission mechanism can be gleaned from the shape of the SED. An AGN can emit a significant fraction, often a majority, of its infrared luminosity at shorter wavelengths, $\lambda < 60\mu$m, as long as the obscuring columns are not so large as to be optically thick at these wavelengths. Starburst dominated galaxies, on the other hand, produce the bulk of their infrared emission at $\lambda > 60\mu$m. The ratio of the luminosities in these two wavelength regimes, L(60-200μm)/L(3-60μm), thus provides a rough estimate of the primary driver of the infrared component. A histogram of this ratio is presented in Fig. 14, in which only the sources having at least two grey body components with T < 1000 K are included. For comparison, the luminosity ratio from an average SED of low reddening starburst galaxies (Schmitt et al. 1997) is also indicated. All of the AGN in the sample have infrared luminosity ratios less than the starburst fiducial value (=0.76) by a factor or four or more (the maximum ratio is 0.20 corresponding to 27% of starburst contribution), suggesting that the infrared in these sources is dominated by the central engine. The RQQ and SSRQ have similar average ratios, 8% of the total IR emission is produced by a starburst.

Since the dominant IR source is the AGN, which differs in SSRQ and RQQ, other factors have to be taken into account to explain the similarity of their IR luminosities and average spectra. These factors can be the dust covering factor, its amount and geometric distribution. A higher dust covering factor in RQQ, due to larger total dust mass and/or a particular geometric distribution, may account for the similar IR radiation. Aspects of this hypothesis are attractive, since the presence of more circumnuclear material may be related to the physical conditions that hinder the jet formation and/or development in RQQ. However, if larger dust covering factors were present in RQQ, a higher probability to observe a RQQ through optically thick dust would be expected and a large fraction of RQQ with absorption features in the soft X-ray would be observed. Observations do not support these predictions (see section 2). Moreover, the similarity in the observed IR luminosities and spectra requires a fine tuning between the dust heating source, the dust amount and its geometric distribution, which makes this explanation improbable. We propose another scenario in which the dust properties (amount and distribution) and the heating source are similar in SSRQ and RQQ. The dust distribution contributing in the far-IR probably extends from the more external regions of the AGN, and is predominantly heated by the optical and UV radiation fields filling these external regions which are similar in both classes. At relatively large distances from the centre, the AGN components are similar in both types of quasars, towards the innermost regions, where the soft X-rays are emitted and a jet is formed, SSRQ and RQQ become different. The high energy photons escape from the centre without significant dust absorption and provide an important probe of the central radiation source. Observations indicate that the soft X-ray radiation is higher in SSRQ (see Fig. 7) in agreement with the proposed scenario.

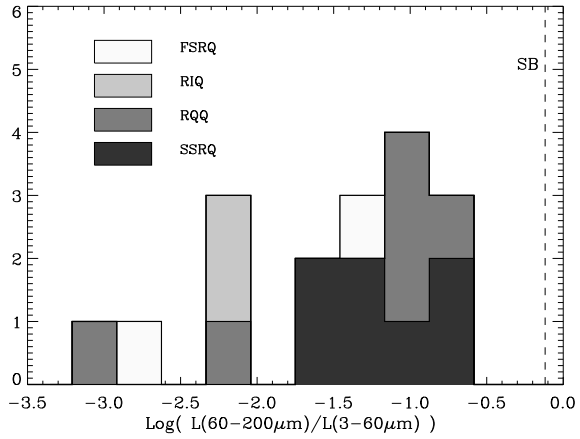

Fig. 14. Histogram of the ratio L(60-200μm)/L(3-60μm) for the different classes: RQQ, SSRQ, FSRQ, and RIQ. The dashed line represents the value derived from the average SED of a sample of low reddening starburst galaxies.

From this analysis it is suggested that the main difference between RQQ, and SSRQ takes place in the innermost nuclear regions where the emitted power is higher in SSRQ than in RQQ, while the AGN external regions (dust distribution and optical/UV source) have similar properties in both types of quasars.

Since FSRQ and SSRQ show similar properties in the IR, once the non-thermal contribution is subtracted, this conclusion can be also extended to FSRQ.

6. Conclusions

Continuum observations from radio to soft X-ray energies have been presented for a sample of 22 quasars characterized by different degrees of radio emission. The IR data were obtained with ISOPHOT and IRAC1, and the mm data with IRAM, SEST and SCUBA. Further IR and mm data, and some radio and soft X-ray fluxes, were drawn from the literature. The availability of a broad band SED

for several types of quasars allows us to separate the dominant spectral components in the radio and IR energy bands, and thus to compare their spectral properties in different types of quasars. The spectral analysis and the comparison of luminosities emitted in the radio, IR, and soft X-ray energy bands yields the following results:

1. *What is the dominant mechanisms emitting at IR energies in RLQ and RQQ?*
   In our quasar sample the dominant mechanism emitting in the far/mid-IR is thermal emission from dust heated by the optical and UV radiation produced in the outer regions of the AGN. A starburst contributes to the IR emission at different levels, but always less than the AGN ($\leq$27%). The presence of thermal IR emission in FSRQ remains rather uncertain. Among the three FSRQ of the sample we cannot derive any conclusion for two of them, and for a third one (B2 2201+31A) the observed data suggest a dominant thermal component at $\lambda \leq 60\,\mu$m.
2. *Do RLQ and RQQ have the same dust properties (temperature, source size, mass, and luminosity)?*
   The equilibrium temperature of dust grains, the size and the mass of the dust distribution, and the emitted luminosity have been evaluated for all quasars. The estimated sizes of the observed dust components lie between 0.06 pc and 9.0 kpc, and the temperatures between 43 K and 1900 K. The total luminosity observed in the IR, obtained by integrating the grey body components, varies over a wide range: 2–760$\cdot 10^{11}$ $L_\odot$. The amount of emitting dust in all types of quasars also varies in a broad range: $6\cdot 10^4$–$4\cdot 10^7$ $M_\odot$. The distribution of any of these parameters does not differ significantly among the different types of quasars.
3. *Does an interplay between the radio and the IR components exist?*
   A bright and flat non-thermal component can be sufficiently strong in the IR to mask the dust emission in some sources, particularly FSRQ. However, this does not mean that the dust emission is absent. After subtracting an IR synchrotron component extrapolated from the radio, the residual IR emission had similar spectral shape and luminosity, regardless of the radio properties.

These results are based on the analysis of a small sample, and have to be confirmed by the study of larger samples. ISOPHOT has doubled the number of quasars with IR detections in the sample presented here. A great deal of additional progress on understanding the IR properties of quasars is expected when all of the quasar data available in the ISO archive will be fully analyzed and studied.

Acknowledgements. We are grateful to D. Carrillo, S. Paltani, and R. Walter for preparing the observation program of ISOPHOT Chopper Observations. We thank the Time Allocation Committee for awarding discretionary ISO observing time to this project. Martin Haas, and Péter Ábrahám are acknowledged for help in the ISOPHOT data reduction. R. Neri, and D. Nuernberger are acknowledged for assistance with the IRAM interferometer data reduction. BJW and EJH were supported in this project by NASA grant NAGW-3134. This research has made use of NASA's Astrophysics Data System Abstract Service, as well as the NASA/IPAC Extragalactic Database (NED) which is operated by the Jet Propulsion Laboratory, California Institute of Technology, under contract with the National Aeronautics and Space Administration.

References

Andreani P., Franceschini A., Granato G. 1999, MNRAS, 306, 161
Antonucci R., Barvainis R., Alloin D. 1990, ApJ, 353, 416
Barthel P.D. 1989, ApJ, 336, 606
Barvainis R. 1987, ApJ, 320, 537
Barvainis R. 1997, in Proc. of ESA/IAC Conference *Quasar Host*, eds. D. Clements & I. Perez-Fournon (Springer-Verlag, Berlin)
Barvainis R., Antonucci R. 1989, ApJS, 70, 257
Barvainis R., Antonucci R., Coleman P. 1992, ApJL, 399, 19
Barvainis R., Lonsdale C., Antonucci R. 1996, AJ, 111, 1431
Becker R.H., White R.L., Edwards A.L. 1991, ApJS, 75, 1
van Bemmel I.M., Barthel P.D., Yun M.S. 1998, A&A, 334, 799
Bloom S.D., Marscher A.P., Moore E.M. et al. 1999, ApJS, 122, 1
Blundell K.M., Beasley A.J. 1998, MNRAS, 299, 165
Brinkmann W., Yuan W., Siebert J. 1997, A&A, 319, 413
Chini R., Biermann P.L., Kreysa E., Gemünd H.-P. 1989, A&A, 221, L3
Colina L., Pérez-Olea D. 1995, MNRAS, 277, 845
Donea A.-C., Biermann P.L. 1996, A&A, 316, 43
Draine B.T., Lee H.M. 1984, ApJ, 285, 89
Edelson R.A., Malkan M.A. 1987, ApJ, 323, 516
Elvis M., Wilkes B.J., McDowell et al. 1994, ApJS, 95, 1
Ennis D.J., Neugebauer G., Werner M. 1982, ApJ, 262, 460
Falcke H., Biermann P.L. 1995, A&A, 293, 665
Falcke H., Malkan M., Biermann P.L. 1995, A&A, 298, 375
Falcke H., Sherwood W., Patnaik A.R. 1996, ApJ, 471, 106
Francis P.J., Hooper E.J., Impey C.D. 1993, AJ, 106, 417
Gabriel C., Acosta-Pulido J., Heinrichsen I., Skaley D. et al. 1997, *The ISOPHOT Interactive Analysis PIA, a calibration and scientific analysis tool* in Proc. of the ADASS VI Conference, ASP Conf. Ser., Vol. 125, eds. G. Hunt & H.E. Payne
Gear W.K. 1988, *Millimetre and Submillimetre Astronomy*, eds. R. D. Wolstencroft & W. B. Burton, (Kluwer Academic Publishers, The Netherlands)
Gezari D.Y., Pitts P.S., Schmitz M. 1997. Catalog of Infrared Observations, 4th Edition, Unpublished.
Ghosh T., Gopal-Krishna Rao, A.P. 1994, A&AS, 106, 29
Granato G.L., Danese L. 1994, MNRAS, 268, 235
Granato G.L., Danese L., Franceschini A. 1997, ApJ, 486, 147
Gregory P.C., Condon J.J. 1991, ApJS, 75, 1011
Guilloteau S., Delannoy J., Downes D. et al. 1992, A&A, 262, 624
Haas M., Chini R., Meisenheimer K. et al., 1998, ApJ, 503, L109

Heckman T.M., Chambers K.C., Postman M. 1992, ApJ, 391, 39
Hes R., Barthel P.D., Hoekstra H.1995, A&A, 303, 8
Hildebrand R.H. 1983, QJRAS, 24, 267
Hoekstra H., Barthel P.D., Hes R. 1997, A&A, 319, 757
Holland W.S., Robson E.I., Gear W.K. et al. 1999, MNRAS, 303, 659
Hughes D. H., Robson E. I., Dunlop J. S., Gear, W. K. 1993, MNRAS, 263, 607
Hughes D.H., Dunlop J.S., Rawlings S. 1997, MNRAS, 289, 766
Immler S., Pietsch W., Aschenbach B. 1998, A&A, 331, 601
Kapahi V.K. 1995, JApA, 16, 1
Kellermann K.I., Sramek R., Schmidt M. et al. 1989, AJ, 98, 1195
Kessler M.F., Steinz J.A., Anderegg M.E. et al. 1996, A&A, 315, L27
Klaas U., Laureijs R. J., Radovich M. Schulz B. 1998, Report on the ISOPHOT Calibration Accuracies, ISO Science Op. Center Report (SAI/98-092/Dc)
Kobayashi Y., Sato S., Yamashita T. et al. 1993, ApJ, 404, 94
de Kool M., Begelman M.C. 1989, Nat., 338, 484
Kuhn O., Bechtold J., Cutri R. et al. 1995, ApJ, 438, 643
Kühr H., Witzel A., Pauliny-Toth I.I.K., Nauber U. 1981, A&AS, 45, 367
Kukula M.J., Dunlop J.S., Hughes D.H., Rawlings S. 1998, MNRAS, 297, 366
Laureijs R.J. 1999, ISOPHOT Report: Point spread function fractions to the ISOPHOT C100 and C200 arrays (Version 1.0, 29/June/99)
Laureijs R.J., Klass U., Richards P.J., Schulz B. 1998, ISOPHOT Data Users Manual Version 4.0, SAI/95-220/Dc
Lawrence A., Rowan-Robinson M., Efstathiou A. et al. 1991, MNRAS, 248, 91
Lawson A.J., Turner J.L. 1997, MNRAS, 288, 920
Lemke D., Klaas U., Abolins J. et al. 1996, A&A, 315, L64
Lister M.L, Gower A.C., Hutchings J.B. 1994, AJ, 108, 821
Lonsdale C.J., Morison I. 1983, MNRAS, 203, 833
Mathis J.S., Whiffen G. 1989, ApJ, 341, 808
McLeod K.K., Rieke G.H. 1994, ApJ, 431, 137
Miller P., Rawlings S., Saunders R. 1993, MNRAS, 263, 425
Mitchell K.J., Dennison B., Condon J.J. et al. 1994, ApJS, 93, 441
Neugebauer G., Oke J.B., Becklin E.E., Matthews K. 1979, ApJ, 230, 79
Neugebauer G., Miley G.K., Soifer B.T., Clegg P.E. 1986, ApJ, 308, 815
Neugebauer G., Green R.F., Matthews K. et al. 1987, ApJS, 63, 615
Niemeyer M., Biermann P.L. 1993, A&A, 279, 393
Pier E., Krolik J.H. 1992, ApJ, 401, 99
Pier E., Krolik J.H. 1993, ApJ, 418, 673
Polletta M., Courvoisier T.J.-L. 1999, A&A, 350, 765
Reid A., Shone D.L., Akujor C.E. et al. 1995, A&AS, 110, 213
Robson E.I., Gear W.K., Brown L.M.J. et al. 1986, Nat., 323, 134
Robson E.I., Leeuw L.L., Stevens J.A., Holland W.S. 1998, MNRAS, 301, 935
Rowan-Robinson M. 1995, MNRAS, 272, 737
Sanders D.B. 1999, in Proc. of the The Ringberg Workshop, *Ultraluminous Galaxies: Monsters or Babies* (Ringberg Castle, Sept, 1998)
Sanders D.B., Phinney E.S., Neugebauer G. et al. 1989, ApJ, 347, 29
Sanders D.B., Scoville N.Z., Soifer B.T. 1991, ApJ, 370, 158
Schartel N., Walter R., Fink H.H., Trümper J. 1996, A&A, 307, 33
Schlickeiser R., Biermann P.L., Crusius-Wätzel A. 1991, A&A, 247, 283
Schmitt H.R., Kinney A.L., Calzetti D., Storchi Bergmann T. 1997, AJ, 114, 592
Scoville N.Z., Padin S., Sanders D.B. et al. 1993, ApJ, 415, L75
Siebert J., Brinkmann W., Drinkwater M.J., Yuan W. et al. 1998, MNRAS, 301, 261
Silva L., Granato G.G., Bressan A., Danese L. 1998, ApJ, 509, 103
Sodroski T.J., Bennett C., Boggess N. et al. 1994, ApJ, 428, 638
Sopp H.M., Alexander P. 1991, MNRAS, 251, Short Comm., 14P
Steppe H., Paubert G., Sievers A. et al. 1993, A&AS, 102, 611
Sun W.-H., Malkan M.A. 1989, ApJ, 346, 68
Tanner A.M., Bechtold J., Walker C.E., Black J.H. 1996, AJ, 112, 62
Taylor J.R. 1982, *An introduction to Error Analysis, The Study of Uncertainties in Physical Measurements*, University Science Books
Taylor G.L., Dunlop J.S., Hughes D.H., Robson E.I. 1996, MNRAS, 283, 930
Teräsranta H., Tornikoski M., Valtaoja E. et al. 1992, A&AS, 94, 121
Terlevich R., Tenorio-Tagle G., Franco J., Melnick J. 1992, MNRAS, 255, 713
Tornikoski M., Valtaoja E., Teräsranta H. et al. 1996, A&AS, 116, 157
Urry C.M., Padovani P. 1995, PASP, 107, 803
Véron-Cetty M.-P., Véron P. A catalogue of Quasars and Active Nuclei (8th Edition), European Southern Observatory Scientific Report, N. 18 - June 1998
Wang T., Brinkmann W., Bergeron J. 1996, A&A, 309, 81
Wang J., Cen X., Xu J., Qian T. 1997, ApJ, 491, 501
Weedman D.W. 1986, *Quasar Astronomy*, Cambridge University Press
White R.L., Becker R.H., 1992, ApJS, 79, 331
Wilkes B.J., Elvis M. 1987, ApJ, 323, 243
Wilkes B.J., Tananbaum H., Worral D.M. et al. 1994, ApJS, 92, 53
Wilkes B.J., Hooper E.J., McLeod K.K. et al. 1999, in Proc. of ESA/SP-427 Conference *The Universe as seen by ISO*, eds. P. Cox & M.F. Kessler (ESA Pubblications Division, The Netherlands)
Wilson A.S., Colbert E.J.M. 1995, ApJ, 438, 62
Yuan W., Brinkmann W., Siebert J., Voges W. 1998, A&A, 330, 108

Part II

The HST project

Chapter 7

The Hubble Space Telescope

The Hubble Space Telescope is a cooperative program of the European Space Agency (ESA) and NASA. HST is an observatory first dreamt of in the 1940s, designed and built in the 1970s and 80s, and operational only in the 1990s. HST is a 2.4-metre reflecting telescope which was deployed in low-Earth orbit (600 kilometres) on 25 April 1990. On-orbit servicing is applied to maintain HST for its 15- year design life.

After the launch of HST in 1990 a spherical aberration was discovered. The effects of spherical aberration were fully obviated installing the Corrective Optics Space Telescope Axial Replacement (COSTAR) on December 1993. The functionality of HST was then fully restored.

HST's current complement of science instruments include three cameras, two spectrographs, and fine guidance sensors (primarily used for astrometric observations). As shown in Figure 7.1, HST's Scientific Instruments (the Wide Field Planetary Camera 2, the Faint Object Camera, the Near Infrared Camera and Multi-Object Spectrometer, and the Space Telescope Imaging Spectrograph) are mounted in bays behind the primary mirror. HST receives electrical power from two solar arrays, which are turned (and the spacecraft rolled about its optical axis) so that the panels face the incident sunlight. Two high-gain antennas provide communications with the ground (via the Tracking and Data Relay Satellite System).

The coordinate system that is fixed to the telescope consists of three orthogonal axes: V1, V2, and V3. V1 lies along the optical axis, V2 is parallel to the solar-array rotation axis, and V3 is perpendicular to the solar-array axis. The roll angle is defined as the angle about the V1 axis between a given orientation and nominal orientation.

Table 7.1 gives a summary of the current optical performance of the instruments on board HST.

Each orbit lasts about 95 minutes, with time allocated for housekeeping functions and for observations. Housekeeping functions include turning the telescope to acquire a new target, or avoid the Sun or Moon, switching communications antennas and data transmission modes, receiving command loads and downlinking data, calibrating and similar activities.

When possible two scientific instruments are used simultaneously to observe adjacent target regions of the sky. During observations the Fine Guidance Sensors (FGS) track their respective guide stars to keep the telescope pointed steadily at the right target.

The great potential of the HST is to provide photometrically and geometrically accurate images of astronomical objects over a relatively wide FOV, with high angular resolution across a broad range of wavelengths inaccessible from the ground (ultraviolet and near-infrared).

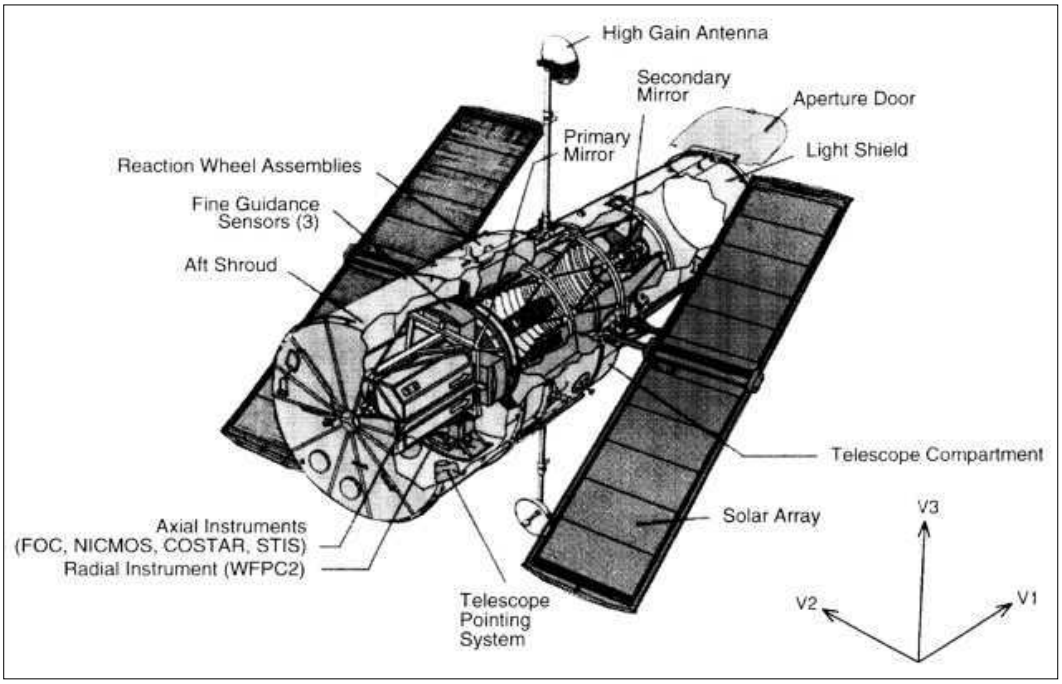

Figure 7.1: The Hubble Space Telescope. Major components are labeled, and definitions of V1,V2,V3 spacecraft axes are indicated.

Table 7.1: HST Optical Characteristics and Performance

Aperture	2.4 m
Wavelength coverage (MgF_2-overcoated aluminum)	1100Å to 2.6 μm
Focal ratio (without COSTAR)	f/24
Plate scale (on axis, without COSTAR)	3.58 arcsec/mm
FWHM of WFPC2 images (at 6328Å)	0.053 arcsec
WFPC2 encircled energy within 0.″1 radius (at 6328Å)	55-65%
FWHM of NICMOS images (at 1.6 μm)[a]	0.14 arcsec
NICMOS encircled energy within 0.″3 radius (at 1.6 μm)[a]	93%

[a] Expected performance.

HST has been and is being devoted to the study of the Solar system, of stars, of the interstellar medium, of stellar populations and systems (globular clusters, the Galaxy Halo, Giant HII regions), of galaxies (nuclear structure, mergers, starbursts, morphology) and clusters, of AGNs (host galaxy, environs, evolution, jets) and of cosmology.

7.1 The Science Instruments

Currently, there are four instruments mounted on HST. Their imaging capabilities are summarized in Table 7.2 and a more detailed description is given in the following sections. In

Table 7.2: HST Instrument Imaging Capabilities

Instrument	Field of View (arcsec)	Projected Pixel Spacing on sky (arcsec)	Wavelength Range (Å)
WFPC2	154×154	0.10	1200 - 11 000
	35×35	0.0455	1200 - 11 000
FOC f/96[1]	14×14	0.014	1150 - 6500
NICMOS	11×11	0.043	8000 - 19 000
	19×11	0.075	8000 - 25 000
	51×19	0.20	8000 - 25 000
STIS	51×51	0.05	2500 - 11 000
	25×25	0.024	1650 - 3100
	25×25	0.024	1150 - 1700

[1] The maximum FOV is $14''\times14''$, at full resolution it is $7''\times7''$.

this work, observations performed with the instruments WFPC2 and NICMOS are presented. Therefore, a description of these instruments only is given in the next sections.

7.1.1 Wide Field Planetary Camera 2

The original Wide Field/Planetary Camera (WF/PC1) (WFPC is pronounced "wiff-pik") was changed out and displaced by WFPC2 in December 1993. WFPC2, developed in 1985 by the Jet Propulsion Laboratory in Pasadena (California) contains internal optics to correct the spherical aberration.

The WFPC2 is designed to provide digital imaging over a wide field of view (FOV). It has three "wide-field" charge-coupled devices (CCDs), and one high-resolution (or "planetary") CCD. Each CCD covers 800×800 pixels and is sensitive from 1200 to 11,000Å. All four CCDs are exposed simultaneously, with the target of interest being placed as desired within the FOV. The three Wide Field Camera (WFC) CCDs are arranged in an "L"-shaped FOV whose long side projects to $2\farcs5$, with a projected pixel size of $0\farcs10$. The Planetary Camera (PC) CCD has a FOV of $34''\times34''$, and a projected pixel size of $0\farcs046$. The four cameras, or chips, are called PC1, WF2, WF3, and WF4. Their FOV is illustrated in Figure 7.2.

A variety of filters may be inserted into the optical path. Polarimetry may be performed by placing a polarizer into the beam.

Spectral Filters

The WFPC2 contains 48 filters mounted in 12 wheels of the Selectable Optical Filter Assembly (SOFA). These include a set of broad band filters approximating Johnson-Cousins UBVRI, as well as a set of wide U, B, V, and R filters, and a set of medium bandwidth Strömgren u, v, b, and y filters. Narrow band filters include those for emission lines of Ne V (3426Å), CN (3900Å), [OIII] (4363Å and 5007Å), He II (4686Å), (4861Å), He I (5876Å), [OI] (6300Å), H_α(6563Å), [NII] (6583Å), [SII] (6716Å and 6731Å), and [SIII] (9531Å).

In Figure 7.3 seven curves are shown corresponding to U, B, y, V, R and I filters and one centred on the H_α line. The reported filters correspond to those used in this work.

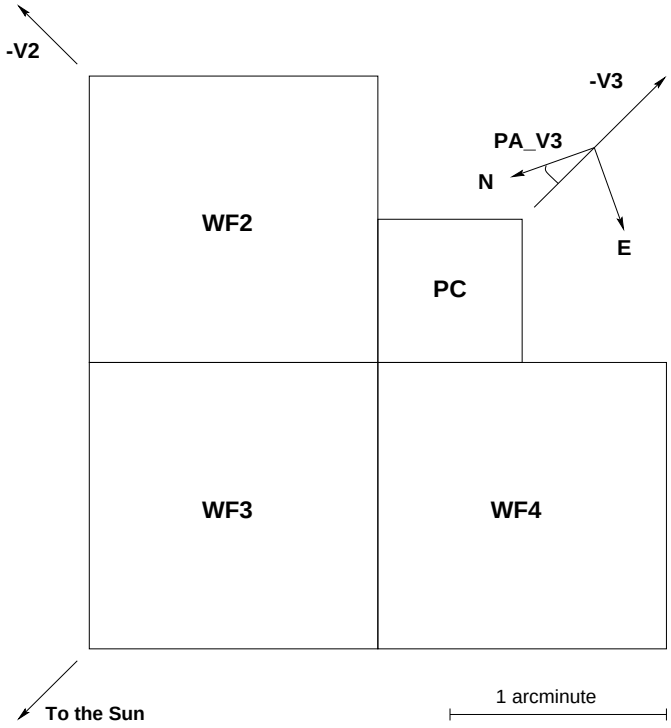

Figure 7.2: WFPC2 Field-of-View Projected on the Sky. The position angle of V3 varies with pointing direction and observation epoch, and is given in the calibrated science header by keyword PA_V3.

There are two narrow band "quad" filters, each containing four separate filters which image a limited FOV: the UV "quad" contains filters for observing redshifted [OII] emission. There is also a set of narrow band linear ramp filters (LRFs) which are continuously tunable from 3170Åto 9762Å; these provide a limited FOV with diameter $10''$. At ultraviolet wavelengths there is a solar-blind Wood's UV filter (1200-1900Å).

Finally, there is a set of four polarizers set at four different angles, which can be used in conjunction with other filters for polarimetric measurements. However, due to the relatively high instrumental polarization of WFPC2, they are best used on strongly polarized sources (>3% polarized). Sources with weaker polarization will require very careful calibration of the instrumental polarization.

Main steps of the data calibration procedure

The standard data calibration procedure or pipeline processing is based on a software library provided by the STScI. It consists the following steps:

1. Mask correction: identification of charge transfer traps and other pixels affected by the traps. For this step a static mask reference file containing a map of permanently bad pixels is required.

2. Perform the A-to-D correction: correction of each pixel value of the science data for analog–to–digital conversion errors.

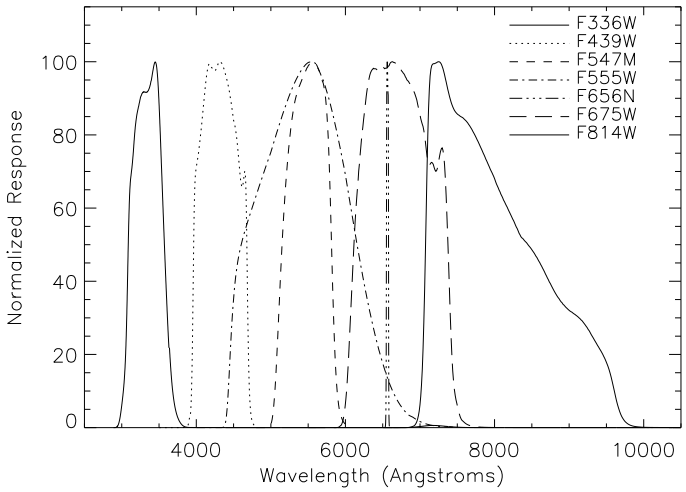

Figure 7.3: A selection of normalized WFPC2 filter curves. The reported curves, from the left to the right, correspond to the filter names listed in Figure, from the top to the bottom.

Each CCD pixel absorbs energy from photons of light that impinge upon it, releasing electrons within the semiconductor. The accumulated electrons from a particular pixel are trapped in a specific location corresponding to that pixel. The analog-to-digital converter (ADC) is a device that converts the CCD pixel voltage signal (from trapped electrons) to Data Numbers (DNs) that can be stored in computer memory.

The A-to-D converter produces small errors when converting from electrons to DN values. The errors are systematic and a statistical correction can be applied (the largest correction for WFPC2 is 0.1%).

3. Bias level subtraction: a mean bias level is subtracted from each pixel. This value, one for each chip, is derived from a subset of the overscan region for each chip.

4. Position-dependent bias patterns subtraction: removal, from the image, of small scale bias values that vary from pixel-to-pixel, still present after the subtraction of the global bias values.

5. Subtraction of dark current: thermally-induced dark currents, as well as a faint glow caused by cosmic rays striking the corrector plates, are removed for exposures greater than 10s.

6. Flat-field correction: multiplication of the science image by a flat field reference image.

   This corrections takes into account several effects: *a*) variations over the FOV of the photometric response in the science image caused by differences in the quantum efficiency and in the electron gain of each CCD; *b*) a large-scale vignetting caused by the telescope and WFPC2 mirrors, their support structures, and WFPC2 filters; *c*) optical distortions are introduced by field flatteners in front of each chip and *d*) artifacts created by dust particles on the pyramid, CCD window, and detectors.

7. Shutter Shading Correction: the WFPC2 has two shutter blades. When an exposure begins, one shutter blade is moved off the light path. The exposure ends when the second shutter blade moves to block the light path. Although the blades move rapidly, their finite motion can cause exposure time variations over the FOV for total exposure times of 1s or less, creating a "shading" effect in the image. This correction is necessary only for exposures less than 10 seconds.

8. Cosmic ray removal: cosmic rays are recognized by comparing two images taken on the same target and with the same filter. A new corrected image is obtained combining the information from the two real images.

9. Flux calibration: several conversion tables are available to convert DNs to fluxes according to the chosen photometric system (e.g., AB or STMAG, UBVRI systems). The conversion factors are different for each chip.

10. Mosaic the four images: the four images corresponding to the four CCDs are then combined in a larger L-shape image.

7.1.2 Near Infrared Camera and Multi-Object Spectrometer

The Near Infrared Camera and Multi-Object Spectrometer (NICMOS) is an HST instrument providing the capability for infrared imaging and spectroscopic observations of astronomical targets. NICMOS covers a wavelengths range from 0.8 to 2.5 μm. NICMOS provides access to this complete spectral range without hindrance from atmospheric emission or absorption at a sensitivity and angular resolution not possible from the ground.

NICMOS contains three cameras designed for simultaneous operations. The NICMOS optics offer three adjacent but not spatially contiguous FOV of different image scales. The instrument contains a variety of filters (20), grisms, and polarizers. Not all filters are available in all cameras. The specialized optical elements, such as the polarizers and grisms, cannot be crossed with other filters, and can only be used in fixed bands.

The three 256×256 pixel cameras of NICMOS are designed to provide diffraction limited sampling to 1.0 micron (Camera 1), 1.75 micron (Camera 2), and offer via Camera 3 a relatively large FOV.

The basic capabilities of the instrument are:

- IR imaging:
  NICMOS provides its highest sensitivity from 1.1 to 2 μm, where it is superior to an 8m class telescope.

- Grism Spectroscopy:
  Camera 3 has three grisms which provide a multi-object spectroscopic capability with a resolving power of R equal to 200 over the full FOV of the camera. Their wavelength ranges are 0.8 to 1.2 μm, 1.1 to 1.9 μm, and 1.4 to 2.5 μm. Because the grisms are slitless, the spectra of spatially resolved objects are confused and multiple objects can overlap.

- Imaging Polarimetry:
  Three polarizing filters with pass directions of 0, 120, and 240 degrees are provided for the wavebands 0.8-1.2 μm in Camera 1 and 1.9-2.1 μm in Camera 2.

- Coronagraphy:
  A 0.″3 arcsec radius occulting hole and cold mask, in the intermediate resolution Camera 2, provides a coronagraphic imaging capability.

A detailed description of the three cameras is reported below.

Camera NIC1

NIC1 offers the highest available spatial resolution with an $11'' \times 11''$ FOV and 0.″043 size pixels (equivalent to the WFPC2 PC pixel scale). The filter complement includes broad and medium band filters covering the spectral range from 0.8 to 1.8 μm and narrow band filters for Paschen$_\alpha$ λ 1.8756 μm, He I λ 1.083 μm, [Fe II] λ 1.64 μm, and [S III] λ 0.953 μm, both on and off band. It is also equipped with the short wavelength polarizers (0.8 to 1.3 μm).

Camera NIC2

NIC2 provides an intermediate spatial resolution with a 19.″2×19.″2 FOV and 0.″075 size pixels. The filters include broad and medium band filters covering the spectral range from 0.8 to 2.45 μm. The filter set also includes filters for CO λ 2.293Å, Brackett$_\gamma$ λ 2.166Å, S2(1-0) λ 2.122 μm, Paschen$_\alpha$, HCO_2 +C_2, and the long wavelength polarizers (1.9-2.1 μm). Camera 2 also provides a coronagraphic hole with a 0.3 arcsec radius.

Camera NIC3

NIC3 has the lowest spatial resolution with a large 51.″2×51.″2 FOV and 0.″2 size pixels. It includes broad filters covering the spectral range 0.8 - 2.3 μm, medium band filters for the CO band (and an adjacent shorter wavelength continuum region), and narrow band filters for H_2S2 (1-0) λ 2.122 μm, [Si VI] λ 1.962 ţm, Paschen$_\alpha$, [Fe II], and He I. Camera 3 also contains the multi-object spectroscopic capability of NICMOS with grisms covering the wavelength ranges 0.8-1.2 μm, 1.1-1.9 μm, and 1.4-2.5 μm.

Techniques for Dithering, Background measurement and mosaicing

The background appears spatially uniform (variations no larger than a few percent across the NIC3 FOV) and does not vary much with time. However, direct measurement of the background are required whenever the background is significant relative to the source(s) of interest. Background images are obtained by offsetting the telescope from the target to point to an empty region of the sky.

Multiple exposures with small offsets in the pointing of the telescope are usually necessary for NICMOS observations. The offset technics and the circumstances in which they are required are the following:

1. "Dithering" to permit the removal of dead or non-calibrated (i.e., non-correctable) pixels on the detector, and detector's non-uniformities (i.e., sensitivity variations).

   Dithered images can be easily reassembled into a single image to minimize bad pixels and to correct for the thermal contribution in the long wavelength regime.

   2) "Dithering" or "chopping" to measure the background associated with an astronomical source,

   3) "Mosaicing" to map a source larger than a single detector FOV.

Individual motions are limited to no more than 40 arcsec. These are intended to be used to perform small dithers, to measure backgrounds for compact sources, and to accomplish sequences of overlapping exposures for the construction of mosaics.

Several motions can be perform up to 1440 arcsec. These are intended for the measurement of the background at one or more locations significantly removed from the target pointing. Each non-contiguous background pointing will be assembled into its own final image in addition to the target pointing by the calibration pipeline.

Main steps of the calibration procedure

The raw data are calibrated using a standard set of NICMOS calibration programs provided by the STScI. A list of calibration reference files, available at the Calibration Data Base System (CDBS) at STScI, are required in the calibration process.

The steps of the initial calibration stage are listed below. Some of them are very similar to those applied in the calibration procedure of WFPC2 data, therefore we will not give details; for the others refer to the NICMOS Data Handbook (Dickinson et al. 1999).

1. Flag known bad pixels in the data quality array.
2. Calculate a noise model for each pixel.
3. Subtract the bias level.
4. Correct for non-linearity.
5. Scale (when necessary) and subtract the dark image.
6. Flat field to bring each pixel to a common gain.
7. Convert the image data to count rate units.
8. Calculate various image statistics (e.g., median).
9. Store the photometric calibration in image header keywords.
10. Correct for cosmic ray events and pixel saturation (in MULTIACCUM data).
11. Calculate estimates of the background.
12. Analyze the internal engineering telemetry for potential problems with the observation.

In case of multiple exposures, after this initial procedure, the images are combined in a mosaic.

The final step of the calibration is the conversion from count rate (CR $\equiv$ DNs s^{-1})[1] to fluxes. This is simply achieved by multiplying by a conversion factor available in the NICMOS Data Handbook (Dickinson et al. 1999).

[1]NICMOS calibrated data are given in count rate, differently from WFPC2 data that are in DN.

7.2 Main HST results in the extragalactic domain

The high spatial resolution of HST has allowed astronomers to study the photometric structure of elliptical galaxy nuclei with unprecedented detail. The main result from a large number of different studies (e.g., Lauer et al. 1995; Carollo et al. 1997) has been that at the $\sim 0\farcs1$ resolution limit of HST, virtually all galaxies have power-law surface brightness cusps. Some surface brightness profiles show a steep slope down to the resolution limit and no clear break (Faber et al. 1997). This kind of profile has been interpreted as sign of a BH in the centre of the galaxy (e.g., Bahcall and Wolf 1976; Young 1980), but this is still debated.

With HST it has been possible to study the dust and ionized gas in **early-type galaxies** at ~ 10 times better resolution than before. Interestingly, this has revealed the existence of previously unknown structures: nuclear disks, with typical sizes of 0.1–1 kpc. In some cases the disks are seen only in ionized gas emission (e.g., M87; Ford et al. 1994), while in other cases they have strong associated dust absorption, visible as a dust lane across the nucleus (e.g., NGC 7052; van der Marel and van den Bosch 1998). HST observations show nuclear dust in $\sim 80\%$ of early-type galaxies (van Dokkum and Franx 1995). The dust morphology is often patchy, and not always in the form of a disk.

Images of distant galaxies from the Hubble Space Telescope (HST) have provided direct evidence for the evolution in galaxy populations and morphology.

A potentially large population of quasars not visible in optical surveys was uncovered among X-ray and far-infrared sources. This finding has suggested that many quasars may be obscured at visible wavelengths by surrounding dust. Much new information about the host galaxies of quasars has been revealed by studies based on infrared imaging performed with NICMOS (McLeod and McLeod 2001).

Bibliography

Bahcall J.N., Wolf R.A. 1976, ApJ, 209, 214
Carollo C.M., Franx M., Illingworth G.D., Forbes D. 1997, ApJ, 481, 710
Dickinson M., STScI NICMOS Group 1999, "NICMOS Data Handbook"
Faber S.M., Tremaine S., Ajhar E.A., Byun Y.-I. et al. 1997, AJ, 114, 1771
Ford H.C., Harms R.J., Tsvetanov Z.I., Hartig G.F. et al. 1994, ApJ, 435, L27
Lauer T.R., Ajhar E.A., Byun Y.-I., Dressler A. et al. 1995, AJ, 110, 2622
McLeod K.K., McLeod B.A. 2001, ApJ, 546, 782
van der Marel R.P., van den Bosch, F.C. 1998, AJ, 116, 2220
van Dokkum P.G., Franx M. 1995, AJ, 110, 2027
Young P. 1980, ApJ, 242, 1232

Chapter 8

The HST program

Spiral galaxies show generally several components : stellar populations, star forming regions, ionized gas regions, molecular gas complexes and dust. The formation of these components, their spatial distribution, their interplay and evolution are subject of several studies aimed at understanding the spiral structure, the flow of material through the spiral arms, the processes of star formation and HII region ionization, the dust distribution over the galaxy and its related extinction.

In this framework, we defined a research project based on a large collection of data in the radio, infrared and optical domains of one of the best laboratories in space for galactic structure and star formation studies: the grand design spiral galaxy M51.

8.1 Scientific objectives

The proposed research project involves several topics of main interest in the current astrophysical research:

1. the spiral structure, the physical processes in flow, the location along the arms of different components (molecular and ionized gas, forming stars, dust);
2. the morphology (typical sizes of the observed components, their concentration and location);
3. the colours of the galaxy at different radii and in the nucleus, in the arm and in the interarm regions;
4. the dust distribution over the galaxy and its effects (extinction and reddening);
5. the nuclear structure (bar, AGN, morphology);
6. the high mass star formation.

8.2 The HST project

The project has been developed at the California Institute of Technology under the vision of Prof. N.Z. Scoville, and it is based on optical-infrared data obtained with the Hubble Space

Telescope (HST), and on radio data obtained with the Owens Valley Radio Observatory (OVRO). The collection of the data started in 1995 and ended in 1999.

The choice of HST was fundamental since it is the only available instrument with the needed capabilities for resolving the galactic components that we intended to study. Ground-based resolution instruments would not distinguish components, as e.g., HII regions whose sizes range from $0\farcs2$ to, at most, $2''$. The high angular resolution of the HST imaging ($0\farcs1$-$0\farcs2$) is thus critical for the study of extragalactic galactic structure properties.

8.3 The spiral galaxy M51

M51 is the nearest grand design spiral galaxy (9.6 Mpc of distance). It shows strongly enhanced star formation along the spiral arms, evidence of a central low luminosity AGN (Rose and Cecil 1983), and it is one of the most famous and well studied interacting systems. The encounter with the companion clearly distorted the disk of M51, increased the global star formation rate (SFR), and excited the spectacular spiral pattern.

An optical image of M51 and its companion is shown in fig. 8.1 with outlined in red the contours of the region observed by HST.

8.4 Observational dataset

The observational dataset is summarized below:

1. Images obtained with NIC3 covering the spiral arms in the inner disk (inner $2\farcm5\times2\farcm5$, correspondent to $\sim$7×7 kpc) have been obtained mosaicing 9 fields in broad band continuum filters (λ 1.1 μm, λ 1.6μm, λ 2.2 μm), and in the narrow filter centred on the Pa_α (λ 1.875μm) emission line.

   Imaging of the nucleus with NIC2 at higher resolution ($0\farcs075$ per pixel, correspondent to $\sim$ 3.5 pc) was also performed using the same filters as in Camera 3.

   Near-IR observations are particularly useful to minimize the obscuring effects of the dust and allow us to more closely examine the region immediately surrounding the AGN and the star formation regions, and to measure the stellar arms and populations.

   The near infrared maps are good tracers of the population II component. The hydrogen recombination Pa_α line traces the starforming sites and can be used to determine the extinction effects on those sites.

2. WFPC2 images have been obtained of the inner disk ($4\farcm7\times3\farcm7$, correspondent to $\sim$13×10 kpc) in broad band continuum filters (Iλ 8386Å, Rλ 6796Å, Vλ 5151Å, Yλ 5361Å, Bλ 4176Å, Uλ 3447Åfilters) and in the narrow filter centred on the $H_\alpha\lambda$ 6561Å emission line.

   The blue continuum traces the young ($t \simeq 6$ Myr) and massive stars, while the continuum at long wavelengths traces older stars ($t \simeq 10$ Myr) as the red supergiants.

   Optical-optical and optical-infrared colours can be used to study the dust distribution and the effects of extinction on the stellar light. The hydrogen recombination H_α line map can be used to study the starforming sites and determine the current SFR.

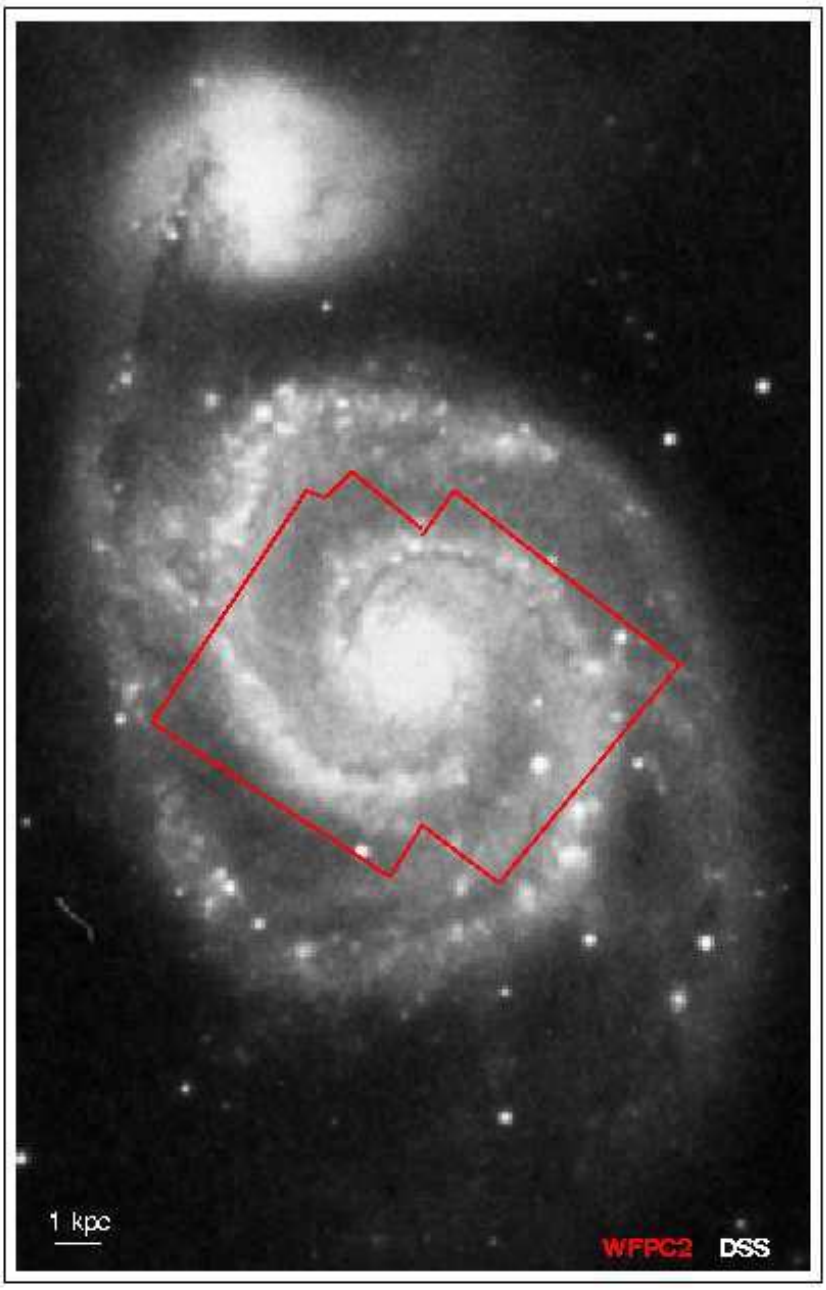

Figure 8.1: Optical image of the spiral galaxy M51 (from the *Digital Sky Survey*) and its companion NGC 5195. The red lines correspond to the inner region observed by HST.

3. High resolution (2.″5, correspondent to ∼90-140 pc) millimetre-CO data of the inner 2.′5×2.′5 have been obtained using OVRO. These data have been analyzed, and some results already published (Aalto et al. 1999).

CO imaging observations permit to trace the molecular gas distribution and to investigate the physical properties of molecular clouds in the spiral arm and interarm regions.

8.5 Results

The results obtained from our HST program are still in phase of preparation. Up to now, we have submitted a paper and we are preparing a second one. They are the following:

HST Optical and Near Infrared Imaging of M51.
M. Polletta, N. Scoville, S.P. Stolovy, S. Ewald and S. Aalto.

High Mass, OB Star Formation in M51: HST H_α and Pa_α Imaging.
N.Z. Scoville, M. Polletta, S. Ewald, S.P. Stolovy, R. Thompson and M. Rieke, AJ submitted

These two works form the subject of the next two chapters.

Bibliography

Aalto S., Huettemeister S., Scoville N.Z., and Thaddeus P., 1999, ApJ, 522, 165
Rose J.A., Cecil G. 1983, ApJ, 266, 531

Chapter 9

HST Optical and Near Infrared Imaging of M51

9.1 Introduction

Modelling the structure and the morphology of spiral galaxies requires accurate maps of the mass-tracing stellar population. Photometric mapping of spiral galaxies yields both detailed morphology and a set of global physical parameters. Mapping the position and amplitude of massive spiral arms is important for testing theories of spiral density waves and of star formation driven by the spiral structure. Unfortunately, mapping is difficult because of obscuration caused by the prominent dust lanes and patches and of the presence of young stars which can contribute much to the light in many colours but only little to the total stellar mass (Schweizer 1976). The effects of dust extinction act on the arms and the interarm regions to different degrees at different wavelengths (i.e., they are minimized in near-IR observations). Heavy extinction by dust can both delineate and confuse the underlying galactic structures. Dust extinction is highly effective whether or not the dust lies in an actual screen or is intermixed with the stars. Dust extinction is greatly reduced in the near infrared ($A_K \sim 0.1\ A_V$). Near-IR images, therefore, provide a more reliable picture than optical images of the stellar mass distribution, particularly in the region immediately surrounding the nucleus and in the spiral arms.

The arm surface brightness are higher at optical and near-infrared wavelengths than those of the interarm zones of the disk, they often have dust lanes at their edges, and they are sites of more concentrated star formation. The interarm regions are a useful source of information about the distribution of the stellar population and of the dust in the disk, while the arms offers the opportunity to study the spiral structure and the star formation process.

M51 (NGC 5194), also known as the "Whirlpool Galaxy", is the first galaxy in which spiral structure was observed (Parsons 1850), and one of the most famous and well studied interacting systems. The nucleus of M51 offers an interesting variety of spectacular phenomena: an active nucleus (Rose and Cecil 1983); a radio jet, directed into the plane of the disk, creating shocks and inflating bubbles of gas in the disk (Crane and van der Hulst 1992); a bar (Rand and Kulkarni 1990); large cluster of stars with enhanced associated star formation; dust lanes (Grillmair et al. 1997) and dense molecular gas (Scoville et al. 1998).

In M51 three structures with different density waves and pattern speeds are observed (Zaritsky et al. 1993; Elmegreen et al.1989; Toomre 1978; Byrd and Howard 1989). They are

probably the result of a combination of causes: the gravitational interaction and a preceding encounter with the companion (NGC 5195), a pre-existing spiral structure and the bar. The encounter with the companion not only excited the spectacular spiral pattern, but also increased the global star formation rate (SFR). The spiral arms show strongly enhanced star formation sites, several massive cloud complexes, and chains of very bright stellar associations with many high mass stars.

The process responsible for the enriched star formation observed in correspondence of the arms in spiral galaxies is still a debated question. Several mechanisms have been proposed: external triggers such as shocks caused by density waves in spiral arms (Roberts 1969), gravitational instabilities (Kennicutt 1989; 1994) or compression of molecular gas in the interface between colliding clouds (Scoville et al. 1986; Tan 2000). The last mechanism may play a major role in star formation in tidal encounters since an increase in the cloud velocity dispersion is expected, leading to a larger number of cloud collisions.

According to the standard scenario of star formation in trailing spiral galaxies, stars and gas enter the arms on their concave inner edges and leave them on their convex outer edges. As the interstellar gas travels over the gravitational potential of the disk, it is periodically compressed. Molecular gas clouds overtake the spiral arm from behind and concentrate into the density wave. Large-scale shock fronts may then appear near the inner edges of the spiral arms (where the gravitational potential is larger). The interarm molecular clouds, after being shocked by the spiral density waves, condense gravitationally and collapse along the length of the arm forming clumps that then form stars (Elmegreen 1979). The condensation of spiral arm gas into 10^7 $M_\odot$ clouds and star complexes caused by the shocks is expected to be rapid. If the typical times where too long, the gas would flow out of the arm and disperse in the presence of greater shear and higher tidal forces in the interarm region (Elmegreen 1994). In case of strong shocks, the gravitational collapse and star formation occur quickly once the gas enters the spiral arms and most of the condensed material will be still close to the density wave shock, and then to the starforming site (Elmegreen 1994). This scenario predicts the lack of displacement between the cores of molecular clouds and new born stars.

The galaxy M51 has received quite a lot of attention for studies of spiral structure and star formation. With 0.″5–1.″1 resolution, various studies have shown no obvious correlation between the peaks in the molecular emission and spiral structure and no global evidence was found for large enhancements in the molecular emission in the arms. These observations challenged the star formation theorists because of the different distribution of the star forming material and of new born stars, more concentrated along the spiral arms. However, later studies based on CO observations measured an enhancement of molecular gas concentration in the arms (Rydbeck, Hjalmarson and Rydbeck 1985; Lord and Young 1990). Higher resolution observations in the radio continuum and in the millimetre lines show the presence of most molecular clouds in the inner edge of the spiral arms (Tilanus et al. 1988; Tilanus and Allen 1989; Aalto et al. 1999). The HII regions that dominate the appearance of M51 at optical wavelengths are not obviously displaced to the outside of the molecular and dust arms in the maps presented by Vogel, Kulkarni and Scoville (1990) and Sauvage et al. (1996). However, the lack of displacement in these maps may be explained if the offset is comparable to their spatial resolution of $7'' \simeq 300$ pc. Most of the gas phases involved with star formation can be mixed at that resolution.

We present high resolution images of M51 (NGC 5194) in the continuum B V R I J H K bands, and in the $H_\alpha(\lambda 6563\text{Å})$, $Pa_\alpha(\lambda 1.87\mu\text{m})$ and CO ($\lambda 2.3\mu$m) emission lines. The images were taken with WFPC2 and NICMOS on board the Hubble Space Telescope.

The organization of the paper is the following: the observations are presented in section 9.2, the morphological analysis of the galaxy in section 9.3 and of the inner region in section 9.4, the analysis of radial profiles in section 9.5 and spatial comparison between the different tracers in section 9.7.

9.2 Observations

Hubble Space Telescope (HST) observations of M51 were performed at optical wavelengths with the Wide Field and Planetary Camera 2 (WFPC2) and in the near-IR with Camera 3 of the Near Infrared Camera Multi-Object Spectrograph (NICMOS). This large dataset groups data obtained in our own programs 7375 and 7237, and archive data obtained in programs 5123 and 5777. Details concerning all of the observations presented in this work (date, program number, exposure, filter, wavelength, rotation angle) are given in Table 9.1. High resolution ($2\farcs5$, corresponding to ∼116 parsec) images at 2.6 mm (Aalto et al. 1999)

Table 9.1: Observing Log

Instrument	Program ID	Date	Filter Name	Peak λ (μm)	Exposure/s (sec)	Orientation angle[a] (deg)
WFPC2	5123	Jan 24, 1995	F656N (H_α)	0.6561	400 + 1400	93.1998
			F547M (y)	0.5361	260 + 600	
	5777	Jan 15, 1995	F439W (B)	0.4176	700 + 700	101.541
			F555W (V)	0.5151	600	
			F675W (R)	0.6796	600	
			F814W (I)	0.8386	600	
	7375	Jul 21, 1999	F336W (U)	0.3447	600 + 600	275.905
			F439W (B)	0.4176	600 + 500	
			F555W (V)	0.5151	600 + 600	
			F656N (H_α)	0.6561	1300 + 700	
			F675W (R)	0.6796	500	
			F814W (I)	0.8386	700 + 300	
NICMOS3	7237	Jun 28, 1998	F110W (J)	1.0998	288	−113.168
			F160W (H)	1.5940	288	
			F187N (Pa_α)	1.8740	576	
			F190N	1.9005	576	
			F222M (K)	2.2160	288	

[a] For WFPC2 it corresponds to PA-V3: angle between the axis V3 of the camera and the North. For NICMOS it corresponds to the angle between the y axis of the camera and the North. Both angles are expressed in degrees.

obtained with the Owens Valley Radio Observatory (OVRO) are also included in the datasets.

9.2.1 WFPC2 data reduction

Ten WFPC2 images were combined into high resolution images ($0.1''$ per pixel, corresponding to $\sim$ 4.6 parsec) of the central $3'.7 \times 3'.2$ (corresponding to 10 kpc $\times$ 9 kpc) region. The mosaiced images from the different programs cover slightly different portions of M51. The whole region was observed in 4 broad optical continuum bands (I, R, V, B) and in the narrow band corresponding to the H_α emission line. Half of the region ($2'.7 \times 2'.7 \simeq$ 7.4 kpc$\times$7.4 kpc) was observed in the optical continuum bands y and U with the same resolution as the other images. Eight of the twelve fields were imaged in two exposures for cosmic ray suppression, the remaining four fields in one exposure (see exposures in Table 9.1).

The first phase of the data reduction (bias and dark correction and flat fielding) was carried out at the STScI by the automatic standard pipeline. During the second phase of the data reduction, the cosmic rays removal was performed. This correction was applied using two different methods, according to the availability or not of two exposures on the same region and with the same filter.

When two exposures were available, the pixels affected by cosmic rays were identified by comparing the signals in the two exposures measured in the same pixel location. If the difference between the signal in the two exposures was higher than a threshold defined for each filter, the highest value was set equal to the lowest one. This method does not correct pixels affected by cosmic rays in both exposures. Therefore, a further correction was performed by masking those pixels for which the difference between their signal and the average signal in a surrounding region of 9×9 pixels was higher than a second threshold value. The threshold depends on what expected for a point source for a specific filter and WFPC2 chip. The masked pixels were replaced by the median of the unmasked pixels in the surrounding 3×3 region. We applied this procedure twice, each time on the last cleaned images. The procedure was also applied to observations with only one exposure. Since this last cleaning is efficient only when a cosmic ray affects isolated pixels, observations with a single exposure remain still contaminated by many cosmic rays after its application. In single exposure observations, pixels still affected by cosmic rays were singled out if their signal was a few times (the threshold value depends on the filter and on the WFPC2 chip) higher than the signal of the pixel adjacent on one side or below. The contaminated pixels were replaced by the weighted mean of the eight surrounding pixels (the weight corresponds to the distance of the surrounding pixels from the central one). This process was repeated twice more on the resultant images with different threshold values.

The criteria applied to recognize cosmic ray could not distinguish the signal from stars with that from a cosmic ray. To avoid this problem, at the end of the cosmic ray cleaning process, we checked the replaced pixel locations. We assumed that a pixel contained a bright star if it was also flagged in one of the other filters. In such cases, the modified (cleaned) value was replaced with the original pixel value.

The four images, after cosmic ray removal, were combined using the Image Reduction and Analysis Facility (IRAF) [1] task WMOSAIC. Cosmetic blemishes such as bad columns, bad spots on the chips and regions in between two chips were replaced by a weighted mean of the surrounding 3×3 pixels (the weight is given by the distance) or by interpolating across the feature. Each of the five pairs of combined images taken at the two different pointings in the

[1] IRAF is distributed by the National Optical Astronomy Observatories, which are operated by the Association of Universities for Research in Astronomy, Inc., under cooperative agreement with the National Science Foundation.

galaxy with the same filter were then mosaiced into a single image.

The broad band continuum mosaics left uncovered two small regions ($\sim 24'' \times 7''$ and $20'' \times 4''$) close to the nuclear region (at $\sim 35''$ to the north and $15''$ to the south of the galactic centre, respectively). Since the y image covered these holes, we replaced them, in the four continuum images (I, R, V, and B), using the y image after applying a scaling factor. The scaling factor was derived from the mean of the ratio between the average y and broad-band continuum signals in their area of overlap.

The broad/medium filter data were, finally, flux calibrated using the PHOTFLAM parameter as indicated in the WFPC2 Instrument Handbook (Biretta et al. 2000). The noise[2] in the final broad-band B, V, R and I continuum images is 36, 30, 48 and 63 μmJy arcsec^{-2}, respectively.

The continuum to be subtracted from the two F656N images (one for each of the two programs 7375 and 5123) was taken from one of the continuum images available for the two programs. The F814W image was chosen in program 7375 because it is not contaminated by H_α emission (while the F555W and F675W filters contain some contribution from H_α). The F547M image was used in program 5123 because it was the only continuum image available. These continuum images were individually scaled by a constant factor derived from the average ratio between the F656N and F814W/F547M fluxes for a sample of stars and fields without point sources in regions of low H_α emission.

The narrow filter data were flux calibrated using equation (11) in Holtzman (1995) and the filter throughput value at the redshifted wavelength of the H_α line. The F656N filter has a peak transmission at 6561Å and a width $\Delta\lambda = 22.0$Å (as defined in the WFPC2 Instrument Handbook). The H_α(F656N) filter is partially contaminated by the [NII] 6548Å and 6584Å lines. The filter transmission at the redshifted wavelength of the H_α line is 91.2%, $\sim 98.7\%$ for the [NII]λ6548Å and null for the [NII]λ6584Å line. In most HII regions the contribution from [NII]λ6548Å and [NII]λ6584Å is $< 4\%$ of the H_α emission (Wang et al. 1997), therefore, we estimate that $\sim 1\%$ of the measured flux is due to the [NII] emission. Being aware of the contamination from [NII] 6548Å , we will refer to the to the continuum-subtracted F656N image as H_α.

Background variations and diffuse H_α emission were removed from the H_α imaging subtracting a smooth version of the same image after filtering the higher values.

In Figure 9.1, the resultant continuum V-band mosaic is shown. In Figure 9.2, a colour composite image with the B-band image in the blue display, the V-band image in the green display and the I-band and the continuum subtracted H_α image in the red display is reported. In both figures, the orientation is such that North is up and East on the left, the major axis of the galaxy is 10° clockwise from the North (PA = 170°), and the near side of the galaxy disk is the eastern half (Tully 1974).

9.2.2 NICMOS data reduction

M51 was observed in the near-IR by Camera 3 of NICMOS using the wide-band F110W (1.1035 μm) and F160W (1.5931 μm), the medium-band F222M (2.216 μm) and the narrow-band F187N (Pa_α, 1.8738 μm) and F190N (1.9003 μm) filters. Blank sky frames for background subtraction were also obtained with the F222M filter. NICMOS Camera 3 uses a 256×256 HgCdTe array with plate scales of $0''.203859$ and $0''.203113$ per pixel in x and y,

[2]The noise corresponds to the standard deviation of the signal in all of the pixels whose values are lower than twice the standard deviation associated with the whole image.

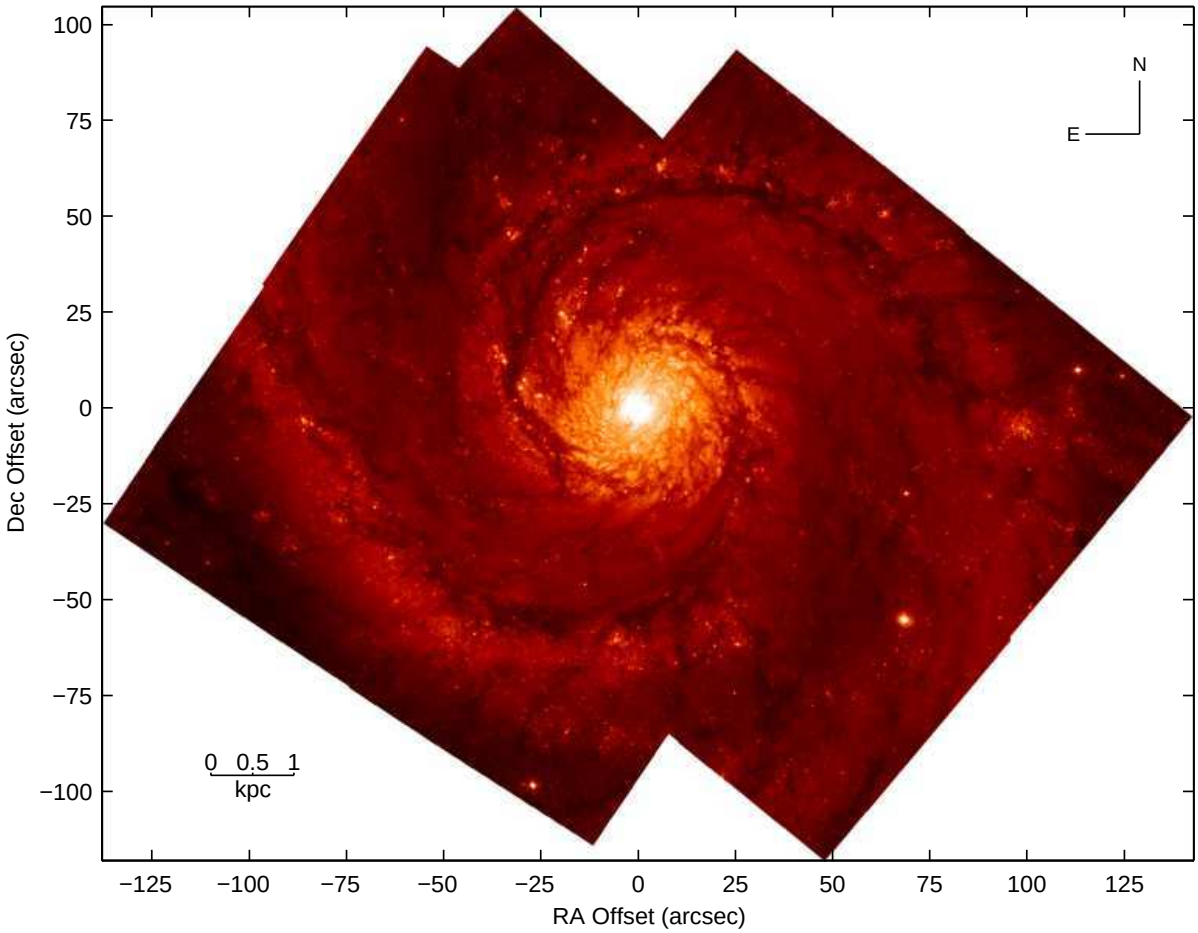

Figure 9.1: Image of M51 taken by WFPC2 with the filter V (5151Å).

providing a $\sim 52\farcs19 \times 52\farcs00$ field of view (Thompson et al. 1998). Camera 3 observations were made by executing 9 different pointings (frames), covering a square region made of 3×3 frames centred on the galaxy nucleus. For each of the 9 positions, 4-point spiral dithers per filter setting separated by $2''$ were performed, for a total of 36 images. At each dither position, non-destructive readouts (MULTIACCUM) were obtained, with 32 seconds of integration time per dither position for the medium and broad filters and 64 seconds for the narrow filters and for the background observations with the F222M filter. The total integration time per filter setting was thus 288 seconds for the broad and the medium filters, and 576 seconds for the narrow filters. More details (date, program number, exposure, filter, wavelength, rotation angle) about these observations are reported in Table 9.1.

The data were reduced using the CALNICA version 3.3 task (Bushouse and Stobie 1998) in IRAF/STSDAS and the reference files (static data quality, detector read noise, detector non-linearities files) from the Space Telescope Science Institute (STScI) NICMOS pipeline, with the exception of the flat-field, and dark frame corrections that were provided by the NICMOS Instrument Development Team.

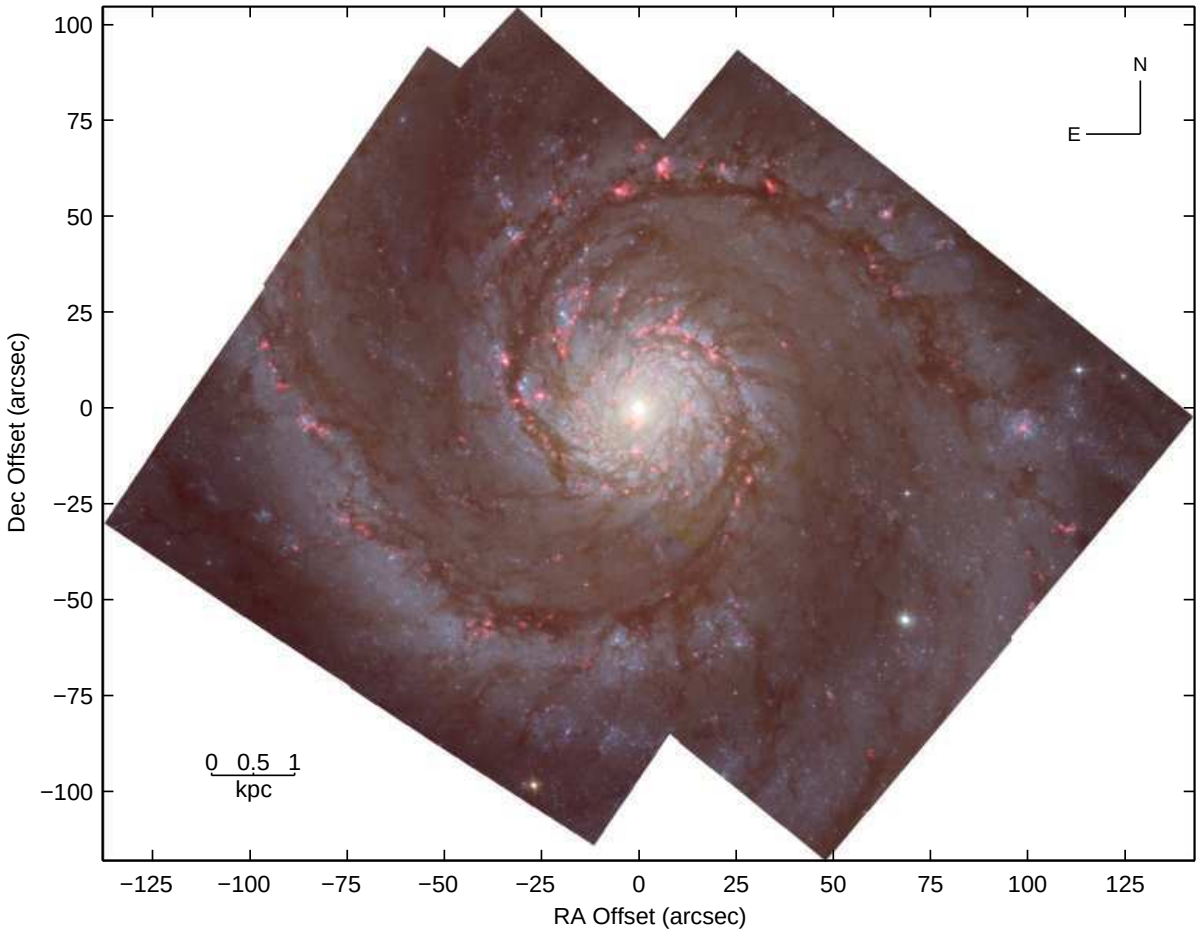

Figure 9.2: Colour composite image of M51 using the WFPC2 continuum subtracted H_α and the I-band image for the red display, the V-band image for the green display and the B-band image for the blue display.

In order to remove offsets in flux between the images in adjacent fields, we compared the signal of each frame with that of the next frame in a region of overlap without bright sources. Relative offsets were thus derived for each frame and the absolute value was such that the average flux in regions without emission sources was close to zero. The offsets were then subtracted from each image. The subtracted values were on average 48% of the noise. After this procedure, the 36 images were shifted and mosaiced using the NICMOSAIC and NICSTIKUM IRAF tasks (Lytle D. 1998, private communication). After mosaicing, the broad/medium filters images were flux calibrated using scaling factors of 2.612, 2.675, and 6.641 μJy (ADU/sec)$^{-1}$ at 1.10, 1.60, and 2.22 μm, respectively (Rieke et al. 2001). The corresponding magnitude zero points (on the Vega system) were calculated assuming 1775, 1083 and 668 Jy at 0 mag for 1.10, 1.60, and 2.22 μm, respectively. As a check on the flux calibration, we compared our measured fluxes within a $37\farcs50$ aperture centred on the M51 nucleus with the J, H and K band magnitudes measured in ground-based imaging

by Aaronson (1977). The differences in magnitudes were $m_J - F110 \simeq -0.12$, $m_H - F160 \simeq 0.07$, and $m_K - F222 \simeq 0.29$ mag. At 1.10μm a difference is expected since the standard J filter is quite different from the F110W filter (e.g., the central wavelengths are 1.22 μm for the standard J filter and 1.10 μm for the F110W filter). The narrow filter images were calibrated following the NICMOS Data Handbook (Holfeltz et al. 1999) instructions and using the reported filter parameters PHOTFLAM and FWHM. The noise in the F110W, F160W, F222M, F187N and F190N filter images is 33, 48, 46, 62 and 59 μJy (arcsec)$^{-2}$, respectively.

The F190N image was subtracted from the 187N image to obtain an image in the Pa_α emission line. A further cleaning procedure to remove background variations and diffuse Pa_α emission was applied to the Pa_α image consisting in the subtraction of a smooth version of the same image after filtering the higher values.

In Figure 9.3, the continuum H-band image is shown. In Figure 9.4, a colour composite image with the J-band image in the blue display, the H-band image in the green display and the K-band image and continuum subtracted P_α in the red display is reported.

9.3 Morphology

9.3.1 Optical images

In order to better show the morphological structures in M51, a smoothed radial intensity gradient was removed from each image. The radial gradient corresponds to the square root of an image obtained by interpolating the median of the first fifth lowest values in rings 2 pixels wide. A colour composite image of M51, obtained combining the H_α, I, V, and B images after dividing by their radial gradient, is shown in Figure 9.5.

The optical continuum bands reveal the two spiral arms: the North-East (NE) arm being brighter ($\sim$ 20% on average in V-light; see top panel of Figure 9.6) than the South-West (SW) arm where a broad ($\sim$ 3″–8″$\simeq$ 140–370 pc wide) dust lane is visible. The two main arms terminate at approximately the same radius, diametrically across the nucleus at about 1 kpc where a bifurcation is observed in both arms, more pronounced in the SW arm. Both arms show a small bump at two diametrically opposed positions 32″ ($\sim$ 1.5kpc) from the nucleus. The bumps mark a change in the inclination of the tangents to the arms.

Two large regions with very blue colours are observed on the inner edge of the SW arm at about 1.5 kpc of distance from the nucleus. These regions are associated with strong H_α and B-light emission, indicating current massive star formation. Similar regions containing multiple clusters of young stars are observed along the outer parts of both spiral arms.

In the central region, a stellar bar extends to about 600 pc in radius along the major axis ($\sim$36° West from the North) and to about 300 pc along the minor axis.

A schematic representation of the described structures is shown in Figure 9.7.

Many dust features are seen as extincted optical light. Among the most striking features are the dust lanes in the central kpc region, those along the spiral arms, and on the outer edge of the arms (spurs). The spurs are oriented almost radially, extending from the outer part of the arms towards the interarm region. They are often coupled with chains of stars and HII regions. On average, the spurs are $\sim$ 1″ wide and inclined by $\sim$ 40° to the arm. The pitch angles[3] of these dust features are quite large, up to 96° . These are more important

[3]The pitch angle is defined as the angle between the local tangent to a structure (e.g., an arm, a spur) and

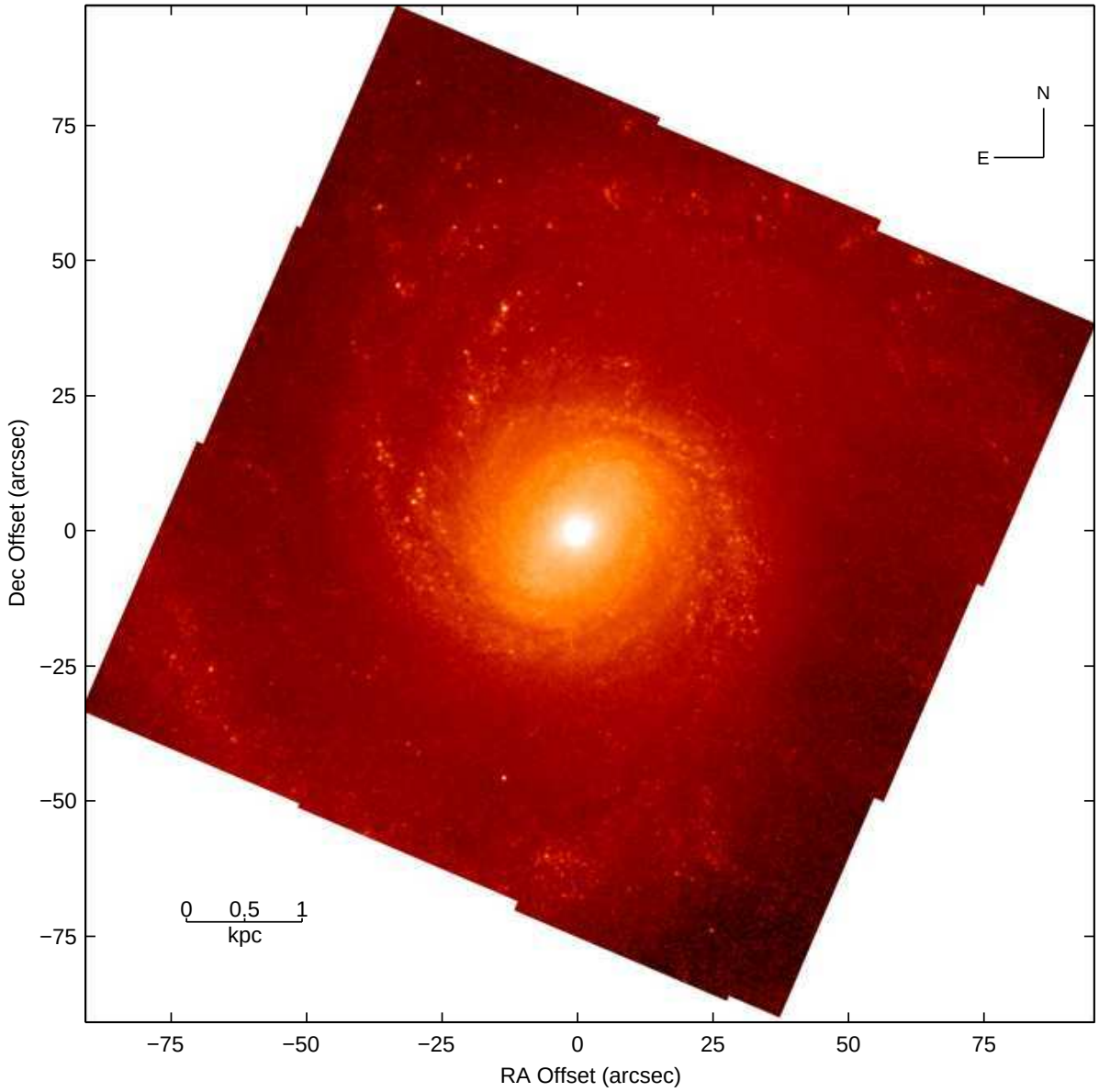

Figure 9.3: Image of M51 taken by NICMOS Camera 3 with the filter H (1.60 μm).

than the pitch angles of the spiral arm. A comparison between the pitch angles of the arms as defined by the CO and H_α emission and those of the spurs as a function of the azimuth angle is shown in Figure 9.8. The spurs' pitch angles were derived at the half length point of the spur after outlining them by 'eye' in the B-band image. The average pitch angle value for the spiral arms traced in CO and H_α ranges from $\sim$15° to 19° and for the spurs is about 64° .

The H_α image shows a bright source at the centre (see section 9.4.2 for a discussion of the

the tangent to the circle at a defined point.

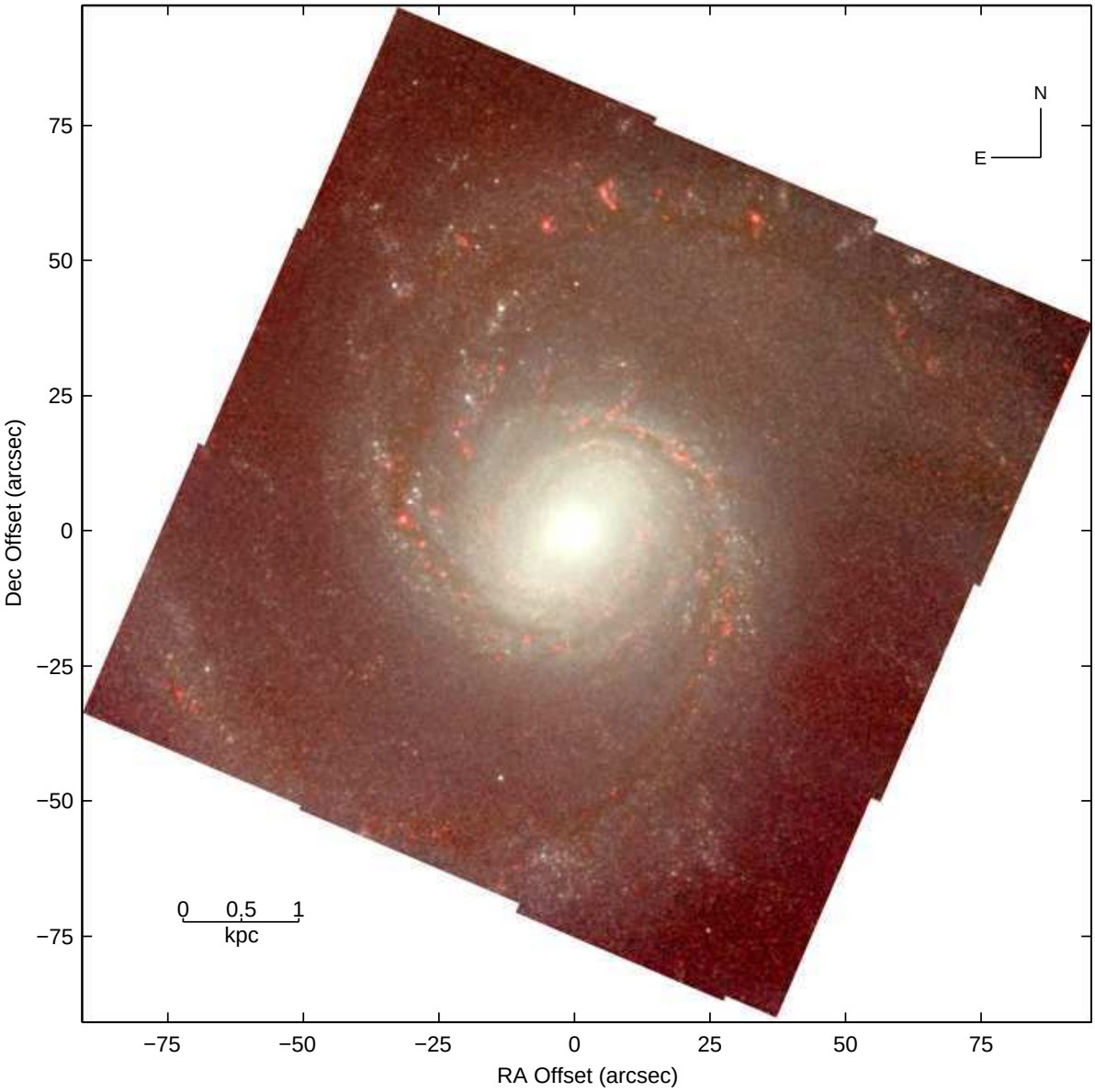

Figure 9.4: Colour composite image of M51 using the NICMOS continuum subtracted Pa_α and the K-band image for the red display, the H-band image for the green display and the J-band image for the blue display.

nuclear H_α emission). At the opposite ends of the bar, the H_α is not stronger as observed in many barred galaxies (Knapen and Beckman 1996). The H_α emission along both arms is not continuous, although outlining the spiral arms. Interarm H_α emission is present in large portions of the disk, but is usually weak, and arises from small, isolated regions, which are, however, in some cases lined up along CO clouds and spurs.

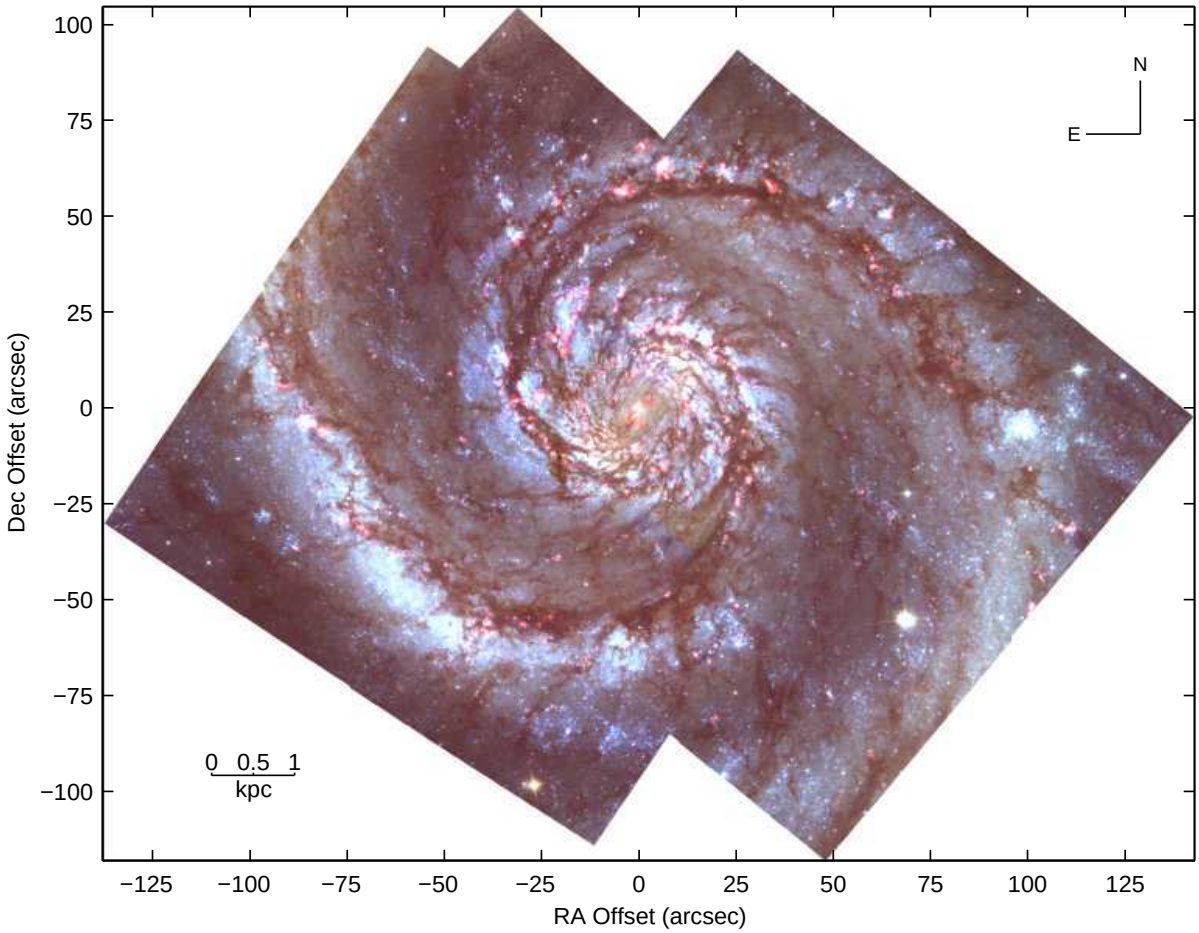

Figure 9.5: As Figure 9.2 after dividing the broad-band images by a radial gradient (see text).

9.3.2 Optical and CO images

The molecular spiral arms appear with great clarity in CO images. Comparison of the optical images of M51 with the CO map shows that the pattern of dust lanes spreads in a similar fashion to the CO emission. Along the arms the CO coincides with the dust lanes. Some of the spurs seen in optical images are also observed in the CO map. The contours of the CO emission overlayed on the optical image are shown in Figure 9.9.

9.3.3 Near-Infrared images

A colour composite image of M51, obtained combining the Pa_α, K, H, and J images after dividing by their radial gradient, is shown in Figure 9.10.

The near-IR images show very well the nuclear bar. A peak in the infrared luminosity is observed in correspondence of the bar ends. The bar is larger than in the optical, extending to $\sim$ 800 pc from the centre along the major axis and to $\sim$ 500 pc from the centre along the minor axis. The emission from the nucleus, both in the broad band and in the narrow

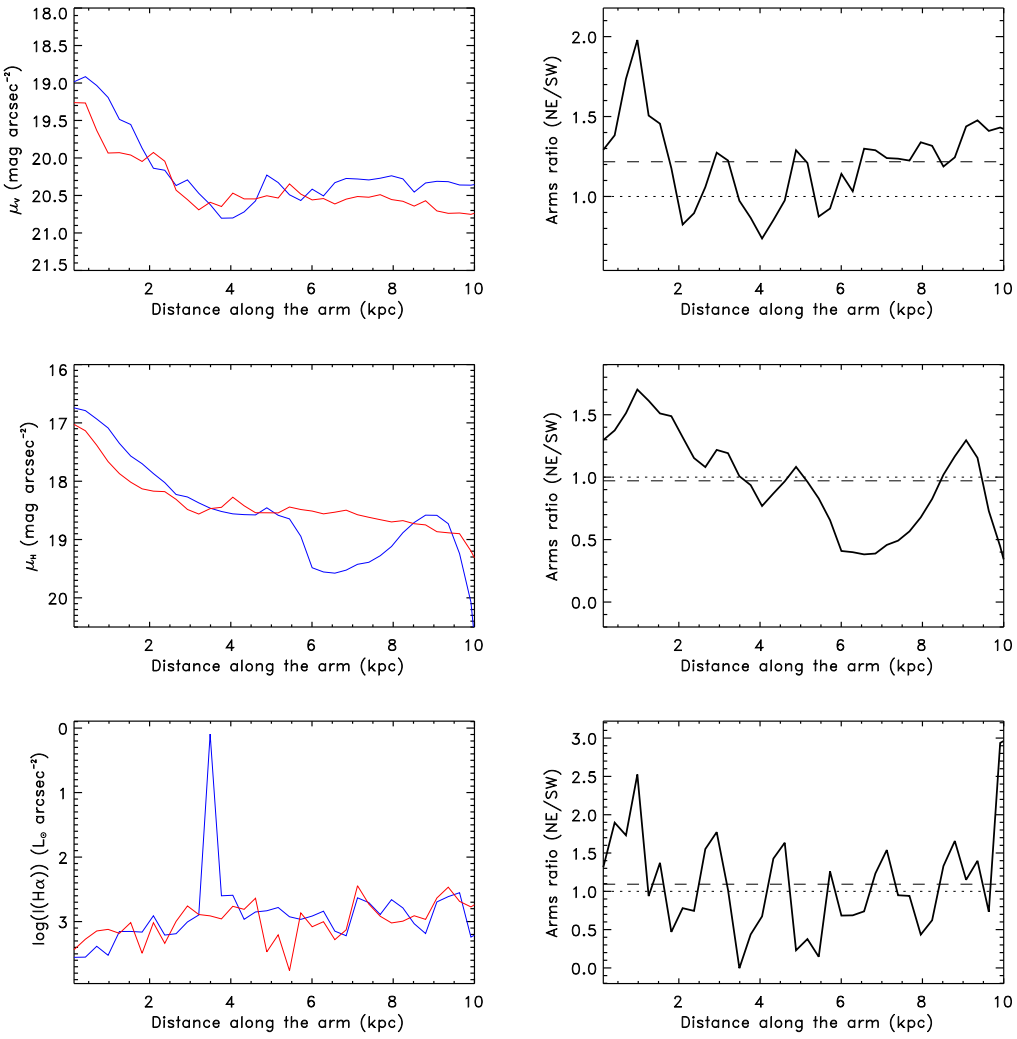

Figure 9.6: Arm profiles and ratios between the emission in the arms and in the interarm regions are plotted as a function of the distance along the arms (NE in blue and SW in red) in V, H and H_α light.

filters, is distributed on a circular region, without showing any preferential direction. The Pa_α emission traces well the dust lanes associated to the spiral arms and to the spurs.

A visual comparison of the NICMOS and WFPC2 mosaics shows that many discrete clumps and point sources (mostly OB associations) are nearly as prominent in the near infrared as they are in optical. They show many similarities also in the appearance of the dust lanes and spurs, visible in the J image.

However, most of the features observed in the optical images are not visible in the near-infrared images. This may be explained by the different origin of the emission (i.e. different star ages and populations), different spatial resolution, different sensitivity and signal to noise ratio.

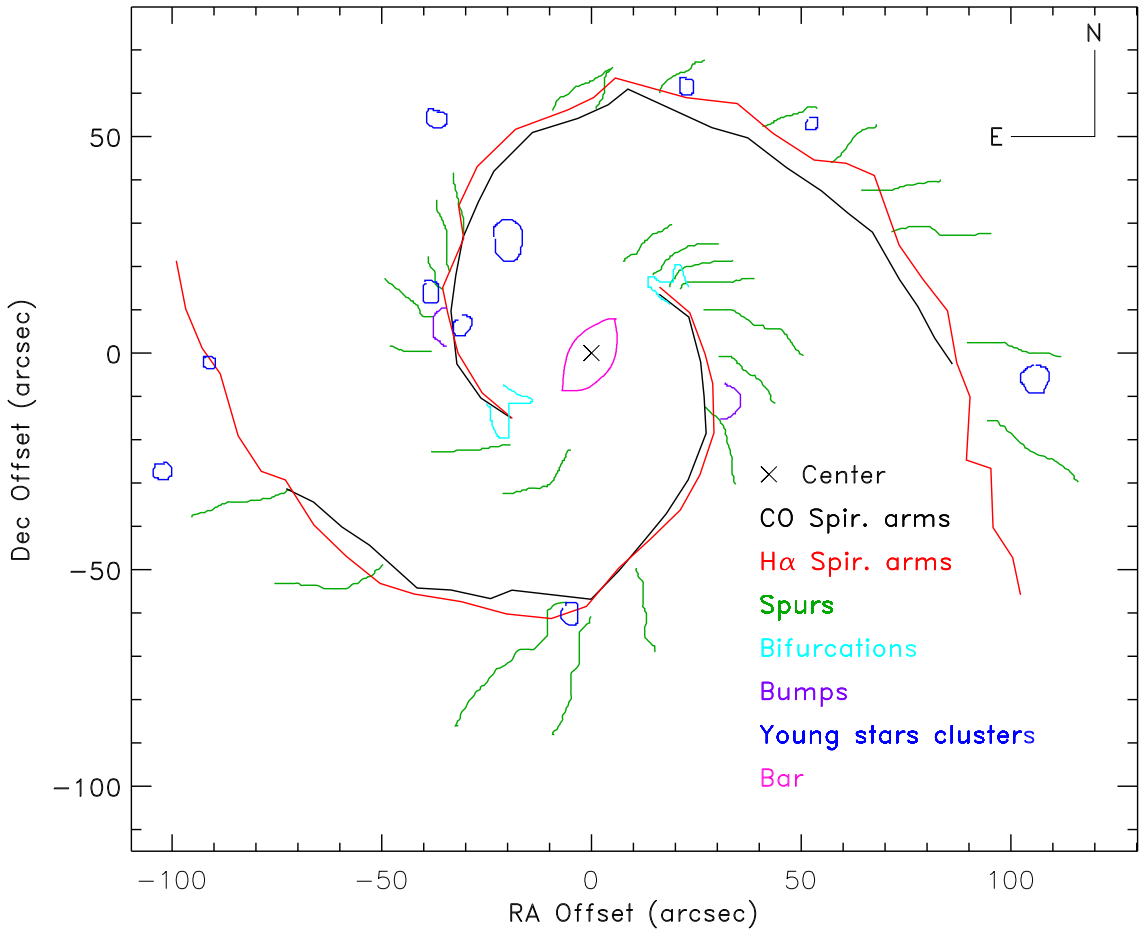

Figure 9.7: Schematic representation of the various structures observed in the optical image of M51 (see section 9.3). The central cross marks the centre of the galaxy. The black and red solid curves represent the spiral arms as traced by CO and H_α emission, respectively. The green lines represent the spurs. The features drawn in light blue outline the bifurcations at the end of the arms. The purple features indicate the bumps along the arms. The blue circles outline young star clusters. The central oval shows the contours of the bar.

9.4 The inner kpc structure

The central kpc of M51 hosts several complex structures that WFPC2 delineates with unprecedented detail, dust lanes of different thickness, the stellar bar, ionized gas. A colour composite image of the 4×4 kpc central region of M51 in the optical I, V and B WFPC2 bands is shown in Figure 9.11. The same region with H_α emission included is shown in Figure 9.12. The image shows the ends of the arms, the stellar bar and a spectacular net of dust filaments which disappears or becomes much weaker where the central stellar bar appears.

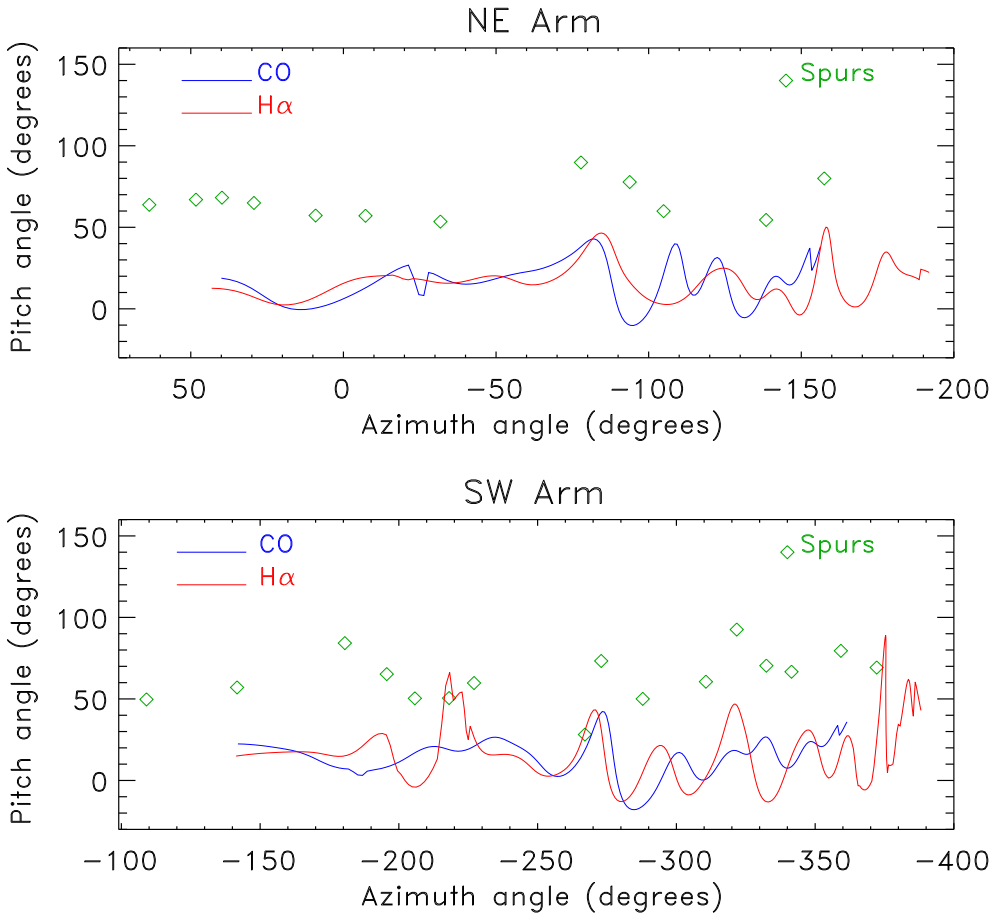

Figure 9.8: Pitch angle *versus* the azimuth angle of the spiral arms (NE arm in the upper panel; SW arm in the bottom panel) as traced by the CO (blue curve) and H_α (red curve) images and of the spurs (green diamonds).

9.4.1 Dust filaments

The dust filaments outline cells of less obscured material. The cells were defined by 'eye' as shown in Figure 9.13. Their sizes range from 38 to 132 pc.

The observed structure resembles to the high resolution (1.95 pc scale), two-dimensional hydrodynamical simulation obtained by Wada and Norman (1999) of the interstellar medium in the central kpc region of a galactic disk. In Figure 9.14, the density and temperature distribution, obtained from their simulation are reported. The model takes into account self-gravity of the gas, galactic rotation, radiative cooling, and heating due to UV background radiation. According to the simulation results, a gravitationally and thermally unstable disk evolves, in a self-stabilizing manner, into a globally quasi-stable disk that consists of cold ($T < 100$ K), dense clumps and filaments surrounded by hot ($T > 10^4$ K), diffuse medium. The cold gas forms a quasi-stationary, filamentary structure very similar to the dust filaments observed in M51 (see Figures 9.11 and 9.13). The hot gas, characterized by low-density holes

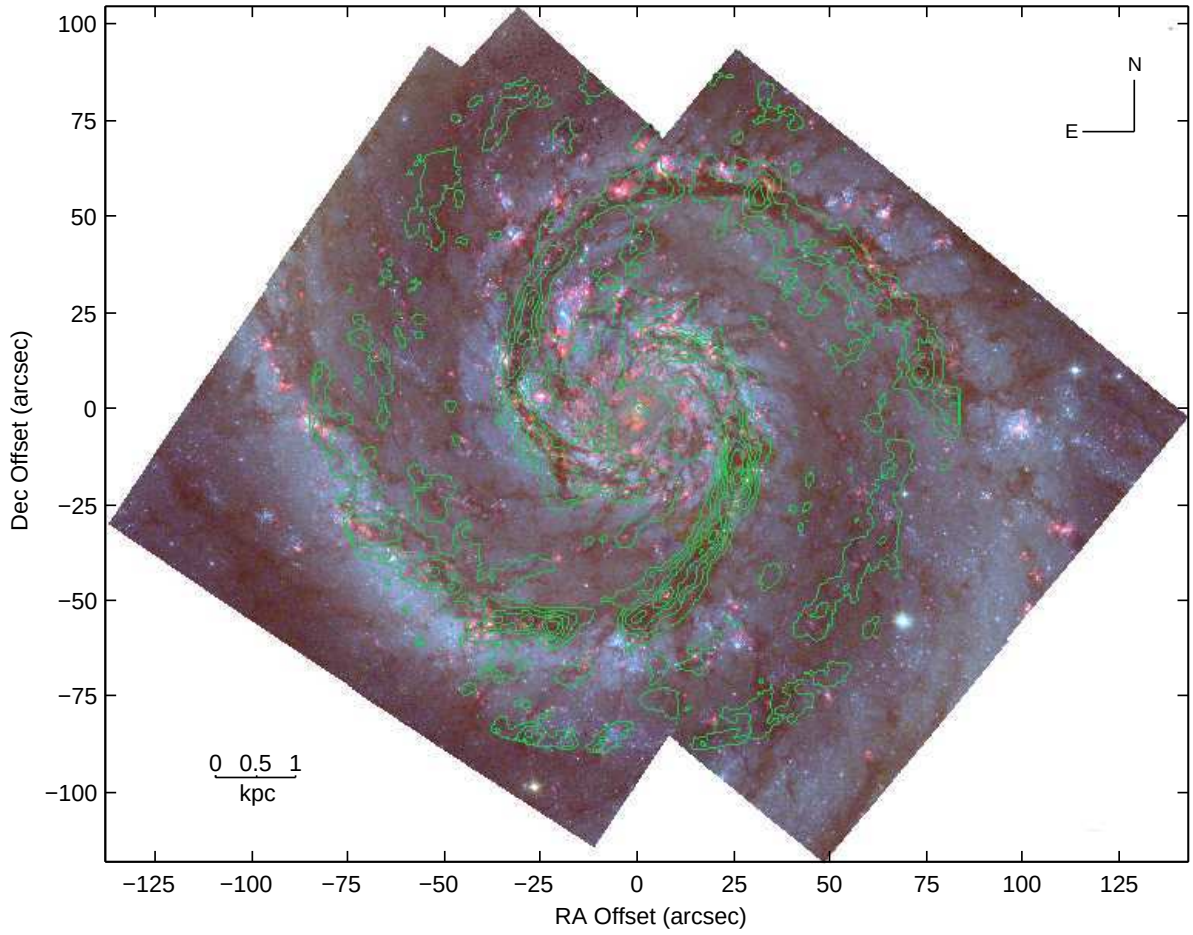

Figure 9.9: Overlay of the CO image on the optical image shown in Figure 9.2.

and voids, is produced by shock heating. The shocks derive their energy from differential rotation and gravitational perturbations due to the formation of cold dense clumps. They find a characteristic size for the highest density clumps of about 5–50 pc, very similar to the dusty filaments observed range in M51. It is worth to say that the simulation is valid for a gas distribution and does not take into account the presence of dust, the gravitational potential induced by the bar and the effects of star formation.

9.4.2 The radio jet and the surrounding gas

We compared the nuclear H_α emission in the nucleus with a VLA radio image taken at 20 cm (Condon 1987) which shows well the emission from the radio jet (see Figure 9.15). Strong H_α emission is observed in the nuclear region which extends from the centre to $\sim$ 200 pc toward the South. This is strongly correlated with the radio emission from the jet. The radio and H_α jets show some distortions and an abrupt and wide termination that might be explained by the interaction with the surrounding material. The possible excitation mechanism for the gas

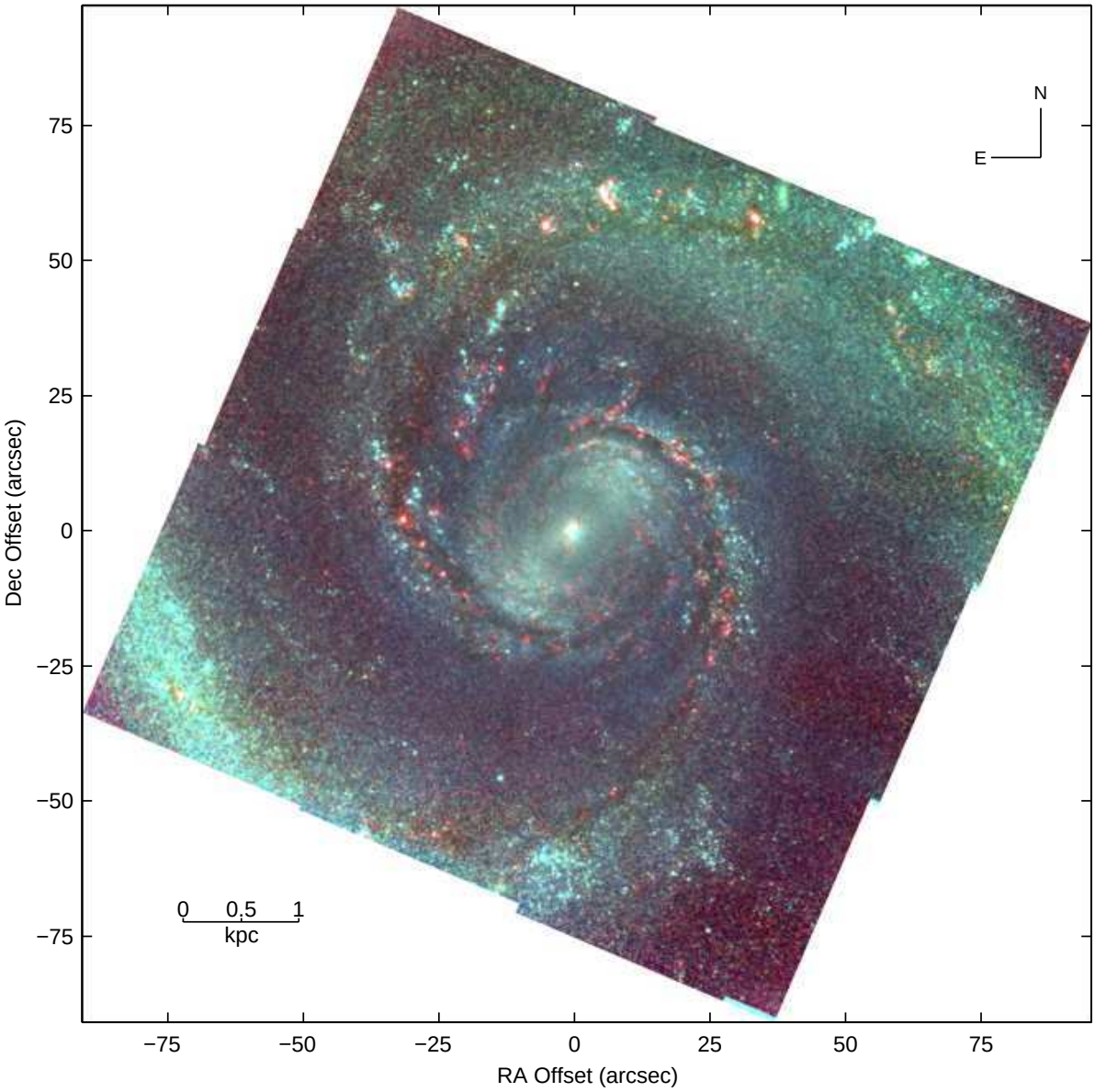

Figure 9.10: Colour composite image of M51 using the NICMOS continuum subtracted Pa_α and the K-band image for the red display, the H-band image for the green display and the J-band image for the blue display. In the continuum images a radial gradient. North is up and East on the left is removed.

could be photoionization by light beamed from the active nucleus of M51, skocks induced by the relativistic plasma responsible for the radio jet, and stellar photoionization. An analysis of the optical images does not reveal any OB association in the same region where H_α emission is observed. The lack of visible young stars could be due to the high nuclear extinction, but if this were true, we would not see the H_α emission either.

The jet is only seen on one side, while on the opposite side an arched extended radio

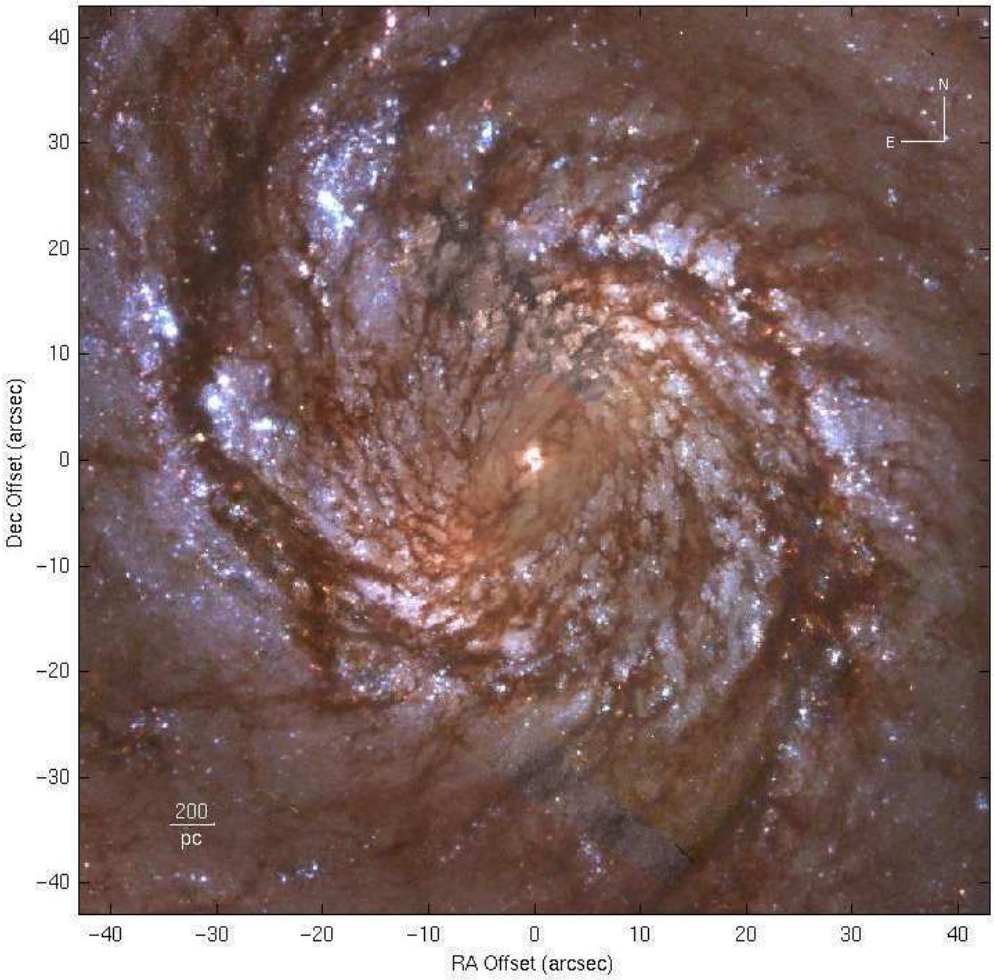

Figure 9.11: Colour composite image of the inner 4 kpc of M51 using the WFPC2 I-band image for the red display, the V-band image for the green display and the B-band image for the blue display. North is up and East on the left.

emission is observed. In correspondence of this component, discrete HII regions are located. At a distance of $\sim$ 120 pc from the arch, a second arch of HII regions, almost parallel to the radio extended emission is present. The arched shape suggests a correlation between the extended radio emission and the ionized gas. An inspection of the HII regions distribution on a larger scale shows that the H_α arch belongs to a ring around the source, therefore, its origin is probably unrelated to the jet.

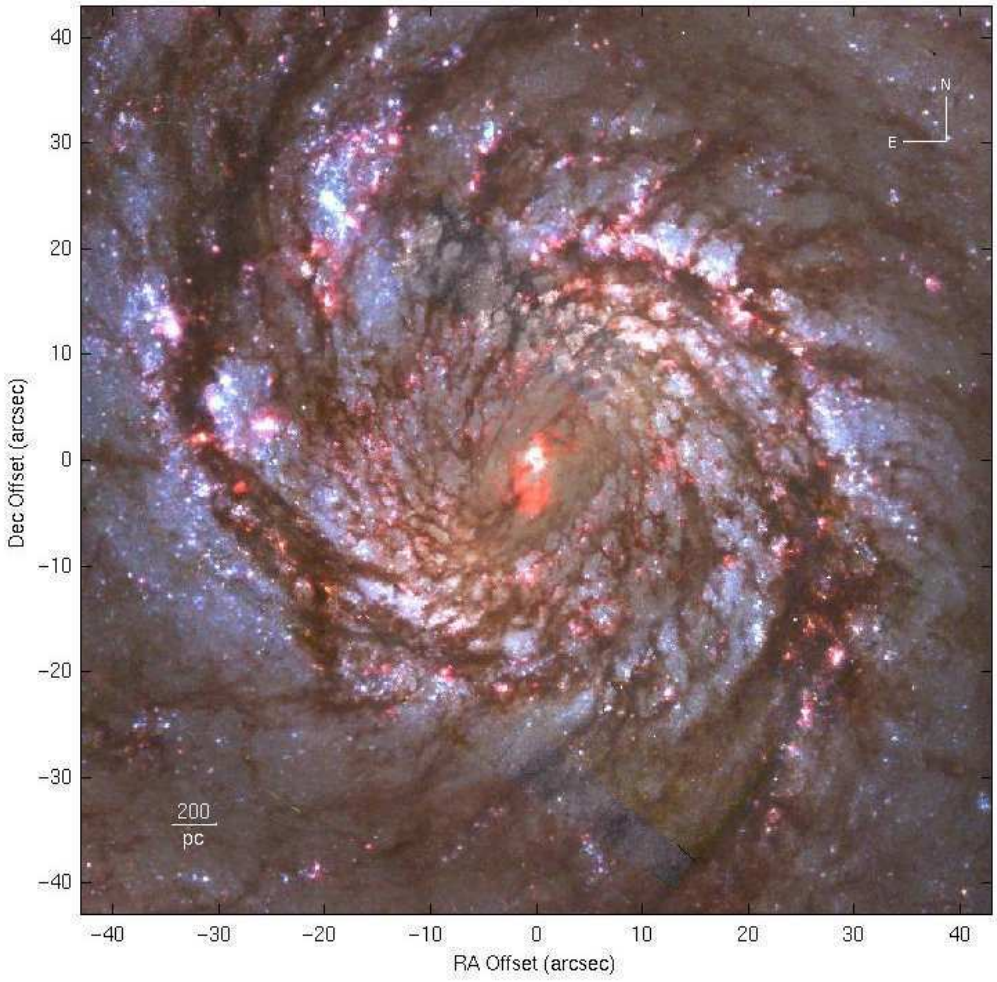

Figure 9.12: Colour composite image of the inner 4 kpc of M51 using the WFPC2 continuum subtracted H_α and the I-band image for the red display, the V-band image for the green display and the B-band image for the blue display. North is up and East on the left.

9.5 Radial profiles

The radial profiles as surface brightness in the optical bands (B, V, R and I) and in the near-IR bands (J, H and K) are shown in Figure 9.16. All curves are azimuthally averaged radial profiles, made by integrating in 0.″5 wide annuli centred on the nucleus of the galaxy, after galaxy deprojection. We assumed an inclination angle of the galaxy $i = 20°$ and the position angle of the major axis PA = 170° (Tully 1974). Three foreground stars have been removed in the optical images before producing the average profiles. Their emission is so bright that

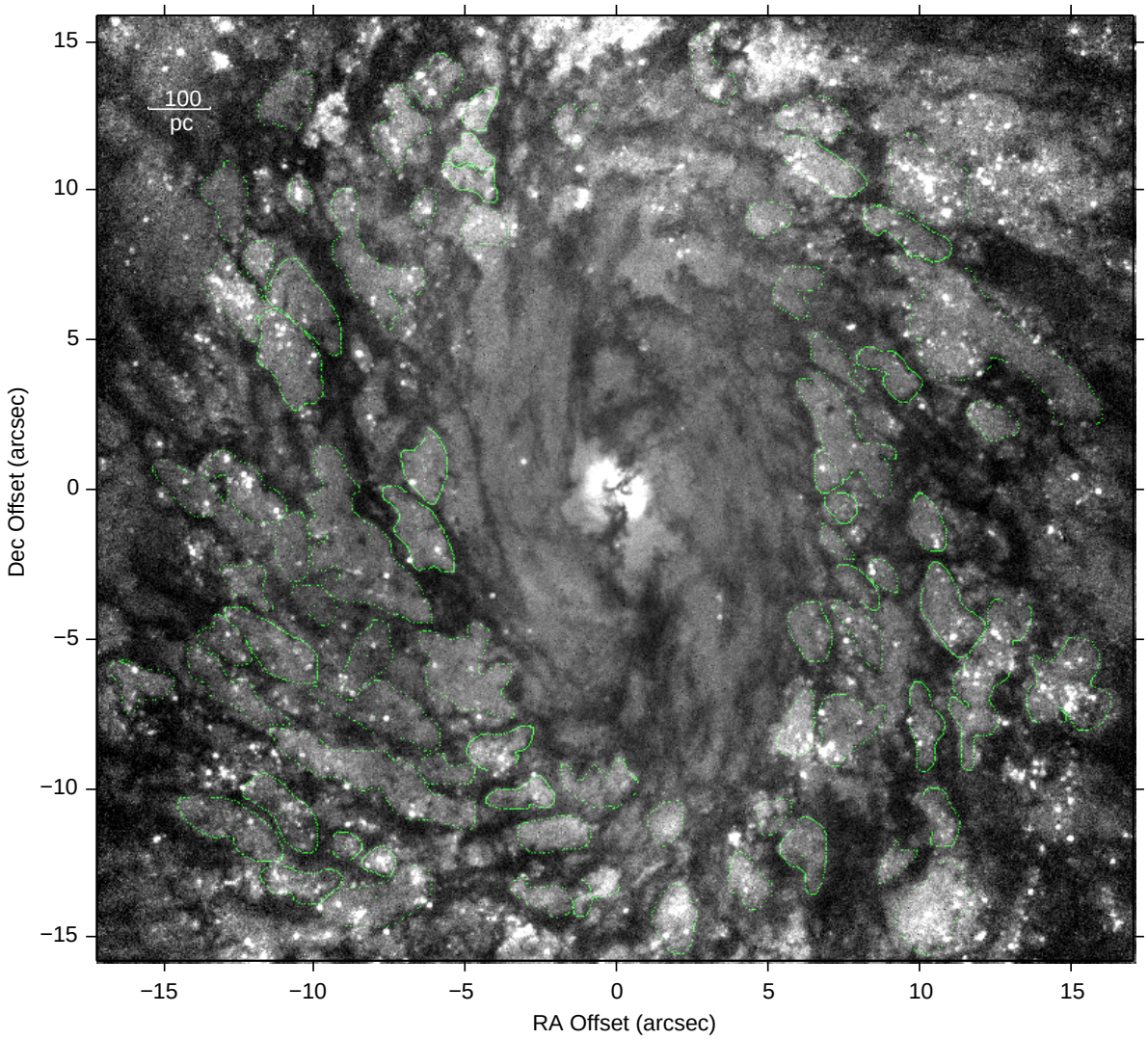

Figure 9.13: Image of the central 34″× 32″ (1.6 × 1.5 kpc) region of M51 taken by WFPC2 with the filter y (5361Å). Some cells, as defined by dust filaments, are outlined in green. North is ∼42° counterclockwise from the declination axis.

would produce peaks in the profile modifying the real profile of M51.

Azimuthally averaged profiles of the surface brightness can usually be decomposed into a central bulge and an exponential disk. Since the bulge in M51 is small compared to the disks, no bulge-disk decomposition procedure was adopted, but the inner limiting radius for measuring each disk profile was taken well outside the bulge (>1.8 kpc). The exponential decline of the disk is shown by the straight lines in Figure 9.16. For an exponential radial profile, the intensity in a spectral band decreases towards larger radii as $I(R) \propto e^{-R/R_s}$, where I is the intensity (in $L_\odot$ pc^{-2}) and R_s is the scale length. The surface brightness, μ, derived from the intensity as $\mu = -2.5\ log(I/I_0)$, will then be proportional to the radius, R. The expected relationship between μ and R is $\mu = 1.086R/R_s$ + constant. From this

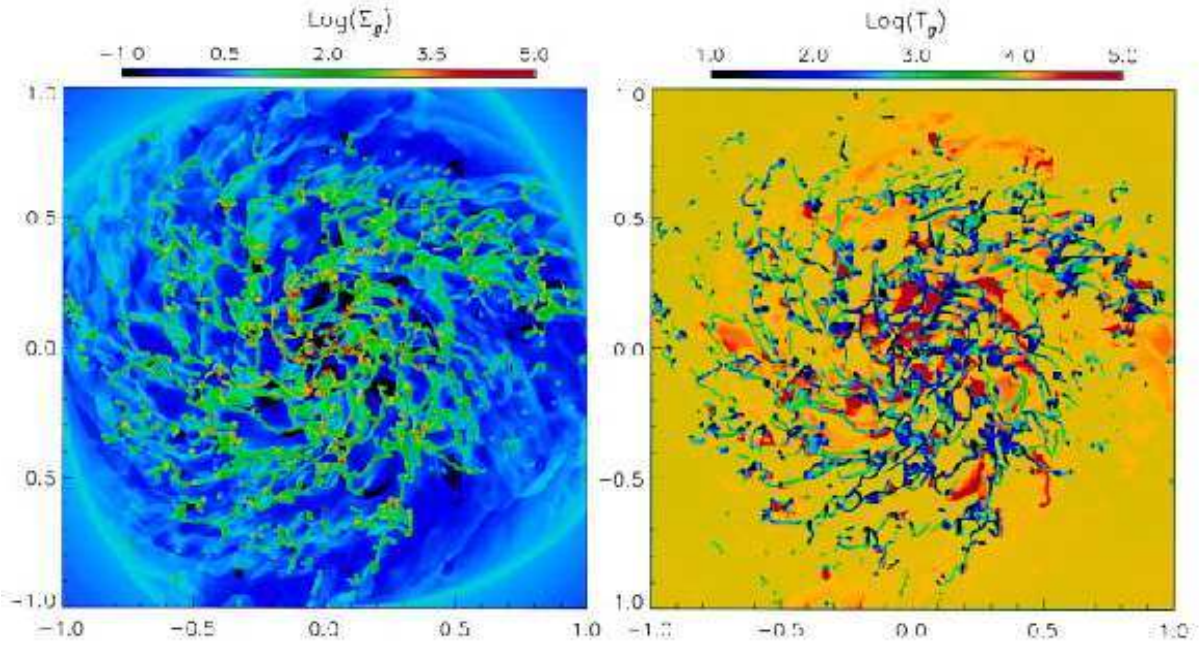

Figure 9.14: Density (left) and temperature (right) map at $t = 166$ Myr in the central 2 kpc $\times$ 2 kpc region of a galactic disk obtained as simulated by Wada and Norman (1999) . The colour bar is log-scale. The density range is 10^{-1} to 10^5 $M_\odot$ pc^{-2}, and temperature range is 10 – 10^8 K.

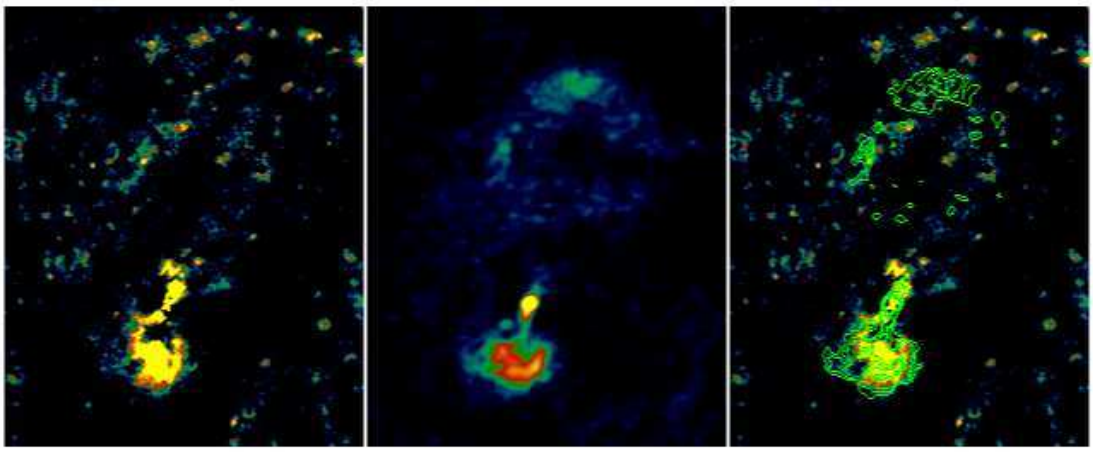

Figure 9.15: From the left to the right: H_α image of the central $21'' \times 26''$of M51, the same region at 20 cm and H_α image with the radio contours overplotted.

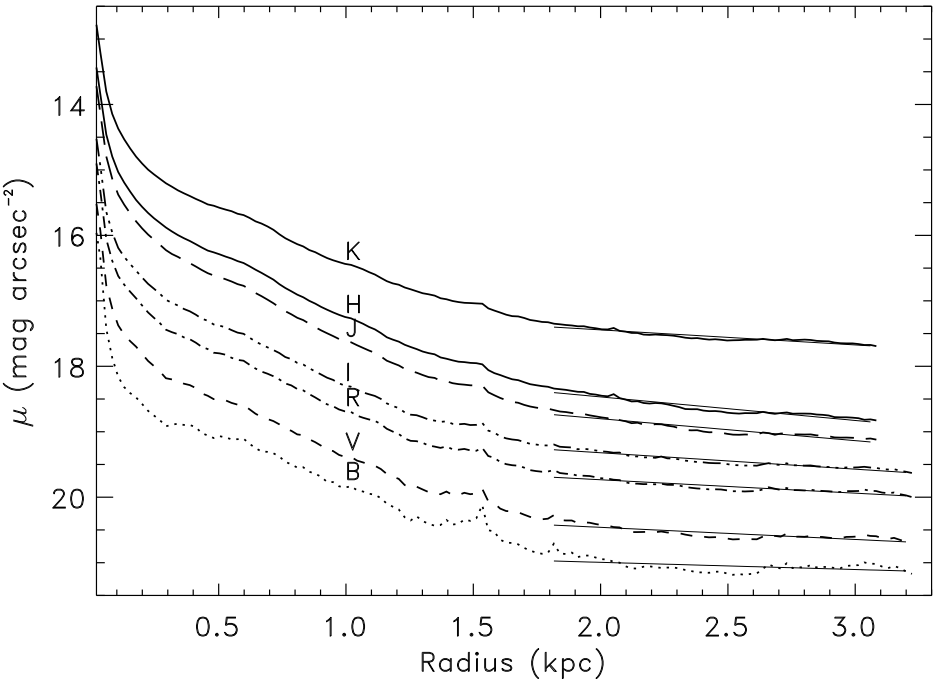

Figure 9.16: Radial surface brightness profiles in 0.″5 wide bins of optical and near-IR continuum bands. Also plotted are the linear fits to the surface brightness profiles that best fit in the range over which the lines have been drawn (R >1.8 kpc).

Table 9.2: Observationally derived scale lengths

Photometric	Scale Length R_s (arcsec)			
Band	Total	NE Arm	SW Arm	Interarm
B	212 ± 51	−39 ± 4	123 ± 27	329 ± 106
V	126 ± 12	−70 ± 210	157 ± 227	106 ± 7
R	114 ± 7	−118 ± 220	286 ± 265	84 ± 4
I	93 ± 4	−219 ± 254	134 ± 211	74 ± 3
J	70 ± 3	−278 ± 299	128 ± 218	53 ± 2
H	65 ± 3	−923 ± 865	137 ± 20	48 ± 2
K	101 ± 5	−345 ± 86	95 ± 8	95 ± 4

relationship, it is possible to derive the scale length R_s. The exponential scale-lengths R_s were calculated for all the continuum bands profiles and reported in Table 9.2.

Earlier studies suggest that the scale lengths tend to decrease systematically, but not strongly, with increasing wavelength. This effect can be attributed to extinction by moderate

amounts of dust, with radial metallicity gradients as a possible contributing factor (Elmegreen and Elmegreen 1984; Prieto et al. 1992; Evans 1994; Peletier et al. 1994, Beckman et al. 1995, de Jong 1995).

As expected the measured scale lengths decrease with the wavelength (of a factor 3 from the B to the H scale length), but an increase is observed at 2.22 μm. This might be due to the contribution from very old stellar population that have longer timescale ($\sim 2\times 10^7$ yrs) and might have a different distribution, but also an error in the images calibration. We compared our profiles with those obtained by Rix and Rieke (1993) at optical and near infrared wavelengths. We find our fluxes systematically brighter at large radii. The difference in fluxes at a radius of $40''$ is of the order of 15, 10, 28, 30, 57, 28 and 67% for the J, H, K, I, R, V, and B filters, respectively. This difference could be due to the different techniques used to derive the profiles and subtract the background. We will attempt to resolve this difference using ground-based aperture photometry. Being aware of a possible calibration problem, we proceeded in the analysis of the radial profiles.

9.5.1 Definition of arm and interarm regions

The properties of the exponential disk, i.e., of the underlying stellar mass distribution, can be better revealed by the brightness profiles of the interarm regions only rather than by those associated to the whole galaxy because of the large absorption and star formation undergoing in the arms. The large effects due to large dust absorption and star formation observed in the arms can be removed by separating the single regions, arms and interarm. This distinction allows us also to investigate the interaction between the different components of the interstellar medium (ISM) and the processes leading to star-formation in the arms by comparing the properties of the arm with those of the interarm regions.

The arm and interarm regions were defined by analyzing the maps of the deprojected galaxy in the CO, H and I bands. Any pixel (excluding bright foreground stars) with a value 1.3 times higher than the median intensity of the average profile at its radius was attributed to the arm regions. An outline was then obtained of the arms. Selected regions completely separated from the main arms or large protuberances off the arms were selected by 'eye' and then removed from the arm regions. A few zones were also added to the arm edges as suggested by a comparison of the selected regions with the I band image after dividing by the radial gradient. Figure 9.17 shows the outline of the adopted spiral arm region.

The azimuthal average radial profiles for the interarm and arm zones are shown in Figure 9.18.

The scale lengths measured for the profiles of each component (the two arms and the interarm) are reported in Table 9.2. The arm surface brightness can not be fitted by exponential profiles. This is probably caused by the starforming regions distributed along the arms. The interarm profiles show an exponential decline towards larger radii, as expected for the disk population. The scale lengths increase towards shorter wavelengths ($H \rightarrow B$). This is probably a consequence of a corresponding increase of the effects of dust extinction at shorter wavelengths. The scale lengths obtained for all of the profiles, with the exception of that obtained in the B-band, are shorter when they are calculated in the interarm region only than when the whole region is considered. This can be due to the removal of the light coming from the large number of star forming regions distributed in the arms.

From the measured scale lengths the amount of extinction in the different regions of the galaxy can be derived. This usually requires a model in which the dust is uniformly

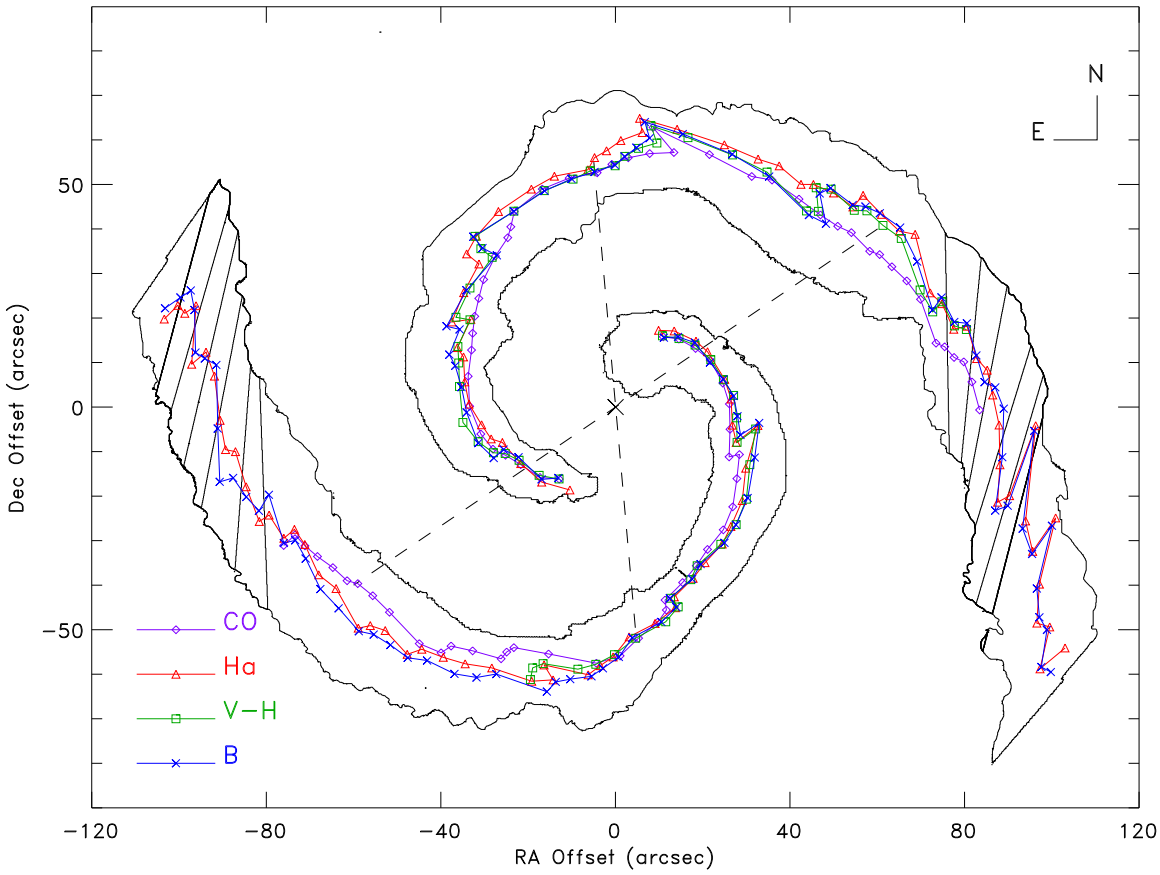

Figure 9.17: Centroid positions along the arms in different tracers (CO in purple, H_α in red, V−H in green and B in blue). The boundary between the arm and the interarm regions is outlined by the black solid curve (see section 9.5). In a portion of the two arms we report an example of some tilted boxes whose widths are double (for a better display) compared to the width used for deriving the centroid positions. The dashed lines connect two diametrically opposed regions with large and small offsets.

distributed. This assumption is obviously unrealistic, since the dust is patchy. This analysis will be performed once the difference in the radial profiles published by Rix and Rieke (1993) will be understood.

9.5.2 Arm/Interarm Contrast

In order to compute the intensity variations at different wavelengths along the arms we selected a series of equidistant points (separated by $\sim 0\farcs5$) along each arm. A region (box) $1\farcs2$ wide and perpendicular to the arms was then defined, for each point. The average flux measured in the boxes along the two arms and the ratio between the flux in the NE arm and in the SW arm in the V, H and H_α light are shown in Figure 9.6.

The NE arm is brighter than the SW arm at optical wavelengths (see also Figure 9.5).

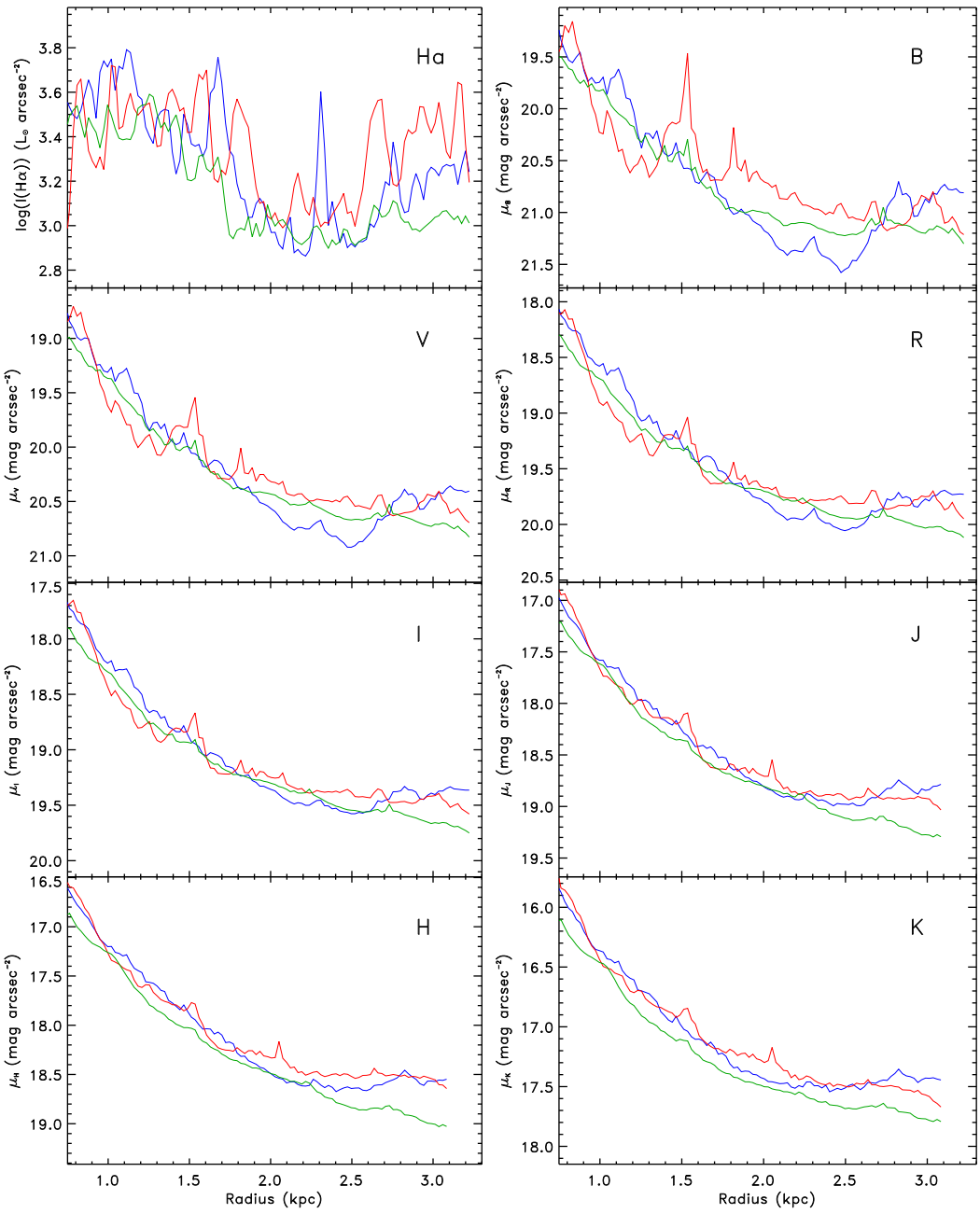

Figure 9.18: Radial surface brightness intensity profiles in 0.″5 wide bins of optical and near-IR continuum bands in selected regions: NE arm (blue curve), SW arm (red curve) and interarm (green curve). The radial profile in 5″wide bins of the intensity of the H_α emission line in logarithmic scale is also plotted.

In the near infrared and in H_α the profiles of the two arms are more similar. The observed differences can be the result of dust extinction and galaxy inclination.

9.6 Color analysis

The near-IR images primarily trace the stellar distribution, while the optical wavelength images trace both the stellar distribution and the dust. The dust distribution is therefore better traced in optical-IR colours than solely in optical or IR colours separately. The IR-optical colours also have the advantage of being less affected by the high albedo of dust grains and resultant scattering in the optical that can mask the effects of the dust at some optical depths (Witt, Thronson and Capuano 1992).

The dust features are best outlined in a colour image combining the shortest optical wavelength available (B) with the longest in the near-IR (K). For our analysis we use the V and the H images instead of the B and K images because of their better signal to noise ratio, and because the effects of extinction are still very different at these two wavelengths (e.g., a foreground dust screen with $A_V \sim 5$ will extinct 99% of the background V light and 58% of H light). The V−H colour image is shown in Figure 9.19. The most extincted regions are the brightest in the image.

The dust traces very well the spiral arms. The highest extinction is observed along the arms in the inner 1.5 kpc. The SW arms is clearly more affected by extinction than the NE arm, but both show a similar decrease in the V−H colour at larger distances from the centre. The interarm spurs and the nuclear filaments are also seen. Their typical extinction is lower than the arm dust lanes. The bar ends are very extincted and seem to follow the spiral pattern. The dust distribution is very clumpy. Straight filaments extend along the bar major axis from a radius of $\sim 10''$ from the centre of the galaxy to the bar ends.

9.7 Spatial displacements of the different tracers.

Assuming a velocity pattern for the material moving through the arms, the measure of the displacement between different tracers provides an estimation of the time elapsed between the beginning of the molecular gas compression and the formation of OB stars and HII regions. The speed of the gas along the direction perpendicular to the arm is assumed to be 30 km s^{-1} (Roberts and Stewart 1987).

The molecular and ionized gas, the young stars, and the dust are traced by CO, H_α, B and V−H, respectively.

We assume that the distribution of maximum gas density in the past follows the current distribution of molecular clouds.

In order to derive the spatial offsets between the different tracers, we divided the arm regions in boxes $1''$ wide forming an angle of 60° with the local perpendicular to the spiral arm. The inclination angle of the boxes takes into account the orbit of the material that enters in the arm, flows along the arm and emerges from the outer edge of the arms into the interarm region.

In each box, the centroid position (see Figure 9.17), its corresponding radius and azimuth angle, in the different tracers, were measured. The measured offsets in each box between the location of the B, V−H and H_α centroids and the CO centroid along the arms are plotted as function of the arm lengths in Figure 9.20 for the two arms. The offset values do not depend on the width of the arms, as shown in Figure 9.17.

For our calculations, we need the displacement along the direction perpendicular to the arms potential. Since the centroids are located in narrow boxes, the difference in the inclina-

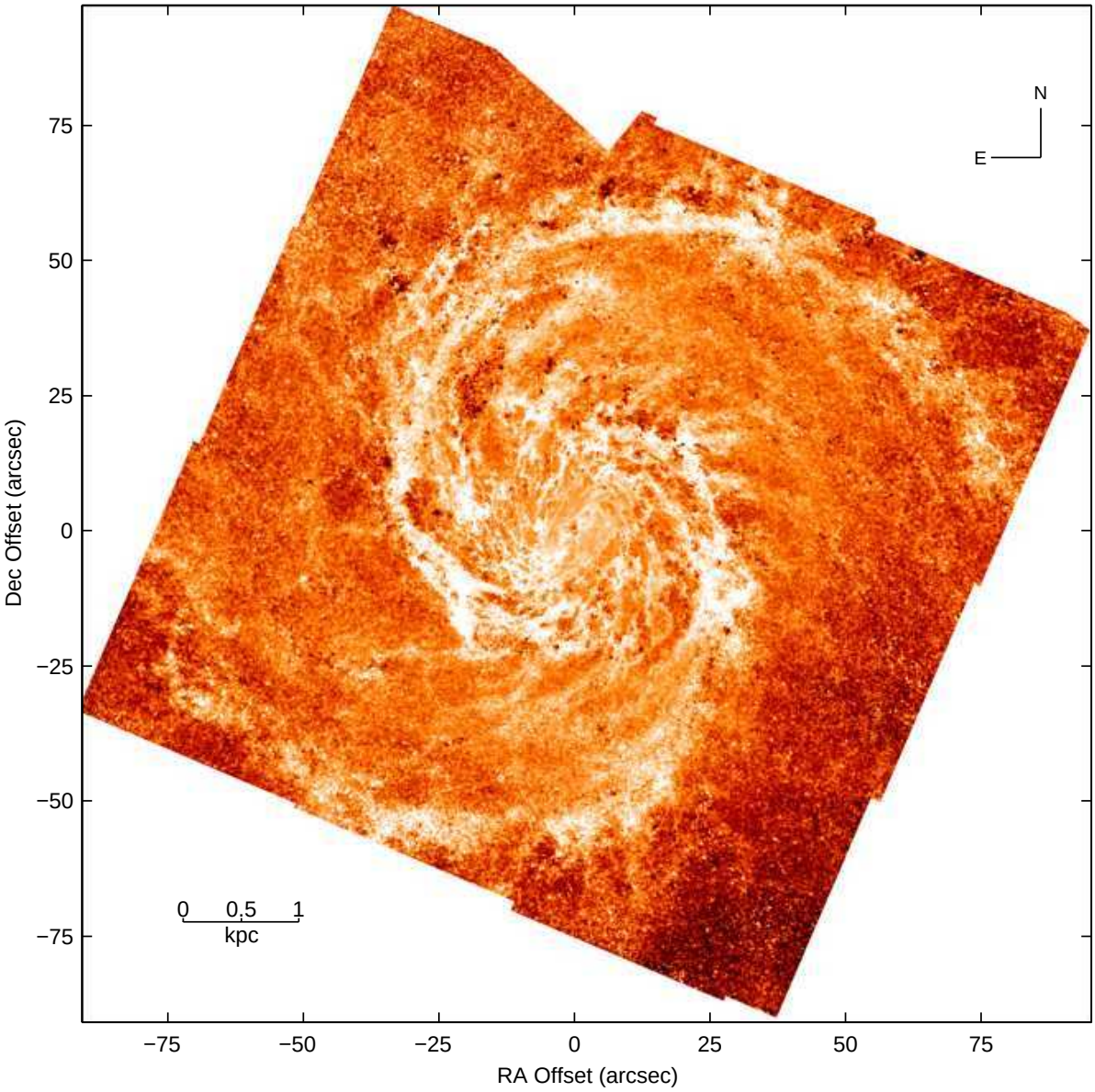

Figure 9.19: V−H colour image of M51. The brightest regions trace the more opaque regions (i.e., the dust).

tion to the arm between the angle formed by the line connecting two centroids and the major axis of the box is negligible. Therefore, the projected offsets were simply multiplied by the cosine of the inclination angle of the boxes (i.e., 60°).

The offsets measured along the direction orthogonal to the arms are, on average, 84 and 139 pc between the H_α and the CO peaks in the NE and SW arms, respectively. These distances correspond to an elapsed time of $\sim$ 2.8 and 4.5 Myr. The offset measured between the B continuum and the CO is on average $\sim$ 110 pc in both arms, corresponding to $\sim$

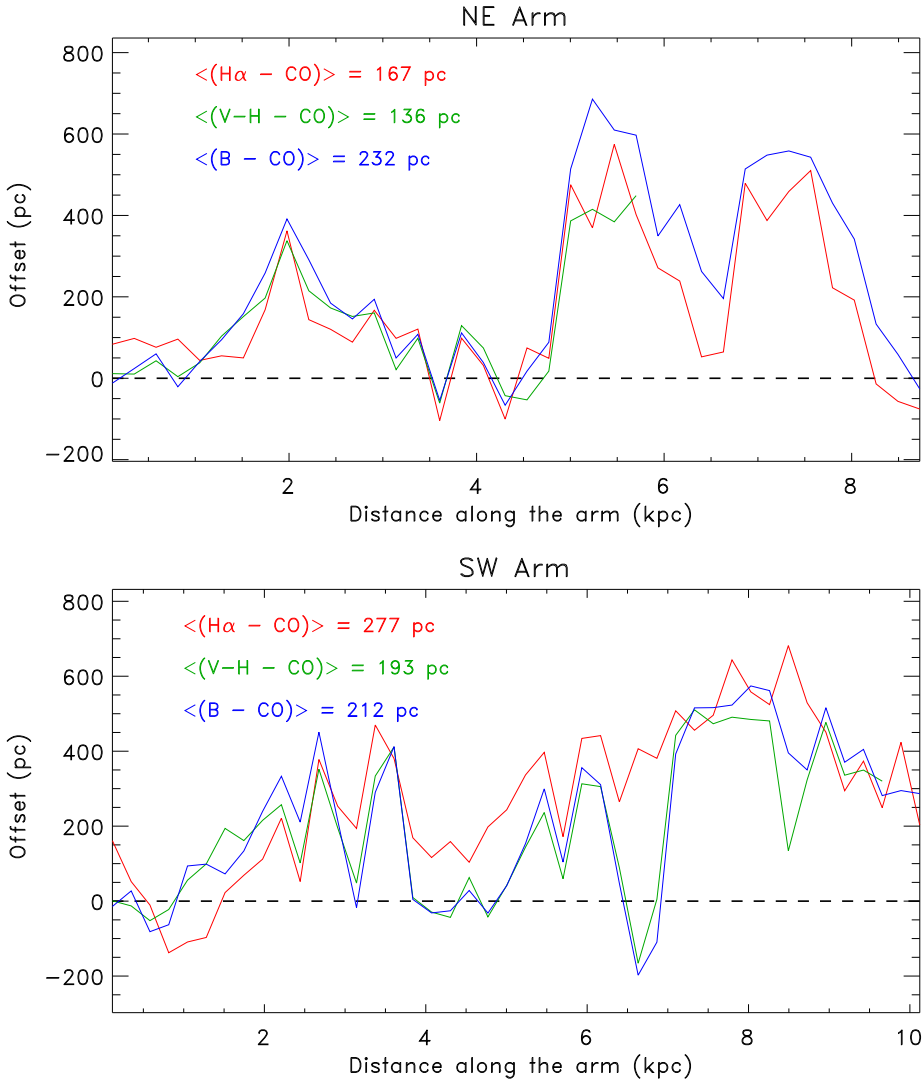

Figure 9.20: Offsets between the centroid positions of H_α (red curve), V−H (green curve), B (blue curve) and of CO along the arms.

3.6 Myr. A smaller offset is measured between the colour V−H and the CO, $\sim$ 68 and 97 pc, corresponding to $\sim$ 2.2 and 3.2 Myr. The whole process, from the compression of the molecular gas to the gas ionization by the new formed stars, takes then about 3-5 Myr.

The measured displacements have been compared with the amplitude of the spiral arms in the B light. The results are plotted in Figures 9.21 and 9.22 for the NE and the SW arms, respectively. The B light represents the lighting up of the protostars as they reach the main sequence. The B light is characterized by two different distributions below and above a threshold in the offset values. This threshold is located at $\sim$ 250 pc (corresponding to a time of 4.10 Myr) for all the tracers. Below this threshold, the stellar luminosity in the B-band is very spread, varying up to 2 magnitudes, above the threshold the distribution

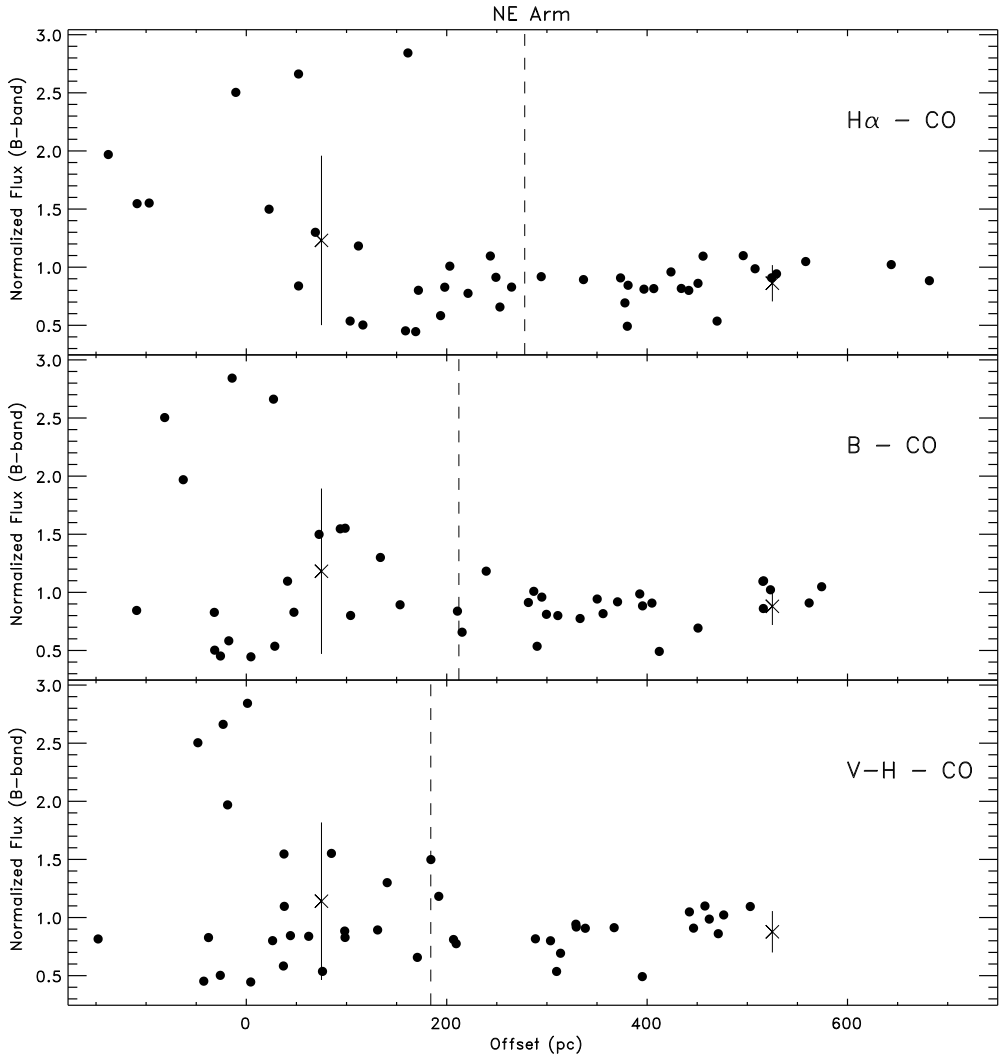

Figure 9.21: Normalized flux in the B-band along the NE arm as a function of the spatial offsets between the centroid positions of H_α and CO (top panel), V−H and CO (middle panel) and B and CO (bottom panel). The dashed lines represent the average offset values. The two crosses indicate the average B fluxes obtained for offsets below and above 250 pc, respectively. The positions of the crosses along the offset axis is arbitrary. The error bar corresponds to 1σ.

of B luminosities flattens, varying, at most, of 1 magnitude (see error bar associated to the crosses in Figures 9.21 and 9.22). Once the molecular gas gets concentrated, the stars can be observed only within a time scale separation of at most 4 Myr. The low B luminosities below the threshold might be due to dust extinction, those stars might be still embedded in large clouds cores and partially hidden by dust. Low offset values trace the most recent star formation.

The derived timescales are very short even if the real velocity were lower than the assumed value. Since the value we used was obtained from a generic model, it might not apply to M51.

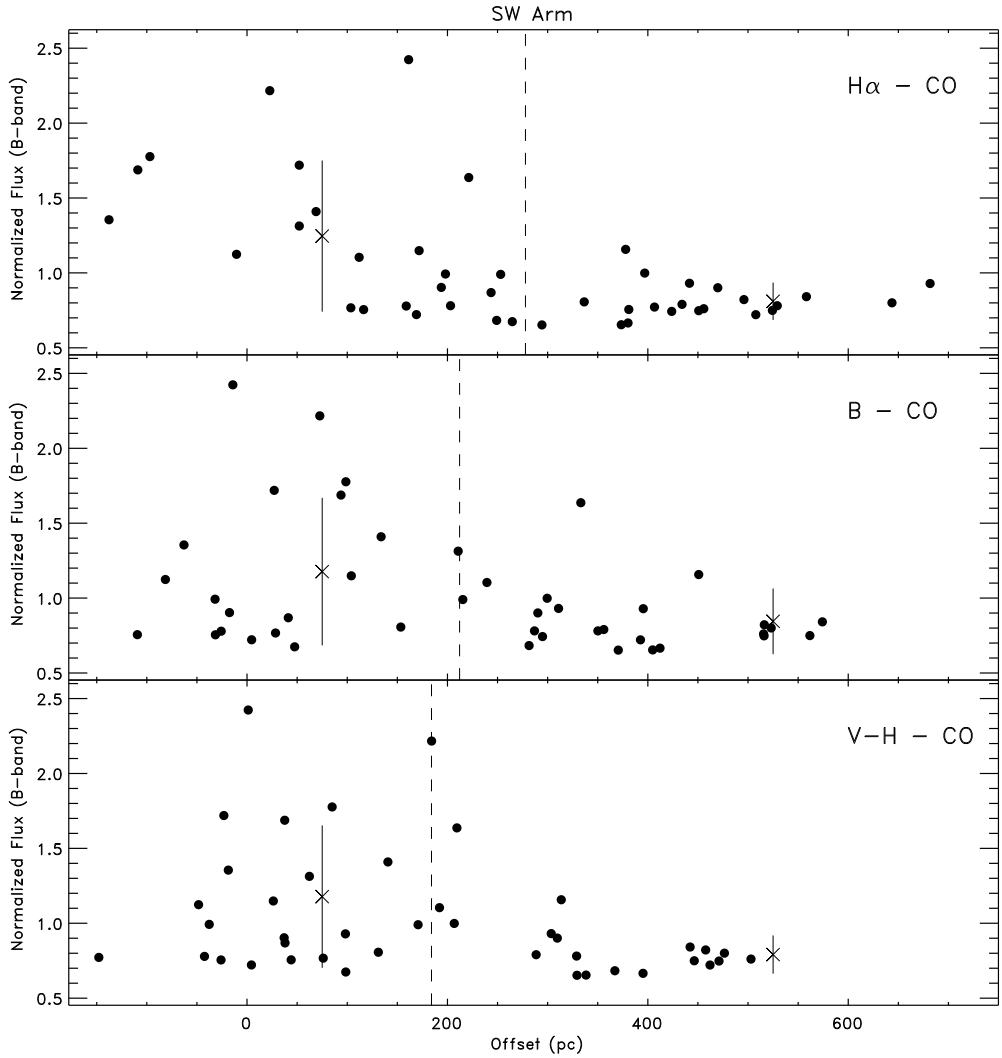

Figure 9.22: Normalized flux in the B-band along the NE arm as a function of the spatial offsets between the centroid positions of H_α and CO (top panel), V−H and CO (middle panel) and B and CO (bottom panel).The dashed lines represent the average offset values. The two crosses indicate the average fluxes obtained for offsets below and above 250 pc, respectively. The error bar corresponds to 1σ.

However, even with a velocity of 10 km s^{-1}, instead of 30 km s^{-1}, the estimated timescale would be still short (12.3 Myr).

Symmetries appear between the two arms in the star formation sites of similar age. Two examples are shown in Figure 9.17 as indicated by two dashed lines that connect two diametrically opposed regions with large and small offsets. These symmetries suggest a link between the spiral structure (e.g., resonances in the density waves) and the star formation. The symmetry suggests a correlation between the star formation and the spiral arm density waves. The stars do not form only from the collapse of the individual clouds, but from the

interaction of clouds and the spiral structure.

It is worth to notice that, even if several molecular clouds are accompanied by a patch of H_α emission, their intensities are not correlated. The brightest HII regions generally do not coincide with the largest molecular clouds. The lack of correlation between the more active star formation sites and the larger local surface density of molecular gas disfavour the cloud-cloud collisions process as origin of the formation of high mass stars.

The comparison between the H_α and the CO maps suggests a link between the star formation pattern and the spiral density waves. Our result is in agreement with earlier studies. Knapen et al. (1992) found a pattern of dips and strong peaks in the arm-interarm efficiency ratio, which is symmetric in the two main arms of M51. The fact that the efficiency ratios are consistently larger than unity along both arms has been interpreted as strong evidence for triggering of the massive star formation in the spiral arms. García-Burillo, Guélin and Cernicharo (1993), using IRAM CO data of slightly higher resolution than those used by Knapen et al. (1992), confirmed the findings of the latter authors on relative arm/interarm contrasts.

9.8 Conclusions

HST images at optical and near-infrared wavelengths of the grand-design spiral galaxy M51 were presented and discussed.

The high spatial resolution and sensitivity provided by the HST shows several new structures in M51 with unprecedented detail and give new insights on the dust distribution. The sizes of these structures can be constrains for theoretical models of galactic structures formation. Several dust lanes are observed in the arm, interarm and nuclear regions. The sizes of these dust lanes range from ~ 50 pc of width in the interarm region to $\sim 140 - 370$ pc along the arms. The formers extend from the arms to the interarm region forming an angle to the arm of $\sim 40°$. A net of dust filaments is observed in the central kpc of the galaxy. These filaments are regularly spaced ($\sim$40–130 pc). This dusty net can be caused by hydrodynamic instabilities in a non self-gravitating disk (i.e., turbulent gas motion driven by the inflow of material from larger radii) (Wada and Norman 1999). The dusty net disappears where the central stellar bar appears.

Several associations of massive OB stars with associated ionized gas (traced by H_α emission) are observed along the spiral arms and in the circumnuclear region. These regions are sites of enhanced star formation. Strong H_α emission is observed in the nuclear region, which is strongly correlated with the radio emission from the jet. The observed correspondence suggests an interaction between the jet and the surrounding material.

The radial profiles of the stellar (continuum bands: K, H, J, I, R, V, B) tracers are a useful tool to estimate the effects of extinction as a function of the radius, in the arm and interarm regions. The profiles become flatter going from long to short wavelengths.

Since the arms are sites of strong star formation and extinction, the radial profiles have been calculated separately for the interarm and the arm regions. The exponential curve is not a good fit for the arms' profiles probably because of their enhanced star formation. The interarm profiles are still exponentially decreasing and more similar to the profiles of the whole galaxy. A flattening of the interarm profiles at shorter wavelengths is observed, but less pronounced compared to that measured in the profiles relative to the whole galaxy.

We trace massive stars using observations of the blue continuum, the molecular gas

through CO lines observations, the dust by near-IR−optical colours (i.e., V−H), the ionizing photons emitted by the new born stars by hydrogen recombination lines (e.g., $H_\alpha\lambda 6563$Å and $Pa_\alpha\lambda$ 1.87μm).

Assuming a velocity pattern for the material moving through the arms, the measure of the displacement between the different tracers provides an estimate of the time elapsed between the beginning of the molecular gas compression and the formation of OB stars and HII regions. We derived a maximum timescale of 4 Myr.

An inspection of the distribution of starforming sites along the two spiral arms suggests a link between the star formation process and the spiral structure itself.

Bibliography

Aalto S., Huettemeister S., Scoville N.Z., Thaddeus P., 1999, ApJ, 522, 165
Aaronson M. 1977, Ph.D. Thesis, Harvard University
Beckman J., Peletier R.F., Knapen J.H., Mate M.J., Gentet L.J. 1995, in "The Opacity of Spiral Disks", eds. J. Davies and D. Burstein (Dordrecht: Kluwer)
Biretta J.A. et al. 2000, WFPC2 Instrument Handbook, Version 5.0 (Baltimore: STScI)
Bushouse H.A., Stobie E. 1998, ADASS, 7, 300
Byrd G.G., Howard S. 1989 "M51's Material Arms and Density Waves in Dynamics and Interactions of Galaxies", ed. R. Wichen
Condon J.J. 1987, ApJS, 65, 485
Crane P.C., van der Hulst J.M. 1992, AJ, 103, 1146
de Jong R.S. 1995, Ph.D. Thesis, Univ. of Groningen
Elmegreen B.G. 1979, ApJ, 231, 372
Elmegreen B.G., Lada C.G. 1979, ApJ, 214, 725
Elmegreen D.M., Elmegreen B.G., 1984, ApJ Suppl., 54, 127
Elmegreen B.G., Elmegreen D.M., Seiden P.E. 1989, ApJ, 343, 602
Elmegreen B.G. 1994, ApJ, 433, 39
Evans R. 1994, MNRAS, 266, 511
García-Burillo S., Guélin M., Cernicharo J. 1993, A&A, 274, 123
Grillmair C.J., Faber S.M., Lauer T.R., Hester J.J et al. 1997, AJ, 113, 225
Holfeltz S., Calzetti D., Bergeron E. et al. 1999, NICMOS Data Handbook Version 4.0 (Baltimore: STScI)
Holtzman J.A., Burrows C.J., Casertano S., Hester J.J. et al. 1995, PASP, 107, 1065
Kennicutt R.C., Edgar B.K., Hodge P.W. 1989, ApJ, 337, 761
Kennicutt R.C., Tamblyn P., Congden C.W. 1994, ApJ, 435, 22
Knapen, J.H., Beckman J.E., Cepa J., van der Hulst J.M., Rand R.J. 1992, ApJ, 385, 37
Knapen J.H., Beckman J.E. 1996, MNRAS, 283, 251
Lord S.D., Young J.S. 1990, ApJ, 356, 135
Peletier R.F., Valentijn E.A., Moorwood A.F.M., Freudling W. 1994, A&A Suppl., 108, 621
Prieto M., Beckman J.E., Cepa J., Varela A.M. 1992, A&A 257, 85
Rand R.J., Kulkarni S.R. 1990, ApJ, 349, L43
Rieke et al. 2001, (in preparation)
Rix H.-W., Rieke M.J. 1993, ApJ, 418, 123
Roberts W.W. 1969, ApJ, 158, 123
Roberts W.W., Stewart G.R. 1987, ApJ, 314, 10
Rose J.A., Cecil G. 1983, ApJ, 266, 531
Rydbeck, Hjalmarson and Rydbeck 1985
Sauvage M., Blommaert J., Boulanger F., Cesarsky, C.J. et al. 1996, A&A, 315, L89

Schweizer F. 1976, ApJS, 31, 313
Scoville N.Z., Sanders D.B., Clemens D.P. 1986, ApJ, 310, L77
Scoville N.Z., Yun M.S., Armus L., Ford H. 1998, ApJ, 493, L63
Tan J.C. 2000, ApJ, 536, 173
Thompson R.I., Corbin M.R., Young E., Schneider, G. 1998, ApJ, 492, L177
Tilanus R.P.J., Allen R.J., van der Hulst J.M., Crane P.C. Kennicut R.C. 1988, ApJ, 330, 667
Tilanus R.P.J., Allen R.J. 1989, ApJ, 339, L57
Toomre A. 1978, in "The Large Scale Structure of the Universe", eds. M.S. Longair & J. Einasto (Dordrecht: Reidel)
Tully R.B. 1974, ApJS, 27, 437
Vogel S., Kulkarni S., Scoville N.Z 1988, Nature, 334, 402
Wada K., Norman C.A. 1999, ApJ, 516, L13
Wang J.C.L., Heckman T.M., Lehnert M.D. 1997, ApJ, 491, 114
Witt A.D., Thronson H.A., Capuano J.M. 1992, ApJ, 393, 611
Zaritsky D., Rix H.W., Rieke M. Nature 1993, 364, 313

Chapter 10

High Mass, OB Star Formation in M51: HST H_α and Pa_α Imaging

We have obtained H_α and Pa_α emission line images covering the central $3'$– $4'$ of M51 using the WFPC2 and NICMOS cameras on HST to study the high-mass stellar population. The $0\farcs1$ – $0\farcs2$ pixels provide 4.6 – 9 pc resolution in M51 and the H_α/Pa_α line ratios are used to obtain extinction estimates. A sample of 1882 H_α emission regions was catalogued using an automated and uniform measurement algorithm. Their sizes are typically 10 – 100 pc. The luminosity function for the H_α emission regions is obtained over the range $L(H_\alpha) = 10^{36}$ to 10^{39} erg s^{-1}. No regions were found above $L(H_\alpha) = 10^{39}$ erg s^{-1}; this is approximately a factor of 6 lower than the maximum seen in earlier ground-based studies which may have blended multiple regions at the high end. Our luminosity function is also somewhat steeper ($dN/dlnL \propto L^{-1.2}$) on the high luminosity tail than ground-based determinations ($L^{-0.5\rightarrow-0.8}$) – probably also a result of resolving previously blended regions.

To analyse the variations of HII region properties *vis-à-vis* the galactic structure, the spiral arm areas were defined independently from mm-CO, infrared and optical continuum imaging. Although the arms constitute only 30% of the disk surface area, the arms contain 80% of the catalogued HII regions. The luminosity function is somewhat flatter in the nuclear and spiral arm regions than in the interarm areas; however, this is very likely the result of increased blending of individual HII regions in those regions with higher surface densities. No significant difference is seen in the sizes and electron densities of the HII regions in spiral arm and interarm regions. For 326 regions which had $\geq 5\ \sigma$ detections in both Pa_α and H_α, the observed line ratios indicate visual extinctions in the range $A_V = 0$ to 5 mag. The mean extinction was $A_V = 3.2$ mag (weighting each region equally), 2.4 mag (weighting each by the observed H_α luminosity) and 3.01 mag (weighting by the extinction-corrected luminosity). On average, the observed H_α luminosities should be increased by a factor of ~ 9, implying comparable increases in global OB star cluster luminosities and star formation rates. The full range of extinction-corrected H_α luminosities is between 2×10^{36} – 2×10^{39} erg s^{-1}. The most luminous regions have sizes ~ 100 pc so it is likely they are blends of multiple regions. The upper limit for individual clusters is therefore probably a factor of a few lower. The derived range of cluster masses is 100 – 2000 $M_\odot$. This range is roughly comparable to HII regions ranging between 1/3 of M42 (the Orion Nebula) and W49 (the most luminous Galactic radio HII region). The upper limit to the luminosity function corresponds to an ionizing photon production rate $Q_{Lyc\ up} = 1.4 \times 10^{51}$ s^{-1} (with no corrections for dust absorption of the

Lyman continuum or UV which escapes to the diffuse medium). The total star formation rate in M51 is estimated from the extinction-corrected H_α luminosities to be $\sim 5M_\odot$ yr^{-1} (assuming a Salpeter IMF between 1 and $120M_\odot$) and the cycling time from the neutral ISM into these stars is 10^9 yr.

We develop a simple model for the UV output from OB star clusters as a function of the cluster mass and age in order to interpret constraints provided by the observed luminosity functions. Both the width of the peak in the luminosity function and the -1.2 power-law index strongly rule out flat **cluster** mass spectra, but are consistent $N(M_{cl})/dM_{cl} \propto M_{cl}^{-3}$. The highest mass clusters ($\sim 2000M_\odot$) correspond to a mass such that the IMF is first populated up to ~ 120 $M_\odot$, but this cluster mass is only 1% of that available in a typical GMC. We suggest that OB star formation in a cloud core region may be terminated at the point that radiation pressure on the surrounding dust exceeds the self-gravity of the core star cluster. This occurs at a stellar luminosity-to-mass ratio ~ 1000 $L_\odot/M_\odot$; which happens for clusters ≥ 750 $M_\odot$. We have modelled the core collapse hydrodynamically and find that a second wave of star formation may propagate outwards in a radiatively compressed shell surrounding the core star cluster – this triggered, secondary star formation may be the mechanism for formation of super star cluster (SSC) seen in starburst galaxies.

10.1 Preamble

Were it not for the small number of youthful, luminous stars and their ongoing genesis, much of the beauty, vigour and evolution that is our fascination in the universe would be lost to the distant past. Energizing and enriching the disks of galaxies are the most massive stars of each generation. In youth, they illuminate the bright nebulae which so elegantly outline the spiral arms of distant galaxies; in death, their cataclysmic supernovae replenish the interstellar environment with gases, enriched in heavy elements. From these ashes the future generations of stars will arise. The springs of rejuvenation are giant molecular clouds encompassing millions of solar masses of cold gas. Inside these ponderous cocoons, the metamorphosis of stars takes place in dusty darkness.

10.2 Introduction

High mass OB stars play a critical role in the energetics and dynamics of the ISM and in the highest luminosity phases of galactic structure and evolution, specifically the luminous spiral arm and starburst activity. Nevertheless, the mechanisms for formation of OB associations remain poorly understood and indeed, it is uncertain whether high and low mass stars are formed by the same or different processes. HII regions have long been a primary probe of high-mass star formation and the properties of OB star clusters. The hydrogen recombination line fluxes (e.g., H_α) or radio free-free continuum are proportional to the HII region emission measure. The latter is proportional to the total Lyman continuum emission rate of the associated high-mass stars under the assumption that all ionizing photons are locally absorbed. Thus the H_α luminosity of an emission region is indicative of the Lyman continuum emission and hence the mass of high-mass stars (correcting for extinction and assuming an IMF). The luminosity function of the HII regions can then be used to study the distribution of masses and birth rates of OB associations. M51 is a Rosetta stone for studies of OB star formation – on account of its proximity – 9.6 Mpc (Sandage and Tammann 1975); its grand design spiral

pattern; its orientation – i = 20° (Tully 1974) and its abundant, dense ISM (Scoville and Young 1983).

M51 has been the focus of numerous ground-based H_α studies (Kennicutt, Edgar and Hodge 1989; Rand and Kulkarni 1990; van der Hulst et al. 1988; Rand 1992; Rozas et al. 1996; Petit et al. 1996; and Thilker et al. 2000), and these studies have contributed much of what is currently known regarding OB associations in other spiral galaxies. The distribution of HII region H_α luminosities was approximately fit by a truncated power-law with (N(L) d ln(L) $\propto L^{-0.55 \rightarrow -0.75}$) – on the high luminosity end. In several previous H_α studies (e.g., Rand 1992 and Thilker et al. 2000), the luminosity function appears steeper in the interarm regions than in the arms (exponent $-0.93 \rightarrow -0.96$ versus $-0.48 \rightarrow -0.72$). The bright end ($L(H_\alpha) \geq 10^{38.8}$ erg s^{-1}) of the HII region luminosity function contributes the bulk ($\geq 50\%$) of the discrete HII region luminosity (Rand 1992), but approximately 55% of the total H_α luminosity originates from diffuse ionized gas (DIG), i.e., not in discrete regions (Rand 1992; Greenawalt et al. 1998). Based on ground-based imaging, it remains uncertain whether the DIG is blended low luminosity regions or truly diffuse gas.

We have recently completed a comprehensive study of M51 comprised of HST (WFPC2 and NICMOS) imaging of the optical and near infrared continuum (Polletta et al. 2001) and the H_α and Pa_α emission lines (this paper). Related mm-CO interferometry has been presented in Aalto et al. (1999). The former probes the stellar disk, the dust, and the OB star formation while the latter probes the dense, molecular ISM which is the birthsite of OB star clusters.

The $0\farcs1$ – $0\farcs2$ resolution available with HST imaging corresponds to 4.6 – 9.3 pc. These sizes correspond to those of individual resolved Galactic HII regions (e.g., the Orion Nebula). For comparison, ground-based H_α imaging at resolutions $\geq 1''$-$2''$ corresponds to at least 50 – 100 pc, the size of a large Galactic giant molecular cloud (GMC). The latter resolution will clearly blend multiple sites of OB star formation which occur within a single GMC (for example M42 and NGC 2024 in the Orion GMC). At the same time, the ground-based resolution element will also contain enormous volumes of intervening neutral gas. The high angular resolution of the HST imaging is thus critical for the study of extragalactic HII region properties.

To date there have been surprisingly few studies of extragalactic HII regions using HST. A recent study of M101 by Pleuss et al. (2000) clearly demonstrates the advantages of HST. Specifically, the break in the luminosity function (LF) slope at $\log(L(H_\alpha)) = 10^{38.6}$ seen in many ground-based imaging studies disappeared, and multiple HII regions were resolved into individual regions of lower luminosity, resulting in a very different distribution of HII region sizes.

10.2.1 Our Study

This paper which presents HII emission line imaging addresses the following specific issues:

1) the global luminosity function of the HII regions and their associated OB star clusters;

2) comparison of the form of the luminosity function with theoretical expectations;

3) variations in the luminosity function from arm to interarm regions and between the nuclear region and the galactic disk;

4) the HII region sizes and densities; and

5) analysis of the reddening and extinction of the HII regions based on the observed ratios of H_α/Pa_α lines.

Table 10.1: M51 H_α and Pa_α Observations

Instrument	Prog. ID	Date	Filter	λ (μm)	Exposure/s (sec)	Orientation angle[a]
WFPC2	5123	Jan 24, 1995	F656N (H_α)	0.6561	400 + 1400	93.1998
	5123		F547M (y)	0.5361	260 + 600	
	7375	Jul 21, 1999	F656N (H_α)	0.6561	1300 + 700	
			F814W (I)	0.8386	700 + 300	
NICMOS3	7237	Jun 28, 1998	F187N (Pa_α)	1.8740	576	−113.168
			F190N	1.9005	576	

[a]For WFPC2 it corresponds to PA-V3: angle between the axis V3 of the camera and the North. For NICMOS it corresponds to the angle between the y axis of the camera and the North.

To address these issues in a meaningful way and fully understand the observational limitations, we develop automated routines for the definition of the HII region boundaries and a model to simulate the blending of multiple regions. The temporal evolution of the Lyman continuum emission from an OB star cluster is also modelled and constraints on the cluster mass distribution are derived from the observed luminosity function of HII regions. Lastly, we analyse the physical processes important in determining the masses and sizes of OB star clusters forming within a molecular cloud core.

In the following sections, we present the observations and images for H_α and Pa_α (10.3, 10.4), discuss the definition and measurement of the HII regions (10.5), use the H_α/Pa_α ratio to estimate the extinction of the individual HII regions (10.7) and hence derive the observed and extinction-corrected luminosities (10.6, 10.7). The size and density distributions for arm and interarm regions are discussed in 10.8. In 10.9, we compare briefly the HII region properties with those in the Galaxy. In 10.10 we present a simple model invoking instantaneous OB star formation with a standard IMF to provide a context for interpretation of the observational data. We also develop a model for the formation of OB star clusters in which the mass of the core cluster is limited by radiation pressure once the cluster has accumulated $\sim 1000 M_\odot$. In 10.11, we use the total fluxes in H_α to estimate the overall Lyman continuum production and star formation rate in M51.

10.3 Observations

HST imaging of M51 using both WFPC2 and NICMOS was obtained in several observing programs as discussed in Polletta et al. (2001) and summarized in Table 10.1.

10.3.1 WFPC2

The WFPC2 continuum and H_α images were obtained in 1995 January (Ford, Tsvetanov and Kriss 1996) and in 1999 July by Scoville and Ewald (filling in the areas not covered in the Ford

et al. archive data). The raw images were flat-fielded using the automatic standard pipeline at the STScI and cosmic rays were removed using our own procedure. The complete calibration procedures are described in Polletta et al. (2001). For subtraction of continuum from the F656N image, which includes H_α and continuum, the y-band (F547M) image was used in the earlier epoch and I-band (F814W) for the later epoch. The broad band continuum image was first scaled by a constant such that the signal strengths on a sample of stars balanced those in the F656N image.

10.3.2 NICMOS

NICMOS (187N and 190N) images were obtained as part of the NICMOS GTO program with a mosaic of 9 NIC3 fields covering most of the area of the WFPC2 images. NICMOS Camera 3 uses a 256×256 HgCdTe array with plate scales of $0''.203859$ and $0''.203113$ per pixel in x and y, providing a $\sim 52''.19 \times 52''.00$ field of view (Thompson et al. 1998). The F187N and F190N filters with effective wavelengths of 1.87 and 1.90 μm were used to obtain on and off-band images. The FWHM resolution is $0''.19$ at 1.87 μm. Observations at each of the 9 mosaic positions were done using a spiral dither in each filter setting and at each dither position, non-destructive reads (MULTIACCUM) were taken. The total integration times for each filter are listed in Table 1.

The data were reduced and calibrated using the CALNICA version 3.3 task (Bushouse and Stobie 1998) in IRAF[1]/STSDAS and the reference files (static data quality, detector read noise, detector non-linearities files) from the Space Telescope Science Institute (STScI) NICMOS pipeline, with the exception of the flat-field, and dark frame corrections that were provided by the NICMOS Instrument Development Team. The dithered images were then shifted and mosaiced using the NICMOSAIC and NICSTIKUM IRAF tasks (D. Lytle 1998, private communication). The images were mosaiced with relative offsets determined from common stars in the overlap regions and rotated with north up and east to the left using the data-header orientation angle (see Polletta et al. 2001).

10.3.3 WFPC2 and NICMOS Flux Calibration

Flux calibration of the WFPC2 images is done as described in Polletta et al. (2001). For the NIC3 images, we employ scale factors of 5.050×10^{-5} and 5.033×10^{-5} Jy (ADU/sec)$^{-1}$ at 1.87 (Pa_α) and 1.90 μm (Rieke et al. 2001). The rms noise in the final images is typically 62 and 59 μJy (arcsec)$^{-2}$ at 1.87 and 1.90 μm. As a check on the flux calibration, three of the coauthors of this paper independently calibrated the H_α and Pa_α images with similar results (within 10%).

The H_α filter on WFPC2 transmits the [NII] lines (6548.1Å and 6583.4Å in to H_α and stellar continuum. At the redshift of M51 ($z = 0.00154$), the transmissions are 98.7, 0.0 and 91.2% for the two redshifted [NII] lines and H_α, respectively. Adopting a total flux in the [NII] lines of $0.4 \times H_\alpha$ in M51 (Wang, Heckman and Lehnert 1997) and a flux ratio of 1:3 for the two [NII], we find that the detected line flux will be 1.012 times that of H_α. This fortuitously happens because the redshift reduces transmitted flux of H_α by nearly the same

[1]IRAF is distributed by the National Optical Astronomy Observatories, which are operated by the Association of Universities for Research in Astronomy, Inc., under cooperative agreement with the National Science Foundation.

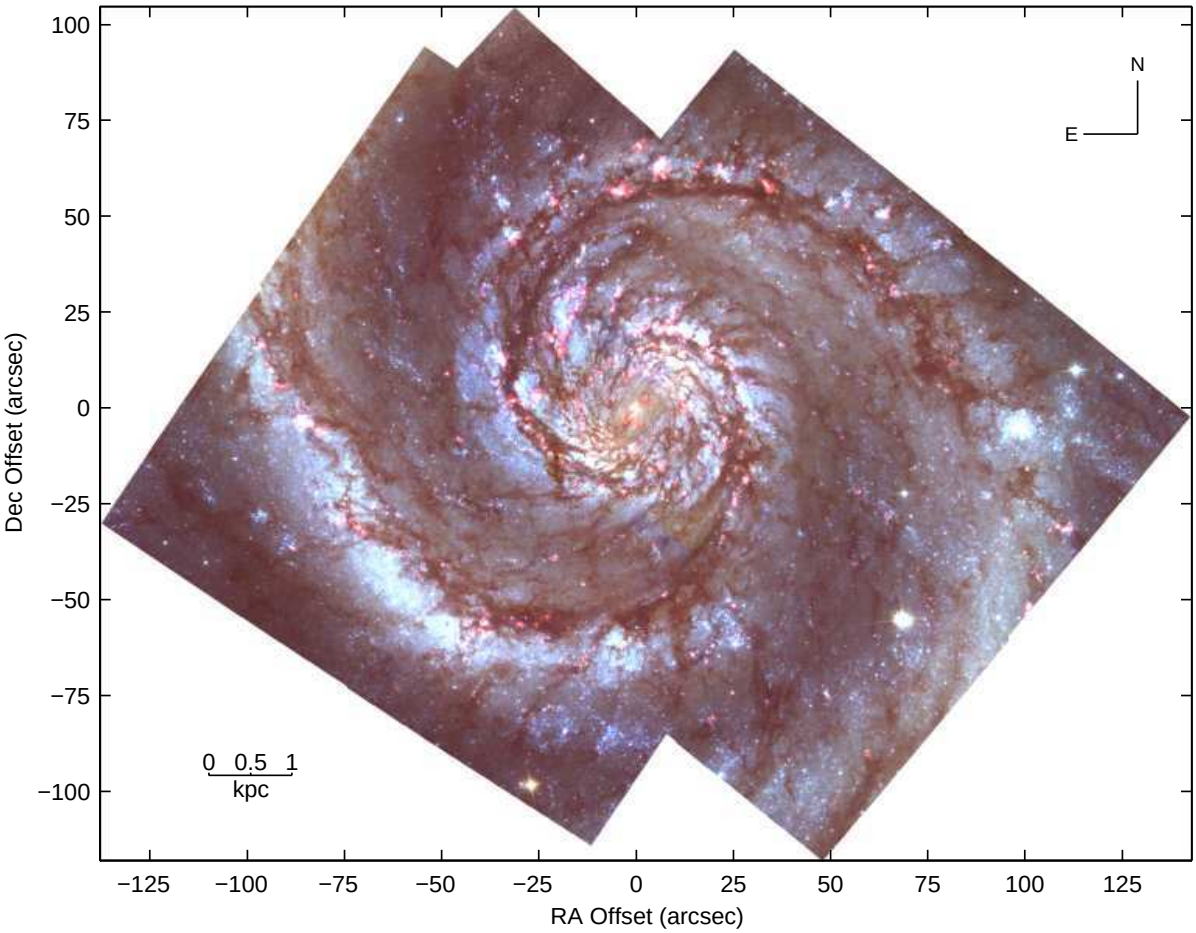

Figure 10.1: The full mosaic of WFPC2 H_α (continuum subtracted) images for the central $281'' \times 223''$of M51. The H_α emission is shown in red and continuum V and B bands are in green and blue, respectively. (In the red, we also added the I band image in order to balance the colours on the stars.)

amount that the transmitted flux of the 6548.1Å [NII] line is increased. We therefore neglect this 1% correction.

10.4 Images

The mosaic of continuum-subtracted H_α images is shown in Figure 10.1 for the central $281'' \times 223''$. The H_α and the continuum I band are displayed in red, and the continuum V and B bands in green and blue, respectively. H_α emission extends out $10''$ from nucleus at PA $\sim -15^\circ$ and bright, discrete H_α emission regions outline the spiral arms. The locations of bright H_α emission are closely associated with the dark dust lanes, but relative to the dust (and the mm-CO emission, see Polletta et al. 2001), the H_α is often displaced to the outside or leading edge of the arms. In the standard picture of spiral pattern streaming

shown in Figure 10.2, this offset implies that the HII regions develop subsequent to the time of maximum concentration of the dust and molecular clouds. Close inspection of Figure 10.1

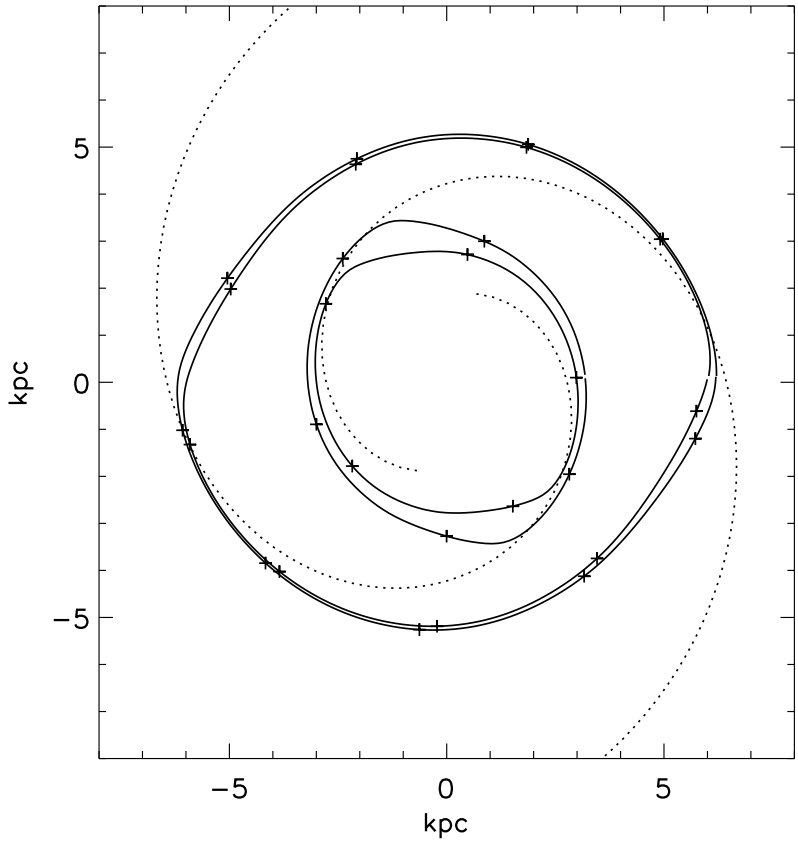

Figure 10.2: The flow streamlines are shown for material at 3, 3.2, 6 and 6.2 kpc in a spiral potential like that of M51 based on the model of Roberts and Stewart (1987) with the spiral arms starting at R = 2 kpc and PA=15° . Since the pattern speed is approximately half the circular velocity, the gas approaches the spiral arm from the underside, is deflected along the arm toward smaller radius and then leaves the arm on the front. Orbit crowding is due to the spiral arm streaming motions. The cross-marks correspond to 250 Myr time intervals.

also reveals a number of smaller dust lanes and HII regions in the interarm regions both to the east and west of the nucleus. Two very luminous associations of stars are also seen – one approximately 32″ NE of the nucleus with surrounding H_α emission, the other 99″ W of the nucleus, just outside the spiral arm. The latter region is remarkable in being very large in extent ($\sim$ 7″ or 326 pc in diameter) and in having very little H_α emission. The continuum colours and the lack of H_α suggest that this is an aging association in which the O-stars have mostly evolved off the main sequence ($\geq 10^7$ yr, see 10.10).

The NICMOS Pa_α (red) image is shown in Fig. 10.3 overlayed on the I (red), V (green) and B (blue) continuum. In Fig. 10.4, the Pa_α (green) is combined with the H_α (red) in order to highlight those regions with relatively high Pa_α/H_α ratios, indicating particularly high dust

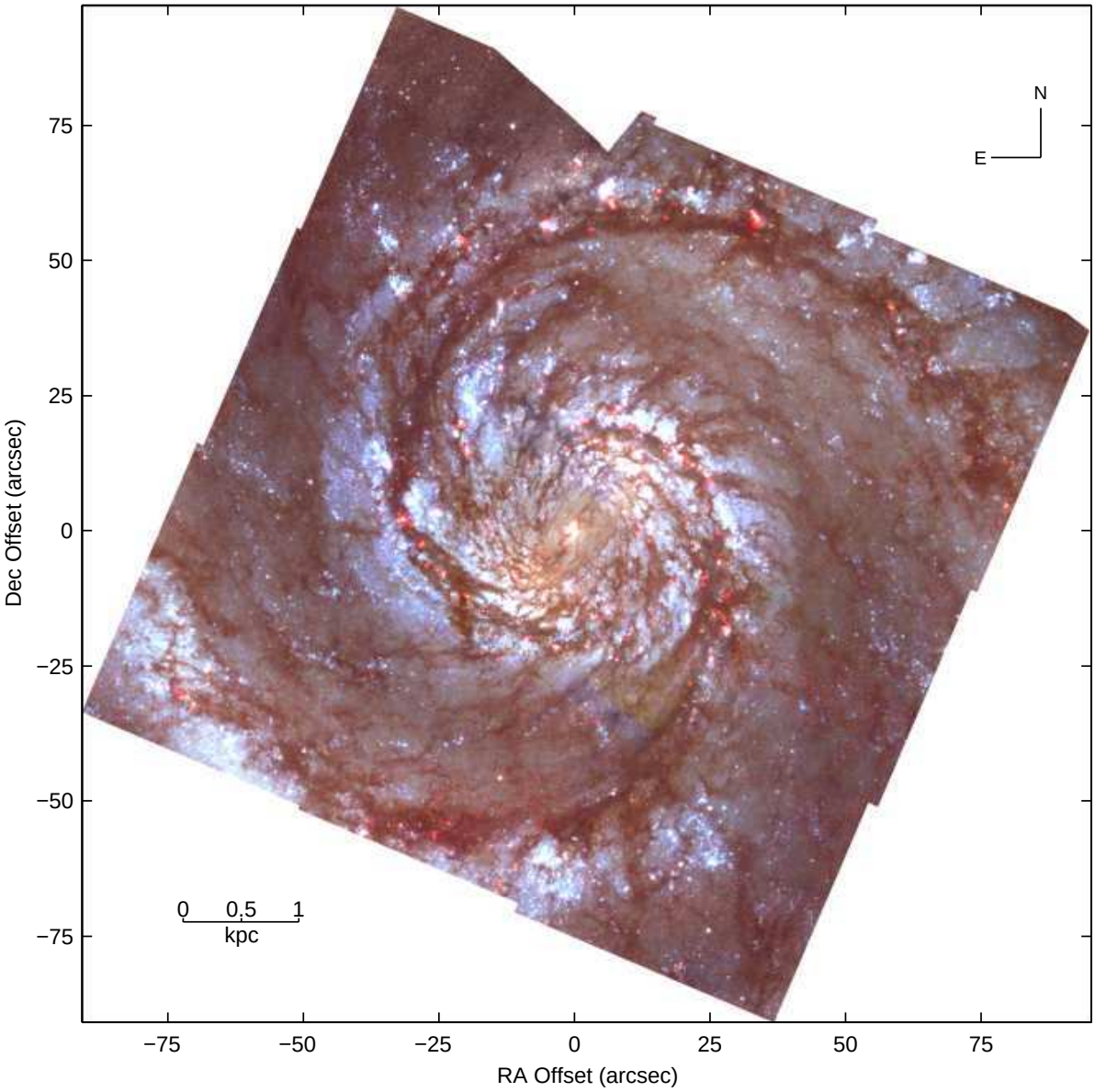

Figure 10.3: The mosaic of NIC3 Pa_α (continuum subtracted) images covering the central $186'' \times 188''$ of M51. The Pa_α emission is shown in red and continuum V and B bands are in green and blue, respectively. (In the red, we also added the I band image in order to balance the colours on the stars.)

reddening. Although generally Pa_α shows the same emission regions as H_α, it is clear even from visual inspection of Figure 10.4 that many of the arm and interarm HII regions have considerable reddening. There are several regions appearing green in Figure 10.4, implying strong Pa_α but only very weak H_α. Many HII regions also exhibit strong gradients in the Pa_α/H_α ratio.

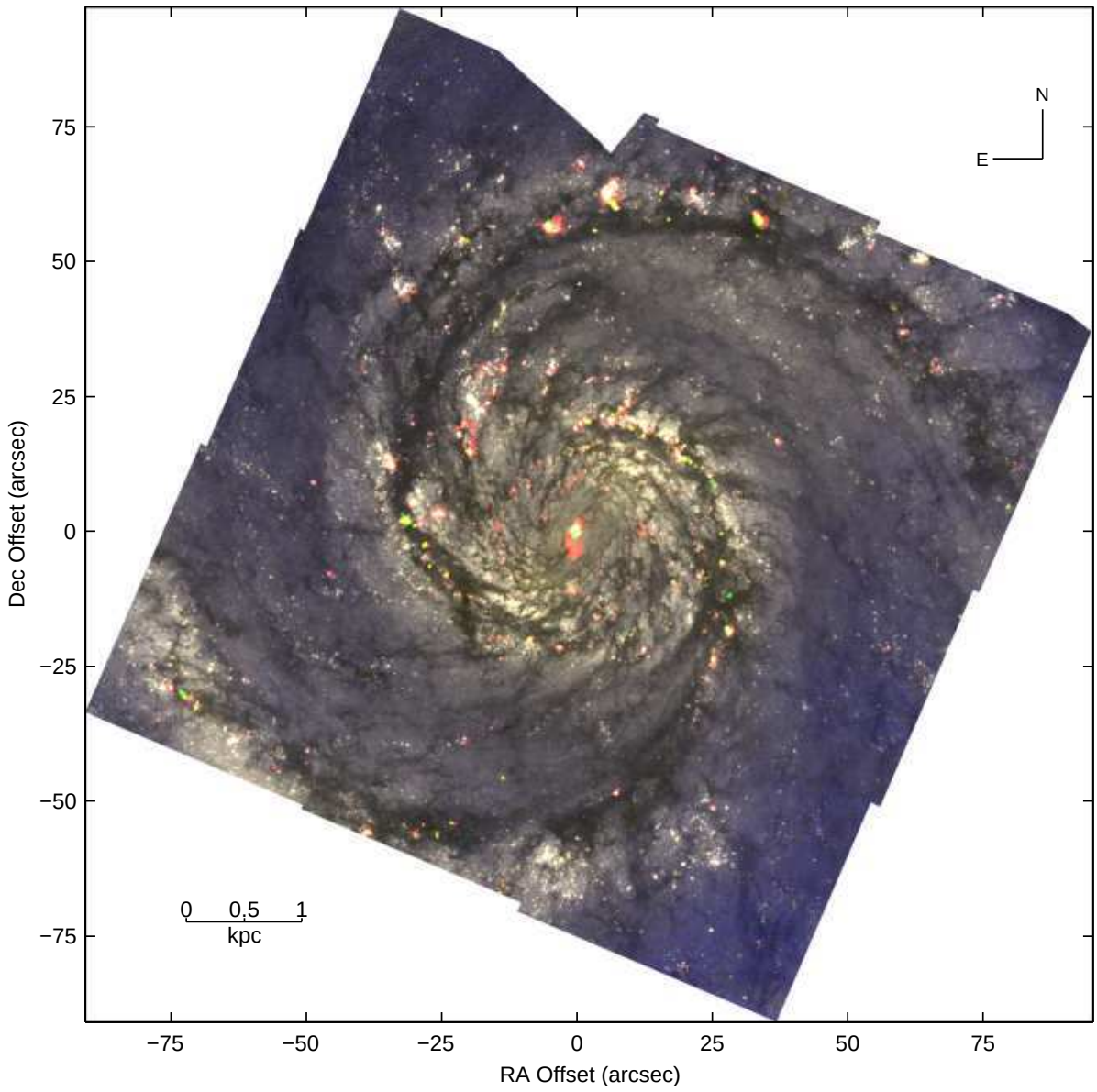

Figure 10.4: The H_α (red) and Pa_α (green) images are shown for the area of overlap. The blue was made by the colour H−V in order to show the dust lanes. In all the displays, we added the V band image with radial gradient subtracted (see Polletta et al. 2001) to show the background disk stars. Areas with yellow colour have strong H_α and Pa_α.

10.5 HII Region Parameters

In measuring HII regions, the high angular resolution HST is critical to resolving regions associated with individual OB star clusters. HST-NICMOS also enables measurement of Pa_α (which can not generally be done from the ground); in combination with H_α, this line provides a probe of the dust extinction. These points are illustrated well in Figure 10.5. The four panels show a region approximately 60″ N of the nucleus – in the upper panels, the full resolution H_α and the H_α smoothed to 1.″5 resolution (to simulate ground-based imaging); in the lower left, the full resolution Pa_α; and in the lower right the H_α (red) and Pa_α (blue). The lower right panel clearly illustrates the large variations in reddening from one region to another. For example, the southern end of the NW complex is strongest in Pa_α while the northern region in the complex are brightest in H_α. Comparison of two the H_α images in the upper panels illustrates the importance of high angular resolution for resolving the multiple, distinct HII regions which often exist in a single complex.

10.5.1 HII Region Definition and Measurement

Measured HII region properties will be fundamentally dependent on both the resolution of the images and the procedures used to define the boundaries of the emission regions. For example, higher resolution images will resolve some of the larger regions into multiple components (and hence reduce the number of the most luminous regions). In addition, the criteria adopted to resolve (or break up) blended regions can be critical. Algorithms to separate out the regions from the background and break up blended regions might invoke logic based on *a priori* understanding of the characteristics of Galactic HII regions. Lastly, it should be obvious that data with higher sensitivity might join multiple regions which would have appeared separate at lesser sensitivity.

The HII region measurement process may be broken into three steps: 1) the definition of the boundaries of emission regions at a specified intensity threshold, 2) the resolution of multiple strong peaks within a single boundary into separate, discrete emission regions and 3) measurement of HII region parameters such as peak and integrated fluxes, sizes and positions. Clearly, the breaking up of blended features is the most difficult (and subjective) step – for this reason we developed an automated procedure (rather than an interactive process). This has the advantage that the results can be carefully compared for different input parameters and the algorithm will be applied uniformly across the entire image. Thus, extensive trials of the selection parameters were used to test their effects on the results. The diffuse background was first removed from the emission line images. This background was obtained by setting each pixel to the 30 percentile in a histogram of pixels for the area 64 $\times$ 64 pixels centred on each pixel. The adopted percentile was chosen from trials with the goal being to avoid significant Malmquist bias and at the same time, avoiding the removal of line emission in areas with large HII region complexes. Sixty-four pixels corresponds to approximately 300 pc linear scale. Removal of the background was done in order to suppress residual continuum possibly resulting from colour changes in the starlight in different regions of the galaxy. In addition, we wished to remove diffuse line emission in order to measure the discrete HII regions. After removing the background, the noise (σ) was estimated from areas not including strong emission. Then all pixels below a 2.5σ threshold for significant line emission were zeroed out.

Our adopted logic for definition of the boundaries of the emission regions was: start from

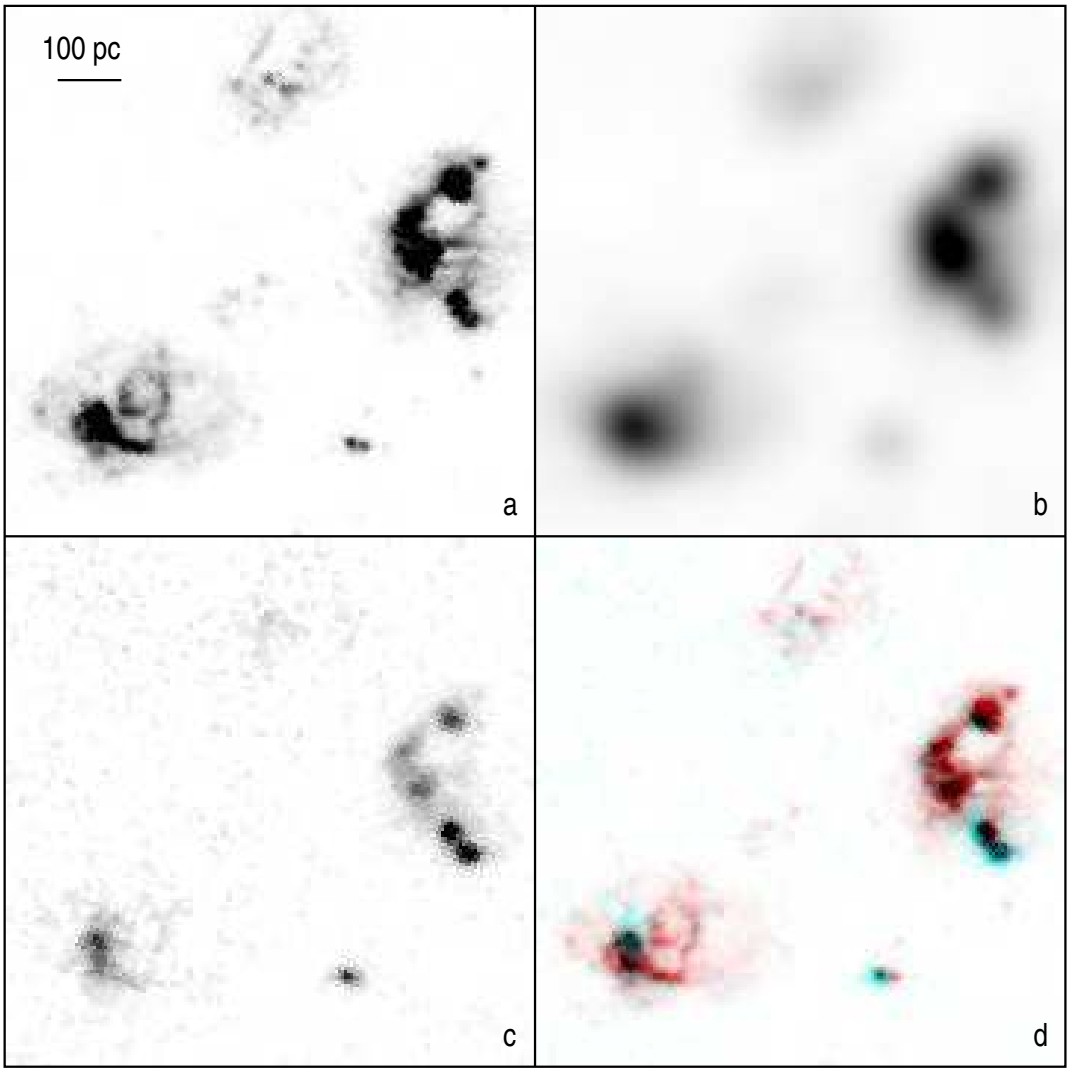

Figure 10.5: The HII region structure revealed by the HST H_α and Pa_α images is demonstrated for a small area approximately 60″ north of the nucleus. In this area, we show the HST H_α and Pa_α images at their full resolution (in left panels). In the upper right panel, the H_α image was smoothed with a 1.″5 FWHM Gaussian to simulate typical ground-based resolution. In the lower right panel, the H_α (red) and Pa_α (blue) are shown. The length bar corresponds to 100 pc, twice the typical diameter of Galactic GMC; typical Galactic HII regions have diameters 10 to 20 times smaller. This comparison illustrates well that the ground-based and HST imaging are clearly studying very different physical structures – the former, **associations** of OB star formation, the latter, perhaps individual OB star formation regions. It is also clear that significant differences can be seen in the H_α and Pa_α, presumably due to the higher extinction in H_α.

the brightest pixel, find all pixels connected to this peak down to a level of 65% of the peak value; then repeat the procedure starting from the brightest remaining pixel; and so on until there are no pixels left above the adopted threshold for a "significant" peak (here taken to be 6σ). Once a simple logic like that above is adopted, the only complication is that as one is

collecting the neighbouring pixels around a peak, one must also check that those new pixels would not more appropriately associate with one of the peaks found earlier in the process. In such instances where there were multiple regions neighbouring on a pixel, the pixel was attached to the region which had the highest average value for its neighbouring pixels.

Our procedure involved the following steps:

1) Find the peak pixel remaining in the image.

2) Let this pixel be the basis for starting a new "peak".

3) Generate a list of all pixels above 65% of this peak value.

4) For each of the pixels found in # 3, associate it with the new peak or whichever pre-existing peak has the highest average in pixels which touch the pixel in question. As pixels are assigned to HII regions, they are also removed from the original image to avoid further consideration. Any of the pixels in the list from # 3 not touching on a previous HII region are left in the image for later consideration. Thus one is gradually working down in intensity through the image.

5) If there are remaining pixels above 6σ which could form the basis for a new peak, then go back to step # 1.

6) Lastly, for any regions with more than 3 pixels, a curve of growth analysis was done to correct for flux outlying pixels beyond the lowest non-zero pixel value. To derive the growth curve individually for each HII region, we measured the total flux within each HII region as a function of the cutoff pixel intensity (starting from the peak value and working down to 2.5σ). These measurements were then fit by a straight line and then the fit was extrapolated to 0 intensity cutoff value. In nearly all cases this correction resulted in less than a 25% increase in the flux.

In the course of refining the measurement technique several of the parameters were experimented with and the results compared with what we would have selected by 'eye' as distinct HII regions. For example, the percentage of the peak flux above which pixels can be added and the level below which the image was truncated (finally adopted at 2.5σ) were varied. A sample area north of the nucleus is shown in grey scale in Fig. 10.7 and the derived features are illustrated in Fig. 10.8.

The algorithm was also tested on a simulation image in which spherical HII regions with a uniform distribution of Lyman continuum output were positioned randomly within a 3-d spatial cube. The cube was then projected on two dimensions and processed with the HII region finding algorithm. The HII regions found agreed very closely with the input HII region locations and sizes. The simulation and measurement was run for increasing numbers of input HII regions ranging from 10 to 150 in order to test the effects of blending.(Given the input sizes of the HII regions and the size of the 3-d cube, the case with 150 regions corresponded to very severe blending.) In all instances, the HII region finding algorithm found the correct number and parameters for the input regions (to within $\leq 10\%$). Test fits for the dependence of the total luminosity on the measured diameter D was typically $L \propto D^{2.75}$, compared to the theoretical D^3 dependence – probably due to limited spatial resolution. The fact that the results came so close to recovering the input parameters was particularly reassuring in the case of the 150 region simulation since the images were heavily blended in this case.

Once the boundaries of the H_α emission regions were defined, the peak and integrated fluxes were catalogued with the emission centroid coordinates. The number of pixels in the region and the size was derived from the $(\text{area})^{1/2}$.

As a check of the HII region definition and measurement routines, we compared our results for selected individual regions with ground-based H_α measurements (Rand 1992, Petit et al.

1996, Thilker et al. 2000). Although Rand (1992) did not publish his individual HII region measurements, he did provide us with his HII region list in tabular form. Figure 10.6 shows the locations of the H_α emission regions from Rand's and our samples. Generally, good

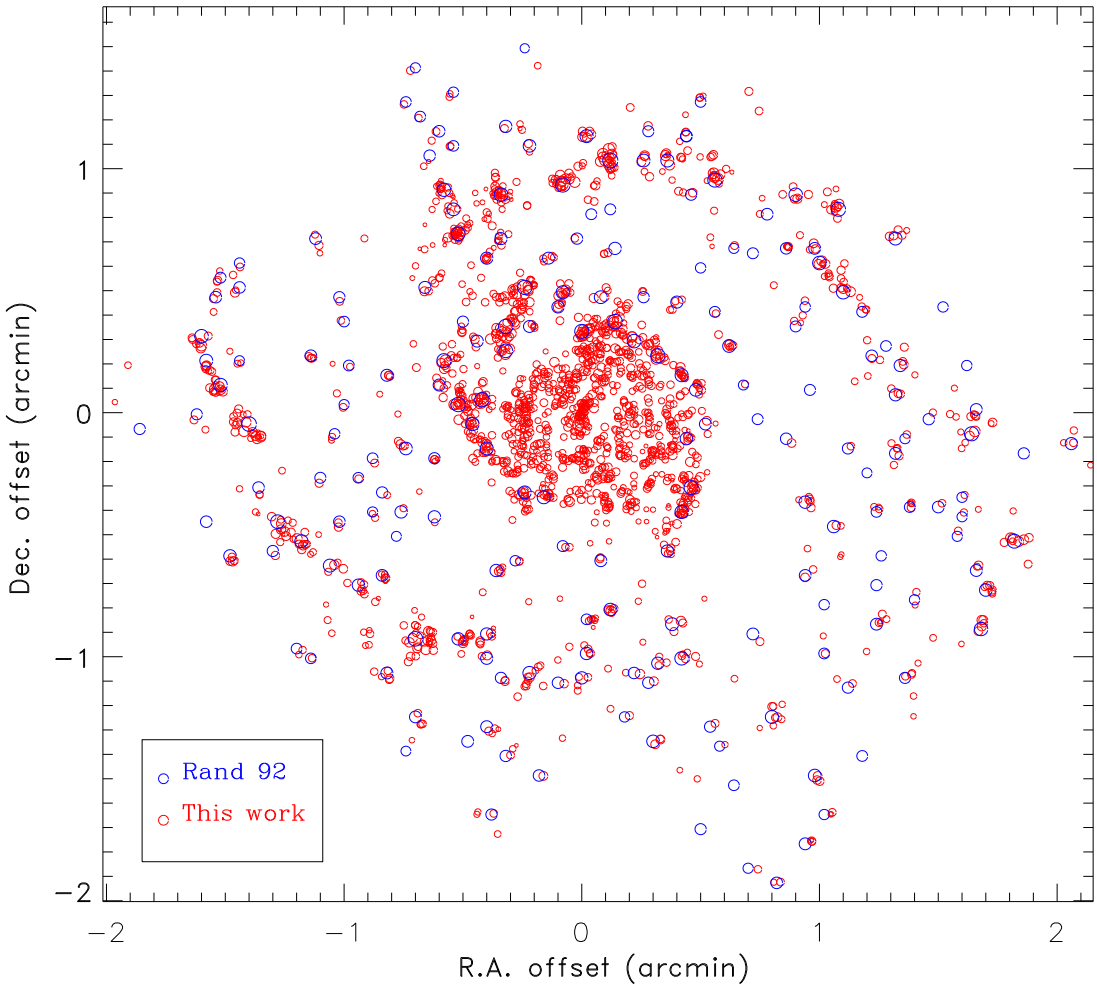

Figure 10.6: The locations of the H_α emission regions selected by our automated procedure are shown together with those measured interactively by Rand (1992). In general, there is very close correspondence between the two samples, although in many instances we have catalogued multiple regions where Rand had just one. The outer areas were not covered in our images and therefore a number of Rand's HII regions do not have a counterparts in our sample; the converse is true in the nuclear region which was excluded from Rand's analysis due to blending.

agreement can be seen in the areas of common coverage (i.e. excepting the nucleus which was not measured by Rand and the outer disk which was not covered in our images). However, in virtually every region, the higher resolution HST data resolves multiple HII regions within individual regions identified in the ground-based imaging. This is illustrated in Figure 10.5 which shows the HST data in a small area north of the nucleus at the original HST resolution

and smoothed to 1.″5 resolution to simulate ground-based imaging. There were a few regions catalogued by Rand which we did not find. We therefore also compared with the HII region catalogue of Petit et al. (1996) and in virtually all cases the regions catalogued by Rand but not seen by us were also not present in Petit et al. (1996).

Comparison of our fluxes with Rand's was not straightforward since he did not remove the large-scale diffuse background but rather a local background and most of his regions were multiply resolved here; nevertheless, the results appear consistent. For 10 regions with well-defined, bright H_α emission, the integrated fluxes were found to agree within 30% in all cases. Thilker et al. (2000) compared their results with Rand's (1992) measurements and good agreement, suggesting that theirs would also agree with ours if they had the same resolution. The peak fluxes and sizes are of course resolution dependent and agreement would not be expected.

Thilker developed an iterative group algorithm for delineation of HII region structures and he kindly made his routines available. Although we preferred to use our own algorithm for reasons of simplicity, familiarity with our routine and speed of execution, we did test the two procedures in the same area of the northern spiral arm shown in Figures 10.5 and 10.8. The regions which were defined were consistent but not identical with those from our algorithm and this is probably due to the fact that Thilker's routine is iterative and makes assumptions for the possible morphologies of the HII regions.

In the course of refining the measurement technique several of the parameters were experimented with and the results compared with what we would have selected by "eye" as distinct HII regions. For example, the percentage of the peak flux above which pixels can be added and the level below which the image was truncated (finally adopted at 2.5σ) were varied. Figure 10.8 shows the derived features for the sample area north of the nucleus shown in Figure 10.7.

The final list has 1882 H_α emission regions : 1746 having at least 3 pixels and 1664 having 5 or more pixels. The largest region had 664 pixels – this is undoubtedly a blend of several emission regions which we could not separate due to the high level of emission from diffuse ionized gas (DIG) in that region. The total flux of the 1882 HII regions constitutes 49.7% of the total H_α flux from the area of the galaxy covered in the WFPC2 images. (Due to its length, the table of listed HII regions is not included here but it may be obtained from NED.)

Our algorithm was also run on the Pa_α image (using the same parameters specified in terms of the image noise level), yielding 800 regions. All except three of these regions (mentioned below) were inside one of the previously found H_α regions; however, in most cases the boundaries were somewhat different. Usually, the Pa_α region was smaller in size, due to the intrinsically lower flux and SNR of Pa_α. In a few instances, the peak of the Pa_α was very significantly shifted from the H_α peak and it appears that these are regions with particularly high extinction at the location of maximum Pa_α emission. For both H_α and Pa_α, we saved the pixel values within each region so that the line ratios could be analysed pixel-by-pixel (see 10.7.2).

10.6 Luminosity Functions

The 'apparent' H_α luminosity function (uncorrected for extinction) is shown in Figure 10.9 together with those derived by Rand (1992) and Petit et al. (1996). All luminosity functions exhibit roughly similar shapes but the two ground-based luminosity functions extend at least

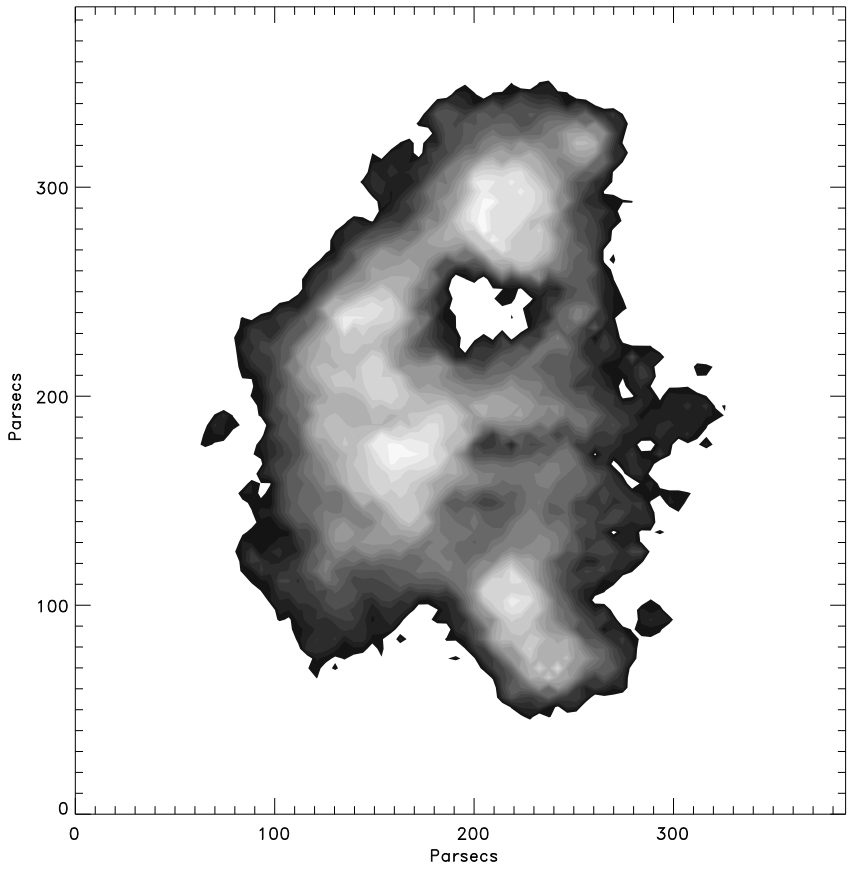

Figure 10.7: The H_α emission in a portion of the area shown in Figure 10.5 is shown in logarithmic grey-scale.

a factor of 5 higher in luminosity. This is due to the fact that all of the most luminous regions catalogued in the ground-based studies were either resolved into multiple regions in our sample, or they were in the outer galaxy which was not covered in our images.

To characterize the luminosity function, we express it as a truncated power law: in differential form,

$$\frac{d\ N(L(\mathrm{H}_\alpha))}{d\ ln\ L(\mathrm{H}_\alpha)} = N_{up} \left(\frac{L_{up}}{L(\mathrm{H}_\alpha)} \right)^\alpha \tag{10.1}$$

and in integral form,

$$N(\geq L(\mathrm{H}_\alpha)) = \frac{N_{up}}{\alpha} \left[\left(\frac{L_{up}}{L(\mathrm{H}_\alpha)} \right)^\alpha - 1 \right] \tag{10.2}$$

(McKee and Williams 1997). As pointed out by McKee and Williams (1997), this form has the advantage of having clear physical interpretations for the parameters. Specifically, L_{up} is

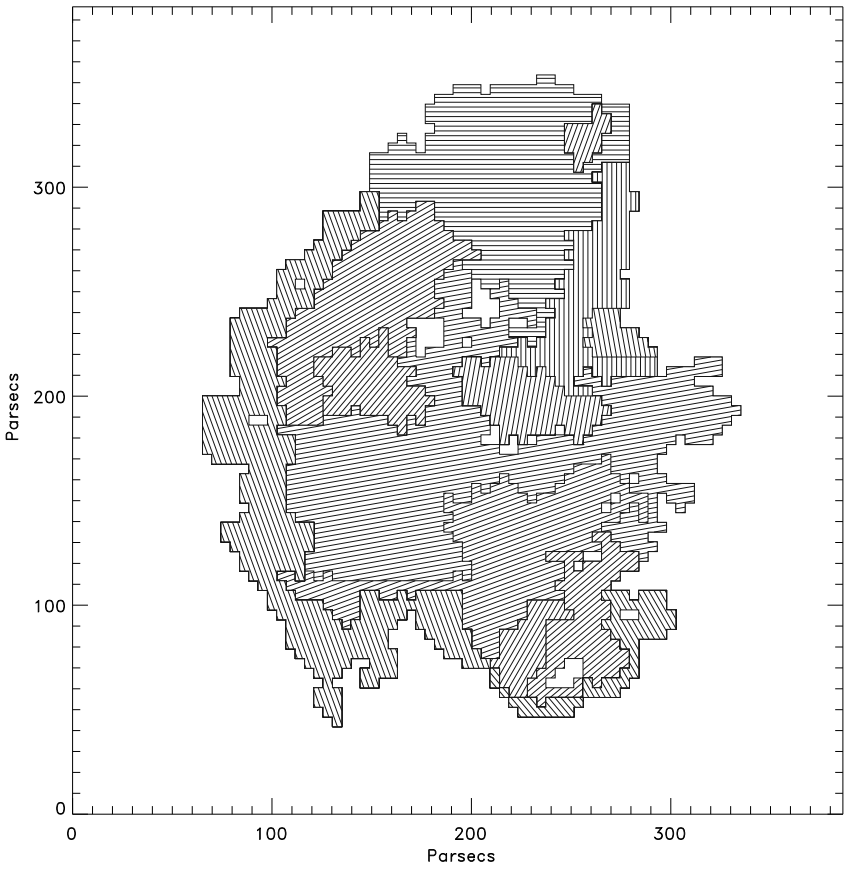

Figure 10.8: The defined H_α emission region boundaries are shown with size similar for the sample area north of the nucleus shown in Figure 10.7.

the highest luminosity region, N_{up} is approximately the number of regions between 0.5 L_{up} and L_{up} for $\alpha \sim 1$ and N_{up}/α is the number of regions expected above L_{up} if the distribution were not truncated (i.e., one can directly see if the distribution is "significantly" truncated or terminated by low number statistics).

A power-law fit to the 'apparent' luminosity function yields $\alpha = -1.21 \pm 0.01$, compared to -0.55 and -0.27 derived for the Rand (1992) and Petit et al. (1996) samples over the range $\sim 4 \times 10^{37}$ – 5×10^{38} erg s^{-1}. (Since these fits are for source counts binned logarithmically in L(H_α), the exponents should be decreased by 1 for N(L)dL.) Our power-law index is substantially steeper than that derived from previous studies (Kennicutt, Edger and Hodge 1989, Rand 1992, Petit et al. 1996, Thilker et al. 2000) due to the fact that the higher angular resolution resolves the more luminous, apparently blended regions. The slope derived here is similar to that of Galactic radio HII regions ($\alpha = -1 \rightarrow -1.3$; see 10.9).

In addition to a steeper slope, we also find that the 'apparent' luminosity function does not extend to such high luminosities. The lower 'apparent' luminosities obtained here are compensated by high extinction corrections (see 10.7). The mean extinction derived below for the discrete H_α emission regions is $A_{H\alpha} = 0.798 \times \langle A_V \rangle = 0.798 \times 3.2 = 2.55$ mag. If

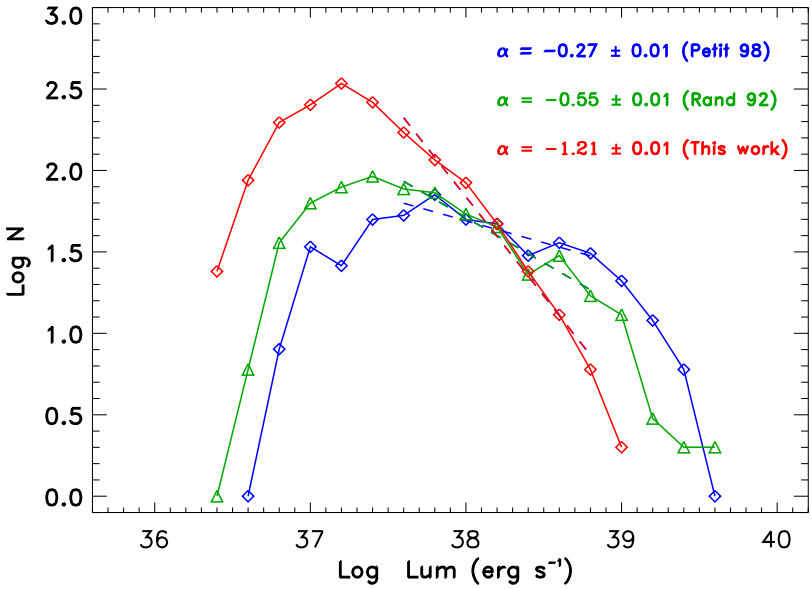

Figure 10.9: The observed H_α luminosity function for all HII regions defined and measured in the WFPC2 images (not corrected for extinction) is compared with the luminosity functions derived from ground-based imaging by Rand (1992) and Petit et al. (1996). The fact that the HST luminosity function appears to shift to lower luminosity is due largely to the ability to separate individual HII regions which become blended in ground-based images (see text). Typical extinctions of $A_{H\alpha} = 0.798$ $A_V = 0.798 \times 3.2$ will shift the luminosity functions a factor of 5.9 higher.

this is applied on-average to all HII regions, then the observed H_α luminosity functions are increased by a factor of 10.6.

The 'apparent' luminosity functions differentiated between arm, interarm and nuclear areas are shown in Fig. 10.10. These three areas are defined and illustrated in Polletta et al. (2001). Over the luminosity range $L(H_\alpha) = 1.6{\times}10^{37}$ to $8{\times}10^{38}$ ergs s^{-1}, logarithmic power-law fits have exponents $-1.23{\pm}0.01$, $-1.53{\pm}0.02$, and $-0.93{\pm}0.02$ for the arm, interarm and nuclear regions, respectively. Thus, the luminosity function is significantly flatter in the nucleus and the spiral arms than in the interarm regions. Rand (1992) and Thilker et al. (2000) also found a steeper luminosity function in the interarm regions (exponent $-0.93 \rightarrow -0.96$ versus $-0.48 \rightarrow -0.72$); however, the actual values of their slopes in the interarm and arm areas are somewhat different from ours.

There are several possible explanations for the flatter luminosity functions in the arms and the nucleus compared to the interarm regions: 1) the surface density of HII regions is higher in the nucleus and the arms, causing more blending which in turn produces a large number of apparently high luminosity regions; 2) the OB star cluster mass functions are significantly different in the different areas; and 3) the interarm HII regions and associated OB star clusters are, on average, older and therefore have evolved to lower Ly continuum output levels. The only way there could be a systematically older population of clusters in the interarm regions than in the arms would be if the OB star clusters in the disk formed within the arms and

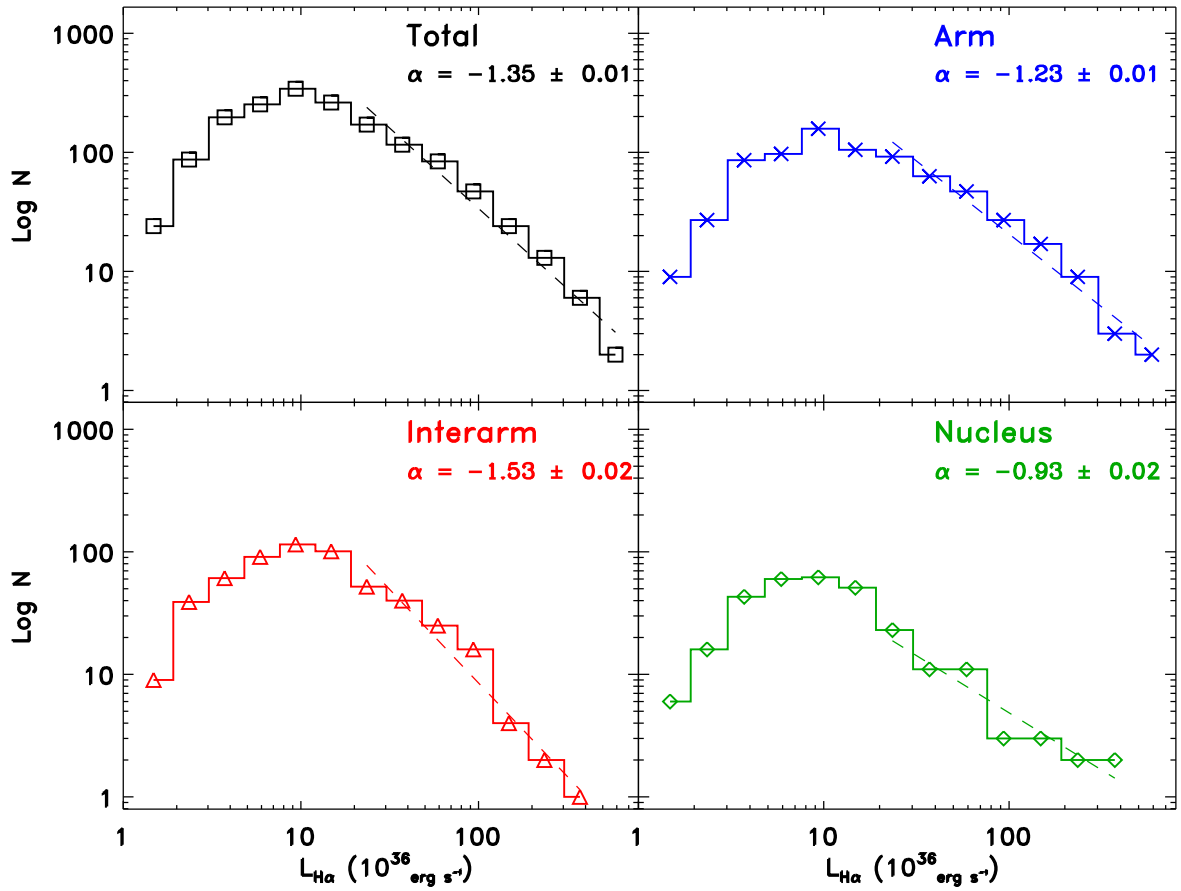

Figure 10.10: The observed H_α luminosity functions separated for arm, interarm and nuclear regions. The definition of these areas is defined and shown in Polletta et al. (2001). The power-law fits to the high luminosity tail are also shown. A significant flattening of the luminosity function is seen in the nucleus and spiral arms, compared to the interarm regions.

then aged as they moved into the interarm regions. Unfortunately, the cluster evolution is too quick ($\leq 3 \times 10^6$ yr; see 10.10) compared to the time ($\geq 3 \times 10^7$ yr) needed to migrate into the interarm regions for this explanation to work. Although the second explanation can not be ruled out at present, we think that the level of blending expected in the nucleus and the spiral arms is entirely consistent with the notion that many of the most luminous regions are, in fact, blends. One supporting piece of evidence for this is the clear trend for the most luminous regions to be the most extended and to have the lowest densities (see 10.8).

In none of the luminosity functions do we see evidence of the break in the slope at $L(H_\alpha) \sim 10^{38.6}$ ergs s^{-1} which was reported in ground-based studies (Kennicutt, Edger and Hodge 1989 and Rand 1992). This break occurs at about the point at which the luminosity distribution might be affected by blending of multiple HII regions.

10.6.1 Lyman Continuum Emission Rate

The observed HII regions range in luminosity from $L(H_\alpha) = 5\times10^{36}$ – 10^{39} erg s^{-1}. For case B recombination the H_α luminosity is

$$L(H_\alpha) = 3.55 \times 10^{-25} \left(\frac{T_e}{10^4 K}\right)^{-0.91} n_e n_p V \text{ erg s}^{-1} \tag{10.3}$$

where V is the volume of the HII region (Osterbrock 1989). Since absorptions by He do not significantly reduce the number of photons available to ionize H (Osterbrock 1989), the required Lyman continuum production rate, Q_{Lyc}, is then given by

$$Q_{Lyc} = 7.32 \times 10^{11} L(H_\alpha) \left(\frac{T_e}{10^4 K}\right)^{0.11} \text{s}^{-1}. \tag{10.4}$$

The observed H_α luminosities therefore translate to $Q_{Lyc} = 3.7 \times 10^{48}$ – 7×10^{50} s^{-1} for $T_e = 10^4$ K.

10.7 HII Region Extinctions from H_α/Pa_α

For case B recombination in an ionization-bounded HII region, the intrinsic flux ratio for H_α/Pa_α is 8.15 and the non-Lyman series lines should be optically thin (Osterbrock 1989). The observed flux ratios can be less than 8.15 due to the higher extinction at the λ = 6563Å (H_α) compared to 1.87μm (Pa_α). We have used the observed ratios to estimate the mean extinctions of each HII region detected in both lines, using the relation

$$A_V = 3.75 \times \log\left(\frac{8.15\ F(Pa_\alpha)}{F(H_\alpha)}\right) \text{mag}. \tag{10.5}$$

The constant in equation (10.5) was derived assuming the standard Galactic extinction curve (Rieke and Lebofsky 1985, Cardelli et al. 1989) and assuming the dust is distributed in a foreground screen, uniformly covering the pixel.

From the H_α and Pa_α images, we measured the average H_α/Pa_α flux ratios (smoothing the H_α to the same resolution as Pa_α) and extinctions at all pixels within the HII region boundaries using only pixels which had both H_α and Pa_α detected at $\geq 5\sigma$. 326 HII regions met the criteria. Values assigned to each HII region were obtained by averaging the pixel ratios and extinctions, rather than from ratios of the integrated HII region fluxes. The distribution of average flux ratios and A_V for the 326 regions is shown in Figure 10.11. The mean extinctions are: $A_V = 3.2$ mag (weighting each region equally), 2.4 mag (weighting each by the observed HII region luminosity) and 3.0 mag (weighting by the extinction-corrected luminosity). The derived mean extinctions are in reasonable agreement with the values (A_V = 0.8 – 4 mag) obtained by van der Hulst et al. (1988) for a sample 37 HII regions in M51 comparing H_α and radio free-free fluxes at 8″ resolution. For 14 of the regions, the Balmer decrements yielded considerably lower values (in the range A_V = 0.4 – 2.4 mag; van der Hulst et al. 1988) but these are optically biased towards lower extinction regions. It should be pointed out that since the HII region boundaries were defined from the H_α images, the analysis above excludes regions of extremely high extinction in which the Pa_α emission is

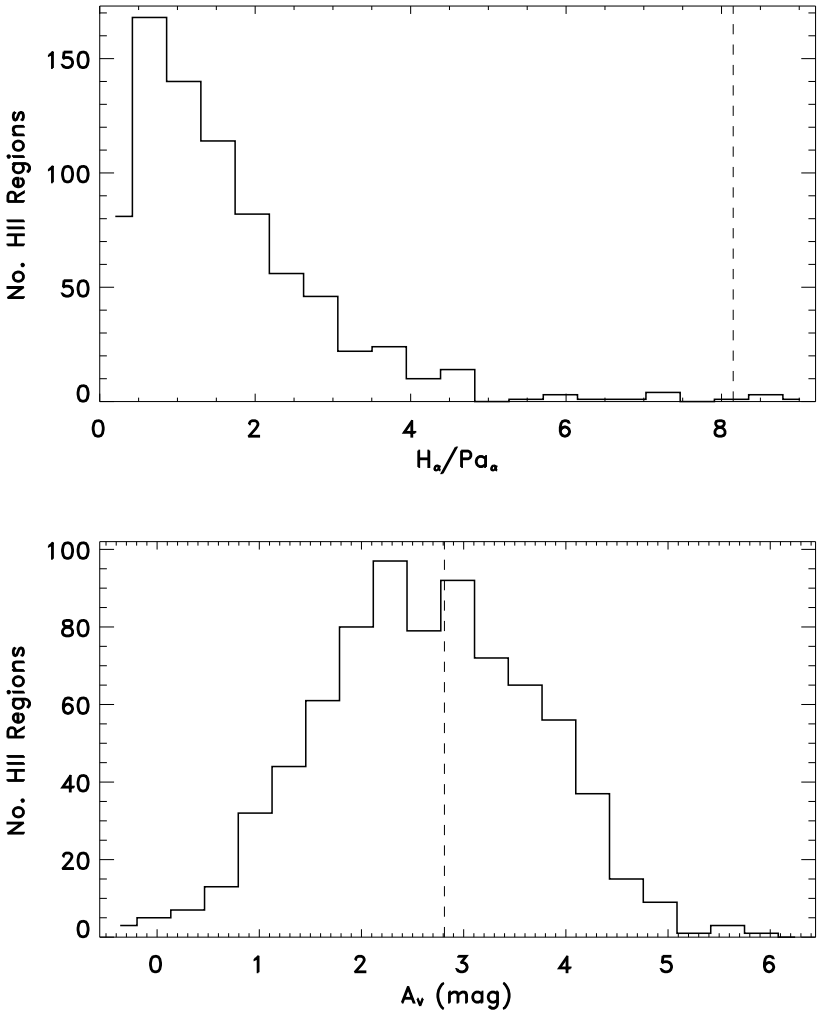

Figure 10.11: Upper Panel: The measured flux ratios (H_α/Pa_α) for 326 HII regions with boundaries defined from H_α (shown in Figure 10.8), restricted to those pixels detected at $\geq 5\sigma$ in both Pa_α and H_α. For case B recombination in an ionization bounded HII region with no extinction, the intrinsic ratio is 8.15 (dashed vertical line). The lower measured H_α/Pa_α ratios reflect the higher extinction at the wavelength of H_α (6563Å) than that of Pa_α (1.87 μm). Lower Panel: The distribution of average visual extinctions for the HII regions inferred from the measured flux ratios assuming an intrinsic ratio of 8.15 and the standard ISM extinction curve (Rieke and Lebofsky 1985, Cardelli et al. 1989). Dashed vertical line is the average extinction $A_V = 3.2$ mag. (The extinctions were determined at individual pixels and then averaged for each region.)

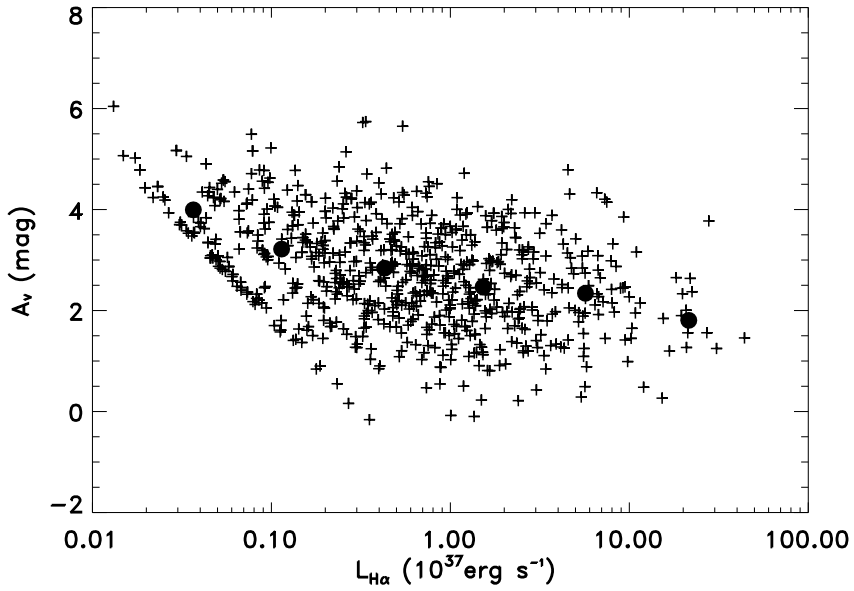

Figure 10.12: The derived extinctions as a function of 'apparent' H_α luminosity for 326 HII regions with boundaries defined from H_α (shown in Figure 10.8) restricted to those pixels detected at $\geq 5\sigma$ in Pa_α and H_α. The extinctions were determined for individual pixels within each HII region and then averaged. The solid circles are the averages for equal logarithmic bins in H_α luminosity.

significantly offset from H_α. The derived extinctions would have very likely been higher if the Pa_α had been used to define the HII regions. We used H_α for delineating the HII region boundaries simply because of the higher SNR.

In Figure 10.12, the derived extinctions of the 326 regions are plotted against the 'apparent' (not extinction-corrected) H_α luminosities. In this figure, the filled circles are the average values in separate luminosity bins. No strong correlation (or anti-correlation) is seen between the 'apparent' luminosities and the derived extinctions (as might be expected if the flux variations were largely due to extinction variations). The filled-circle averages show a weak correlation in the sense that the fainter regions have somewhat higher extinction, but the dispersion within bins is clearly much larger than the trend.

We also measured the flux ratios and derived extinctions for all pixels in the H_α and Pa_α images which were both detected at $\geq 5\sigma$, independent of whether or not they were inside one of the discrete H_α regions. The results (shown in Figure 10.13) are entirely consistent with those found within the discrete HII regions (Figure 10.11). When the selection threshold was increased to 10σ, the results were very similar, implying that the larger extinction values are not simply the result of poor signal-to-noise or a bias in either image.

10.7.1 Extinction Gradients Across HII Regions

Detailed comparison of the H_α and Pa_α images reveals that most individual HII regions also have very large variations in the H_α/Pa_α ratio across their areas. (It is for this reason that the

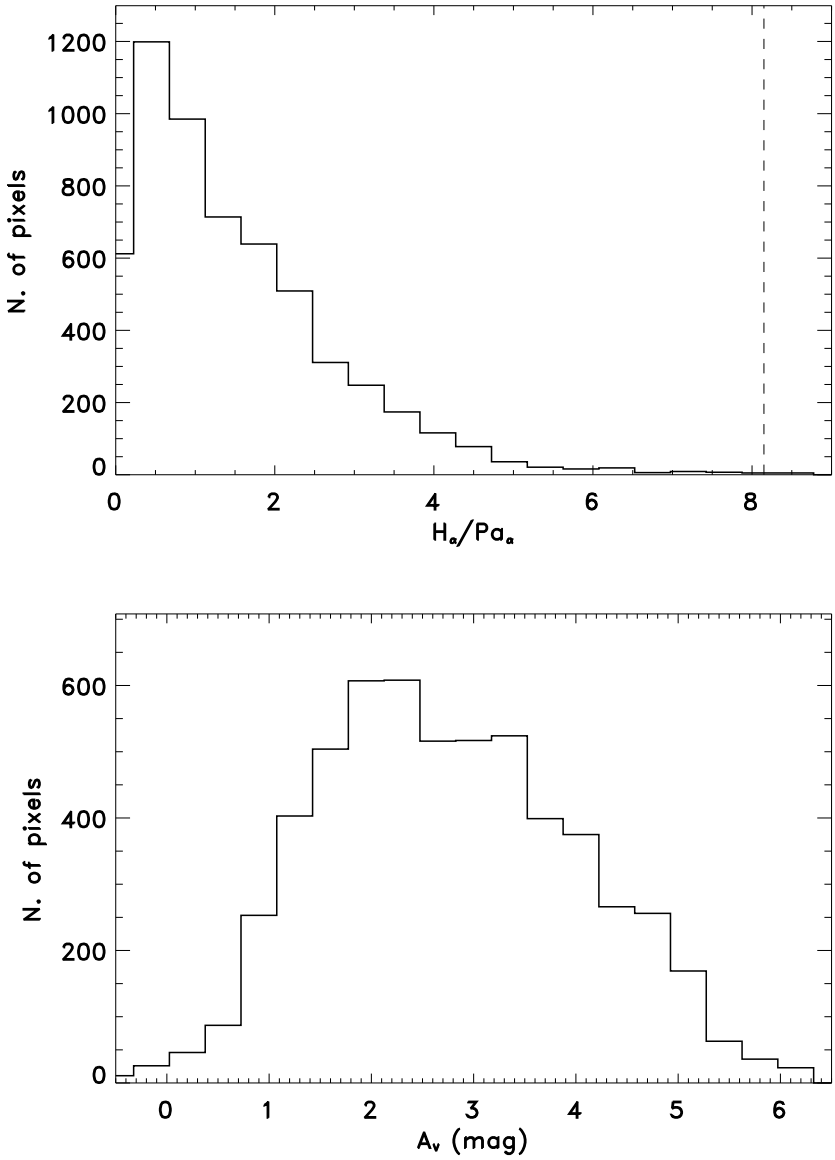

Figure 10.13: Upper Panel: The measured flux ratios (H_α/Pa_α) for all individual pixels detected at $\geq 5\sigma$ in both Pa_α and H_α. For case B recombination in an ionization bounded HII region with no extinction, the intrinsic ratio is 8.15 (dashed vertical line). Lower Panel: The derived visual extinctions for the same pixels obtained from the measured flux ratios assuming an intrinsic ratio of 8.15 and the standard ISM extinction curve (Rieke and Lebofsky 1985, Cardelli et al. 1989).

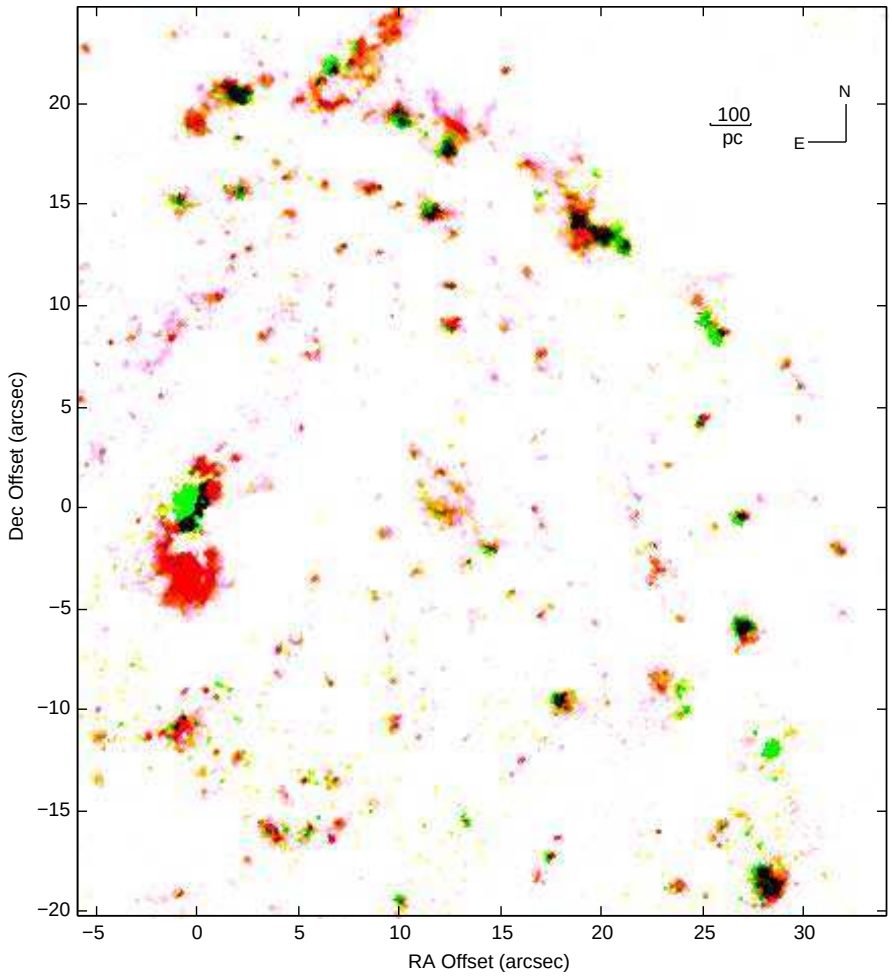

Figure 10.14: The H_α (red) and Pa_α (green) are shown for the area to the west of the nucleus with all continuum removed. Although virtually all reasonably bright H_α emission regions are seen in Pa_α, extremely large variation in the line ratio are apparent from region to region and the morphology of individual regions can be very different in H_α and Pa_α.

ratios and extinctions for each region were computed in 10.7 as averages of the values from individual pixels rather than from ratios of the integrated fluxes.) In Figure 10.14 the area to the west of the nucleus is shown with H_α in red and Pa_α in green (with no continuum added). Several of the emission regions show entirely different morphology and peak locations in the optical and near infrared lines. The gradients and peak offsets vary from region to region; they therefore are not due to misalignment of the images. In fact, there are several examples in this image of emission regions seen in Pa_α which are hardly detected in H_α, indicating extinctions in excess of 4 mag. There are also many regions which are seen in H_α but not Pa_α but this is simply due to the intrinsically high flux of H_α together with the lower sensitivity of the Pa_α image.

10.7.2 Extinction-Corrected HII Region Luminosities

The extinction-corrected H_α luminosity is obtained from

$$L(H_\alpha)_{cor} = 10^{0.320 \times A_V} \times L(H_\alpha)_{uncor} \tag{10.6}$$

using the standard ISM extinction curve (Rieke and Lebofsky 1985) for which $A_{H\alpha} = 0.798$ A_V. For the mean extinction and the luminosity-weighted extinction ($A_V = 3.2$ and 3.0 mag, respectively; Sec. 7), the observed luminosities are increased by factors of 10.6 and 9.1. Since the former value is biased towards lower luminosity regions, we will adopt the latter for an average correction factor of

$$< f_{H\alpha\ ext-cor} > \simeq 9 \tag{10.7}$$

as an appropriate general extinction correction where individual extinctions are not available.

The 'extinction-corrected' and 'apparent' luminosity distributions are shown in Figure 10.15 for the 326 regions detected in both H_α and Pa_α. The 'extinction-corrected' distribution ex-

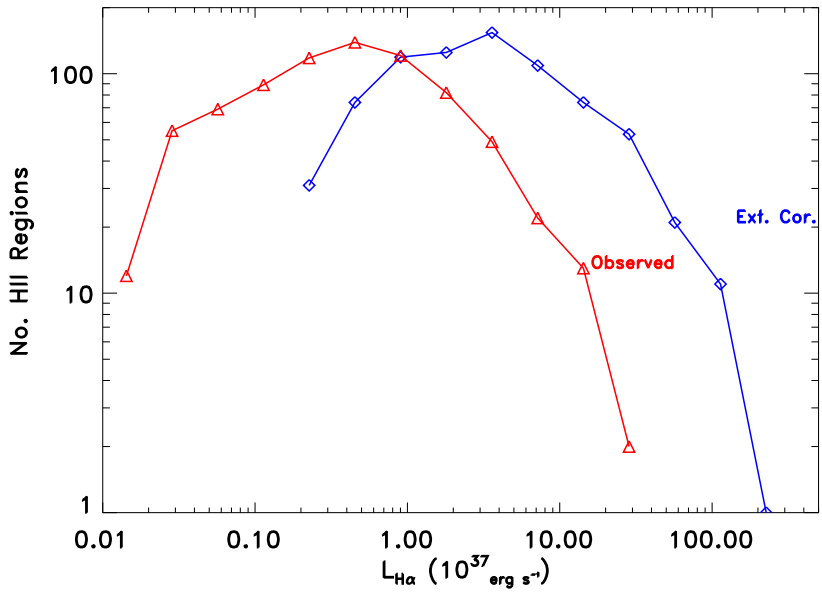

Figure 10.15: The H_α luminosities as observed for the 326 regions for which the extinction was derived and as corrected for extinction. These distributions should not be interpreted as luminosity functions since they include only those pixels in each region detected at $\geq 5\sigma$ in both lines.

hibits a broad peak at approximately $L(H_\alpha) = 2{\times}10^{37}$ erg s^{-1} and the most luminous region is at $2{\times}10^{39}$ erg s^{-1}. The falloff on the low luminosity side is probably not real since the sample has a detection threshold and there are no regions from below the threshold which can populate the low end after being corrected for extinction. The distributions shown in Figure 10.15 should not be interpreted as luminosity functions since they do not include all pixels in each region, only those pixels detected at $\geq 5\sigma$ in both lines.

10.8 HII Region Sizes and Densities

The HII region luminosities and their Lyman continuum emission rates constrain the implied masses of the OB star clusters; similarly the sizes and electron densities of the HII regions reflect on the evolution of their Strömgren spheres and the surrounding ISM.

10.8.1 Sizes

The distribution of HII region sizes (D = $2\times(\text{area}/\pi)^{1/2}$) is shown in Figure 10.16 for all regions with at least 2 pixels. They range from 10 to 250 pc in diameter; those $\geq$ 120 pc were not plotted since they are clearly blends. The lower limit of 10 pc is due to the minimum 2 pixel criterion. The mean sizes are 28 – 33 pc in arm, interarm and nuclear regions. Both the shapes of the distributions and the mean sizes are the same for all three areas. The majority of the HII regions have size $\leq$ 40 pc and thus may, in fact, be due to a single or a few OB star cluster(s). Those regions with larger sizes are very likely blended superpositions of multiple (but possibly related) OB associations.

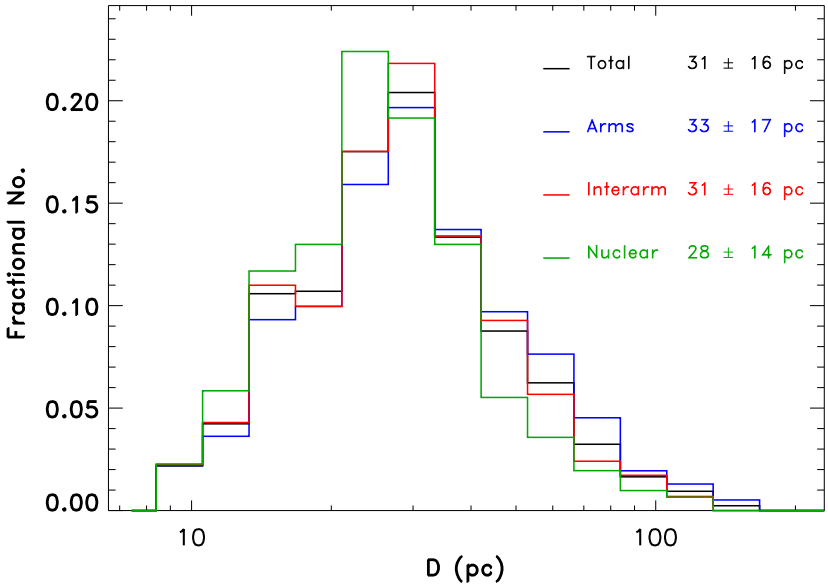

Figure 10.16: The distribution of HII region diameters are shown for regions containing at least 2 pixels, separated between arm, interarm and nuclear regions. No significant difference is seen in the diameter distributions between the different regions. The mean sizes are given for all regions smaller than 100 pc. Regions with size $\geq$ 120 pc were not plotted since these are certainly blends of multiple regions.

10.8.2 n_e

Since the H_α luminosities are proportional to the volume-integrated emission measures, the mean electron density can be obtained using the measured sizes:

$$< n_e >= 43 \left(\frac{(L(H_\alpha)_{cor}/10^{37} \text{ erg s}^{-1}) \ (T/10^4 \ \text{K})^{0.91}}{(D/10 \text{ pc})^3} \right)^{1/2} \text{cm}^{-3}. \quad (10.8)$$

In equation (10.8), we normalized to typical values of $L(H_\alpha)_{cor} = 10^{37}$ ergs s^{-1} and a size of 10 pc. The derived $< n_e >$ for the HII regions are distributed mostly between 5 and 30 cm^{-3}. In Figure 10.17 the HII region luminosities and sizes are plotted as functions of mean electron density. The sharp boundaries to the distributions on the lower side are

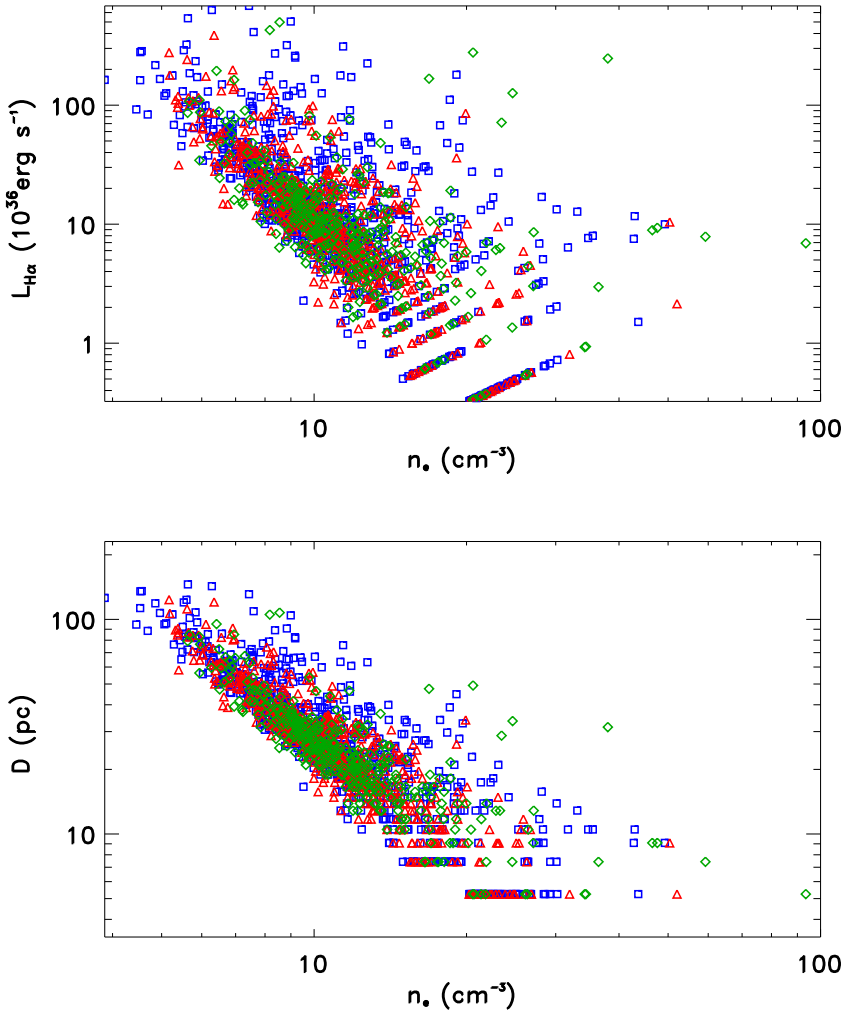

Figure 10.17: The 'apparent' H_α luminosities (upper panel) and HII region diameters are plotted as functions of mean electron density with the arm, interarm and nuclear regions plotted in blue, red, and green, respectively.

due to the surface brightness threshold and the minimum size of 1 pixel within the HII region. The average value is $< n_e > \simeq 13$ cm^{-3} for sizes less than 40 pc. If the apparent n_e

are corrected for the average extinction correction (equation (10.7)), the mean densities are increased by a factor of 3 to $< n_e > \simeq 39$ cm^{-3} which is similar to that of resolved Galactic HII regions ($n_e \sim 100$ cm^{-3}). This suggests that we are observing similar HII regions in M51 – specifically, our HII region sample at sizes less than 40 pc is not strongly corrupted by blended regions. In the above estimates we have made no corrections for the fact that many of the HII regions are only marginally resolved; such corrections would of course increase the mean densities further. Some of the larger regions undoubtedly do include substantial empty or neutral volumes. Moreover, there are substantial gradients in the H_α surface brightness within individual regions, indicating that the internal densities are non-uniform and commonly increase several-fold at the peaks.

In Figure 10.18, the HII region luminosities are plotted as a function of their measured sizes. There is a clear trend for the more luminous regions to be more spatially extended with L $\propto D^2$. Although such a trend is certainly expected, since more luminous OB associations can ionize a larger volume of gas, the observed dependence is shallower than the D^3 dependence expected if the electron densities were constant. Specifically, the more luminous and larger regions appear to have lower average n_e. The lower limit of the data points in Figure 10.18 is of course caused by the observational threshold on the surface brightness; however, this does not account for the decrease in density for larger regions. (If the larger regions had the same densities as the smaller regions, they would more easily make it into our sample.) The proper explanation for the correlation is probably that the larger regions are blended and they include substantial empty or neutral volumes. Alternatively, these large HII regions may have expanded outside their progenitor GMCs.

10.9 Comparison with Galactic HII Regions

For comparison with Galactic HII regions we make use of radio continuum observations of the free-free continuum to avoid Galactic line-of-sight dust obscuration. Radio studies have concentrated on 'compact' HII regions which are relatively young and have high surface brightness. Schraml and Mezger (1969) observed 18 free-free emission complexes at $\lambda = 2$ cm with $2'$ resolution (typically corresponding to 0.5 – 5 pc) and we make use of their sample for our discussion. Their results are summarized in Table 3 for M43, M42 (Orion Nebula), IC1795 (W3), W51, and W49 (ordered with increasing luminosity).

Comparing the implied L(H_α) of the Galactic HII regions with the extinction-corrected H_α luminosities (Figure 10.15), it can be seen that the first value in the M51 distribution function corresponds to approximately 1/3 of M42, the midpoint of the peak with M42, and W49 with the second to last point. Since W51 and W49 are the most luminous Galactic HII regions and Figure 10.15 includes only a limited subset of M51 HII regions (detected in both Pa_α and H_α), we conclude that the M51 sample spans approximately the full range from the least luminous to most luminous Galactic compact HII regions. In the full sample of M51 regions (Fig. 10.9), the most luminous is at an 'apparent' L(H_α) = 10^{38} erg s^{-1}; if this region has a modest extinction, its luminosity might be a few times that of W49. For reference, we note that the 30Dor cluster in the LMC is a few times more luminous than W49. The diameter of the 30Dor stellar cluster is ~ 20 pc and the associated H_α emission extends over ~ 100 pc.

Although the luminosity range of M51 HII regions is similar to that of the Galactic regions listed in Table 3, their sizes are typically several times larger and their mean densities lower.

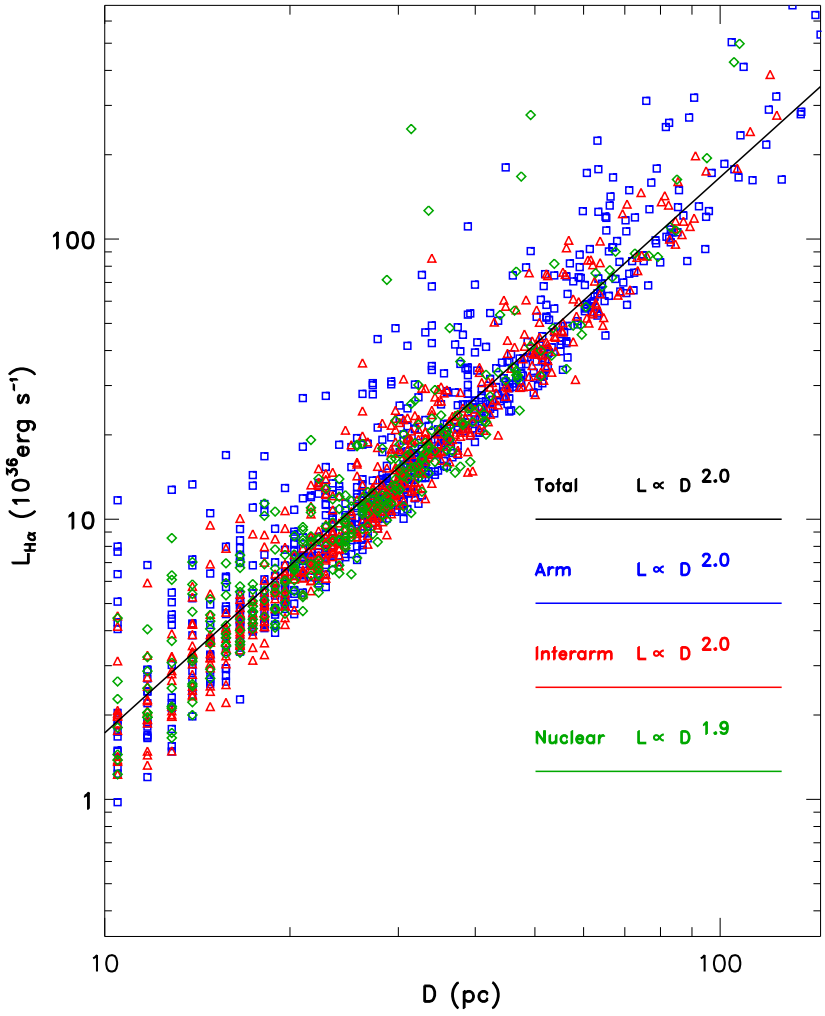

Figure 10.18: The observed luminosities of the HII regions are plotted as a function of HII region diameter.

These differences have several likely explanations: the Galactic regions were selected for high surface brightness free-free emission (i.e., compact radio HII regions) in order to avoid possible extended, missing flux; the M51 regions are still only marginally resolved and undoubtedly would include compact cores at higher resolution; or some of the Galactic regions may be in an earlier stage of their evolution before they have fully expanded. Despite these differences, the ionizing luminosities are similar and it is those luminosities which we use in the next section to probe the OB star cluster mass distributions and temporal evolution in M51.

The luminosity function of Galactic radio HII regions has been fit by Smith and Kennicutt (1989) and McKee and Williams (1997) who found power law indexes of 1.3 and 1.0, respectively – consistent with our value of 1.2. Although McKee and Williams (1997) derive an upper limit for the Lyman continuum emission rate from Galactic HII regions of Q_{Lyc}

Table 10.3: Galactic Compact HII Regions[a]

Region	Diameter (pc)	n_e (cm^{-3})	U (pc $cm^{2/3}$)[b]	Q_{Lyc} (s^{-1})	$L(H_\alpha)$ (ergs s^{-1})[c]
M43	0.6	610	20	2.5×10^{47}	3.5×10^{35}
M42	0.7	2237	55	5.3×10^{48}	7.1×10^{36}
IC1795(W3)	2.3	400	179	1.8×10^{50}	2.5×10^{38}
W51	4.9	372	208	2.9×10^{50}	3.9×10^{38}
W49	8.4	536	276	6.6×10^{50}	9.1×10^{38}

[a]Data obtained from 2-cm radio continuum observations of Schraml and Mezger (1969). [b]Excitation parameters ($U = R_s n_e^{2/3}$) from Schraml and Mezger (1969) have been summed for all HII region components except in the case of W51 where we took only the strongest component since this direction is along a spiral arm tangent and there is likely to be confusion. [c]Implied extinction-corrected $L(H_\alpha)$ ($=1.37\times10^{-12}$ Q).

$= 4.9\times10^{51}$ s^{-1} (including a correction of 25% for absorption by internal dust), the actual maximum observed is only 10^{51} s^{-1}. The latter value is consistent with our M51 extinction-corrected upper limit $Q_{Lyc\ up} \sim 1.7\times10^{51}$ s^{-1} which has no corrections for dust absorption of the ionizing photons or UV escaping into the diffuse medium. The latter factor adopted in the McKee and Williams (1997) study is very large (1/0.29 = 3.45). They obtained this number by assuming the entire discrepancy between the far-infrared COBE measurements of [NII] and the sum of the Ly continuum from discrete HII regions was due to leakage of ionizing UV out of the regions measured in radio free-free. Alternatively, much of the discrepancy might be due to older OB associations than are detected in the radio surveys, ionization by other sources or even uncertainties in the analysis of the COBE data. We do not include this factor in view of its large uncertainty and because we wish to compare discrete HII regions in M51 with comparable objects in the Galaxy.

10.10 OB Star Clusters and HII Region Evolution

In order to understand the nature of the constraints provided by the observed HII region H_α luminosities and their distribution, we develop here a simplified model for OB star clusters and HII region evolution. The critical constraints which we wish to understand are:

1) the slope of the luminosity function on the high luminosity end (d N(L)/d ln L $\propto$ $L(H_\alpha)^{-1.2}$, equation (10.1)) – to what extent is this due to the evolutionary decay of the Lyman continuum emission from clusters as they age, as opposed to the mass spectra of the clusters and their high-mass stars; and

2) the existence of an 'approximate' maximum luminosity for individual OB star clusters at $L(H_\alpha) \sim 10^{39}$ erg s^{-1}. (This maximum is surprising in view of the fact that it corresponds to a cluster of only a few $\times10^3 M_\odot$ yet GMCs contain $10^{5-6} M_\odot$ of molecular gas; there is thus sufficient mass available to form much more massive clusters.)

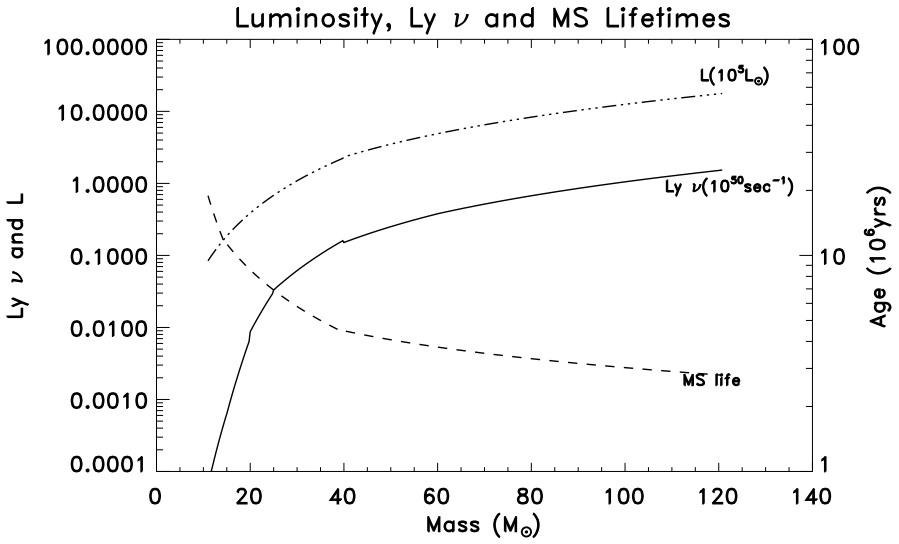

Figure 10.19: The adopted Lyman continuum production, stellar luminosity and main sequence lifetimes are shown as a function of stellar mass. The Lyman emission rate is from Vacca, Garmany and Shull (1996) and the main sequence lifetimes and luminosities are from Renzini and Buzzoni (1986) and Maeder (1987) for $\leq 10M_\odot$; and $\geq 10M_\odot$, respectively.

10.10.1 Model Stellar and Cluster Parameters

For each OB star cluster, we assume the star formation occurs on a timescale short compared to stellar evolution timescales. We adopt a Salpeter initial mass function (IMF) with $N(m_*)dm_* \propto m_*^{-2.35}$ over the range m_l – m_u (here, taken to be 1 and $120M_\odot$, respectively) rather than the local Galactic IMF (Scalo 1987). The Salpeter IMF is consistent with the recent determinations for OB associations which have power-law indexes in the range $-2.1 \rightarrow -2.45$ (Massey et al. 1995) and the 30Dor cluster in the LMC (Selman et al. 1999).

The stellar lifetimes and Lyman continuum emission rates are based on stellar models with constraints provided by observations of individual high-mass stars. Main sequence lifetimes and bolometric luminosities are from Renzini and Buzzoni (1986) and Maeder (1987) for $\leq 10M_\odot$ and $\geq 10M_\odot$, respectively. For reference, the MS lifetimes are 8.6, 4.5, 3.8 and 3.3 $\times 10^6$ yr for 20, 40, 60 and $80M_\odot$. The ionizing photon production rates (Q_{Lyc}) are from Vacca, Garmany and Shull (1996). These are shown in Figure 10.19.

In building up the population of a star cluster, our numerical modelling takes account of the fact that for low cluster masses, the highest masses in the IMF are populated discretely – that is fractional stars are not permitted. The maximum stellar mass is therefore determined by the condition that the integrated mass higher on a smooth IMF is equal to this stellar mass. This logic is then followed down to successively lower stellar masses on the main sequence (MS). Once assembled, we then track the evolution of the Lyman continuum output, removing high-mass stars after their MS lifetimes.

10.10.2 Lyman Continuum Emission Rates

The computed Ly continuum emission rates (Q_{Lyc}) and maximum stellar mass (m_u) are shown as functions of cluster age and cluster mass in a contour plot (Figure 10.20). For the lowest mass clusters, the initial constant Ly continuum phase lasts longer than for the higher mass clusters, due to the fact that the lowest mass clusters have none of the very short lifetime, highest mass stars. The Lyman continuum output shown in Figure 10.20 illustrates well the constraints on the cluster properties provided by the H_α emission. The extinction-corrected H_α (or Pa_α) luminosities constrain Q_{Lyc} to lie on a given contour line (top panel) and this defines the locus of viable cluster masses and lifetimes.

In Figure 10.21, the maximum initial stellar mass and Ly continuum production rate are shown as functions of the cluster mass. We find that the initial Ly continuum ($Q_{Lyc\ initial}$) is conveniently fit by a power-law function of the lower and upper mass cutoffs for the IMF (m_l and m_u) and the initial cluster mass (M_{cl}):

$$Q_{initial} = 9.1 \times 10^{46} \left(\frac{m_l}{1\mathrm{M}_\odot}\right)^{0.23} \left(\frac{m_u}{120\mathrm{M}_\odot}\right)^{1.3} \left(\frac{\mathrm{M}_{cl}}{\mathrm{M}_\odot}\right) \left(1 - exp\left(-\frac{\mathrm{M}_{cl}}{740\mathrm{M}_\odot}\right)\right)^{0.39} \mathrm{s}^{-1}. \tag{10.9}$$

The numerical result and the fit given by equation (10.9) are shown in Figure 10.21.

Assuming formation of all stars in the cluster in a time short compared to the stellar evolution times, the Lyman continuum emission rate remains constant until an age equal to the MS lifetime ($\sim 3.5 \times 10^6$ yr – see Fig. 10.19) of the highest mass stars that were formed. Subsequently, Q_{Lyc} decays with an e-folding time of $\sim 3 \times 10^6$ yr out to $2{\times}10^7$ yr at which point the Ly continuum is fairly insignificant. In Figure 10.22 (upper panel), the temporal decay of the Ly continuum is shown for four cluster masses; data for other cluster mass can be read from Figure 10.20.

Lastly, we show in Figure 10.22 (bottom panel) the total output of Lyman continuum photons integrated over the lifetime of the cluster as a function of cluster mass. The vertical axis is normalized by the cluster mass. Above masses $\sim 10^3\mathrm{M}_\odot$, the Lyman continuum output per unit mass is approximately constant. This arises because the upper main sequence has been fully populated and increasing the cluster mass further simply adds all stars in the same proportion. Above $10^3\mathrm{M}_\odot$, the Ly output is 10^{55} per $\mathrm{M}_\odot$ of stars between 1 and $120\mathrm{M}_\odot$. This result is most useful for estimates of time- and global-averaged star formation rates (see 10.11).

10.10.3 Cluster Masses

The extinction-corrected H_α luminosities reported in section 10.6.1 imply a range of Lyman continuum emission rates, $Q_{Lyc} = 3.7{\times}10^{48} \rightarrow 7{\times}10^{50}\ \mathrm{s}^{-1}$. This corresponds to cluster masses of 300 – $7{\times}10^3\mathrm{M}_\odot$ for zero-age clusters (see Figure 10.21). For cluster masses exceeding $\sim 5{\times}10^3\mathrm{M}_\odot$, the IMF is populated up to within 20% of the upper mass limit (for an IMF extending between 1 – $120\mathrm{M}_\odot$). Above this mass, the stellar population is saturated (Oey and Clarke 1999) and the Lyman continuum production rate grows linearly for further increases in the cluster mass. Approximately 20% of the cluster mass is in OB stars with $m_* \geq 10\mathrm{M}_\odot$. If the Salpeter IMF is extended to $0.1\mathrm{M}_\odot$, the total mass is increased by a factor of 2.5.

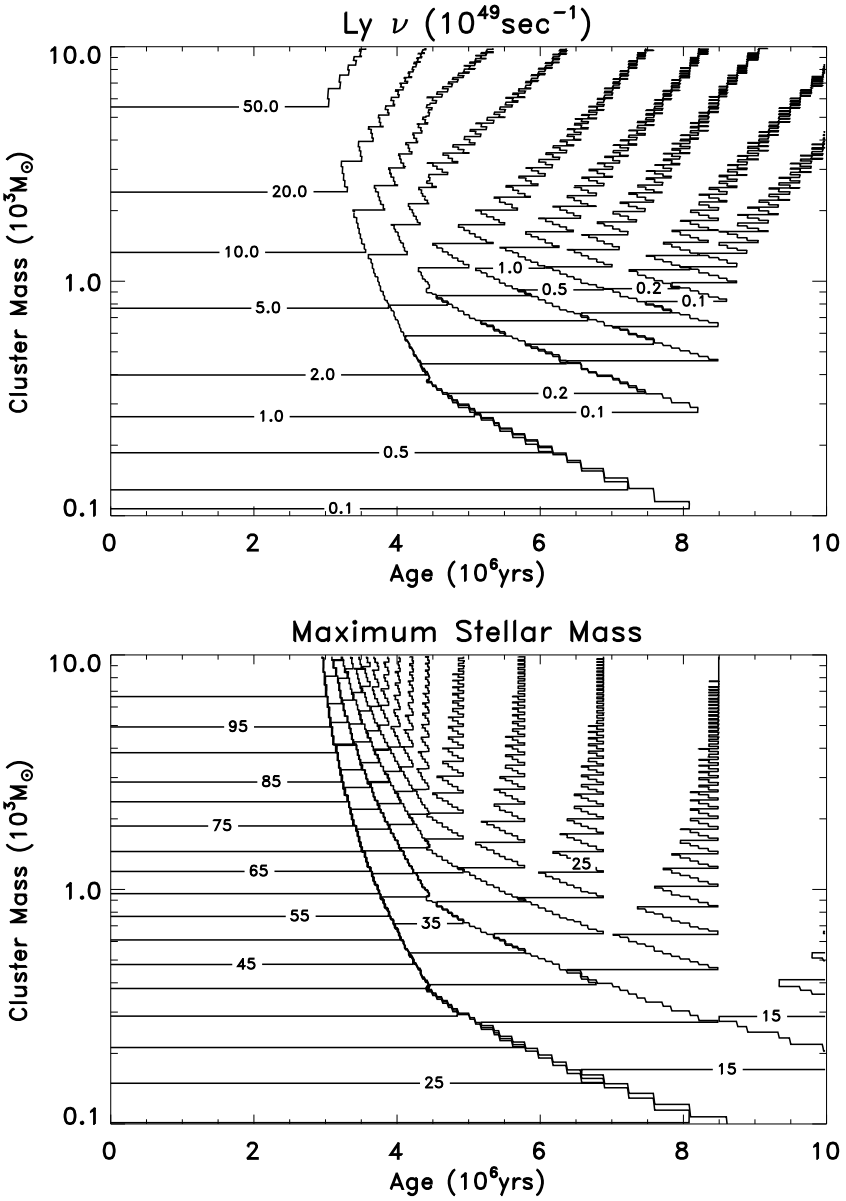

Figure 10.20: The Lyman continuum emission rate (top) and maximum mass star (bottom) are shown in contour form as functions of cluster age and total cluster mass (with stars distributed with a Salpeter IMF between 1 and 120$M_\odot$). The jagged features in the contours are due to main sequence expiration at successively lower mass OB stars as the clusters age.

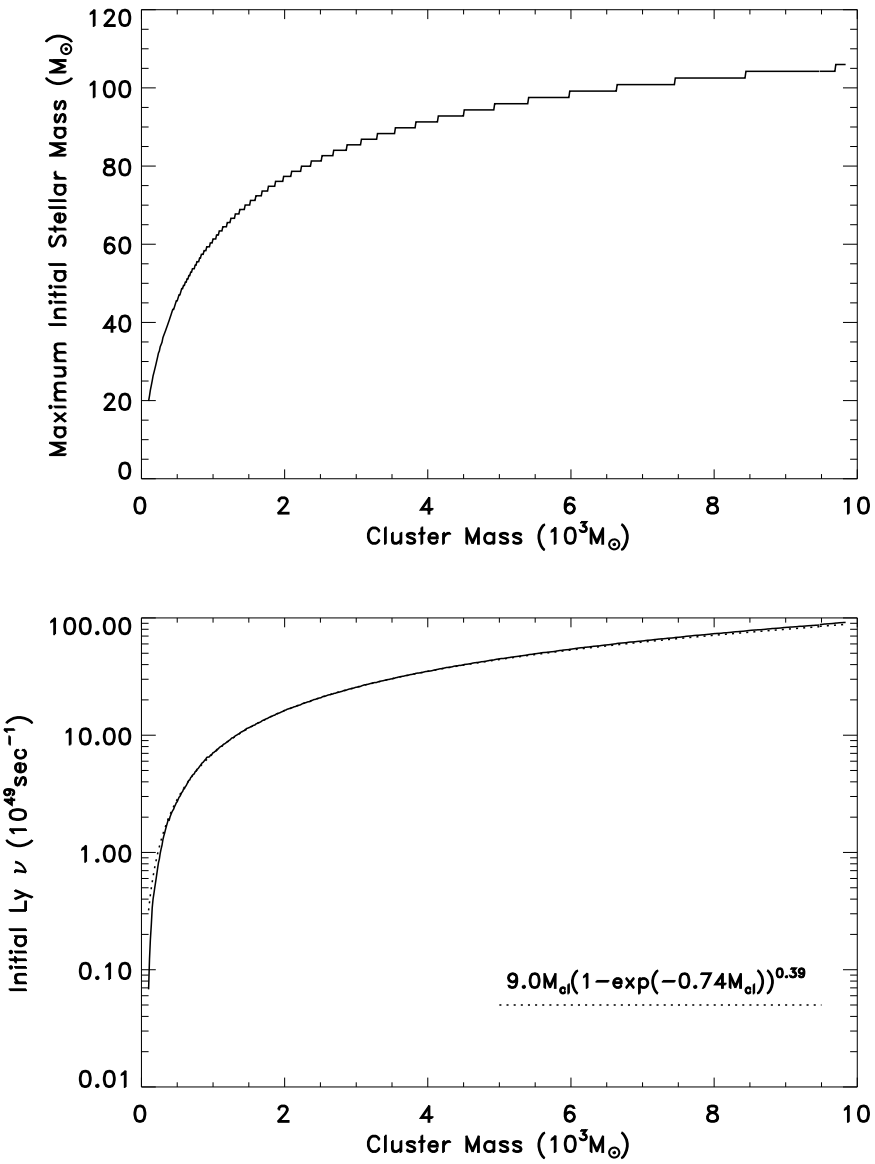

Figure 10.21: The initial maximum stellar mass (top) and the initial (zero age) Lyman continuum emission rate (bottom) are shown as functions of the total cluster mass. In the bottom panel, the solid line is the result of numerical integration of the stellar mass function and Lyman production rates and the dotted line is a functional fit to these results (in units of 10^{49} s^{-1} for cluster masses in units of $10^3 M_\odot$). (See equation (10.6).)

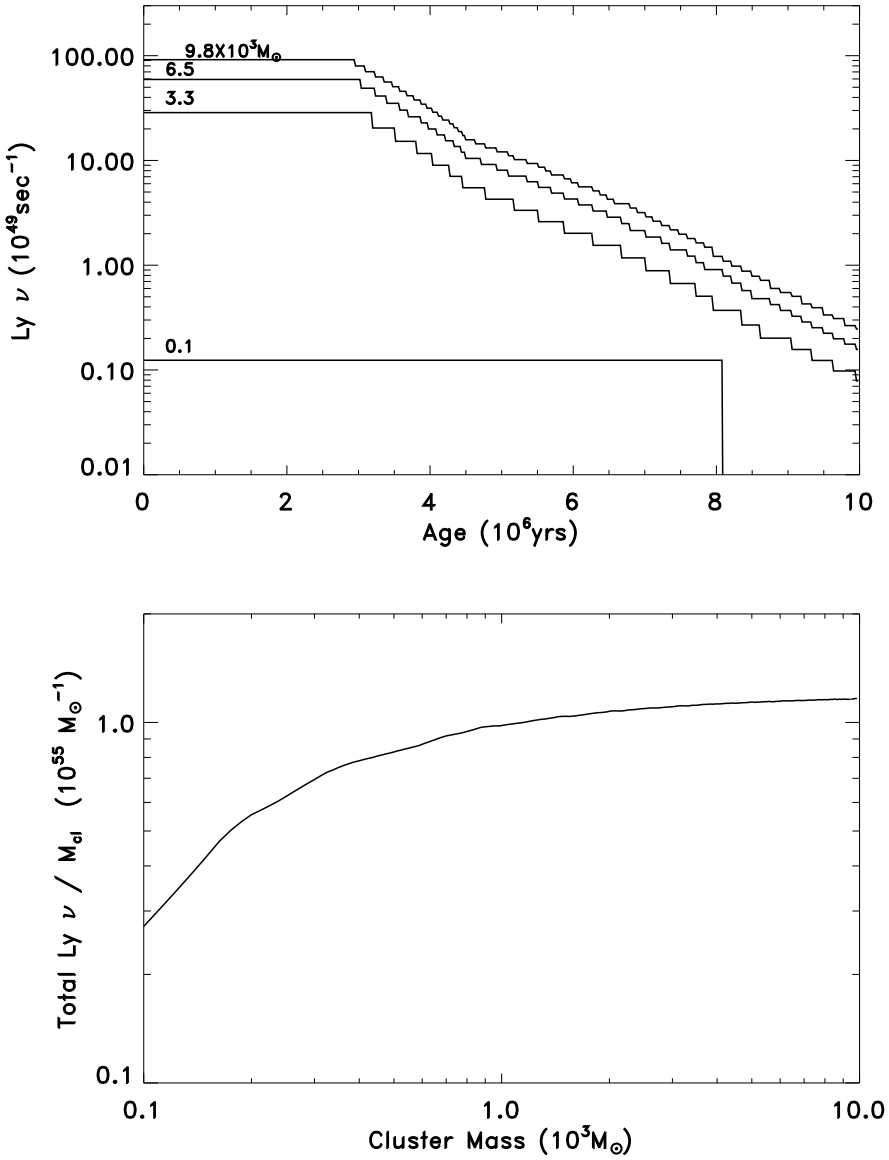

Figure 10.22: The top panel shows the Lyman output of clusters with initial masses of 0.2, 3.4, 6.6, and 9.9 $\times 10^3 M_\odot$. The steps are due to the main sequence termination of successively lower mass stars as the cluster ages and the decay is approximately exponential in time with an e-folding time of $\sim 3 \times 10^6$ yrs. The bottom panel shows the total MS Lyman continuum output (per unit mass of the cluster) integrated over the cluster life.

10.10.4 HII Region Luminosity Functions

Assuming approximately coeval star formation, the temporal evolution of the Lyman continuum luminosity from the clusters is determined by stellar evolution of the highest-mass stars. The luminosity function of the HII regions can then be modelled by sampling uniformly in time the Lyman output from each cluster mass, weighted by the initial mass distribution of clusters.

In analogy with the treatment of stellar IMF, we assume that the initial **cluster** masses can also be represented as a power-law:

$$\frac{N(\mathrm{M}_{cl})}{d\mathrm{M}_{cl}} \propto \mathrm{M}_{cl}^{\Gamma}. \tag{10.10}$$

In Figure 10.23-top, the normalized number-density of clusters per logarithmic interval in Ly continuum output is shown as a function of Γ; in Figure 10.23-bottom, the resulting power-law index for the logarithmic luminosity functions is shown. Sample luminosity functions for 5 values of the mass power-law index $\Gamma = 0 \rightarrow -4.5$ are plotted in Figure 10.24.

The temporal evolution of the Lyman output is similar for clusters above $\sim 10^3 \mathrm{M}_{\odot}$ and these clusters dominate the high end of the luminosity function. The power-law index of the cluster mass distribution therefore directly determines the luminosity function index. The model luminosity functions in Figure 10.24 clearly show that flat or nearly flat distributions of cluster mass are ruled out since they imply a very broad luminosity-function peak and a precipitous falloff (at a luminosity determined by the upper limit to the cluster masses, here taken to be 10^4 $\mathrm{M}_{\odot}$). On the other hand, a reasonable match to the observed luminosity function can be obtained with Γ in the range $-2.8 \rightarrow -3.2$ (see Fig. 10.23-bottom) for the observed luminosity range. We conclude therefore that the cluster logarithmic mass spectrum has a power-law index $\Gamma \sim -3$ and $N(\mathrm{M}_{cl})/d\mathrm{M}_{cl} \propto \mathrm{M}_{cl}^{-3}$.

Subsequent to our work, we discovered that Thilker et al. (2001) had done a similar analysis modeling a power law distribution of initial cluster masses to obtain the mass spectrum from fitting the HII region luminosity function. They obtain $N(\mathrm{M}_{cl})/d\mathrm{M}_{cl} \propto {\mathrm{M}_{cl}}^{-1.75 \rightarrow -2.25}$. Allowing for the fact that the luminosity derived here is steeper by 0.6 in the exponent, their result is reasonably consistent with ours. Both studies, taken together, provide strong evidence of a steeply falling cluster mass spectrum.

10.10.5 Upper 'Cutoff' of Cluster Mass

The existence of an upper 'cutoff' luminosity ($\mathrm{Q}_{Lyc} \sim 10^{51}$ s^{-1}) could be due to either there being an insufficient number of clusters in M51 to sample higher on the cluster mass function or to a physical limitation which limits the formation of higher mass clusters. We noted earlier that N_{up}/α should be interpreted as the expected number of clusters above L_{up} if the luminosity function were not terminated. For the luminosity function shown in Figure 10.9, $\mathrm{N}_{up}/\alpha = 6 \pm 2$. This is a 2σ departure from 0, we therefore rule out the first explanation for the cutoff.

Here we briefly explore the possibility that there is a physical mechanism limiting the buildup of clusters more massive than a few $\times 10^3$ $\mathrm{M}_{\odot}$. In the following, we track the feedback of radiation pressure on buildup of a stellar cluster in a molecular cloud core. The important role of radiation pressure in high-mass star formation has not been amply recognized.

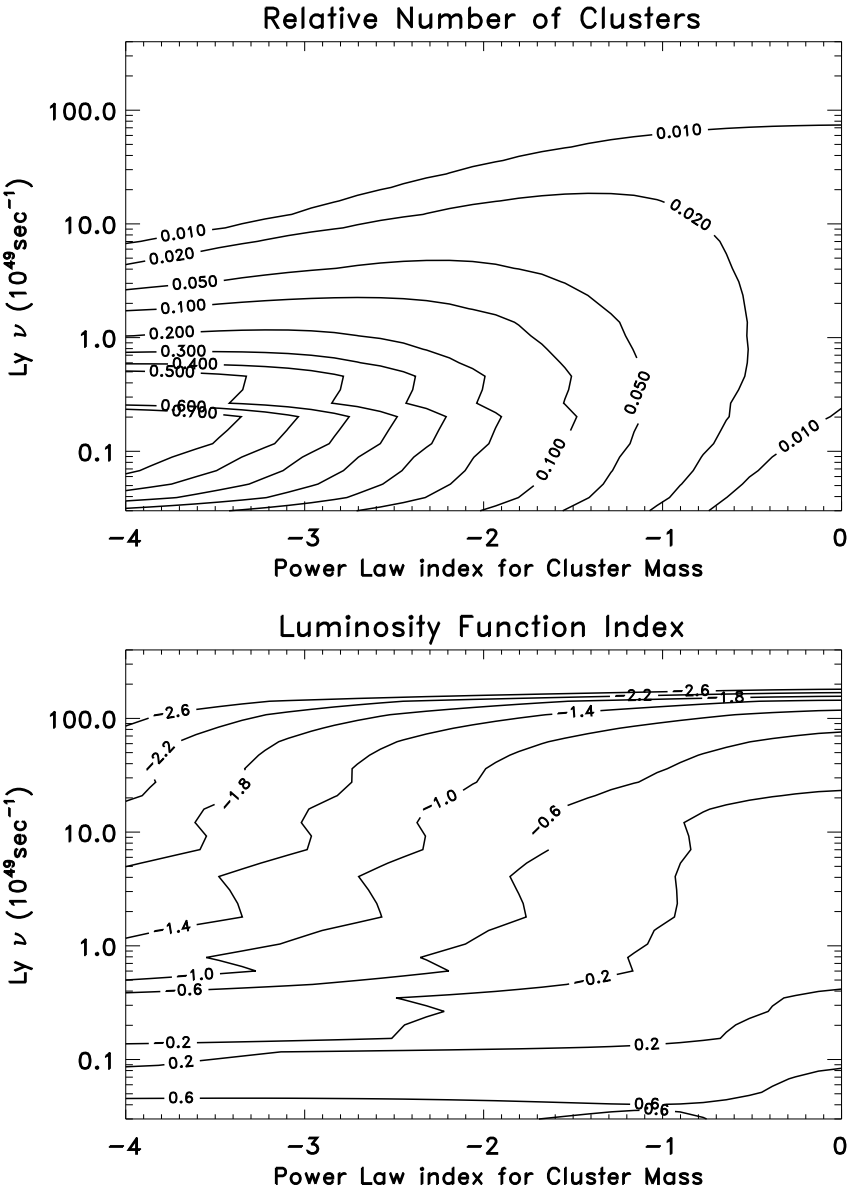

Figure 10.23: The relative number of clusters per logarithmic interval in total Lyman continuum emission rate (top) and the power-law index of the logarithmic luminosity function (bottom) are shown as a function of power-law index for the cluster mass function.

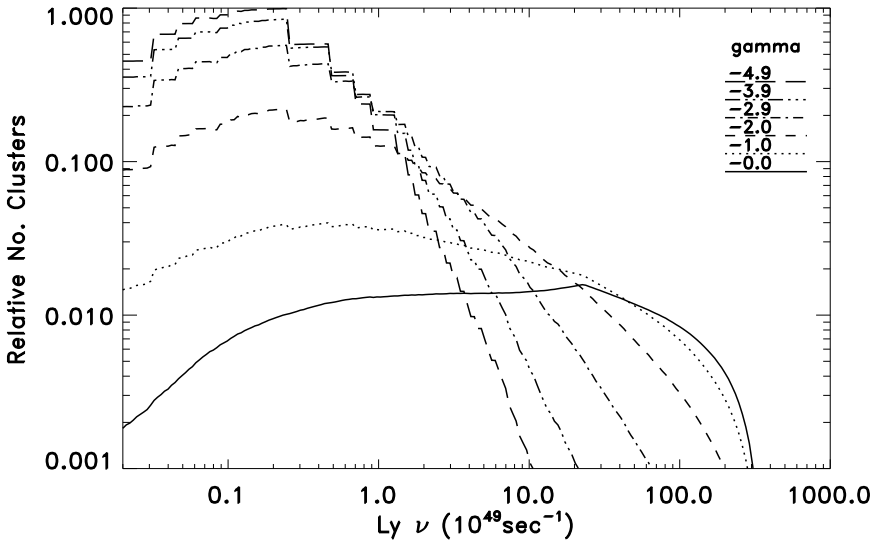

Figure 10.24: The expected luminosity functions are shown for 5 values of the cluster mass power-law index (Γ). The normalized luminosity functions per logarithmic interval in Lyman continuum emission rate were computed assuming an equal probability of observing a given cluster at any time during its active lifetime.

We posit a simple model for cluster buildup in which the protocluster forms initially at the centre of a molecular cloud core. We assume the stars within the cluster have a Salpeter IMF – thus since lower mass stars form with a higher probability the initial low mass cluster will have only low mass stars. However, as the cluster grows and becomes more massive, the IMF is populated to progressively higher mass. The gas, which was initially in free-fall, feels the gravitational attraction of the interior mass M_R (stars plus the interior core gas). We assume that gas accreted inside the adopted cluster radius is added to the cluster and the total cluster mass is instantaneously redistributed with the Salpeter IMF. (This approach thus neglects the complication that low or high mass stars might preferentially form at different epochs due differences in the physics of their formation or their different pre-main-sequence evolutionary times.) Thompson et al. (1998) find evidence that the low and high mass star formation in NGC 2264 is coeval to within 10^3–10^4 yr.

Initially, the cluster will contain only a few low-mass stars and the gas dynamics will be entirely determined by the self-gravity of the cloud core and cluster. Since we neglect rotational or magnetic stresses, this is clearly the **most favourable** situation for accretion and maximal growth of the cluster. On the other hand, as the cluster becomes more massive and populates the upper main sequence, the higher luminosity-to-mass ratio of high-mass stars will result in increased radiation pressure on the surrounding dust – eventually terminating further accretion to the cloud core. The outward radiation pressure will dominate self-gravity at radius R when

$$\frac{L < \kappa >}{4\pi R^2 c} \geq \frac{GM_R}{R^2} \tag{10.11}$$

where $< \kappa >$ is the **effective** radiative absorption coefficient per unit mass.

Although the original stellar radiation is primarily UV and visible, the dust in the cloud core absorbs these photons and reradiates the luminosity in the infrared. The 'effective' absorption coefficient takes account of the fact that outside the radius where $A_V \sim 1$ mag, the luminosity is at longer wavelengths where the dust has a reduced absorption efficiency. For the standard ISM dust-to-gas ratio (Bohlin 1975), $A_V = 1$ mag corresponds to a column $N_H = 2{\times}10^{21}$ cm^{-2}. We therefore adopt

$$< \kappa >= 312 \ \frac{\lambda_V}{\lambda_{eff}(R)} \ \ \mathrm{cm}^2 \ \ \mathrm{g}^{-1} \tag{10.12}$$

and $\lambda_{eff}(R)$ is the absorption coefficient-weighted mean wavelength of the radiation field at radius R and we adopt a λ^{-1} variation of the absorption efficiency with wavelength.

Combining equations (10.11) and (10.12), we find that the radiation pressure will exceed the gravity of the cluster stars when

$$(\mathrm{L/M})_{cl} \ \geq 42 \frac{\lambda_{eff}}{\lambda_V} \frac{\mathrm{L}_\odot}{\mathrm{M}_\odot} \tag{10.13}$$

If $\lambda_{eff} \sim 3$ μm, $\lambda_{eff}/\lambda_V \sim 10$. Thus, for clusters with luminosity-to-mass ratios exceeding $\sim$ 500 $\mathrm{L}_\odot/\mathrm{M}_\odot$, radiation pressure will halt further accretion. This luminosity-to-mass ratio is reached at about the point when the upper main sequence is first fully populated, i.e., a cluster with approximately 2000 $\mathrm{M}_\odot$; distributed between 1 and 120$\mathrm{M}_\odot$. In the above discussion, we conservatively adopt luminosities corresponding to the main sequence rather than the much larger, short term pre-MS luminosities. This assumption is thus most conservative in estimation of the radiation pressure effects. We have also assumed the density of dust and gas to be only a function of radius. If the material is instead contained in optically thick clumps (possible individual pre-stellar condensations) or a disk, then the strength of the radiation pressure compared to gravity is reduced by a factor which depends on the opacity of the clumps and their areal covering factor at each radius. Since neither of these factors are constrained by existing observations, we have adopted the simplest case of uniform areal coverage and spherical symmetry.

In the above, we assumed the most favourable conditions for cluster growth – free-fall collapse and no rotational or magnetic impediments. Additional outward pressure can of course arise from the hot ionized gas associated with the OB stars and their stellar winds; these effects are undoubtedly important later in the evolution of the cluster but they are also more dependent on the HII region geometry. By contrast, radiation pressure is inescapable during the early phases of cluster formation and therefore must play a central role in regulating the initial cluster growth. The subsequent dynamic evolution of cloud core will be affected by all three: radiation pressure, HII expansion and stellar winds.

10.10.6 OB Star Cluster Formation and Expanding Associations

To understand better the limit on the core stellar population of OB star clusters, we have numerically modelled the collapse of a cloud core with a growing star cluster. The cloud core, having an initial power-law radial density profile,

$$n = n_0 \left(\frac{R}{R_{cl}} \right)^{-2} \tag{10.14}$$

is assumed to start in free-fall collapse with $\mathrm{V}_R = \mathrm{V}_{ff} = -(2\mathrm{GM}_R/\mathrm{R})^{1/2}$. In the subsequent dynamic evolution of the cloud core, envelope gas getting inside the adopted cluster radius R_{cl} (taken to be 0.01 pc) is added to the cluster with an efficiency of 50%. At each time step, the cluster mass is distributed into stars with a Salpeter IMF and the cluster luminosity updated.

To compute the radiation pressure at each radius we adopt an effective wavelength for the radiation from

$$\lambda_{eff}(R) \simeq \frac{T_V \lambda_V}{(1 - e^{-\tau_V(R)}) T_D(R) + T_{cl} e^{-\tau_V(R)}} \tag{10.15}$$

where

$$T_D(R) = 70 \left(\frac{L}{10^5 \mathrm{L}_\odot} \right)^{1/5} \left(\frac{2 \times 10^{17}}{R} \right)^{2/5} \quad \mathrm{K} \tag{10.16}$$

This scaling with L and R is based on infrared observations of the OMC-1 cloud core (Werner et al. 1976). Eqs. (10.15) and (10.16) provide a reasonable approximation to the variation of dust temperature in an **optically thick** cloud heated by a central luminosity source. Due to the high opacity of the cloud core, the dust is heated mainly by reradiated emission from interior shells (as opposed to direct stellar photons). For the effective temperature of the cluster luminosity, we adopt a constant value T_{cl} = 30,000 K, independent of the cluster mass.

The Lagrangian form of the hydrodynamic equation of motion was advanced in time with gravity, thermal and radiation pressure terms. Mass shells were distributed logarithmically with the less massive shells on the inside in order that the transition from $\tau_V = 0 \rightarrow 5$ was well resolved. Artificial viscosity with a coefficient of 3 was introduced to stabilize the radiatively compressed shells (Christy 1967). The gas was taken to be isothermal with an 'effective' sound speed of 1 km s^{-1}. The initial density scale had $\mathrm{n}_0 = 10^8$ cm^{-3} at 0.01 pc and the cloud core extended out to a radius such that its total mass was $2{\times}10^4 \mathrm{M}_\odot$.

The density and velocity profiles at 50,000 yr intervals after the initial free-fall collapse are shown in Figure 10.25. As expected from the discussion above, the radiation pressure becomes dominant over gravity for the inner shells of the infalling gas when the cluster has reached $\sim 500 \mathrm{M}_\odot$. At this point, the infall of the inner shells is reversed and they rapidly accelerate outwards and collide with the still infalling, exterior shells. The outer shells have high dust opacity (to the central cluster) and therefore are not subjected to such high radiation pressures.

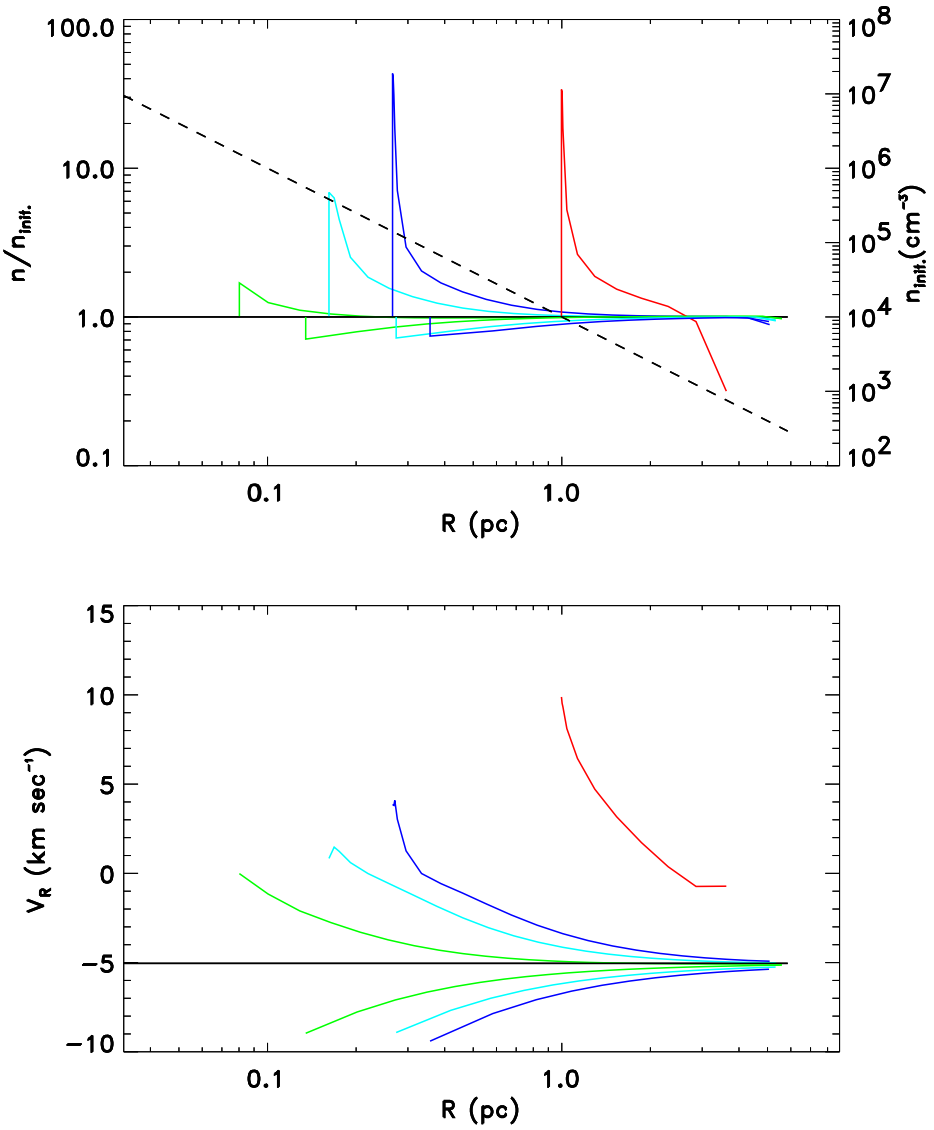

Figure 10.25: The density profile for the cloud core, cluster formation is shown at 0(black), 50(green), 100(turquoise), 150(blue), and 500(red) $\times 10^3$ yrs. The initial state was free-fall collapse in a R^{-2} density distribution normalized to 10^8 cm^{-3} at 0.01 pc. The final mass of the core cluster was $881 M_\odot$ (compared to 5800 $M_\odot$ for free-fall collapse) and the luminosity was $10^6 L_\odot$. The core accretion was fully halted by radiation pressure within 100,000 yrs. After that the radiatively compressed shell moves outward at 2 – 6 km s^{-1}. Since the compressed shell is likely to be Rayleigh-Taylor and Jeans unstable and star formation may continue in the outward moving shell.

Where the outward and inward moving gas collide, a dense, shock-compressed shell forms and accelerates outwards. Typical outward radial velocities are $\sim$ 2 to 6 km s^{-1} and the density of the shocked layer is greatly enhanced over that of the initial density profile (Figure 10.25). At this point, further accretion to the cluster core is effectively shut off. For the parameters used in this calculation, the cluster ended up with $881M_{\odot}$ after 500,000 yr. Without radiation pressure, free-fall collapse with the same parameters would have produced a cluster mass of 5800 $M_{\odot}$ in the same interval.

It is interesting to note that the outward moving shell may propagate a second phase of stimulated star formation into the cloud envelope. The compressed gas in this shell can be unstable, collapse and fragment into a second generation of stars. The density of the compressed layer is typically enhanced a factor of 100-1000, becoming 10^{5-6} cm^{-3} at radii of a few pc. At T = 50 K these densities yield a Jeans length of $\sim$ 1/3 pc and mass of $50M_{\odot}$. This second-generation star formation could become a significant enhancement to the initial cluster core mass provided the density scale n_0 is high enough. Eventually the density in the outward moving shell will drop due to spherical divergence and the falloff of the outer envelope density. The shell would then no longer be unstable and stimulated star formation would stop. Stars formed within the expanding shell will of course have a net outward radial velocity of a few km $s^{-1}$and be unbound from the core cluster. Evidence of radial expansion in OB associations is seen in the I Orion subgroup d (Trapezium cluster; Blaauw 1964) with a radial expansion of 2.5 km s^{-1} at the outer edge (R$\sim$ 0.7 pc) of the cluster. It would be interesting to analyse the Hipparcos data for nearby OB star clusters to look for evidence of similar expansions. Dreher et al. (1984) discovered a ring (R $\sim$ 0.4 pc) of ultra-compact HII regions in the W49 complex, each of which is ionized by an internal star or star cluster; it is interesting to speculate this ring of high mass star formation might correspond to the second wave of triggered star formation discussed above.

Recent observations of luminous IR galaxies have shown considerably more luminous (presumably more massive) super star clusters (SSC; e.g., Whitmore et al. 1999). In the context of the discussion above, it might be speculated that such clusters could form as a result of a particularly prodigious second-wave of triggered star formation in unusually massive and dense molecular clouds. The galaxies hosting SSCs are largely interacting starburst systems (e.g., M82 and the 'Antennae' galaxies) in which the molecular clouds are likely to be both more massive and of higher density. Clearly, if the density remains high further out from the star cluster core, the triggered wave of star formation can propagate further and generate a more massive and more extended cluster.

A similar scenario for stimulated star formation in successive OB associations was suggested by Elmegreen and Lada (1977). In their model, the compression wave was due to expansion of the hot, ionized Strömgren sphere rather than radiation pressure and the motivation was to account for the temporal sequence of **separate** OB associations. Their model is somewhat different in both the physical mechanism for gas compression and the scale – separate as opposed to individual associations. The model described above is discussed in more detail in a forthcoming paper.

10.11 Total Lyc and Star Formation Rates

The total H_{α} luminosity can be used to estimate the overall Lyman continuum output and formation rate of OB stars in M51. In doing this, we separate the diffuse and discrete HII

Table 10.4: M51 H_α and Lyman Continuum

Region	HII Type[a]	Obs. L(H_α)[b] (erg s^{-1})	$< A_V >$[c] (mag)	$f_{H_\alpha}^{ext-cor\,d}$	Ext. Cor. L(H_α)[e] (erg s^{-1})	Q_{Lyc}^{f} (s^{-1})
WFPC Area	Discrete	4.66×10^{40}	3.	9.0	4.2×10^{41}	3.1×10^{53}
WFPC Area	Diffuse	4.71×10^{40}	1.	2.1	9.9×10^{40}	7.2×10^{52}
WFPC Area	All	9.37×10^{40}			5.2×10^{41}	3.8×10^{53}
M51 Total[g]	All	1.80×10^{41}			1.0×10^{42}	7.3×10^{53}

[a]'Discrete' if contained in our HII region sample; otherwise 'diffuse'. [b]H_α luminosity. [c]Adopted visual extinction A_V in mag. [d]Factor to multiply the observed H_α by, see equations (10.6) and (10.7). [e]Extinction-corrected H_α luminosity. [f]Required Lyman continuum emission rate. [g]The total H_α flux in M51 (Rand 1992). The total extinction corrected luminosity and Q were computed by multiplying the WFPC totals by a factor 1.92, based on the ratio of the observed H_α in the WFPC and total areas.

regions and we must make corrections for the outer galaxy not covered in the WFPC2 images. In Table 4, we summarize the observed H_α luminosities, the adopted 'typical' extinctions, extinction-corrected H_α luminosities and implied Lyman continuum outputs for the separate components and regions of the galaxy.

For the discrete HII regions, we adopt $A_V = 3.2$ mag (see Sec. 7) and therefore increase their luminosity by a factor of 9 (equation (10.7)). For the diffuse gas, the extinction is probably less and we adopt $A_V \simeq 1$ mag and thus increase the diffuse luminosity by a factor of 2.1 (equation (10.6)). (The extinction of the diffuse gas could not be reliably estimated from our Pa_α since it would require extremely accurate determination of the backgrounds. The adopted 1 mag is simply based on the presumption that since the diffuse gas is more widespread, both between the dust clouds and at higher scale height, its extinction is lower than for the discrete HII regions measured here.) The H_α emission in the outer galaxy which was not covered in the WFPC2 images was estimated by multiplying the luminosity measured in the WFPC2 area by a simple scale factor (= 1.92). This factor is equal to the ratio of the total observed H_α flux in M51 (Rand 1992) to that measured by us in the WFPC2 area.

The total Lyman emission rates for the WFPC2 area and M51 are 3.8 and 7.3×10^{53} s^{-1}. A first order estimate of the global OB star formation rates (SFR) can be obtained by assuming the Lyman continuum output is dominated by clusters at or above the point at which the main sequence is first fully populated. This occurs above $10^3 M_\odot$ and above this point the Lyman output is directly proportional to the cluster mass (see Figure 10.22 – bottom panel). For the initial constant phase:

$$\frac{Q_{Lyc}}{M_{cl}} = \left(\frac{10^{50}\ s^{-1}}{2000\ M_\odot}\right) = 5 \times 10^{46}\ s^{-1}\ M_\odot^{-1} \qquad (10.17)$$

for $\tau \leq 3\times10^6$ yr. Thus the two Lyman continuum outputs given above require approximately 0.76 and $1.46\times10^7 M_\odot$ of stars between 1 and $120 M_\odot$. Since the UV output drops rapidly

after 3×10^6 yr, we estimate the steady-state star formation rate as 2.5 and 4.9$M_\odot$ yr^{-1} for the WFPC2 and total M51 areas.

A more accurate estimate of the star formation rates should make use of the derived cluster mass spectrum. For a steady-state star formation, the Lyman continuum output is given by :

$$Q_{Lyc} \;=\; \iint \dot{n}_0 \; M_{cl}^{-\Gamma} \; Q_{Lyc}(M_{cl},\tau) \; dM_{cl} \; d\tau \tag{10.18}$$

where $\dot{n}_0$ is constant in the production rate of clusters (i.e., SFR = $\int \dot{n}_0 \; M_{cl}^{1-\Gamma} dM_{cl}$). In Fig. 10.26, the steady-state Lyman output is shown as a function of Γ for a SFR = 1$M_\odot$ yr^{-1} using the model developed in the previous sections with a Salpeter IMF from 1 $\rightarrow$ 120$M_\odot$ and letting the integral in τ extend longer than the lifetimes of OB stars. For the mass power index derived above for the M51 OB clusters ($\Gamma \simeq -3$), the output in steady-state is 1.75×10^{53} s^{-1} for 1$M_\odot$ yr^{-1} (Fig. 10.26) implying :

$$\begin{aligned} SFR(1 \rightarrow 120 M_\odot) &= 5.71 \times 10^{-54} \;\; Q_{Lyc} \;\; M_\odot \mathrm{yr}^{-1} \\ &= 4.18 \times 10^{-42} \;\; L(H_\alpha)_{cor} \;\; M_\odot \mathrm{yr}^{-1} \end{aligned} \tag{10.19}$$

The inferred rates are increased by a factor of 2.5 if the IMF is extended down to 0.1$M_\odot$. This relation yields a SFR for the same mass range just 18% less than that derived by Kennicutt, Tamblyn and Congden (1994). The agreement is quite amazing given the fact that their relation was derived using Kurucz (1992) model atmospheres (rather than the Vacca, Garmany and Shull 1996 observationally-constrained ionizing outputs) and they did not assume a cluster mass spectrum. Using equation (10.19), the implied star formation rates (1 $\rightarrow$ 120$M_\odot$) are 2.17 and 4.17$M_\odot$ yr^{-1} for the WFPC2 area and the entire galaxy, respectively.

The total mass of star forming gas can be estimated from single dish CO observations (e.g., Scoville and Young 1983). The H_2 mass within 4 kpc radius is approximately $3\times10^9 M_\odot$ and the total for the galaxy is $6\times10^9 M_\odot$ (Scoville and Young 1983 after scaling for an N_{H_2} / I_{CO} = 2.2×10^{22} cm^{-2} / K km s^{-1}rather than 50% larger value used there). The implied cycling times for a typical H nucleus to pass into a new generation of stars is therefore 1.2×10^9 yr for both the inner galaxy and total M51. On the one hand, this time would be shortened if the star formation associated with the HII regions extends below 1$M_\odot$; on the other hand, approximately 50% of the mass absorbed in the stars actually gets recycled back into the ISM through stellar evolution on a timescale of 10^9 yr (Norman and Scoville 1988).

10.12 Conclusions

High resolution HST imaging of H_α and Pa_α has been used to analyse the properties of HII regions and OB star formation in M51. The critical aspects of these data are : the high resolution (4 – 9 pc as compared with $\sim$100 pc in earlier ground-based imaging) which enables the clear separation of individual star formation regions, the ability to determine and correct for dust extinction using the H_α/Pa_α flux ratio and the high sensitivity which enables us to probe HII regions with luminosity well below that of M42 (the Orion Nebula). From the observational data we find:

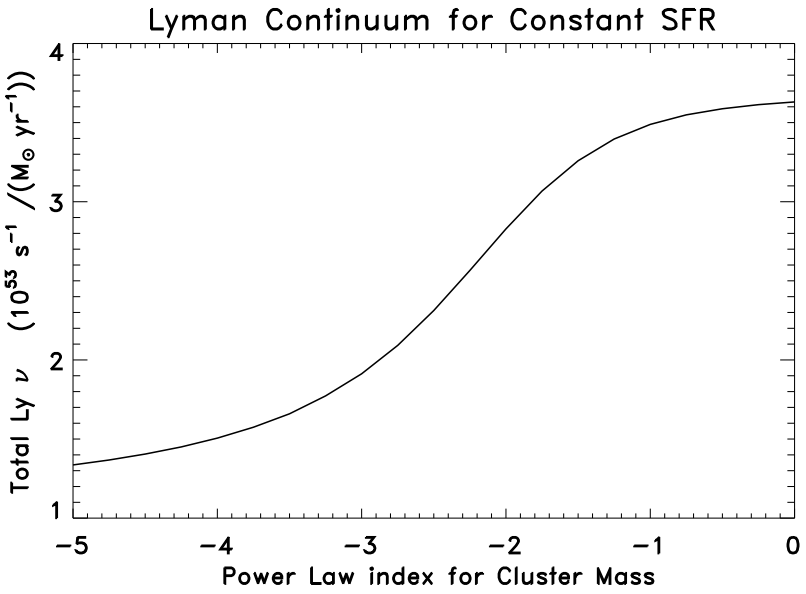

Figure 10.26: The Lyman continuum output is shown for a star formation rate which is constant for a time greater than the MS lifetime of OB stars (i.e., $\geq 5\times10^6$ yrs) for a range of power law indexes for the cluster mass spectrum. For example, for the derived index of $\Gamma \simeq$ -3, the Lyman continuum is 1.75×10^{53} s^{-1} for each 1 $M_\odot$ per yr of stars formed with a Salpeter IMF from $1 \rightarrow 120 M_\odot$.

1) A total of 1882 H_α emission regions were defined (using automated procedures). The total flux of these discrete regions constitutes about 50% of the total H_α emission in the central $281'' \times 223''$ of M51. The observed H_α luminosities range from 10^{36} to 10^{39} erg s^{-1} and their diameters are mostly from 10 to 100 pc with a mean value of $\sim$30 pc. (For the higher luminosity and usually larger regions, the mean electron density is generally lower, suggesting that some of these regions are likely to be blends of multiple HII regions.)

2) The observed H_α luminosity function exhibits a broad peak at $L(H_\alpha) \sim 10^{37}$ erg s^{-1}, falling as $L(H_\alpha)^{-1.2}$ on the high luminosity side. No evidence is seen for the break in the luminosity function at $\log(L(H_\alpha))=10^{38.6}$ erg s^{-1} reported in ground-based studies. Compared with ground-based determinations, the luminosity function derived here is much less populated at high luminosity – very likely most of the regions above 10^{39} erg s^{-1} seen in ground-based studies were blends of multiple lower luminosity regions which are separated here.

3) Significant differences are seen in the luminosity functions of spiral arm, interarm and nuclear HII regions with the nuclear and spiral arm luminosity functions being flatter.

4) For 326 regions which had $\geq 5\ \sigma$ detections in both Pa_α and H_α, the observed line ratios were used to derive the overlying visual extinction assuming standard Galactic dust extinction curves and intrinsic line ratios given by case B recombination. The implied extinctions range from $A_V = 0$ to 5 mag, with an intensity-weighted mean value of $< A_V > = 3.2$ mag. Thus the observed H_α luminosities should be increased by an average factor of 9.5, implying similar increases in the OB star cluster luminosities and implied star formation rates. The high extinctions underscore the need for extinction estimates in analyzing the properties of

HII regions and their associated OB star clusters.

5) The extinctions are also highly variable from region to region and across individual regions. (In deriving the estimates quoted above, the line ratios were computed pixel by pixel and then averaged over each region.)

In addition to the observational data, we have modelled the Lyman continuum luminosity as a function of total cluster mass with stars distributed with a Salpeter IMF (1 – 120$M_\odot$) and as a function of cluster age. This model is used to derive the cluster properties. We find:

1) If the full range of extinction corrected H_α luminosities is between 10^{37} and 10^{39} erg s^{-1}, the implied cluster masses are in the range 300 – 7000$M_\odot$. This is roughly comparable to HII regions ranging between M42 (the Orion Nebula) and W49 (the most luminous Galactic radio HII region). The implied masses are increased by a factor of 2.5 if the Salpeter IMF is extended down to 0.1$M_\odot$.

2) For a power-law distribution of cluster masses, we find that the observed peak in the luminosity function at 10^{37} erg s^{-1} clearly rules out flat or slowly falling cluster mass spectra. The observed -1.2 power-law index on the high luminosity tail of the luminosity distribution implies a cluster mass spectra $N(M_{cl})/dM_{cl} \propto M_{cl}^{-3}$.

3) The highest mass clusters are approximately 2000$M_\odot$. The parent molecular clouds are much more massive and one must ask: why do not the OB star clusters generally build up to much greater mass? We suggest that the formation of a massive cluster in a molecular cloud core is likely to be terminated at the point when the luminosity-to-mass ratio of the cluster reaches $\sim$500 $L_\odot/M_\odot$; when radiation pressure begin to dominate the self-gravity of the cluster. This is roughly the point at which the Salpeter IMF first becomes fully populated.

4) A hydrodynamic model with an initial R^{-2} density distribution in free-fall collapse verifies that the core star cluster is likely to self-limit at $\sim 10^3 M_\odot$. At this point, radiation pressure effectively terminates further gas and dust accretion to the central core. However, we also find that a radiatively-compressed shell will then propagate outwards at a few km s^{-1}, possibly triggering a second wave of star formation out to a few pc radius. This may, in fact, be the mechanism for forming the more massive star clusters (SSC) seen in starburst galaxies where the densities are likely to be higher out to larger radii in the cloud envelopes. The stars formed in the expanding shell will have significant outward radial motion and will probably be unbound.

Lastly, we have combined our modelling results with measurements of the total line emission to evaluate the total Lyman continuum output and global star formation rate. From the extinction-corrected H_α luminosity, we find $Q_{Lyc} = 7\times10^{53}$ s^{-1} and SFR(1-120$L_\odot$) = 4.17 $M_\odot$ yr^{-1} using the derived cluster mass spectrum.

The NICMOS project has been supported by NASA grant NAG 5-3042 to the NICMOS instrument definition team. This paper is based on observations with the NASA/ESA Hubble Space Telescope obtained at the Space Telescope Science Institute, which is operated by Association of Universities for Research in Astronomy, Incorporated, under NASA contract NAS5-26555. We are very grateful to Rich Rand for several discussions during the course of our work and for permitting us access to his H_α images. We also thank David Thilker for sharing his HII region photometry software with us and for extremely helpful discussions on our mutual results. We also thank Zara Turgel for proofreading and comments on the manuscript.

Bibliography

Aalto-Bergman S., Huetemeister S., Scoville N.Z., Thaddeus P. 1999, ApJ, 522, 165
Blaauw A. 1964, ARA&A, 2, 214
Bohlin R.C. 1975, ApJ, 200, 402
Bushouse H.A., Stobie E. 1998, ADASS, 7, 300
Cardelli J.A., Clayton G.C., Mathis J.S. 1989, ApJ, 345, 245
Christy R.F. 1967, in "Methods in Computational Physics" (New York: Academic Press)
Dreher J.W., Johnston K.J., Welch W.J., Walker R.C. 1984, ApJ, 283, 632
Elmegreen B.G., Lada C.J. 1977, ApJ, 214, 725
Ford H., Tsvetanov Z., Kriss G. 1996, AAS, 188, 1602
Greenawalt B., Walterbos R.A.M., Thilker D., Hoopes C.G. 1998, ApJ, 506, 135.
Kennicutt R.C., Edgar B.K., Hodge P.W. 1989, ApJ, 337, 761
Kennicutt R.C., Tamblyn P., Congden C.W. 1994, ApJ, 435, 22
Kurucz R. 1992, (private communication)
Maeder A. 1987, A&A, 173, 247.
Massey P., Lang C.C., DeGoia-Eastwood K., Garmany C.D. 1995, ApJ, 326, 188
McKee C.F., Williams J.P. 1997, ApJ, 476, 144
Norman C., Scoville N.Z. 1988, ApJ, 332, 124
Oey M.S., Clarke C.J. 1998, AJ, 115, 1543
Osterbrock D.E. 1989, "Astrophysics of Gaseous Nebulae, Active Galactic Nuclei" (Mill Valley, Ca: University Science Books)
Petit H., Hua C.T., Bersier D., Courtes G. 1996, A&A, 309, 446
Pleuss P.O., Heller C.H., Fricke K.J. 2000, A&A, 361, 913
Polletta M., Scoville N.Z., Ewald S.P., Stolovy S.P. et al. 2001, (in preparation)
Rand J.R. 1992, AJ, 103, 815
Rand J.R., Kulkarni S.R. 1990, ApJ, 349, L43
Renzini A., Buzzoni A. 1986, in "Spectral Evolution of Galaxies", eds. C. Chiosi, A. Renzini (Dordrecht: Reidel), p. 195.
Rieke M.J. et al. 2001, (in preparation)
Rieke G.H., Lebofsky M.J. 1985, ApJ , 288, 618
Roberts W.W., Stewart G.R. 1987, ApJ, 314, 10
Rozas M., Beckman J.E., Knapen J.H. 1996, A&A, 307, 735
Sandage A., Tammann G.A. 1975, ApJ, 196, 313
Scalo, J. 1987, in "Starbursts, Galaxy Evolution" eds. T.X. Thuan, T. Montmerle, J. Than Thanh Van (Paris: Editions Frontieres), p. 445
Schraml J., Mezger P.G. 1969, ApJ, 156, 269
Selman F., Melnick J., Bosch G., Terlevich R. 1999, A&A, 341, 98
Scoville N.Z., Young J. 1983, ApJ, 265, 148
Smith T.R., Kennicutt, R.C. 1989, PASP, 101, 649
Thilker D.A., Braun R., Walterbos R. A.M. 2000, AJ, 120, 3070
Thilker D.A., Walterbos R.A. M., Braun R., Hoopes C.G. 2001, AJ (submitted)
Thompson R.I., Corbin M.R., Young E., Schneider, G. 1998, ApJ, 492, L177
Tully R.B. 1974, ApJS, 27, 437
Vacca W.D., Garmany C.D., Shull J.M. 1996, AJ, 460, 914
van der Hulst J.M., Kennicutt R.C., Crane P.C., Rots A.H. 1988, A&A, 195, 38
Wang J.C.L., Heckman T.M., Lehnert M.D. 1997, ApJ, 491, 114
Werner M.W., Gatley I., Harper D.A., Becklin E.E. et al. 1976, ApJ, 204, 420
Whitmore B.C., Zhang Q., Leitherer C., Fall M. et al. 1999, AJ, 118, 1551

Conclusions

This is the end of a journey that began with a childhood dream of space flights and has reached the centre of distant galaxies. Our "space-ships" were the complex and fascinating orbiting telescopes ISO and HST. Their instruments, my virtual eyes, travelled through the interstellar medium of galaxies to observe stars, dust and molecular clouds.

In the cores of molecular clouds, new stars form. During their lives, stars ionize the surrounding gas and breaks apart molecules to free protons and electrons. These atomic constituents are involved with a game of recombination and separation that is traced by spectacular HII regions in preferential sites of galaxies. We explored these regions, measuring their properties (size, luminosity, density) and their spatial correlation with dust, molecular clouds and new born stars.

Our intragalactic journey continued towards the centre of galaxies where large amounts of dust are distributed. A wide range of temperatures and opacities of the dust were measured and its spatial distribution was determined. Dust is not uniformly distributed, but is organised in filaments, torii, disks, rings and lanes. The dust extinguishes optical and ultraviolet stellar light and line emission produced by the ionized gas, thus modifying the appearance and the spectral energy distribution of galaxies. These effects were studied and quantified.

In some of our galactic destinations a jet was present and extended from the unresolved nucleus to distances larger than the galaxy's major axis. The appearance of the radiation emitted by the jets depends on our position relative to the jet direction. The assumption that active galaxies with a jet are intrinsically the same allowed us to estimate the effects of the jet's presence on the radiation emitted over the entire electromagnetic spectrum. Sources without jets differ from the others only in their inner regions, while at larger distances they are quite similar.

As in many adventurous journeys, some objectives were abandoned and new directions were chosen. Below, we report some extracts from our space log:

1. NLSy1 galaxies have similar infrared properties as "classical" Seyfert 1 galaxies. The distribution of the dust produces different degrees of absorption of the radiation coming from the inner regions. These results suggest that the peculiar properties of these objects are associated to their nuclear regions (e.g., accretion disk, black hole, emission line regions) rather than to the absorbing material. (Chapter 5)

2. The infrared spectra of radio loud and radio quiet quasar has a thermal origin. In some FSRQ, the thermal component can be observed only in the near-infrared, because, the non-thermal contribution from a compact radio source can dominate at longer wavelengths. (Chapter 6)

3. Radio loud and radio quiet quasars differ intrinsically in their inner regions where high energy processes occur. This difference produces larger radio, near-infrared and X-ray luminosities in RLQ than in RQQ. Their infrared luminosities and spectra are instead very similar, suggesting analogous properties in the more external regions of the AGN. (Chapter 6)

4. The mid- and far-infrared emission in quasars is independent of their classification. This result suggests the use of far-IR observations to select complete samples of AGN. (Chapter 6)

5. High resolution optical and infrared images of M51 show complex structures of dust lanes with unprecedented detail. The width of these dust lanes ranges from $\sim$ 50 pc in the interarm regions to $\sim$ 140 – 370 pc along the arms. A quite regular net of dust filaments, spaced by $\sim$ 72$\pm$24 pc, is observed in the inner 1 kpc of radius of the galaxy. The dusty net disappears where the central stellar bar appears. (Chapter 9)

6. Strong H_α emission is observed in the nuclear region of M51 extending from the centre to $\sim$ 200 pc towards the South. This is strongly correlated with the radio emission from the jet. The observed correspondence suggests an interaction between the jet and the surrounding material. (Chapter 9)

7. From the measure of the displacement between the different tracers in the arms, an estimate of the time elapsed between the beginning of the molecular gas compression and the formation of OB stars and HII regions can be derived (after assuming a velocity pattern for the material moving through the arms). The measured offsets between the H_α and the CO peaks in the two arms compared to the arms' amplitude indicate a maximum timescale of $\sim$ 4 Myr. The distribution of starforming sites along the two spiral arms suggests a link between the star formation process and the spiral structure itself. (Chapter 9)

8. The properties (luminosity, size, density) of the HII regions in M51 have been studied with an unprecedented spatial resolution. The results deeply changed our previous knowledge about these regions thanks to the much higher spatial resolution and sensitivity of HST compared to ground-based facilities. The observed properties are similar to those of Galactic HII regions. (Chapter 10)

9. The amount of extinction that affects the ionized gas in HII regions has been measured using the ratio between the recombination lines H_α and Pa_α. The average extinction is $\sim$ 3.2 mag. The intrinsic luminosities are then 9.5 times, on average, higher than the 'apparent' luminosities. (Chapter 10)

10. A model has been developed which predicts the amount of ionizing photons emitted by a distribution of OB star clusters. By comparing the observed luminosity function of the HII regions with the output of the model, the range and the spectrum of cluster masses were derived. The mass of OB star clusters ranges between 200 and 2000 $M_\odot$ and the mass spectrum is $dN(M_{cl})/d\ln M_{cl} \propto M_{cl}^{-1.5}$. (Chapter 10)

11. The maximum mass of a OB star cluster is interpreted as a saturation limit in the process of star formation in a giant molecular cloud. The star formation is terminated when the radiation pressure begins to dominate the self-gravity of the cluster. This limit is reached when the luminosity-to-mass ratio of the cluster is $\sim$1000 $L_\odot/M_\odot$. (Chapter 10)

In addition to this list of scientific results, original methods for data reduction have been developed. These procedures were necessary for most of the data utilised in this work; both ISOPHOT and WFPC2 data. The ISOPHOT standard procedure could not remove many of the problems in the raw data discovered after ISO's launch. Part of the WFPC2 images were obtained with a single exposure. The standard pipeline for the calibration of WFPC2 images could not be applied in such a case. The impossibility to apply standard reduction procedures required a large effort in developing original reduction methods specific to our needs.

This journey gave us a general picture of the complexity of galaxies and of the difficulty in interpreting reprocessed emission (i.e., infrared radiation). In order to better understand the properties of the dust, it is necessary to know the direct emission (e.g., ultraviolet and X-ray observations) and have accurate measurements that constrain the dust composition and size distribution (e.g., infrared spectroscopy).

Appendix

Appendix A

The Initial Mass Function

A fundamental quantity for studies of stars formation is the **initial mass function (IMF)**, $\xi(M)$, that specifies the distribution in mass of a freshly formed stellar population. Specifically, just after a burst of star formation, let there be

$$dN = N_0 \xi(M) dM \tag{A.1}$$

stars with masses in $(M,\ M + dM)$. The normalizing constant N_0 depends on both the magnitude of the burst and the way ξ is normalized.

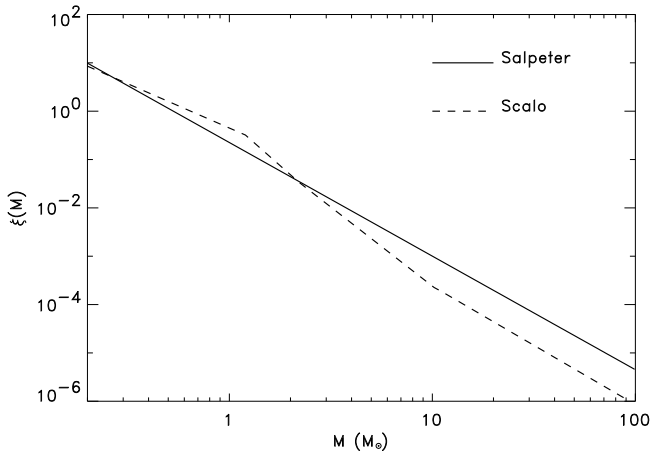

Figure A.1: The IMF, ξ(M), from Salpeter (1955) (solid curve) and from Scalo (1986) (dashed curve) plotted against the stellar mass, M, in solar units. The two curves have been normalized at a total stellar mass of 1 $M_\odot$ pc^{-2} between 0.2 and 100 $M_\odot$.

There is no *a priori* reason to suppose that ξ is a universal function that applies to all starforming regions. However, the available data are consistent with ξ having been the same at $M \leq M_\odot$ for starbursts that have occurred under remarkably different circumstances over the entire age of the Galaxy.

In the past the IMF has been suggested to vary with the peculiar physical conditions of the ISM, as for example a systematic variation of the IMF with metalcontent, in the sense that more metal-poor systems have a flatter IMF (Terlevich 1986; Melnick and Terlevich 1987).

At the moment the information characterizing the IMF in galaxies is not complete and sometimes contradictory (see Scalo 1998 for an updated review on the subject). The IMF, ξ, is frequently assumed to be a simple power of M ($\xi(M) \propto M^{-x}$). The exponent x is usually indicated as the slope of the IMF. In a classic study Salpeter (1955) concluded that the then-available evidence pointed to ξ having the spectral index $x = 2.35$. Following studies suggested that ξ steepens with increasing mass, so that the effective value of the power-law index was less than 2 at small masses and greater than 2 at large masses. Scalo (1986) derived an IMF that can be adequately fitted by three power-law segments (i.e., $\xi \propto M^{-2.45}$ for $M > 10 M_\odot$, $\propto M^{-3.27}$ for $1 M_\odot < M < 10 M_\odot$ and $\propto M^{-1.83}$ for $0.2 < M < 1 M_\odot$) for masses $M \geq 0.2$ $M_\odot$. The Salpeter and Scalo IMFs are reported in Figure A.1.

Recent observational evidences are in favor of a stellar IMF for intermediate and massive stars quite similar in the Magellanic Clouds and nearby spiral galaxies (e.g., Massey et al. 1995) and around the Salpeter form (x=2.35).

Bibliography

Massey P., Lang C.C., De Gioia-Eastwood F., Garmany C.D. 1995, ApJ, 488, 188

Melnick J., Terlevich R. 1987, in Proc. "European Regional Astronomy Meeting of the IAU", 10th, Czechoslovak Academy of Sciences, Vol. 4, 111

Salpeter E.E. 1955, ApJ, 289, 310

Scalo J.M. 1986, Fundam. Cosmic Physics, 11, 1

Scalo J.M. 1998, ASP Conference Series, Vol. 142, 201

Terlevich R. 1986, in "Star Forming Dwarf Galaxies and Related Objects", eds. D. Kunth, T.X. Thuam, and J. T. Thanh Van (France: Editions Frontières), 395

Appendix B

The Doppler Effect and the relativistic boosting

If a source of radiation (a lobe or a jet) moves at a speed $v = \beta c$ along a direction inclined of an angle θ with the line of sight, the observed frequency ν_{obs} will differ from the emitted frequency ν_{em} because of the Doppler effect. The relationship between ν_{obs} and ν_{em} is

$$\nu_{obs} = \frac{\nu_{em}}{\gamma(1 - \beta cos\theta)} = \nu_{em}\mathcal{D} \tag{B.1}$$

where $\gamma = (1 - \beta^2)^{-1/2}$ is the Lorentz factor, and $\mathcal{D}$ Doppler factor.

This effect induces changes in other observational data. Let's consider a radio source of luminosity L_{em} that moves for an observer O with a speed $\beta cos\theta$ and that is still for an observer O'. The observer O' moves at a speed $\beta cos\theta$ for the observer O. When the two observers' position coincides, the O' observer is at a distance d' from the source, and the observer O at a distance $d = d'\mathcal{D}$.

If $S(\nu_{obs})$ and $S'(\nu_{em})$ are the fluxes measured by the two observers at the respective observed frequencies in the frequency ranges $\Delta\nu$ and $\Delta\nu'$. The number of photons per unit of frequency band, per unit of area and per unit of time will be $n(\nu_{obs}) = S(\nu_{obs})/h\nu_{obs}$ and $n'(\nu_{em}) = S'(\nu_{em})/h\nu_{em}$. Since the flux of photons is conserved, we can write

$$S(\nu_{obs}) = n(\nu_{obs})h\nu_{obs} = n'(\nu_{em})h\nu_{em}\mathcal{D} = S'(\nu_{em})\mathcal{D}. \tag{B.2}$$

The flux measured by O' will appear to the observer O shifted in frequency and modified in value. By integrating equation (B.2) over the whole frequencies and taking into account the relationship between the luminosity L and the flux F, $L = F/4\pi d^2$, we derive

$$\begin{aligned} S_{tot} &= \int S(\nu_{obs})d\nu_{obs} = \int S'(\nu_{em})\mathcal{D}d\nu_{obs} = \int S'(\nu_{em})\mathcal{D}^2 d\nu_{em} \\ &= \int \frac{L(\nu_{em})}{4\pi d'^2}\mathcal{D}^2 d\nu_{em} = \int \frac{L(\nu_{em})}{4\pi d^2}\mathcal{D}^4 d\nu_{em}. \end{aligned} \tag{B.3}$$

Therefore, the total flux measured by the observer O over the whole electromagnetic spectrum is given by the total radiated luminosity as expressed by

$$S_{tot} = \frac{L(\nu_{em})}{4\pi d^2}\mathcal{D}^4 = \frac{L(\nu_{em})}{4\pi d*^2} \tag{B.4}$$

where $d* = d/\mathcal{D}$ replace the geometrical distance d.

The flux received from a radio source thus differs from the emitted flux of a factor $\mathcal{D}^4$ that will be < 1 if the source moves toward the observer and *vice versa*. The amplification due to the Doppler effect becomes more important for small inclination angles θ and for $\beta \sim 1$. This effect is called relativistic boosting or Doppler boosting or, relativistic beaming.

If the source spectrum is known, e.g., a synchrotron spectrum $S(\nu) \propto \nu^{-\alpha}$, the monochromatic flux measured by the observer O' at a frequency ν_{obs} will be related to the monochromatic flux measured by the observer O by the following equation

$$S(\nu_{obs}) = S'(\nu_{em})\mathcal{D} = \left[S'(\nu_{obs})\left(\frac{\nu_{em}}{\nu_{obs}}\right)^{-\alpha}\right]\mathcal{D} = S'(\nu_{obs})\mathcal{D}^{1+\alpha} \tag{B.5}$$

From the measured flux, we can derive the monochromatic luminosity emitted by the source at the frequency ν_{obs}

$$S(\nu_{obs}) = S'(\nu_{obs})\mathcal{D}^{1+\alpha} = \frac{L(\nu_{obs})}{4\pi d'^2}\mathcal{D}^{1+\alpha} = \frac{L(\nu_{obs})}{4\pi d^2}\mathcal{D}^{3+\alpha}. \tag{B.6}$$

The flux measured by the observer O is then $\mathcal{D}^{3+\alpha}$ times higher (or less) than the value measured in the case the source would not be moving.

The knowledge of the Doppler factor $\mathcal{D}$ is necessary to derive, from the observed flux, the total luminosity or the monochromatic luminosity emitted by the source (what an observer still in respect of the source would measure), thus removing the systematic effects due to the source motion. This is very useful in comparing objects observed at the same frequency but characterized by different motions because the frequency of the emitted radiation would be different. This is the case in radio sources when the radiation emitted by the nucleus (characterized by relativistic motion) is compared with that emitted by more extended components (characterized by slower motions).

Appendix C

List of Acronyms

AAP	Astrophysical Application Data
ADC	Analog-to-Digital Converter
AGN	Active Galactic Nucleus or Active Galactic Nuclei
AOT	Astronomical Observational Template
BLR	Broad Line Region
BLRG	Broad Line Radio Galaxy
CCD	Charge Coupled Device
COSTAR	Corrective Optics Space Telescope Axial Replacement
CRE	Cold Readout Electronics
DIG	Diffuse Ionized gas
DN	Data Number
DR	Destructive readout
EM	Emission Measure
ERD	Edited Raw Data
ESA	European Space Agency
ESO	European Southern Observatory
FCS	Fine Calibration Source
FOV	Field Of View
FPC	Focal Plane Chopping
FSRQ	Flat Spectrum Radio loud Quasar
FWHM	Full Width at Half Maximum
GMC	Giant Molecular Cloud
GT	Guarantee Time
HST	Hubble Space Telescope
IMF	Initial Mass Function
IR	Infrared
IRAC1	Infrared Array Camera 1
IRAM	*Institut de Radio Astronomie Millimétrique*
IRAS	Infrared Astronomical Saltellite
IRIS	Infrared Imaging Surveyor

IRTS	Infrared Telescope in Space
ISAS	Japanese Space Agency
ISM	Interstellar Medium or Interstellar Matter
ISO	Infrared Space Observatory
ISOCAM	ISO Camera
ISOPHOT	Imaging Photopolarimeter
IUE	International Ultraviolet Explorer
JCMT	James Clerk Maxwell Telescope
LF	Luminosity Function
LWS	Long-Wavelength Spectrometer
NASA	National Aeronautics and Space Administration
NDR	Non-Destructive readout
NGST	Next Generation Space Telescope
NICMOS	Near Infrared Camera Multi-Object Spectrograph
NLR	Narrow Line Region
NLRG	Narrow Line Radio Galaxy
NLSy1	Narrow Line Seyfert 1
PC	Planetary Camera
PG	Palomar Green
PIA	ISOPHOT Interactive Analysis
RG	Radio Galaxy
RI	Reset Interval
RIQ	Radio Intermediate Quasar
RQQ	Radio Quiet Quasar
RSG	Red Super Giant
SCP	Signal per Chopper Plateau
SCUBA	Submillimetre Common-User Bolometer Array
SED	Spectral Energy Distribution
SEST	Swedish-ESO Submillimetre Telescope
SFR	Star Formation Rate
SIRTF	Space Infrared Telescope Facility
SOFA	Selectable Optical Filter Assembly
SRD	Signal per Ramp Data
SSC	Super Star Cluster
SSRQ	Steep Spectrum Radio loud Quasar
SWS	Short-Wavelength Spectrometer
TRS	Thermal Radiation Source
ULIRG	Ultra Luminous Infrared Galaxy
UV	Ultraviolet
WFPC2	Wide Field and Planetary Camera 2

List of publications

Research papers (refereed journals):

1. *A multiwavelength catalog of Seyfert 2 galaxies observed in the 2-10 keV energy band.*
M. Polletta, L. Bassani, G. Malaguti, G.G.C. Palumbo and E. Caroli 1996, ApJS, 106, 399

2. *ISOPHOT observations of Narrow Line Seyfert 1 Galaxies.*
M. Polletta and T.J.-L. Courvoisier 1999, A&A, 350, 765

3. *The Far-Infrared emission of Radio Loud and Radio Quiet Quasars.*
M. Polletta, T.J.-L. Courvoisier, E.J. Hooper and B.J. Wilkes 2000, A&A, 362, 75

4. *HST Optical and Near Infrared Imaging of M51.*
M. Polletta, N.Z. Scoville, S.P. Stolovy, S. Ewald and S. Aalto 2001, in preparation

5. *High Mass, OB Star Formation in M51: HST H_α and Pa_α Imaging.*
N.Z. Scoville, **M. Polletta**, S. Ewald, S.P. Stolovy, R. Thompson and M. Rieke 2001, AJ submitted

Research papers (conference proceedings):

1. *A multifrequency study of the 12 micron sample of Seyfert galaxies.*
M. Dadina, **M. Polletta**, L. Bassani, G.G.C. Palumbo and G. Malaguti 1998, Advances in Space Research, Vol 21, Issue 1-2, p. 115

2. *Narrow Lines and Continuum Emission for a sample of hard X-Ray emitter Seyfert 2 Galaxies.*
M. Polletta, L. Bassani, E. Caroli, G. Malaguti, A. Malizia and G.G.C. Palumbo 1997, ASP Conference Series, Vol. 113, p. 347

3. *Hard X-Ray emission from Seyfert 2 Galaxies.*
M. Polletta, L. Bassani, G. Di Cocco, G. Malaguti and G.G.C. Palumbo 1997, ESA-SP, 382, p. 451

4. *Hard X-Ray emission from Seyfert 2 Galaxies.*
M. Polletta, L. Bassani, G. Di Cocco, G. Malaguti and G.G.C. Palumbo 1997, MmSAI, Vol. 68, p. 143

5. *ISOPHOT observations of the far-infrared luminous galaxy IRAS 13324-3809.*
M. Polletta, T.J.-L. Courvoisier and R. Walter Proceedings of the workshop: "Taking ISO to the limits: exploring the faintest sources in the infrared" 1997, R. J. Laureijs and D. Levine (eds.)

6. *The Integral Science Data Centre.*
T.J.-L. Courvoisier, **M. Polletta** and M. Türler Proceeding of the 3^{rd} Integral Workshop: "The Extreme Universe", Taormina (Italy), September 1998, Gordon and Breach (eds.)

7. *ISOPHOT observations of Narrow Line Seyfert 1 Galaxies.*
M. Polletta and T.J.-L. Courvoisier 1999, ESA-SP, 427, p. 953

8. *ISOPHOT observations of narrow-line Seyfert 1 galaxies.*
M. Polletta and T.J.-L. Courvoisier 2000, New Astronomy Reviews, Vol. 44, p. 551

9. *The Radio and Far-Infrared emission of Radio Loud and Radio Quiet Quasars.*
M. Polletta, T.J.-L. Courvoisier, E.J. Hooper and B.J. Wilkes 2001, New Astronomy Reviews, in press

10. *Starbursting in Spiral Arms and ULIRGs.*
N.Z. Scoville and **M. Polletta** in Proc. of "Starburst Galaxies: Near and Far", 2001, in press